Regenerative Matrices for Oriented Bone Growth in Craniofacial and Dental Repair

Jennifer Patterson

A dissertation submitted in partial fulfillment
of the requirements for the degree of

Doctor of Philosophy

University of Washington

2007

Program Authorized to Offer Degree: Bioengineering

University of Washington
Graduate School

This is to certify that I have examined this copy of a doctoral dissertation by

Jennifer Patterson

and have found that it is complete and satisfactory in all respects,
and that any and all revisions required by the final
examining committee have been made.

Chair of the Supervisory Committee:

Patrick S. Stayton

Reading Committee:

Patrick S. Stayton

Cecilia M. Giachelli

Xingde Li

Date: 9/06/07

In presenting this dissertation in partial fulfillment of the requirements for the doctoral degree at the University of Washington, I agree that the Library shall make its copies freely available for inspection. I further agree that extensive copying of this dissertation is allowable only for scholarly purposes, consistent with "fair use" as prescribed in the U.S. Copyright Law. Requests for copying or reproduction of this dissertation may be referred to Proquest Information and Learning, 300 North Zeeb Road, Ann Arbor, MI 48106-1346, 1-800-521-0600, to whom the author has granted "the right to reproduce and sell (a) copies of the manuscript in microform and/or (b) printed copies of the manuscript made from microform."

Signature Jennifer Patrow

Date 9/06/07

University of Washington

Abstract

Regenerative Matrices for Oriented Bone Growth in Craniofacial and Dental Repair

Jennifer Patterson

Chair of the Supervisory Committee:
Professor Patrick S. Stayton
Bioengineering

Non-healing fractures can result from trauma, disease, or age-related bone loss. While many treatments focus on restoring bone volume, few try to recapitulate bone organization. However, the native architecture of bone is optimized to provide its mechanical properties. Hyaluronic acid (HA) hydrogel scaffold systems with tunable degradation properties were developed for the controlled delivery of osteoinductive and angiogenic growth factors, thus affecting the quantity and quality of regenerated tissue. First, scaffolds delivering bone morphogenetic protein-2 (BMP-2) were evaluated in a rat calvarial bone critical size defect model. BMP-2 delivery from the HA hydrogels had a clear osteoinductive effect *in vivo*. The temporal progression of this effect could be modulated by altering the degradation rate of the scaffold. Interestingly, all three degradation rates tested resulted in similar amounts of bone formation at the latest (six week) time point examined. However, the fastest and slowest degrading scaffolds seemed to result in more organized bone than the intermediate degrading scaffold, which was designed to degrade in 6-8 weeks to match the healing time. Second, this defect model was modified to allow non-invasive imaging using optical coherence tomography (OCT) to temporally characterize tissue regeneration in living animals. The temporal progression of healing could be observed by imaging the migration of

the bone/defect interface over time, particularly for animals receiving HA hydrogels loaded with BMP-2. Additionally, structures consistent with the neovascularization of the implant could clearly be observed at later time points for animals receiving HA hydrogels loaded with vascular endothelial growth factor (VEGF). These structures correlated with the location of blood vessels seen in histological sections and showed interconnectivity and branching in three dimensions.

TABLE OF CONTENTS

LIST OF FIGURES

LIST OF TABLES

ABBREVIATIONS

1,25-$(OH)_2D_3$: 1,25-dihydroxyvitamin D_3

2-D: Two-dimensional

3-D: Three-dimensional

AAV: Adeno-associated Virus

ABTS: 2,2'-Azinobis[3-ethylbenzothiazoline-6-sulfonic acid]

ALP: Alkaline Phosphatase

ANG: Angiopoietin

BAG-75: Bone Acidic Glycoprotein-75

BCA: Bicinchoninic Acid

BMA: *n*-butyl-methacrylate

BMP: Bone Morphogenetic Protein

BMU: Basic Multicellular Unit

BSA: Bovine Serum Albumin

BSP: Bone Sialoprotein

CAM: Chorioallantoic Membrane

CBFA1: Core Binding Factor Alpha 1

CD44: Cluster of Differentiation 44

CIA: Chondrogenic-Inducing Activity

CNTF: Ciliary Neurotrophic Factor

CO_2: Carbon Dioxide

D_2O: Deuterium Oxide

DBM: Demineralized Bone Matrix

DI: Distilled

DMAP: Dimethylaminopyridine

DMSO: Dimethyl sulfoxide

DMEM: Dulbecco's Modified Eagle's Medium

DRG: Dorsal Root Ganglia

DS: Degree of Substitution

DTT: 1,4-dithio-DL-threitol

ECM: Extracellular Matrix

EDTA: Ethylenediamine Tetraacetic Acid

ELISA: Enzyme-linked Immunosorbent Assay

EMF: Embryonic Rat Muscle Fibroblasts

FBS: Fetal Bovine Serum

FGF: Fibroblast Growth Factor

FITC: Fluorescein Isothiocyanate

FIZ: Fibrous Interzone

FLT-1: Fms-Like-Tyrosine Kinase-1 (VEGFR-1)

GAPDH: Glyceraldehyde-3-Phosphate Dehydrogenase

GM-CSF: Granulocyte Macrophage-Colony Stimulating Factor

GMA: Glycidyl Methacrylate

GST: Glutathione-S-Transferase

H&E: Hematoxylin and Eosin

HA: Hyaluronic Acid

HA-GMA: Glycidyl Methacrylate Modified HA

HA-MA: Methacrylic Anhydride Modified HA

HAEC: Human Aortic Endothelial Cells

HEPES: 4-(2-hydroxyethyl)-1-piperazine ethane sulfonic acid

HEPES-BSS: HEPES Buffered Saline Solution

HGH: Human Growth Hormone

HGF: Hepatocyte Growth Factor

HIF-1: Hypoxia-Inducible Factor-1

HMW: High Molecular Weight

IACUC: Institutional Animal Care and Use Committee

IGF: Insulin-like Growth Factor

IHC: Immunohistochemistry

IL: Interleukin

I.V.: Inherent Viscosity

KDA: Kilodaltons

KDR: Kinase Domain Region (VEGFR-2 or Flk-1)

LIF: Leukemia Inhibitory Factor

LMW: Low Molecular Weight

MA: Methacrylic Anhydride

LPS: Lipopolysaccharide

LRAP: Leucine-Rich Amelogenin Peptide

MCF: Microcolumn Formation Zone

M-CSF: Macrophage-Colony Stimulating Factor

ME: Molar Excess

MICROCT: Microcomputed Tomography

MMP: Matrix Metalloproteinase

MWCO: Molecular Weight Cutoff

NACL: Sodium Chloride

NF-κB: Nuclear Factor-κB

NGF: Nerve Growth Factor

NIDCR: National Institute of Dental and Craniofacial Research

NMR: Nuclear Magnetic Resonance

NVP: 1-vinyl-2-pyrrolidinone

OCCM-30: Immortalized Murine Cementoblasts

OCIF: Osteoclastogenesis Inhibitory Factor

OCN: Osteocalcin

OCT: Optical Coherence Tomography

ODF: Osteoclast Differentiation Factor

OPG: Osteoprotegerin

OPN: Osteopontin

OSM: Oncostatin M

OSX: Osterix

PB: Phosphate Buffer

PBS: Phosphate Buffered Saline

PDGF: Platelet-Derived Growth Factor

PECAM: Platelet/Endothelial Cell Adhesion Molecule-1

PEG: Polyethylene glycol

PEO: Poly(ethylene oxide)

PGA: Poly(glycolic acid)

PGE_2: Prostaglandin E2

PLGA: Poly(lactide-co-glycolide)

PLGF: Placental Growth Factor

PMF: Primary Matrix or Mineralization Front

PPF: Poly(propylene fumarate)

PTH: Parathyroid Hormone

PVA: Poly(vinyl alcohol)

RANK: Receptor Activator of Nuclear Factor-κB

RANKL: Receptor Activator of Nuclear Factor-κB Ligand

RBC: Red Blood Cell

RECA: Rat Endothelial Cell Antigen

RGD: Arginine-Glycine-Aspartic Acid

RHAMM: Receptor for HA-Mediated Mobility

RSA: Rat Serum Albumin

RT: Room Temperature

RT-PCR: Reverse Transcription Polymerase Chain Reaction

SDS: Sodium Dodecyl Sulfate

SEM: Scanning Electron Microscopy

TBA BR: Tetrabutyl Ammonium Bromide

TEA: Triethylamine

TEM: Transmission Electron Microscopy

TGF: Transforming Growth Factor

THF: Tetrahydrofuran

TIMP: Tissue Inhibitor of Metalloproteinases

TNF: Tumor Necrosis Factor

TNFR: TNF Receptor

TRAF: TNF-Receptor-Associated Factor

TRAIL: TNF-Related Apoptosis Inducing Ligand

TRANCE: TNF-Related Activation-Induced Cytokine

TRAP: Tartrate-Resistant Acid Phosphatase

TRU: Turbidity Reducing Unit

UHMWPE: Ultra High Molecular Weight Polyethylene

UV: Ultraviolet

UW: University of Washington

VEGF: Vascular Endothelial Growth Factor

VEGFR: VEGF Receptor

VWF: von Willebrand Factor

W_D: Dry Weight

W_S: Wet (or Swollen) Weight

ACKNOWLEDGMENTS

My sincere thanks go to my supervisory committee – to my advisor, Pat Stayton, for suggesting such an interesting project; to Sue Herring, for graciously allowing me to use her surgery suite; to Xingde Li, for providing much useful advice and guidance in addition to a very interesting scientific collaboration; to Ceci Giachelli; and to David Nuckley. I would also like to thank Professor Allan Hoffman and all members of the Stayton/Hoffman lab for general support and technical guidance on the hydrogel/microsphere scaffold fabrication, especially Jeff Anderl, Chad Brown, Jason Hwang, Scott Henry, Emily Crownover, Harch Ooi, and Kenneth Liu. I would particularly like to acknowledge the undergraduate students – Ruth Siew, Aonor Wesley, and Danyelle Thomas – who have worked with me over the years.

This project would not have been possible without a number of collaborations. The OCT imaging was performed in the Biophotonics Research Laboratory, headed by Xingde Li, with assistance from Danling Wang, Yuchuan Chen, Mon Myaing, Yicong Wu, Michael Cobb, Daniel MacDonald, and Xiaoli Li. Another undergraduate student, Michael Pak, assisted immensely with image processing and analysis. Microscopy was performed in the UWEB Optical Microscopy and Microanalysis Facility, headed by Kip Hauch, with assistance from Marc Takeno and Janey Cuy. MicroCT analysis was performed by Angela Lin and Robert Guldberg and Georgia Tech and Philippe Huber and Ted Gross at the Harborview Medical Center. The OPG work was done in collaboration with Marta Scatena and Joe McGonigle, who both also provided helpful discussions on the interpretation of the *in vivo* data and on immunohistochemistry. The LRAP work was done in collaboration with Martha Somerman,

Brian Foster, and Erica Swanson. I was able to develop the "window chamber" model with helpful suggestions and equipment loans from Sue Herring and the Herring lab, including Tricia Emry and Katherine Rafferty, Michael Cunningham, Zi Jun Liu, Pam Gronbeck, and Joanne Birkner. Tissues were sectioned for histology in the UWEB Histology Lab by Kelly Simon and Rod Gamboa. Finally, I would like to thank Colleen Irvin for much useful advice and assistance starting from the early days of graduate school and continuing with the animal studies and histology.

Personally, I would not have made it through this experience of graduate school without a number of close friends and supporters: the Lab formerly known as the Bonadio Lab (Maja Zavaljevski, Joe McGonigle, Elizabeth Leber, and Colleen Irvin), my classmates (especially Jenn Foley, Elena Garcia, Kareen Kreutziger, Alicia Moreno Gonzalez, Maisie Wang, Wayne Kreider, Tony Norman, and Mircan Mujacic), my soccer teammates on Phoenix, the Seasick Pirates and the Tempestuous Monstrosities (especially Jen Flexman, Annabel Tsai, Kregg Philpott, Mike Marino, and Joaquin Drut), the UW Dance Department (especially Hannah Wiley and Jurg Koch), my roommates over the years (Mat Steuck, Rosalie Tepper, Jackie Rettig, Stephanie Yoshida), and numerous other friends (Ryan Salva, Craig Somers, Joe Tien, and Denisa Carrico).

Finally, I would like to thank my family, espcially my parents (Pat and Bill) and my sister Mary Beth (the first Dr. Patterson in the family) for their support now and over many, many years of education.

DEDICATION

To Nanny

Chapter 1
INTRODUCTION

1.1 Significance

In 2002, an expert panel convened by the The National Institute of Dental and Craniofacial Research (NIDCR) identified the "optimization of the non-biological scaffold-tissue response" [1] as well as the elucidation of "the role of angiogenesis on repair and restoration of oral, dental, and craniofacial tissues" [1] as priority research challenges and areas of opportunity for the period of 2004-2009. While these goals are quite broad, this dissertation seeks to address these areas of research by developing and evaluating materials for improved bone regeneration in craniofacial and dental applications. Specifically, the goals of this dissertation are to develop scaffolds with tunable degradation and protein release properties, to utilize these scaffolds to deliver osteoinductive and angiogenic factors in a bone defect site, and to evaluate the tissue response of the scaffolds in an animal model that incorporates noninvasive imaging in addition to standard metrics of bone formation.

Craniofacial bone loss or defect can occur as a result of trauma, genetic disorders, disease, tumor resection, or the process of aging. Over 1.3 million craniofacial bone procedures and 230,000 dental bone grafts are performed in the United States each year [2]. One in every 2,000-5,000 births suffers from a congenital craniofacial defect, such as cleft palate [3]. In addition to pathologies of the craniofacial skeleton, improved strategies for bone repair could benefit patients in orthopaedic, sports medicine, or other bone repair arenas. Osteoporosis, a decrease in bone density often associated with age, leads to fractures in the weakened bones, affecting approximately

1 million Americans each year at a cost of over $14 billion [4]. Osteonecrosis, also called avascular necrosis, results from ischemia that occurs within bone tissue through several mechanisms, including disruption of the vascular network. It is estimated that 50,000 joint replacements in the United States each year (10% of the total) are performed just to treat osteonecrotic complications [4].

The gold standard for bone repair is autograft, bone tissue harvested from another site within the patient. However, the graft size is limited, harvest requires a second surgery, and there can be problems of donor site morbidity. Bone tissue from nonautologous sources, allograft, provides an alternative graft material, but a major disincentive of its use is the potential for an immune reaction. Various synthetic materials have been developed that can provide either permanent or resorbable bone substitutes. While these approaches restore lost bone volume and (in most cases) bulk mechanical support, less attention has been paid to the microarchitecture of the regenerated bone. Degradable, regenerative matrices that direct the formation of mature bone that is ultimately indistinguishable from native, healthy bone would provide an ideal solution.

1.2 Hypothesis

The ability to regenerate spatially organized bone tissue with defined orientations relative to native bone platforms could find wide impact, particularly in dental and craniofacial bone repair. Ultrastructural analysis of cancellous regions of the craniofacial skeleton indicates that trabecular orientation is highly controlled and relates to key mechanical properties of bone [5]. More generally, organization of the collagen in bone into lamellae helps provide its strong anisotropic mechanical strength, which is optimized to withstand directional loading forces. This dissertation seeks to develop matrices for regenerating bone that would result in a well-organized lamellar architecture and that would optimize the temporal progression of healing. These scaffolds should improve healing of bone defects, result in complete tissue regeneration with no

residual scaffold, and, most importantly, improve the quality of the regenerated bone at the micro-structural level.

To achieve oriented bone growth, a strategy that incorporates osteoinductive and angiogenic factors in degradable hydrogel matrices is utilized. This approach seeks to regulate the growth of new tissue by the controlled temporal presentation of regenerative signals. It further looks to attack a fundamental challenge in the field of tissue engineering – developing the necessary vascular network within a regenerating tissue. **The main hypothesis governing this research is that controlled delivery of osteoinductive and/or angiogenic signals from degradable scaffolds may promote the formation and maturation of bone during regeneration**. Additionally, since a degradable scaffold will be used, **a secondary hypothesis is that the proper scaffold degradation rate is essential to optimize the temporal progression of healing**. An additional focus of this dissertation is to demonstrate the potential of *in situ* imaging to monitor the healing response in living animals. Optical coherence tomography (OCT), a non-invasive imaging modality, is used to follow repair and remodeling processes over time as well as to provide information about the performance of the scaffolds *in situ*.

1.3 Specific Aims

These hypotheses were tested in the following specific aims. The first three specific aims addressed the major goals of this dissertation while the fourth specific aim developed methods for the fabrication of more complex scaffolds with features that may further enhance the formation of spatially oriented bone.

1.3.1 Specific Aim 1

Design and characterize hyaluronic acid hydrogel scaffolds with controlled degradation properties for the temporal control of protein release.

1.3.2 Specific Aim 2

Test the effects of controlled release of osteoinductive and angiogenic growth factors from these hydrogel scaffolds in a critical size bone defect model and determine a scaffold degradation rate and growth factor dosage to optimize the quantity and quality of bone formed.

1.3.3 Specific Aim 3

Develop an animal model for *in situ* monitoring of healing using non-invasive imaging and evaluate angiogenesis during bone regeneration in the living animals.

1.3.4 Specific Aim 4

Develop methods for the spatial localization of growth factors within the hyaluronic acid hydrogel scaffolds.

1.4 Approach

Overall, this dissertation research developed scaffolds for bone regeneration based on hyaluronic acid (HA) hydrogel scaffolds with increasing complexity to their design. The scaffolds were tested in a bone defect model and were evaluated by standard and novel techniques to assess their effectiveness.

1.4.1 Specific Aim 1

Regenerative scaffolds were designed to control release of bio-active molecules over a period of weeks. These scaffolds consisted of a degradable hydrogel matrix directly loaded with protein. HA was selected as the matrix material because it is a naturally occurring polymer that can be enzymatically degraded and cleared *in vivo*. Further control of degradation can be engineered into the scaffolds through the addition of

hydrolytically sensitive crosslinks. The negatively charged HA should provide controlled release of cationic proteins due to electrostatic interactions. Additionally, as a hydrophilic material, HA should not be very osteoconductive on its own, which may encourage a vascular network to be established before osteoblasts migrate into the degrading scaffold. During the process of hydrogel formation, different chemical reaction strategies were used to result in hydrogels with different physical properties as well as with different degradation rates. Temporal control of protein release was evaluated for osteoinductive and angiogenic molecules, including bone morphogenetic protein (BMP)-2, vascular endothelial growth factor (VEGF), and osteoprotegerin (OPG). Additionally, biodegradable poly(lactide-co-glycolide) (PLGA) microspheres were formulated to provide additional controlled release components that could be added to the hydrogels to form composite scaffolds.

1.4.2 Specific Aim 2

Since the scaffolds designed in Aim 1 utilized novel combinations of materials and growth factors, it was necessary to demonstrate that the scaffolds could support bone growth *in vivo* as well as to examine the effect of VEGF and OPG delivery on angiogenesis and bone regeneration. The osteoinductive molecule BMP-2 was used to directly promote bone ingrowth and mineralization while the angiogenic molecule VEGF was used to promote an angiogenic response, which was hypothesized to be followed by bone growth and mineralization. Additionally, OPG, a bone protective factor with pro-angiogenic activity, and leucine-rich amelogenin peptide (LRAP), a peptide potentially involved in enamel mineralization, were evaluated in the critical size bone defect model. The degradation rate of the scaffold matrix and the dosage of growth factor used were varied to optimize the healing response. In addition to using bone volume and mineral content as measures of successful bone healing, the organization of the bone matrix was examined using histology.

1.4.3 Specific Aim 3

A novel "window chamber" modification to a traditional rat calvarial critical size defect model was developed by incorporating a viewing chamber for monitoring of angiogenesis and bone ingrowth at multiple time points during the healing process. OCT was utilized to provide high-resolution three-dimensional (3-D) images of the regenerating tissue. Further, time series of images were used to obtain temporal information about healing in the same animal. The ability of OCT to non-invasively image tissue and scaffold architecture was demonstrated and correlated with standard measurement techniques, including histology and immunohistochemistry (IHC).

1.4.4 Specific Aim 4

Spatial localization of inductive signals within the scaffold is believed to affect and possibly orient the migration of cells invading the scaffold/defect. By controlling spatial as well as temporal presentation of growth factors, an enhanced regenerative effect may be obtained. While the demonstration of this spatial effect is beyond the scope of this dissertation, methods were developed to spatially localize protein growth factors within the HA hydrogel matrix.

1.5 Outline of Thesis Contents

Chapter 2 provides background information on bone and angiogenesis as well as puts the scaffold design in the context of current tissue engineering strategies for bone regeneration. Chapter 3, addressing Aim 1, describes the design and fabrication of the HA hydrogel scaffolds. Chapters 4 and 5 examine the *in vivo* response of HA hydrogel scaffolds delivering osteoinductive and angiogenic factors, respectively, and address the goals of Aim 2. Chapter 6 describes a pilot study to test the osteoinductive effects of LRAP as well as introduces the fabrication of PLGA microspheres. These microspheres are applicable to all aims as an additional controlled release component

that can be incorporated in the scaffold design. Chapter 7 introduces the ability of OCT to perform *in situ* imaging by examining changes in scaffold morphology in an *in vitro* imaging study. Chapter 8 specifically addresses Aim 3 by describing results from a study utilizing OCT to follow the temporal progression of healing induced by HA scaffolds delivering osteoinductive or angiogenic molecules. Finally, Chapter 9 presents the overall conclusions of this dissertation research and suggests possible future research directions, including the development of methods to spatially localize proteins within the HA scaffolds, which is the focus of Aim 4.

Chapter 2
BACKGROUND

2.1 Introduction

Tissue engineering represents a burgeoning area of research that has been eloquently defined by Langer and Vacanti as "an interdisciplinary field that applies the principles of engineering and the life sciences toward the development of biological substitutes that restore, maintain, or improve tissue function" [6]. They describe this approach as utilizing three strategies for the development of new tissues: isolated cells, tissue-inducing substances, and cells in a matrix [6]. Tissue engineering further builds on the fundamentals of biomaterials science to develop matrices that can impart regenerative cues and controlled degradation in addition to simple structural support. The implementation of these strategies has provided the basis for the engineering of many tissues of the body. In this dissertation, a tissue engineering approach particularly focused on the use of tissue-inducing substances delivered from a matrix is utilized to generate scaffolds for the regeneration of bone tissue with application to the craniofacial skeleton. This Chapter first introduces the tissues, biological processes, and tissue-inducing substances of relevance. Then, the motivation for the particular scaffold design selected is described in the context of the current state of the art for bone tissue engineering treatments. Finally, the basic principles behind key methodologies used in this dissertation, particularly optical coherence tomography (OCT) and the rat calvarial critical size defect model, are reviewed.

2.2 Bone Composition and Architecture

The 206 bones of the adult human are composed of approximately 35% organic material, including cells and proteins, and 65% inorganic material, primarily the mineral hydroxyapatite [4]. Most bones are comprised of two types of tissue: cortical or compact bone, which forms a dense outer shell (10% porosity), and trabecular or cancellous bone, which is located in the more porous core (50-90% porosity) [7]. The ratio of cortical to trabecular bone is dependent on the anatomical location and function of a given bone. The bones of the craniofacial skeleton, which are of particular interest given the proposed application of this research, primarily have the characteristic of a thin cortical layer surrounding trabecular bone [8].

The major protein found in bone, type I collagen, is responsible for the spatial organization of bone. Figure 2.1 shows differences in bone morphology — woven bone and lamellar bone — that result from two different patterns of collagen orientation. Newly formed bone, called woven bone, is most commonly found in the embryonic skeleton and fracture callus [7], i.e., sites of bone formation or regeneration. Characterized by collagen deposited in a random manner, woven bone has the advantages of rapid formation and isotropic mechanical properties. Mineralization within woven bone is irregular, varying in mineral deposit size and orientation relative to the collagen fibrils [7].

As bone matures, the collagen fibrils are oriented into parallel layers four to twelve micrometers thick called lamellae, which impart directionality to the mechanical properties of the bone [7]. Lamellar bone is stronger than woven bone; however, lamellar bone behaves anisotropically [7]. The collagen component itself, through fibril organization and integrity, affects to the mechanical properties of bone [9]. Specifically, the collagen matrix organization affects the toughness of bone whereas the mineral component of bone contributes to its stiffness [10]. The collagen fibril organization also results in more uniform distribution of mineral deposits [7]. Hydroxyapatite crystals

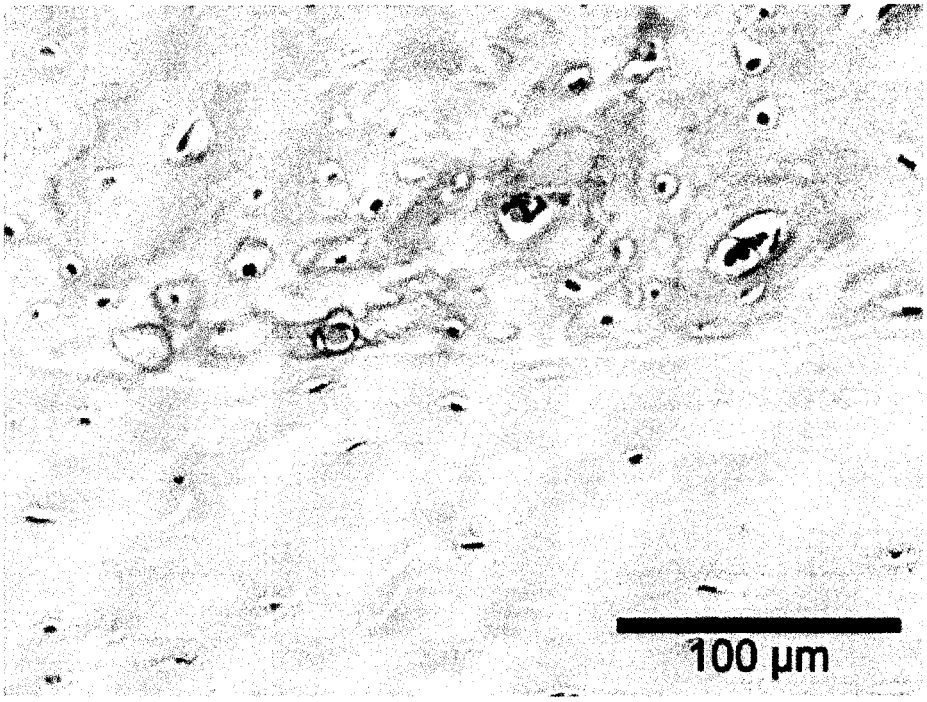

Figure 2.1: Woven *versus* lamellar bone. Hematoxylin and eosin (H&E) stained section showing newly formed woven bone (top) above pre-existing lamellar bone (bottom).

are oriented to so that the plate-shaped apatite crystals run in parallel arrays across the collagen fibrils, as has been observed in both embryonic chick bone [11] and in mineralized turkey tendon, which models portions of newly formed bone [12].

Three types of lamellar bone are found in the cortex — circumferential, concentric, and interstitial — while the fourth is found in the trabeculae, oriented parallel to the long axis of the trabeculum [4]. The orientation of the lamellae is functionally important in both cortical and trabecular tissue types. As early as the seventeenth century, a relationship between bone architecture and mechanical properties was postulated when Galileo observed a correlation between bone size and body weight and activity [13]. In the 1870s, Hermann von Meyer used human cadaver thigh bones to study the orientation of the trabeculae, which follow tensile and compressive force lines [14]. Orientation of the trabeculae has also been found in the craniofacial skeleton, where loads are generated during mastication. Stereological analysis of the pig zygomatic arch showed that trabeculae are anisotropic and oriented orthogonal to the occlusal plane [5]. In humans, the trabeculae of the mandibular condyle are also anisotropic [15] and optimized for mechanical loading [16]. Restoration of the native architecture when regenerating bone in the craniofacial skeleton may be critical to restoring complete function.

2.3 Bone Formation and Modeling

During development, a key step in bone formation is cell migration. Epithelial-mesenchymal interactions lead to cellular condensation and differentation of the cells into chondrocytes and osteoblasts [17]. The process of osteoblast differentiation is characterized by gene expression patterns, as described in subsequent sections. Further, several signaling pathways, such as Wnt signaling, influence both cell differentiation and developmental patterning [17].

Generally, bone is formed through one of three processes. Most bones, including those in the axial and appendicular skeleton, form through enchondral ossification,

which proceeds through a cartilage intermediate [17]. During enchondral ossification, a cartilage model is initially formed from the mesenchyme [17]. Chondrocytes in the epiphyseal growth plate then differentiate, hypertrophy, and die to be replaced by bone [18]. After the chondrocytes enlarge, vascular buds and osteoprogenitor cells invade the cartilage region to initiate the bone formation [13]. Other bones, including the cranium, form through intramembranous ossification, where osteoprogenitor cells directly differentiate and mineralize within the organic matrix. Bone formation during the process of distraction osteogenesis also occurs via intramembranous ossification [13]. Finally, new bone can be deposited on existing bone in a process called appositional bone formation, which primarily occurs during bone enlargement and modeling (changing a bone's shape) [13]. Appositional bone formation can also occur during bone remodeling, which is described in the following section.

2.4 Bone Remodeling

Bone is in a constant state of remodeling with approximately 10% replaced each year [17]. Bone remodeling helps to repair damaged areas of bone and to maintain calcium homeostasis. Changes in the loading pattern of a bone can also lead to bone remodeling. This adaptive response is known as Wolff's law [13]. Additionally, bone located surrounding implants often undergoes remodeling [13].

During physiologic remodeling, the principal cell types of bone are balanced between bone-forming cells (osteoprogenitor cells, osteoblasts, and osteocytes) and bone-resorbing cells (osteoclasts). The organization of bone is preserved by the spatial relationship and temporal cues of bone-resorbing and bone-forming cells. In an arrangement called the basic multicellular unit (BMU), these cells are organized with a leading edge of osteoclasts, a trailing edge of osteoblasts, a vascular capillary, and connective tissue [19]. The trajectory of the BMU, with the path of the BMU differing between cortical bone (forming a tunnel) and cancellous bone (forming a trench) [19, 20], results in the remodeling of bone tissue to maintain its proper architecture.

Controlling cellular migration and differentiation during the process of bone regeneration may recapitulate the processes of bone formation and/or bone remodeling and may result in a more organized regenerated bone tissue.

2.5 Factors Affecting Osteoblast Function and Mineralization

The interplay between different bone cell types is controlled by the action of various growth factors and cytokines as well as cell-cell and cell-matrix interactions. These signals act during the physiologic processes of bone formation and remodeling and can be utilized to stimulate bone regeneration. Based on the *in vitro* culture of osteoblasts, three stages of osteoblast development have been proposed: proliferation, extracellular matrix production, and mineralization [21]. Although additional characterization of marker expression has resulted in the ability to distinguish between a greater number of stages [21], these three steps are also essential for the growth of bone *in vivo*. In this section and the following section on osteoclastogenesis, the basic steps of bone development are reviewed with particular emphasis on stimulatory factors that are relevant to the research in this dissertation as well as the markers that are used to characterize the formation of bone. More extensive reviews of osteoblast and osteoclast differentiation and function can be found in references [20, 21, 17, 22].

2.5.1 Osteoprogenitor Proliferation and Differentiation

Committed osteoblast progenitors, arising from mesenchymal stem cells, can be induced to replicate, migrate, and further differentiate through the action of several growth factors, including the bone morphogenetic proteins (BMPs), transforming growth factor β (TGFβ), platelet-derived growth factor (PDGF), the insulin-like growth factors (IGFs), and some members of the fibroblast growth factor (FGF) family [20]. BMPs have the added ability to induce uncommitted progenitors to differentiate into osteoblasts [20] and are further described in the following subsection. TGFβ, PDGF, the IGFs, and the FGFs also act on a number of other cell types and

may enhance bone formation through their pro-mitogenic effects [23].

Differentiation down the osteoblast lineage is characterized by the expression of the transcription factor, core binding factor alpha 1 (Cbfa1), which is also known as Runx2, the mammalian homolog of the *Drosophila* gene *runt*. Cbfa1/Runx2 promotes the expression of bone-related proteins including osteocalcin (OCN), osteopontin (OPN), bone sialoprotein (BSP), and type I collagen [24]. Cbfa1/Runx2 may also be involved in shaping the cartilage region during enchondral bone formation through regulation of chondrocyte hypertrophy and expression of collagenase-3, which both precede vascular invasion [17]. Homozygous mutation of the Cbfa1/Runx2 gene results in lethality without either intramembranous or enchondral ossification due to a lack of mature osteoblasts [25]. Additionally, there is no invasion of cartilagenous regions by either blood vessels or mesenchymal cells [25]. Interestingly, overexpression of Cbfa1/Runx2 results in osteopenia or impaired bone formation, likely due to incomplete osteoblast differentiation [26]. A second transcription factor downstream of Cbfa1/Runx2, Osterix (Osx), is needed for the differentiation of osteoblasts into a fully mature phenotype [27].

Phenotypically, type I collagen and alkaline phosphatase (ALP) production are considered early markers of osteoblast differentiation while OCN expression and mineralization characterize the later stages [28, 17]. OCN is the most abundant non-collagenous extracellular matrix (ECM) protein forming up to 20% of the non-collagenous protein content, and it is the only bone marker specific to osteoblasts [29]. In studies using knockout mice, OCN was found to be critical to limit bone formation without specific effects on bone resorption or mineralization [30]. Another early osteoblast marker and ECM protein, BSP, is highly expressed during embryonic bone formation, and its expression was found to be most intense at the surfaces of the newly forming bone [31]. BSP expression precedes mineralization, and BSP is believed to play a role in initiating this process [31]. Additionally, BSP binds to collagen and thus may mediate cell attachment to the ECM [32]. In addition to their expression

during skeletal development, these marker proteins also characterize the processes of natural and induced bone regeneration. The temporal progression of bone marker expression was studied in the rat calvarial critical size defect model in response to treatment with DBM [33]. ALP activity peaked at day 7 [33]. BSP and OPN were first expressed at day 2 with rapid accumulation over three weeks, particularly for BSP [33]. These markers present a means of evaluating unmineralized regenerating tissue to determine if it is early in the process of forming bone.

2.5.2 Bone Morphogenetic Proteins

The morphogenetic activity of proteins found in decalcified bone matrix was first shown by Urist in 1965 [34]. The most potent of these proteins [35], BMP-2 (a 32 kDa homodimeric protein), was purified and sequenced by Wozney *et al.* in 1988 [36]. BMP-2 can induce cartilage and bone formation *in vivo* and is an important regulator of skeletal development [37]. At least 14 additional BMP genes have been identified thus far [38]. Most BMPs, except BMP-1, are members of the TGFβ superfamily [39] and are classically characterized by the ability to form ectopic bone [40]. However, in direct comparison of 15 BMPs, BMP-2, BMP-6, BMP-7, and BMP-9 were found to be most active in their ability to induce ectopic bone whereas BMP-3 actually inhibited bone formation [38].

The ectopic bone formation assay has shown that BMP induces bone formation *in vivo* in a process analogous to enchondral ossification with progenitor migration and differentiation into a cartilage intermediate, vascular invasion, calcification of the cartilage region, and bone mineralization and remodeling [41, 42]. *In vitro* studies have also shown that exposure to BMPs can lead to differentiation of osteoprogenitors, suggesting that BMPs can also directly stimulate osteoblast differentiation in a manner similar to intramembranous ossification. For example, BMP-7 induces the expression of Cbfa1/Runx2 in C3H10T1/2 cells [24], and BMP-2, BMP-4, and BMP-6 induce the expression of late stage bone markers (OCN expression and mineral nodule

formation) *in vitro* [43, 44].

BMPs act through type I and type II transmembrane serine/threonine kinase receptors, which is typical for members of the TGFβ superfamily [22]. The type II receptor transphosphorylates the type I receptor, and the activated BMP type I receptor then phosphorylates the transcription factors: Smad1, Smad5, and Smad8 [22]. Smads are related to the Smas (three related *Caenorhabditis elegans* genes) and *Drosophila* Mad (mothers against *decapentaplegic*) [45]. Phosphorylated Smads associate with additional proteins, and the large complex translocates to the nucleus to regulate target gene transcription [22].

The important role of BMP-induced bone formation during skeletal development has been shown in knockout and/or mutant animal models for BMP-5 [46], BMP-7 [47], and BMP-11 [48]. Mice with a short-ear phenotype have additional defects during the earliest condensation stage of skeletal development and were found to have mutations or deletions in the BMP-5 coding region [46]. BMP-7 deficient mice have defects of variable penetrance in skeletal patterning, particularly in the rib cage, skull, and hindlimbs (polydactyly), as well as impaired development of the kidney and eye [47, 49]. BMP-11 plays a role in skeletal patterning as deletion of this gene results in skeletal abnormalities that include anterior transformations of vertebral segments as well as posterior displacement of the hindlimb during development [48]. Some BMPs may be less critical than others as loss of BMP-6 results in only a mild phenotypic abnormality in the developing sternum [50]. Loss of BMP-6 may be compensated for by other BMPs, such as BMP-2, which is coexpressed in hypertrophic cartilage regions in wild-type animals [50]. The results of some of these studies, particularly the effects of BMP-7 on the development of the kidney and eye, indicate that the function of BMP is not limited to bone tissue and that it might have a broader role in development. In fact, BMPs have a range of effects including cell proliferation, apoptosis, differentiation, cell-fate determination, and morphogenesis [51].

2.5.3 Extracellular Matrix Production and Interaction

Cell-matrix interactions also play a role in osteoblast development and migration, particularly through the binding of membrane receptor proteins (integrins) on the cell surface to the amino acid sequence arginine-glycine-aspartic acid (RGD), which is found in several bone matrix proteins, including type I collagen, OPN, and BSP, as well as in fibronectin, thrombospondin, and vitronectin [20, 52, 53]. *In vitro* studies of osteoblast adhesion to RGD-containing proteins as well as synthetic RGD peptides have been used to look at the expression and interaction of integrins (reviewed in [52]). While beyond the scope of this dissertation, the inclusion of cell-adhesive signals such as RGD can add increasing sophistication to regenerative matrices. For example, RGD-modified alginate hydrogels were used to deliver chondrocytes and osteoblasts in a subcutaneous mouse model, which resulted in the organization of the cells into a growth-plate-like architecture *in vivo* [54].

2.5.4 Mineralization

Newly formed bone matrix, osteoid, becomes mineralized through the deposition of hydroxyapatite, which forms by a phase transition from liquid to solid [7]. The onset of mineralization is variable, and it can take 12 to 15 days for osteoid to begin to mineralize [4]. Once mineralization starts, its deposition is fairly rapid with 60% or more forming within hours [7]. Mineral orientation is ultimately determined by the organization of the proteins in the ECM. The mineral deposits are uniformly distributed within the organized collagen fibrils of lamellar bone [7]. Hydroxyapatite crystals associated with collagen fibrils tend to be oriented so that their crystallographic c axes are parallel to the long axis of the fibrils [12, 11]. The periodic arrangement of the crystals suggests that they may be located in channels formed by collagen hole zones, although the crystal sizes exceed the dimensions of individual hole regions [11]. While the mechanisms governing bone mineralization are not fully elucidated, there

is evidence that BSP plays a role in the regulation of mineralization by providing nucleation sites for hydroxyapatite crystals to form [31, 55, 56]. BSP can bind calcium and hydroxyapatite, and it has been shown to be able to nucleate hydroxyapatite precipitation *in vitro* from sub-threshold solutions of calcium and phosphate [56].

The process of mineral deposition in bone shares some similarities to the formation of another highly mineralized biological tissue — the enamel. During enamel formation, ameloblasts secrete proteins that self-assemble to form an organic enamel extracellular matrix [57]. This matrix is then almost entirely replaced with inorganic crystallites, organized into rod structures, in the mature enamel [57]. Key proteins involved in this process are the amelogenins, a family of alternatively spliced products of the amelogenin gene. Amelogenin has been shown to self-assemble into nanospheres of 15-20nm in diameter [58]. The nanospheres align in positively charged domains along the crystallographic *c* axis of hydroxyapatite, which then orients hydroxyapatite crystallite growth preferentially along this axis [59]. Amelogenin has also been used *in vitro* to orient hydroxyapatite deposition on seed crystals [60]. While the full length amelogenin acts to slow the rate of crystal growth, low molecular weight fragments do not have this inhibitory effect [60].

2.5.5 Amelogenin and Leucine-Rich Amelogenin Peptide

Amelogenin, a 20 kDa hydrophobic protein, is also involved in cementogenesis [61] and may be a potential osteoinductive factor. Defects in the craniofacial skeleton were noted in patients with amelogenesis imperfecta [62]. Amelogenin affects BSP expression and mineral nodule formation in a dose-dependent manner in cementoblasts *in vitro*, and amelogenin null mice have reduced BSP production by cementoblasts and nearby osteoblasts *in vivo* [61].

Amelogenin has several alternatively spliced products, including leucine-rich amelogenin peptide (LRAP), a 59 amino acid peptide [63]. LRAP may also have some osteoinductive activity, as it was found to be the peptide responsible for the so-called

chondrogenic-inducing activity (CIA) of dentin matrix [64]. The CIA induced expression of type II collagen in embryonic rat muscle fibroblasts (EMF) *in vitro* and produced a mix of cartilage and bone when implanted with a collagen carrier in rat muscle *in vivo* [64]. In further studies using a recombinant peptide, LRAP has been shown to have chondrogenic and osteogenic activity *in vitro* as well as *in vivo* [65, 66, 67]. Veis *et al.* showed enhanced sulfate incorporation into proteoglycans and expression of type II collagen and Cbfa1/Runx2 in EMF exposed to LRAP *in vitro* [65]. Further, they demonstrated ectopic mineralization and expression of BSP and bone acidic glycoprotein-75 (BAG-75) in a rat thigh muscle model with PLGA implants containing 167μg of LRAP [65]. Veis also indicated that LRAP induces bone formation in a rat calvarial onlay model [66], although the complete study has yet to be published. Like the full-length amelogenin, LRAP additionally affects cementoblasts *in vitro* and may be a signaling molecule involved in cementogenesis [68]. Boabaid *et al.* showed that LRAP down-regulates OCN and up-regulates OPN and osteoprotegerin (OPG) as well as inhibits mineralization for OCCM-30, an immortalized murine cementoblast line, in culture [68].

2.6 Osteoclastogenesis

Osteoclasts are large multinucleated cells derived from hematopoietic stem cells that resorb bone through their characteristic ruffled border, a series of finger-like projections of the cell membrane, which seals to the bone surface through a surrounding clear zone [20]. A vacuolar H^+-ATPase in the ruffled border creates a region of low pH, which causes the mineral component of bone to dissolve [20]. Matrix metalloproteinases and cathepsins K, B, and L are then secreted by osteoclasts to degrade the protein matrix [20].

Recently, interaction of osteoclast progenitors with osteoblast progenitors has been determined to be the primary mechanism of osteoclastogenesis. Direct cell-to-cell contact between osteoblast and osteoclast progenitors was shown to be needed for

stimulation of osteoclast activity in an *in vitro* pit-forming assay [69]. Osteoblast progenitors express the membrane-associated osteoclast differentiation factor (ODF), which is recognized by osteoclast progenitors and leads to their differentiation [70] and activation [71]. ODF is also known as TNF-related activation-induced cytokine (TRANCE) [72] and receptor activator of nuclear factor-κB ligand (RANKL) [73]. RANKL is found in skeletal and lymphoid tissues and is additionally expressed in adult brain, heart, skin, and skeletal muscle [74]. RANKL on osteoblasts can be up-regulated by 1,25-dihydroxyvitamin D_3 [1,25-$(OH)_2D_3$], parathyroid hormone (PTH), tumor necrosis factor α (TNFα), interleukin (IL)-1, IL-6, IL-11, IL-17, prostaglandin E2 (PGE_2), and glucocorticoids [70, 75, 76, 77, 78]. RANKL activates osteoclasts both *in vitro* and *in vivo* [79] and acts on mature osteoclasts by stimulating pit-forming activity [80, 71]. RANKL knockout mice lack mature osteoclasts and have severe osteopetrosis as well as defective tooth eruption, although progenitor cells from these mice can be induced to form osteoclasts *in vitro* [81].

The receptor activator of nuclear factor-κB (RANK), a member of the TNF receptor family, is expressed on osteoclast progenitors [22]. The interaction between RANK on osteoclast progenitors and RANKL on osteoblast progenitors is essential for osteoclastogenesis [20]. RANK knockout mice also exhibit osteopetrosis resulting from a lack of osteoclast differentiation [82]. Signal transduction pathways mediated by RANK cause differentiation and activation of osteoclasts [22]. Particularly, interaction of the cytoplasmic tail of RANK with TNF-receptor-associated factor 6 (TRAF6) results in osteoclast differentiation [22]. Additionally, activation of RANK induces c-Fos, which upregulates genes associated with mature osteoclasts [83, 84]. Lack of these downstream signals, TRAF6 [85] and c-Fos [86], results in osteopetrosis in knockout animal models. Osteoprotegerin (OPG), a soluble decoy receptor for RANKL, inhibits osteoclastogenesis and bone resorption [20] and is described in further detail in the following subsection. Interestingly, growth factors that are known to enhance bone formation, TGFβ [87, 88] and BMP-2 [89], have also been shown to

enhance RANKL and M-CSF stimulated osteoclast differentiation *in vitro*, indicating further interconnections between osteoblastogenesis and osteoclastogenesis.

Since osteoclasts derive from hematopoietic stem cells, which also give rise to monocytes and macrophages, it is not surprising that osteoclast differentiation and activity can be stimulated by several predominantly inflammatory cytokines. Osteoclastogenesis can be stimulated by IL-1, IL-3, IL-6, IL-11, IL-17, leukemia inhibitory factor (LIF), oncostatin M (OSM), ciliary neurotrophic factor (CNTF), TNFα, granulocyte macrophage-colony stimulating factor (GM-CSF), M-CSF, c-kit ligand, PGE_2, lipopolysaccharide (LPS), and glucocorticoids [20, 22, 17]. Some of these cytokines have direct effects on osteoclasts or osteoclast progenitors, i.e., without RANK-RANKL mediated signaling [90, 91, 92, 93, 94, 95]. In *in vitro* studies to determine the mechanism of action of these cytokines, TNFα [90, 92, 93] and IL-6 and IL-11 [91] (all with M-CSF) were shown to induce osteoclast progenitors/monocytes to form multinucleated cells with characteristic osteoclast markers as well as to induce resorption pit formation [90]. IL-1, which acts through the IL-1 type receptor that is expressed on osteoclasts [96], was able to further upregulate TNFα-induced resorption pit formation [90, 92, 94].

2.6.1 Osteoprotegerin

Osteoprotegerin (OPG) is a recently identified member of the TNF receptor (TNFR) family that has a protective effect on bone and enhances bone density [97]. It was independently isolated as osteoclastogenesis inhibitory factor (OCIF) by Tsuda *et al.* [98]. OPG is predominantly secreted as a 110 kDa disulfide-linked homodimeric glycoprotein whose N-terminal half bears strong similarity to the TNFR family and contains its functional domain [97].

In initial *in vivo* studies demonstrating its function, overexpression of OPG resulted in an increase in bone density and osteopetrosis as well as a decrease in the number of tartrate-resistant acid phosphatase (TRAP)-positive osteoclasts [97]. OPG

binds RANKL thus preventing RANK-RANKL interaction and inhibiting osteoclast differentiation [79]. The frequency of OPG production modulates its bone protective effects [17]. OPG also binds another TNF family protein, TNF-related apoptosis inducing ligand (TRAIL), thus blocking apoptosis [99].

Further, OPG may also be able to promote angiogenesis, as it been shown to enhance endothelial cell survival [100]. OPG prevented endothelial cell apoptosis induced by growth factor withdrawal through a nuclear factor-κB (NF-κB) dependent pathway [100]. Additional studies indicated that OPG binds TRAIL and prevents TRAIL receptor-mediated cell death in this *in vitro* system [101].

2.7 Angiogenesis

Angiogenesis is classically defined as the sprouting of new blood vessels from preexisting capillaries [102]. These thin vessels, with walls only one endothelial cell layer thick, are essential for bringing nutrients and oxygen to the tissues of the body. Angiogenesis provides a means of maintaining this vascular network and is critical during the processes of development, ovulation, wound healing, and response to ischemia. Excessive angiogenesis can also be associated with pathologic conditions, including diabetic retinopathy and cancerous tumor growth. A number of molecules have been discovered that have a positive effect on angiogenesis, including VEGF, the FGFs, some ephrin ligands, PDGF, transforming growth factor β (TGFβ), and the angiopoietins [103]. These growth factors act in controlled temporal fashion to promote the initiation and maturation of angiogenic blood vessels [104]. Angiopoietin-2 (Ang-2) may act to destabilize existing vasculature for remodeling [103]. VEGF then initiates angiogenesis, which is followed by the remodeling and maturation of the blood vessels through the actions of angiopoietin-1 (Ang-1) and ephrin-B2 [103].

2.7.1 Vascular Endothelial Growth Factor

One of the most potent angiogenic molecules, vascular endothelial growth factor A (VEGFA), hereafter referred to as VEGF, is a member of a family that also includes VEGFB, VEGFC, VEGFD, and placental growth factor (PLGF) [105]. VEGF is capable of inducing endothelial cell migration *in vitro* [106] and angiogenesis *in vivo* [107]. VEGF is a survival factor for endothelial cells [108] but has also been shown to have effects on other cell types [105]. Interestingly, VEGF appears to be able to induce osteoblast differentiation and migration [109]. Additionally, VEGF is known as a vascular permeability factor because it causes vessels to become hyperpermeable to circulating macromolecules, which was first noted in tumor vasculature [110, 111]. Other factors may be required to promote the formation of mature, nonleaky vessels *in vivo*. VEGF is upregulated in response to lack of oxygen through a hypoxia-inducible transcription element within its promoter [112] as well as through the action of other growth factors including TGFα, TGFβ, FGF, and PDGF [105]. VEGF binds to fms-like-tyrosine kinase-1 (Flt-1, also known as VEGFR-1) and kinase domain region (KDR, also known as VEGFR-2 or Flk-1), two related receptor tyrosine kinases [105]. VEGFR-1 is also upregulated in hypoxic conditions through a hypoxia-inducible factor-1 (HIF-1) dependent mechanism [113]. VEGFR-2 appears to be the major signal transduction pathway for VEGF-induced proliferation, migration, survival, and angiogenesis [105]. Interaction with cell-surface heparan sulfates appears necessary for efficient VEGF binding to its receptors [114, 115, 116].

Initially discovered by Dvorak and colleagues in 1983 [117] and isolated by Ferrara in 1989 [118], VEGF is a heparin-binding 45 kDa homodimeric glycosylated protein, with sequence similarity to the A and B chains of PDGF [106]. Four alternatively spliced variants exist: $VEGF_{121}$, $VEGF_{165}$, $VEGF_{189}$, and $VEGF_{206}$, with increasing binding affinity for heparin. This results in $VEGF_{121}$ being freely diffusible while $VEGF_{189}$ and $VEGF_{206}$ remain bound to the ECM. VEGF can be released from the

ECM by plasmin cleavage as well as through degradation of the heparin matrix by heparinase [119]. Additionally, plasmin can cleave $VEGF_{165}$ into a $VEGF_{110}$ fragment, which is freely diffusible [120]. However, the carboxyl-terminal domain (residues 111-165) contains the heparin-binding region and is necessary for the full mitogenic potency of VEGF [120].

Gradients of growth factors may play a role in the physiologic regulation of cell migration and chemotaxis. The alternative splicing and protease sensitivity of VEGF, as described above, results in different isoforms and peptide fragments of VEGF with differing affinities for the ECM. Keyt *et al.* propose that the graded affinity for heparin of the VEGF isoforms affects the ability of VEGF to diffuse through the tissue and allows the formation of VEGF gradients *in vivo*, which could be a driving force for endothelial cell proliferation and migration towards a VEGF-producing stimulus during wound healing and response to hypoxia [120]. Keyt *et al.* suggest that the following series of events may lead to angiogenesis:

> Initially, cells respond to hypoxia or other stimuli by inducing VEGF transcription [112], resulting in increased expression of long and short forms of VEGF, although $VEGF_{165}$ is probably the most abundant isoform. Compared to the longer forms of VEGF, the diffusible forms would migrate a greater distance, bind VEGF receptors, and trigger endothelial cell proliferation and migration. The intensity of the angiogenic signal would be weakest at the most distant sites, given the lesser mitogenic potency of $VEGF_{110}$ and $VEGF_{121}$. Closer to the site of VEGF synthesis (i.e., ischemic tissues), the concentration of the 165 isoform is expected to be increased due to extracellular matrix binding and the effect of the biochemical gradient would be enhanced with the associated greater mitogenic potency of $VEGF_{165}$. In the most ischemic areas, matrix-associated VEGF is localized to the cells of origin with the highest concentration and

potency. The heterogeneity of VEGF structure and function allows the formation of a biochemical gradient for the migration and chemotaxis of proliferating endothelial cells. In circumstances where plasminogen activation occurs (e.g., tumors and wounds), the presence of plasmin may serve to release stored forms of matrix-bound VEGF to amplify the angiogenic signal. [120]

2.8 Angiogenesis and Bone

Adequate blood supply is necessary for maintaining cell viability in most tissues, and bone is no exception. Blood vessels are found throughout the mineralized matrix of bone, in the Haversian canals of cortical bone, in the periosteum that lines the bone, and in the marrow spaces contained in bone. Angiogenesis, therefore, plays a key role in bone formation and repair. Further, there is increasing evidence that the organization of the vasculature provides cues to direct the architecture of the nearby bone [104]. In this section, the links between angiogenesis/angiogenic factors, vascular orientation, and bone will be reviewed for the processes of enchondral ossification, skeletal development, fracture repair, and distraction osteogenesis. Additionally, the specific actions of VEGF on osteoblasts and osteoclasts as well as the ability of endothelial cells to produce osteoinductive factors will be discussed.

2.8.1 Enchondral Ossification

During enchondral ossification in postnatal bone growth, the invasion of angiogenic blood vessels into the avascular cartilage region initiates several changes that lead to the formation of bone. The apoptotic hypertrophic chondrocytes in the growth plate are eventually replaced by osteoblasts that deposit bone matrix forming trabeculae [18]. A number of pro-angiogenic factors are found in the growth plate [18], with VEGF expressed by the hypertrophic chondrocytes and localized to mineralizing regions of the cartilage [121, 122, 123]. VEGF has been found to be an important

mediator of enchondral ossification, as inactivation of VEGF by a soluble receptor chimeric protein, mFlt(1-3)-IgG, severely impaired blood vessel invasion and subsequent trabecular bone formation [123]. This inhibition was reversible, as bone growth resumed after cessation of mFlt(1-3)-IgG administration, reaching levels comparable to controls [123]. VEGF may also have an effect on chondroclast and osteoblast stimulation as VEGF receptors are found on both cell types, and inhibition of VEGF led to reduced numbers of chondroclasts and increased numbers of osteoclasts at the cartilage-bone junction [123].

Additionally, there is a clear spatial relationship between the cells and matrix within the growth plate. The hypertrophic chondrocytes are arranged in columns, and blood vessels invading from the metaphysis run parallel to these columns [123]. Death of the terminal layer of hypertrophic chondrocytes is followed by cellular condensation and subsequent endothelial cell or blood vascular cell penetration into the vacated lacuna [124]. In the study by Gerber *et al.*, blocking the effects of VEGF with soluble mFlt(1-3)-IgG led to blood vessels that were unable to penetrate the hypertrophic cartilage zone and that were then oriented perpendicular to the columns of chondrocytes [123].

2.8.2 Skeletal Development

While the cranium, jaws, and part of the clavicle form by intramembranous ossification, the majority of the bones of the skeleton form by enchondral ossification. This process is essentially the same as the enchondral ossification during the growth of long bones with one exception. Termed silent or quiescent angiogenesis, the initial blood vessels that invade the cartilage in the secondary ossification center pass from the perichondrium through preexisting canals in the developing cortical bone [18, 125, 126]. Postnatally, the channels form as the blood vessels invade [18]. Initiation of migration of the endothelial cells through these channels still coincides with VEGF expression by hypertrophic chondrocytes; however, the signal for the formation of the channels

remains unknown [18].

More generally, angiogenesis and angiogenic factors are critical for embryonic development. Deletion of even one allele of VEGF is lethal to the embryonic mouse between days E11 and E12 [127, 128]. Since this is approximately the time of mesenchymal condensation prior to the onset of skeletal development, the key role of VEGF in this process had not been elucidated until the development of animal models expressing mutant forms of VEGF that survived to term.

In a mouse model expressing only the $VEGF_{120}$ isoform, skeletal defects were noted with decreased bone development and impaired angiogenesis in sites of both intramembranous and enchondral ossification [129]. As a result of this study, Zelzer *et al.* suggest three mechanisms of action for VEGF in developing bones: increased angiogenesis in intramembranous and perichondrial regions, stimulation of angiogenesis into the hypertrophic cartilage region, and increased activity of osteoblasts [129]. Additional animal models produced cartilage specific knockdown of VEGF through the use of a Cre/LoxP recombination system with deletion of a single VEGF allele in Collagen2a1-Cre transgenic animals [130, 131]. While the majority of animals produced by Haigh *et al.* died before day E10.5, those that survived to E17.5 were smaller, had larger hypertrophic chondrocyte zones in the growth plates, and had decreased vascular invasion of the hypertrophic cartilage region compared to wild type controls [130]. Non-lethal transgenic strains developed by Zelzer *et al.* showed reduced bone mineralization, delayed vascularization of primary ossification centers, delayed removal of terminally differentiated hypertrophic chondrocytes, and chondrocyte death in joint and epiphyseal regions [131]. In addition to the mechanisms described above, this study further implicates VEGF as a protective factor for chondrocytes [131].

2.8.3 Fracture Repair

Establishment of a vascular supply is a crucial step in the regeneration of bone during the process of fracture repair [132]. The initial fracture hematoma and inflammatory

response (fibrous callous) lead to the formation of a cartilage intermediate [133]. Similar to enchondral ossification, hypoxic conditions induce neovascularization of this chondral callus followed by woven bone deposition and calcification [133]. Interestingly, the early fracture callus has a high concentration of hyaluronic acid (HA) [133]. VEGF is localized to large chondrocytes in the periphery of the chondral callus as well as to the region of newly forming woven bone while the surrounding native cortical bone remains negative for VEGF [134].

Serum levels of VEGF were also found to be increased in patients who received a rigid osteotomy for fracture fixation [135]. The additional angiogenic factor, angiogenin, as well as enzymes involved in ECM degradation, including matrix metalloproteinase 9 (MMP-9), tissue inhibitor of metalloproteinases (TIMP)-1, and TIMP-2 were also increased [135]. Similar to callus formation during fracture repair, active bone formation also occurs in response to bone marrow injury that is associated with local bleeding, clotting, and neovascularization [21]. Pro-mitogenic growth factors (e.g., PDGF, FGF, and TGFβ) and the angiogenic growth factor, VEGF, are found in these regions as well [21].

2.8.4 Distraction Osteogenesis

Parallels between blood vessel orientation and mineralization have also been observed during distraction osteogenesis, a process of artificially induced, stepwise lengthening of bone [7, 136]. A low-energy corticotomy is performed keeping the periosteum intact, and after a latency period, the resulting fracture callus is slowly distracted over time [137]. Similar to fracture healing, enchondral ossification can occur early during the period of distraction; however, intramembranous ossification is the primary mechanism of bone formation [137]. Histologically, the distraction gap is organized (starting from the center) with a collagenous fibrous interzone (FIZ), adjacent zones of vascular ingrowth and bone matrix deposition by osteoblasts called the primary matrix or mineralization front (PMF), and a zone microcolumn formation (MCF)

[137]. Newly formed collagen matrix is deposited in parallel to the distraction force [138]. In the MCF, mineralizing bone columns are oriented along longitudinal bundles of collagen [137]. This results in the newly formed bone trabeculae being oriented longitudinally in the direction of the distraction force [139].

Distraction osteogenesis is accompanied by increases in blood supply and blood flow [140, 141]. Choi *et al.* suggest a close temporal and spatial relationship between vascular proliferation and mineralization based on observations in a rat tibial lengthening model [137, 140]. An intense angiogenic response is observed during the earliest phases of distraction [138]. During the latency and distraction periods, angiogenic blood vessels extend from each bone surface but do not cross the FIZ [140]. Characterized as sprouting angiogenesis, the vascular network in the newly formed bone consists of straight vascular branches axially aligned in the direction of the distraction force [140]. By the end of the distraction period, these vessels completely bridge the gap and are oriented in the same longitudinal direction as the microcolumns of new bone, as measured by vascular corrosion casting and scanning electron microscopy [140]. VEGF expression is upregulated with strong expression in the PMF and in the lining osteoblasts of the MCF [137]. In a goat model of mandible distraction, VEGF expression was predominantly found in endothelial cells and osteoblasts in the distraction gap [142]. Temporally, VEGF expression remained high for about a week after the distraction phase, then began to decrease [142].

Another method that uses a mechanical device to stimulate bone remodeling is the forward mandibular positioning of functional appliance therapy. This process initiates bone formation in the glenoid fossa. Both VEGF expression and bone formation are increased, in sequential fashion, in the posterior region of the glenoid fossa of rats fitted with appliances [143]. A two-step treatment strategy resulted in an additional peak of VEGF expression and an overall increase in the amount of bone formed compared to controls that received the same total advancement in one step [144]. Again, a temporal pattern of increased bone formation after the peak of VEGF expression was

observed [144].

2.8.5 Crosstalk between Osteoblasts and Endothelial Cells

VEGF appears to be able to directly affect osteoblasts and osteoclasts, as has been shown in several *in vitro* studies. VEGF was able to induce osteoblast differentiation in cultured progenitors [109, 145]. VEGFR-1 and VEGFR-2 are found on osteoblasts [123, 145], and VEGF causes upregulation of the osteoblast marker, ALP, as well as osteoblast migration [109]. While VEGF does not appear to induce the proliferation of osteoblasts, the 120 and 164 isoforms of murine VEGF can increase mineralization in calvarial explants [129].

Osteoblasts and/or their progenitors are also able to produce VEGF. The murine preosteoblast-like cell line KS483 can produce VEGF in amounts dependent on the differentiation state of the cells [145]. Osteoblast-like cells from human trabecular bone explants as well as the cell line SaOS-2 express VEGF mRNA [146]. 1,25-$(OH)_2D_3$ as well as PTH and IGF-1 further increased VEGF expression in a time and concentration dependent manner [146]. Additionally, in co-cultures of endothelial cells and osteoblasts, the osteoblasts produced VEGF, which then stimulated endothelial cell proliferation [147]. In an organ culture model of fetal mouse metatarsals, BMP-2 administration increased the formation of platelet/endothelial cell adhesion molecule-1 (PECAM-1)-positive tube-like structures [148]. KS483 cells will also produce VEGF in a dose dependent manner when stimulated with BMP-2, BMP-4, and BMP-6 [148]. Interestingly, while other studies showed that VEGF can induce osteoblast differentiation [109, 145], the VEGF produced by the KS483 cells was not necessary for nonstimulated and BMP-stimulated osteoblast differentiation [148].

In a reciprocal way, endothelial cells can be induced to produce osteoinductive factors. Exposure to hypoxia and/or treatment with VEGF can increase BMP-2 mRNA expression in cultured bovine capillary endothelial cells and human microvascular endothelial cells [149]. Endothelial cells are also able to produce OPG as OPG was

found in endothelial cells in the synovial membrane and interface tissue of loosened total hip replacements [150]. Further, *in vitro* production of OPG by endothelial cells could be stimulated by TNFα [150].

However, additional studies have indicated that VEGF and/or endothelial cells may play a role in bone resorption. Endothelial cells share some similarities to osteoclasts. Interestingly, RANK is expressed on the surface of endothelial cells, and RANKL binding to RANK on endothelial cells can stimulate endothelial cell proliferation, migration, and tube formation [151]. Further, RANK expression on endothelial cells is upregulated in response to VEGF and enhances RANKL-mediated angiogenesis [152]. Reduced expression of RANKL and VEGF in allograft treated bone defects compared to autograft treated bone defects [153] also highlights the potential importance of these molecules in stimulating bone remodeling. Adeno-associated virus (AAV) mediated gene therapy with VEGF and RANKL in combination was able to improve healing in defects treated with allograft by increasing resorption of the allograft bone [153].

VEGF can also stimulate osteoclast differentiation [154] and could serve as a substitute for M-CSF in *in vitro* and *in vivo* osteoclastogenesis [155]. VEGF can stimulate osteoclast function in M-CSF deficient osteopetrotic mice [155]. Through increases in VEGF production, ovariectomy also increases osteoclast formation in otherwise osteoclast deficient mice [156]. VEGF stimulates monocyte chemotaxis *in vitro*, presumably through VEGFR-1, which is found on monocytes [157]. VEGF upregulates RANK gene expression in monocytes; however, VEGF alone is insufficient to increase monocyte proliferation or to induce markers of mature osteoclasts *in vitro* [158]. In combination with RANKL, VEGF can induce osteoclast differentiation *in vitro*, similar to the effect of RANKL and M-CSF [155, 159]. VEGF and RANKL can also individually stimulate osteoclast migration in a modified Boyden chamber assay *in vitro* [160]. Additionally, VEGF has been shown to directly enhance survival and pit resorption activity of cultured osteoclasts, which also express VEGFR-1

and VEGFR-2 [154]. Further, VEGF may also be involved in osteolysis associated with cancer and implant wear debris. VEGF and its receptors have been found in osteoclasts in bone lesions resulting from breast cancer metastases [159]. In a mouse osteolysis model stimulated by ultra high molecular weight polyethylene (UHMWPE) particles, RANK and RANKL gene expression is increased, and VEGF expression is upregulated, predominantly in inflammatory cells [161].

2.9 Scaffold Design

As introduced in Chapter 1, the research in this dissertation broadly seeks to address the need for bone repair and regeneration strategies for application to areas of challenged craniofacial bone growth and/or healing. Scaffolds that provide signals to stimulate bone formation as well as that degrade over an appropriate time scale to allow tissue growth should result in the formation of mature lamellar bone that is indistinguishable from the surrounding native bone. Both physiological and exogenously stimulated bone regeneration occur through one or more of three well-established mechanisms of action: osteoinduction or the stimuli-induced differentiation of osteoprogenitor cells; osteoconduction or the promotion of osteoblast migration into the regenerating tissue; and osteogenesis or the modulation of natural processes of bone regeneration carried out by pre-existing osteoblasts [162, 163]. These mechanisms can be exploited for the design of regenerative matrices. In particular, osteoconductive materials can be used as a scaffold to support and encourage cellular ingrowth. These scaffolds can then contain or release osteoinductive molecules to further encourage bone formation.

These principles were utilized to design a scaffold that was relevant to the specific hypotheses to be tested — that controlled delivery of osteoinductive and angiogenic signals will lead to the formation of more mature bone and that controlled scaffold degradation will optimize the temporal progression of healing. With these hypotheses in mind, regenerative scaffolds were designed to meet the following criteria:

- The scaffold materials should be nontoxic, biocompatible, and biodegradable.
- The scaffold degradation rate should be able to be controlled.
- The scaffold matrix should be conductive to the appropriate cell types.
- The scaffold should be formed in a way that is amenable to adding additional osteoconductive molecules or cell adhesion moieties.
- The scaffold should be capable of retaining protein growth factors within the scaffold matrix, providing a generic platform that would retain a broad class of proteins.
- The scaffold should be able to release these growth factors in a controlled fashion.
- The scaffold should be able to provide control over the relative rates of protein release (i.e., targeting a slower or faster release rate for a given protein).
- The scaffold should be capable of releasing multiple proteins at different release rates.
- The scaffold should have the capacity for spatial localization of proteins to provide spatial as well as temporal cues for regeneration.

One scaffold that meets the above criteria is a photo-crosslinked hyaluronic acid (HA) hydrogel with the potential incorporation of poly(lactide-co-glycolide) (PLGA) microspheres for additional control of protein release. HA is both biocompatible and biodegradable, and its properties are further described below. HA hydrogels can degrade both through the action of the enzyme hyaluronidase on the backbone of HA as well as through incorporation of degradable linkers while performing the crosslinking

chemistry. The photo-crosslinking chemistry would also allow the incorporation of other molecules into the scaffold matrix as long as they can be modified to contain a terminal vinyl group. HA should bind cationic proteins through electrostatic interactions, thus giving one level of control over protein release. Further control of protein release rates as well as controlled release of non-cationic proteins can be achieved by encapsulating the proteins in PLGA microspheres, which can then be embedded within the hydrogel. The molecular weight of PLGA used to prepare the microspheres will control their rate of degradation and thus the rate of protein release. Finally, protein can be localized within the scaffold by controlled adsorption into specific regions or through the incorporation of protein-loaded PLGA microspheres into selected areas of the HA hydrogel.

The rationale for the use of the scaffold matrix materials, the current state of the art for their application, and previous uses of gradients and/or spatial patterns are described in the following subsections. While the crosslinking chemistry for the formation of HA hydrogels is not new, the hydrogels are used in a novel application for bone regeneration. A section then follows describing the choice of proteins that will be evaluated in this research, including their previous application as bone regenerating therapeutics. While testing all of the possible material combinations and the potential functions of the scaffold delivery system is beyond the scope of this dissertation, this particular scaffold design offers a generic utility that can be extended to create increasingly more sophisticated devices.

One major limitation to the scaffold design for use in bone regeneration applications is that hydrogels have fairly weak mechanical properties. Bone has a high modulus due to its primary function as a structural support for the body. While the hydrogel scaffold allows for the examination of the interplay between different inductive signals and their temporal and spatial presentation, it would immediately fail when placed in a weight-bearing location. It can, however, be used in nonweight-bearing sites, and thus was tested in a rat calvarial critical size defect model. For use

in any bone defect site, it would be possible to combine the hydrogel scaffold with a fixation device that could be removed once the bone has regenerated. Alternately, the hydrogel material could be used to impregnate a more rigid porous scaffold to create a composite device that would have stronger mechanical properties but still provide control over osteoinductive and angiogenic growth factor release.

2.9.1 Rationale for Use of Hyaluronic Acid (HA)

Hyaluronic acid (HA) was selected as the matrix material for the hydrogel scaffolds. HA is a naturally occurring, hydrophilic, nonimmunogenic, biodegradable glycosaminoglycan, consisting of [α-1,4-D-glucuronic acid-β-1,3-*N*-acetyl-D-glucosamine]$_n$. Naturally derived HA is large in size, with an average molecular weight of several million [164]; however, it can be produced by bacterial fermentation in a variety of smaller sizes as well. HA, first discovered in the vitreous body of the eye, is primarily found in the connective tissues of the body with more than half of the HA found in skin and more than a quarter of the HA found in the skeleton and joints [165]. HA in the ECM of cartilage and synovial fluid of joints acts as a viscoelastic shock absorber and hydrated lubricant [166, 167].

HA accumulation appears to increase during morphogenesis [168], and HA may contribute to fetal scarless healing [169]. HA also plays a role in biological processes that occur during the inflammation, granulation tissue, reepithelialization, and remodeling phases of wound healing [170, 171]. Of particular relevance, HA has been found in high concentrations in the early fracture callus [133], in lacunae surrounding the hypertrophic chondrocytes in the growth plate [172, 173], and in the cytoplasm of osteoprogenitor cells [172]. HA is found in tissues during the early phase of wound healing and may support the migration of fibroblasts and endothelial cells into the wound site [174]. HA binds to fibrinogen and both increases the rate of clotting and loosens the organization of fibrin polymer bundles in the clot [175]. HA can bind to several cell surface receptors, including cluster of differentiation 44 (CD44) [176] and

Receptor for HA-Mediated Mobility (RHAMM) [177, 178, 179]. HA also interacts with several proteins (fibrin, fibronectin, and collagen) and proteoglycans (aggrecan, versican, and chondroitin sulfate) in the ECM [180]. HA may mediate cell migration directly in a receptor mediated process or indirectly by altering ECM architecture and cell adhesivity [180].

HA is degraded and removed from the body through several mechanisms. In skin and joints, a large portion is removed by the lymphatic system to the blood and cleared in the liver by hepatic sinusoidal endothelial cells [165]. It can also be degraded locally through the enzymatic action of hyaluronidase, which is likely the case in bone and cartilage [165]. Hyaluronidase, which acts to break down the HA into smaller oligosaccharides, varies in level among tissues of the body and can also be affected by pathologic states [181, 182]. Hyaluronidase is predominantly produced by macrophages, fibroblasts, and endothelial cells, which are also able to uptake HA [164, 183, 184, 185]. It is likely that the majority of local HA degradation occurs intracellularly within acidic lysosomes after uptake mediated by CD44 [185, 186, 187, 183, 188] because hyaluronidase is only active at acidic pH [187, 183]. For example, alveolar macrophages are able to uptake and degrade HA *in vitro* [185], and HA is found in the cytoplasm of these cells *in vivo* [189]. CD44 was also noted in osteoprogenitor cells in mouse tibia sections, and the osteoprogenitor-like cell line, MG-63, expresses CD44 and can uptake and degrade HA [172]. The level of hyaluronidase freely available in the tissue space, which would be needed to degrade bulk HA hydrogels, is both difficult to estimate and likely to vary depending on the particular site, disease state, and so on. The circulating hyaluronidase level, measured in turbidity reducing units (TRU), is approximately 30 rTRU/mL in the rat, although this can increase to over 1000 rTRU/mL after acute liver injury [182], and has been measured at approximately 6 rTRU/mL in human plasma [190]. Hyaluronidase is also expressed, albeit at low levels on the order of milli-units/mL, in wound tissues, possibly by stromal and/or inflammatory cells [169].

HA may seem like an odd choice as a matrix material for scaffolds designed to regenerate bone, as hydrophilic scaffolds such as ones made from oligo[poly(ethylene glycol) fumarate] [191] and 1-vinyl-2-pyrrolidinone (NVP):*n*-butyl-methacrylate (BMA) [192] have been shown to have a negative effect on bone healing. The NVP:BMA scaffolds, prepared with increasing amounts of NVP thus increasing their hydrophilicity, resulted in decreased mineralization in ectopic demineralized bone matrix (DBM) implants [192]. However, HA has been shown to support bone growth in combination with other osteoconductive molecules. Scaffolds made from HA and collagen were more osteoconductive *in vivo* than collagen scaffolds alone, even though HA itself did not elicit an osteoconductive response [193]. While the most bone was observed with scaffolds containing only 10% HA, significant bone was still formed with scaffolds containing 66% HA compared to collagen controls [193]. HA is also able to increase some markers of differentiation in cultured osteoblasts *in vitro* with dose and size dependent effects [194]. A low molecular weight HA (60 kDa) upregulated OCN gene expression while high molecular weight HAs (900 kDa and 2300 kDa) increased alkaline phosphatase activity and mineralization [194]. Further, viscous solutions of HA have been used to deliver BMP-2 or FGF-2 to enhance healing in a non-union fracture model [195] and a primate fracture model [196], respectively.

As it is likely that osteoblasts will not want to migrate into the hydrophilic HA scaffolds, hydrogels delivering osteoinductive factors might stimulate osteoblasts to migrate to fill the defect as the scaffold degrades. When delivering angiogenic factors, discouraging osteoblast migration may allow a vascular network to be established first. Osteoblasts could then migrate into the remodeled scaffold or fill the volume as the scaffold degrades. In addition to stimulating endothelial cell migration due to angiogenic factors contained in the scaffold, the degrading scaffold itself may increase vascularization as lower molecular weight fragments of HA have been shown to have angiogenic effects [197, 198, 199]. HA oligosaccharides four to twenty-five disaccharides in length induced angiogenesis in the chick chorioallantoic membrane

(CAM) assay while undigested and completely digested HA did not [197]. Further, HA oligosaccharides three to sixteen disaccharides in length stimulated angiogenesis *in vivo* and increased endothelial cell proliferation *in vitro* [184]. Conversely, high molecular weight HA may impede angiogenesis [184, 200] and inhibit HA oligosaccharide-induced endothelial cell proliferation [199].

2.9.2 Hyaluronic Acid Hydrogels

To form the scaffold matrix, HA must be modified to form a stable hydrogel. For optimal performance, the scaffold would degrade over the course of tissue regeneration to allow complete repair of the defect by host tissue. A number of strategies have been developed to crosslink HA into a network, including diepoxy crosslinking, carbodiimide-mediated crosslinking, aldehyde crosslinking, divinyl sulfone crosslinking, and photo-crosslinking (reviewed in [164]) as well as reversible disulfide crosslinking [201]. Photo-crosslinking provides several advantages such as ease of materials handling and ability to perform crosslinking under physiologic conditions. Therefore, a photo-crosslinking method was utilized that was based on previously published reports [202, 203, 204, 205, 206, 207] where reactive methacrylate groups are attached to the HA backbone and free radical polymerization is induced by ultraviolet (UV) irradiation.

While the HA backbone itself should be degradable through the action of hyaluronidase *in vivo*, additional degradable sites can be engineered into the hydrogel network. For example, the crosslinker could include a degradable segment or the linkage formed during crosslinking could provide a site for degradation. The ether linkage formed by crosslinking HA with a diepoxy compound results in crosslinked hydrogel films that are slowly degradable under physiologic conditions [208]. The ester bonds of crosslinked glycidyl methacrylate derivatized dextran (another predominantly linear polysaccharide) can also undergo hydrolysis in a pH dependent fashion [209]. Additionally, HA hydrogels can be further modified with peptide sequences to increase

the functionality of the scaffold [210, 211, 212] or with benzyl groups (the modified polymer is known as Hyaff) to increase their hydrophobicity [213], although these modifications are beyond the scope of this dissertation.

Methacrylate-modified HA should retain the biocompatibility of unmodified HA. Hydrogels produced using a similar chemistry were found to be cytocompatible when exposed to human aortic endothelial cells (HAEC) *in vitro* as well as to support endothelial cell migration in a rat subcutaneous model *in vivo* [207]. While encapsulated cell viability was dependent on macromer concentration, hydrogels made with 2 wt% HA were able to maintain >95% viability of encapsulated fibroblasts, even after culturing for a week *in vitro* [214]. Further, these hydrogels supported neocartilage formation *in vivo* when used to implant encapsulated chondrocytes [214]. Hyaff 11 has been used to encapsulate mesenchymal stem cells that differentiated to form chondrocytes and osteoblasts *in vivo* [215], to encapsulate chondrocyte progenitors for the cartilage portion of osteochondral composite grafts [216, 217], and to support the proliferation and mineral formation of bone marrow stromal cells *in vitro* [218]. Hyaff 11 also supports the attachment, proliferation, and matrix secretion of endothelial cells *in vitro* [219].

The final parameter in selecting HA as a matrix material for the scaffolds is its ability to provide controlled release of proteins, which can be achieved by diffusion dependent on gel mesh size and electrostatic interactions between the negatively charged HA and positively charged proteins. Protein release from nondegradable hydrogels made from a glycidyl methacrylate derivatized dextran occurs by a diffusive mechanism and can be influenced by protein size, crosslink density, and equilibrium water content of the hydrogel [220]. Electrostatic interactions of glycidyl methacrylate derivatized HA (HA-GMA) hydrogels with cationic molecules has been shown for the model drug chlorpromazine HCl, and release could be controlled by altering the ionic strength and pH of the release buffer [204]. Hyaff-11 was found to retain BMP-2 and release an active form of the protein over a period of weeks, presumably due to

interactions between the protein and the HA [151]. Furthermore, HA hydrogels allow control of protein release due to diffusion limitations with further control provided by the incorporation of degradable microspheres within the matrix, as shown with a model protein, bovine serum albumin (BSA) [221].

2.9.3 Biodegradable Microspheres for Controlled Release

For additional control of release, proteins can be formulated into degradable microspheres. There are many well-established ways to prepare microspheres, and the ProLease^{TM} method [222], which is being developed commercially by Alkermes, was chosen to prepare PLGA microspheres. The ProLease^{TM} method offers advantages over other microsphere formulation techniques such as emulsions because there is no aqueous/organic interface formed which may denature proteins. This technique has been used to formulate human growth hormone (hGH) [223] and VEGF [224] into PLGA microspheres with control over release rates and maintenance of protein activity.

PLGA microspheres have been suspended within scaffolds on several occasions: PLGA microspheres containing BSA suspended in a HA hydrogel [221], PLGA or poly(propylene fumarate) (PPF) microspheres in an injectable PPF paste that polymerized *in situ* [225], PLGA microspheres containing BSA embedded in a PLGA scaffold (with a poly(vinyl alcohol) coating to prevent dissolution of the microspheres into the scaffold matrix during formation) [226], PLGA microspheres containing BMP-2 suspended within carboxymethylcellulose hydrogels [227, 228, 229], and platelet-derived growth factor (PDGF)-BB in PLGA microspheres suspended with $VEGF_{165}$ in a PLGA scaffold to provide different release mechanisms and kinetics for the two proteins [230]. While these studies have varied the temporal release of protein, no one has utilized degradable microspheres to control the spatial patterning of proteins within a scaffold.

A second strategy would be to prepare microspheres made of HA itself. HA

microspheres on the order of 5–20μm have been prepared by a water-in-oil emulsion technique using adipic dihydrazide as a crosslinker [231]. These microspheres were utilized for controlled release of plasmid DNA in gene therapy applications and were also conjugated to antibodies for cell targeting [231]. A water-in-oil emulsion with heat cross-linking was used to form HA microspheres for nasal delivery that were 20–30μm in size and contained the model drug gentamicin [232]. These microspheres degraded on the order of 5 hours and provided release profiles characterized by the Higuchi model of release from a matrix [232]. They also increased the intranasal absorption of gentamicin *in vivo* [233]. Other water-in-oil emulsion techniques using varying crosslinking chemistries, such as PEG diglycidyl ether, are being explored by colleagues at the University of Washington. These should result in microparticles with differing degradation and protein release profiles and would allow spatial localization of proteins within an all-HA scaffold.

2.9.4 Gradients in Controlled Release

Spatial patterning of protein can be controlled in a number of ways. As scaffold fabrication technologies become more sophisticated, the ability to spatially pattern proteins, chemical compositions, or even cells is starting to become a reality. A straightforward approach to creating gradients within a device is the lamination of pieces of different chemical compositions. Lamination was used to create non-uniform initial profiles of drug within a photo-crosslinked hydrogel to match theoretical predictions of release from diffusion-limited matrices and thus direct release [234]. Lamination has also been used to localize lipid microcylinders containing nerve growth factor (NGF) in selected regions of agarose gels to establish diffusion gradients and examine directional neurite extension of dorsal root ganglia (DRG) [235]. Differential crosslinking has been applied *ex vivo* to manipulate the resistance to diffusion of a hydrogel matrix and thus direct protein release [236]. In addition to pre-setting a gradient within the device, a gradient can be formed during the device implementation.

Rowley *et al.* used diffusion of calcium, a regulator of the differentiation of skeletal muscle cells, from an alginate hydrogel to generate a spatial functional gradient within a multilayer of cells adherent to the hydrogel [237]. Immobilization of cell adhesion peptides is a way to enhance cell adhesion to or migration into scaffolds, and methods are being developed to spatially pattern these molecules to provide chemical guidance of cellular migration [238].

2.10 Selection of Proteins for Experiments

As described earlier in this Chapter, many proteins have known or hypothesized osteoinductive or angiogenic effects. For this research, four proteins have been selected for evaluation. BMP-2 is a well-known osteoinductive molecule. VEGF is a well-established angiogenic growth factor. OPG has known bone-protective effects and may also be pro-angiogenic. Finally, LRAP has received mixed reports of chondro/osteogenic activity. These candidate molecules, particularly their use in bone regeneration applications and their suitability for use with an HA hydrogel or PLGA microsphere delivery system, are detailed below.

The proteins selected have differing net charges, as indicated by the theoretical pI values shown in Table 2.1, which would affect their ability to interact with HA. These theoretical pI values were calculated using the EMBL WWW Gateway to Isoelectric Point Service, which utilizes values from Lehninger's Biochemistry book [239, 240]. The sequences used to obtain these theoretical pI values are shown in Figure 2.2.

2.10.1 BMP-2

A well-established osteoinductive molecule, BMP-2 is suited for delivery from HA hydrogels due to its basic isoelectric point, both measured (pI > 8.5 [35]) and calculated (pI = 9.16, see Table 2.1). Naturally, BMPs are presented in the context of the ECM and can bind to heparin sulfate, heparin, and type IV collagen [245, 246]. The heparin binding domain contains several basic amino acids, contributing to the cationic

Albumin Sequence, from [241]

```
1   MKWVTFISLL LLFSSAYSRG VFRRDTHKSE IAHRFKDLGE EHFKGLVLIA FSQYLQQCPF DEHVKLVNEL
71  TEFAKTCVAD ESHAGCEKSL HTLFGDELCK VASLRETYGD MADCCEKQEP ERNECFLSHK DDSPDLPKLK
141 PDPNTLCDEF KADEKKFWGK YLYEIARRHP YFYAPELLYY ANKYNGVFQE CCQAEDKGAC LLPKIETMRE
211 KVLTSSARQR LRCASIQKFG ERALKAWSVA RLSQKFPKAE FVEVTKLVTD LTKVHKECCH GDLLECADDR
281 ASLAKYICDN QDTISSKLKE CCDKPLLEKS HCIAEVEKDA IPENLPPLTA DFAEDKDVCK NYQEAKDAFL
351 GSFLYEYSRR HPEYAVSVLL RLAKEYEATL EECCAKDDPH ACYSTVFDKL KHLVDEPQNL IKQNCDQFEK
421 LGEYGFQNAL IVRYTRKVPQ VSTPTLVEVS RSLGKVGTRC CTKPESERMP CTEDYLSLIL NRLCVLHEKT
491 PVSEKVTKCC TESLVNRRPC FSALTPDETY VPKAFDEKLF TFHADICTLP DTEKQIKKQT ALVELLKHKP
561 KATEEQLKTV MENFVAFVDK CCAADDKEAC FAVEGPKLVV STQTALA
```

BMP-2 Sequence, from [36]

```
1   MVAGTRCLLA LLLPQVLLGG AAGLVPELGR RKFAAASSGR PSSQPSDEVL SEFELRLLSM FGLKQRPTPS
71  RDAVVPPYML DLYRRHSGQP GSPAPDHRLE RAASRANTVR SFHHEESLEE LPETSGKTTR RFFFNLSSIP
141 TEEFITSAEL QVFREQMQDA LGNNSSFHHR INIYEIIKPA TANSKFPVTA LLDTRLVNQN ASRWESFDVT
211 PAVMRWTAQG HANHGFVVEV AHLEEKQGVS KRHVRISRSL HQDEHSWSQI RPLLVTFGHD GKGHPLHKRE
281 KRQAKHKQRK RLKSSCKRHP LYVDFSDVGW NDWIVAPPGY HAFYCHGECP FPLADHLNST NHAIVQTLVN
351 SVNSKIPKAC CVPTELSAIS MLYLDENEKV VLKNYQDMVV EGCGCR
```

GST Sequence, from [242]

```
1   MSPILGYWKI KGLVQPTRLL LEYLEEKYEE HLYERDEGDK WRNKKFELGL EFPNLPYYID GDVKLTQSMA
71  IIRYIADKHN MLGGCPKERA EISMLEGAVL DIRYGVSRIA YSKDFETLKV DFLSKLPEML KMFEDRLCHK
141 TYLNGDHVTH PDFMLYDALD VVLYMDPMCL DAFPKLVCFK KRIEAIPQID KYLKSSKYIA WPLQGWQATF
211 GGGDHPPKSD LEVLFQGPLG SPNSRVDSSG RIVTD
```

Figure 2.2a: Protein sequences used for pI calculations.

GST-LRAP Sequence, from [243, 242]

```
1   MSPILGYWKI KGLVQPTRLL LEYLEEKYEE HLYERDEGDK WRNKKFELGL EFPNLPYYID GDVKLTQSMA
71  IIRYIADKHN MLGGCPKERA EISMLEGAVL DIRYGVSRIA YSKDFETLKV DFLSKLPEML KMFEDRLCHK
141 TYLNGDHVTH PDFMLYDALD VVLYMDPMCL DAFPKLVCFK KRIEAIPQID KYLKSSKYIA WPLQGWQATF
211 GGGDHPPKSD LEVLFQGPLG SMPLPPHPGH PGYINFSYEV LTPLKWYQNM IRHPSLLPDL PLEAWPATDK
281  TKREEVD
```

LRAP Sequence, from [243]

```
1   MPLPPHPGHP GYINFSYEVL TPLKWYQNMI RHPSLLPDLP LEAWPATDKT KREEVD
```

OPG Sequence, from [97]

```
1   MNKLLCCALV FLDISIKWTT QETFPPKYLH YDEETSHQLL CDKCPPGTYL KQHCTAKWKT VCAPCPDHYY
71  TDSWHTSDEC LYCSPVCKEL QYVKQECNRT HNRVCECKEG RYLEIEFCLK HRSCPPGFGV VQAGTPERNT
141 VCKRCPDGFF SNETSSKAPC RKHTNCSVFG LLLTQKGNAT HDNICSGNSE STQKCGIDVT LCEEAFFRFA
211 VPTKFTPNWL SVLVDNLPGT KVNAESVERI KRQHSSQEQT FQLLKLWKHQ NKDQDIVKKI IQDIDLCENS
281 VQRHIGHANL TFEQLRSLME SLPGKKVGAE DIEKTIKACK PSDQILKLLS LWRIKNGDQD TLKGLMHALK
351 HSKTYHFPKT VTQSLKKTIR FLHSFTMYKL YQKLFLEMIG NQVQSVKISC L
```

$VEGF_{121}$ Sequence, from [244]

```
27                              APMA EGGGQNHHEV VKFMDVYQRS YCHPIETLVD IFQEYPDEIE
71  YIFKPSCVPL MRCGGCCNDE GLECVPTEES NITMQIMRIK PHQGQHIGEM SFLQHNKCEC RPKKDRARQE
141 NCDKPRR
```

$VEGF_{165}$ Sequence, from [244]

```
27                              APMA EGGGQNHHEV VKFMDVYQRS YCHPIETLVD IFQETPDEIE
71  YIFKPSCVPL MRCGGCCNDE GLECVPTEES NITMQIMRIK PHQGQHIGEM SFLQHNKCEC RPKKDRARQE
141 NPCGPCSERR KHLFVQDPQT CKCSCKNTDS RCKARQLELN ERTCRCDKPR R
```

Figure 2.2b: Protein sequences used for pI calculations (continued).

Table 2.1: Theoretical pI values for proteins of interest.

Protein	pI
Albumin	5.75
BMP-2	9.16
GST	5.67
GST-LRAP	5.70
LRAP	5.79
OPG	8.27
$VEGF_{121}$	5.82
$VEGF_{165}$	7.29

nature of BMP-2. This should also allow it to complex with HA for presentation within the scaffold in a way that mimics its native environment.

Bone healing induced by BMP-2 been evaluated in numerous animal models. The efficacy of BMP-2 can be enhanced by extended localized release, as has been shown in a comparison of immediate *versus* sustained release formulations of PLGA microspheres [229]. More sophisticated devices have been developed to release matrix-bound BMP-2 upon cleavage of a fusion protein by cell-surface associated proteases [247]. These constructs induced significant bone formation when loaded with BMP-2 in rat and rabbit calvarial defect models as well as in a dog pancarpal fusion model [247].

BMP-2 has previously been delivered from a hydrogel system prepared from crosslinked gelatin [248]. Interestingly, Yamamoto *et al.* noted a different pattern of bone growth for the gelatin hydrogels compared to nonwoven poly(glycolic acid) (PGA) fabrics. Bone formed at the edges of gelatin hydrogels containing BMP-2 while ectopic bone formed inside the nonwoven PGA fabrics with BMP-2 [248]. BMP-2 has

successfully been used with HA carriers [195, 249]; however, these preparations were not crosslinked to form hydrogels. Arosarena and Collins utilized an esterified HA sponge and showed significant bone formation when delivering 1μg BMP-2 in a rat mandibular defect model [249]. Eckardt *et al.* demonstrated significant improvements in healing when using BMP-2 with an HA carrier in a rabbit tibial non-union model [195].

Further, BMP-2 may have a synergistic interaction with angiogenesis to enhance bone formation. Gao *et al.* delivered BMP-2 covalently attached to a type IV collagen carrier and showed increased bone formation compared to BMP-2 controls (no carrier), possibly from increased vascularization due to the type IV collagen carrier [250]. BMP delivery has also been associated with angiogenesis *in vivo* [251, 252]. Suwa *et al.* noted networks of new vessels on BMP-hydroxyapatite complexes that also induced bone formation [252].

2.10.2 VEGF

VEGF, as a potent angiogenic molecule, is a natural choice to test with the HA hydrogel scaffold system. Similar to BMP-2, the $VEGF_{165}$ isoform is a cationic protein with heparin-binding affinity. The amino acid sequence of $VEGF_{165}$ contains clusters of basic amino acids around residues 110, 123, and 163 [107]. Its isoelectric point has been measured at 8-8.5 [107] and was calculated to be 7.29 (Table 2.1). For comparison, the freely diffusible $VEGF_{121}$ isoform is not cationic with a calculated pI of 5.82 (Table 2.1) because it is missing the heparin binding domain. Retention of VEGF within the HA hydrogel scaffolds may also mimic natural tissue inductive processes. Keyt *et al.* hypothesize that the affinity of VEGF for its heparin matrix allows it to be released during extracellular matrix degradation [120]. Zisch *et al.* incorporated covalent but enzymatically cleavable linkages to allow VEGF to be released from scaffolds as cells invade, which stimulated angiogenesis [253]. This highlights the importance of controlled, localized delivery of VEGF for optimal effects, as has

also been shown with a calcium alginate microsphere delivery system [254]. Despite using a less-sophisticated scaffold with diffusion controlled instead of cell-demanded release, Elçin *et al.* demonstrated that neovascularization was limited to a region immediately adjacent to the implant [254].

Despite the links between angiogenesis and bone growth as described above, few groups have attempted to deliver angiogenic factors as a treatment to regenerate bone. Street *et al.* showed significant increases in calcified callus with sustained release of VEGF in both a murine femoral "challenged" fracture healing model (dose of 10μg VEGF) and a rabbit radius segmental gap model (dose of 50-1000μg VEGF) [255]. Murphy *et al.* developed mineralized, porous, PLGA scaffolds for the controlled release of VEGF [256], which significantly enhanced the vascularization and mineralization of the scaffolds in a rat calvarial critical size defect model, although there was no significant difference in osteoid compared to the mineralized scaffold without VEGF [257]. Non-mineralized PLGA scaffolds loaded with VEGF improved angiogenesis and bone formation in calvarial defects further challenged by radiation therapy [258]. Also in Mooney's group, Huang *et al.* showed a significant enhancement in bone formation by adding VEGF to scaffolds combining bone marrow stromal cells and plasmid DNA encoding BMP-4 [259]. Similar synergy between VEGF and BMP-4 was also noted by Peng *et al.* [260]. Interestingly, in other studies, Peng *et al.* showed that VEGF delivery alone was insufficient to induce bone formation in the calvarial critical size defect model [261]. However, endogenous VEGF contributed to BMP-2 mediated bone formation as administration of the soluble VEGF receptor, sFlt1, reduced bone formation [261]. Further, exogenous VEGF administration enhanced BMP-2 mediated bone formation, particularly by increasing angiogenesis and cartilage resorption [261].

2.10.3 OPG

Similar to BMP-2 and VEGF, OPG also contains a C-terminal heparin-binding domain [100]. Further, its pI was calculated to be 8.27 (Table 2.1). These properties indicate that it should associate with the negatively charged HA used as the scaffold matrix. Use of exogenously administered OPG to induce bone formation and angiogenesis in a critical size bone defect model has not previously been reported.

2.10.4 LRAP

In contrast to BMP-2, VEGF, and OPG, the fourth protein examined, LRAP, is not cationic. Its pI was calculated to be 5.79 (Table 2.1). Additionally, since the peptide was used as a glutathione-S-transferase (GST) fusion protein, the effect of the GST domain on the pI of the fusion peptide was determined. The pI of GST (5.67, Table 2.1) was fairly similar to LRAP; therefore, the calculated pI of the LRAP-GST fusion was also similar (5.70, Table 2.1). Since the LRAP-GST fusion protein was not cationic, the HA hydrogels should only provide diffusion-controlled release, which was expected to be quite rapid. Therefore, LRAP was formulated only into PLGA microspheres for delivery. As described previously, LRAP has had reports of osteo/chondrogenic activity both *in vitro* and *in vivo* [65, 66, 67]; however, its capacity to regenerate bone has not been tested in a challenged model of healing.

2.11 Optical Coherence Tomography (OCT)

While great strides have been made to design treatments that improve healing, a major limitation in the field of regenerative medicine is the ability to monitor tissue regeneration *in situ* as it is occurring. The current standard requires harvesting and fixing the tissue for analysis, which can lead to artifacts, and requires the use of many animals for longitudinal studies. There is a clear need for a non-invasive imaging technique with the ability to monitor repair and remodeling processes in a

living animal over time as well as with the capability to measure implant and tissue characteristics without fixation artifacts. One such technology is optical coherence tomography (OCT).

OCT has been used since the early 1990s to image samples of biological relevance [262]. Its superb spatial resolution (<10μm) and moderate penetration depth in nontransparent tissue (1 to 2mm) offer advantages over other high-resolution optical imaging techniques [263]. OCT, an optical analog of ultrasound, is a non-invasive imaging modality that utilizes the echo time delay of reflected light to generate an image. Since the speed of light is too fast to measure this delay directly, principles of low coherence interferometry are used. An incident beam of low coherence light is split so that half is sent to the sample and half is sent to a reference mirror of known position. Light reflection in the sample occurs at interfaces of structures with different optical characteristics. Interference between the two reflected beams indicates that light reflected by a structure within the sample travels over the same distance as light reflected by the reference mirror. The reference mirror can be scanned to obtain a depth profile of the sample. Two-dimensional (2-D) and three-dimensional (3-D) images can be obtained by scanning the imaging beam across the sample.

OCT has been used both *in vivo* and *ex vivo* to image tissues ranging from the esophagus [264] to cartilage [265]. Further, it has been used to image tissue engineering constructs *in vitro* [266, 267, 268]. To date, it has not been used to image regenerating bone, although some bone structure has been observed during imaging of the bone-cartilage interface after articular cartilage repair [269]. OCT has been used to image several vascular structures, including arterial wall microstructure [270], *in vitro* tissue engineered blood vessels [271], and subcutaneous blood vessels [272], although no one has used it for imaging of neovessels formed during angiogenesis *in vivo*.

2.12 Calvarial Critical Size Defect Model

The rat calvarial critical size defect model was first used by Ray and Holloway in the 1950s [273]. Defects larger than a critical size will not heal on their own, which provides a means to evaluate the efficacy of treatments to induce bone formation. Further, the defect is placed in the parietal bones, a nonweight-bearing location, which minimizes the effects of loading and motion during the healing process. The size of the defect required to be considered critical size varies with the age of the rat. In rats older than 4 weeks, the critical size is accepted to be greater than 8mm [33]. Defects as small as 5mm in diameter have been considered critical size in adult rats [274].

The process of bone formation in the calvarial defect model has been well-characterized. Similar to the intramembranous ossification process by which the parietal bones form, calvarial defects appear to heal by direct osteoblast differentiation (i.e., without the formation of a cartilage intermediate) [33]. In studies evaluating DBM in the calvarial defect model, Wang *et al.* noted proliferation of mesenchymal stem cells followed by their differentiation into osteoblasts [33]. Only small, spatially distinct regions of cartilage were formed, which were quickly resorbed and replaced by bone [33]. While it seems obvious that osteoblasts and/or osteoblast progenitors can migrate into the defect region from the surrounding native bone, an additional source of progenitor cells is the *dura mater*. Perivascular mesenchymal-type cells (pericytes) in the *dura* have been shown to proliferate and differentiate in response to BMP stimulation [275]. This second source of cells can result in axial as well as the expected radial pattern of new bone formation. Finally, the expression of characteristic bone markers, such as BSP, ALP, and OPN [31, 33], which follow the process of bone healing in this model, provide an additional means to characterize the effects of a treatment. Regions of regenerating tissue that have not yet mineralized can be evaluated to determine if the cells present are osteoblasts or osteoblast progenitors early in the process of

forming bone.

To allow the capacity for OCT imaging of healing in the defect site, the traditional calvarial defect model had to be slightly modified. While OCT has a moderate penetration depth in nontransparent tissue, the skin over the defect would preclude imaging of the bone below. To keep the skin out of the way, a "window chamber" was implanted over the defect site. The "window chamber" had two purposes: the cover glass provided a transparent, thin cover to image through into the defect site while the stainless steel chamber prevented closure of the skin over the defect site. This procedure is similar to the "head cap", a long-term implant for electrophysiologic recording [276, 277], which has also been used to attach a fiberscope for high resolution imaging of the brain using two-photon microscopy [278]. A simplified cranial window has been used extensively by Jain and colleagues to image angiogenesis near the brain [279]. However, the "window chamber" differs significantly from the "head cap" and cranial window because it preserves the bone around the margins of the defect to allow normal healing to occur, thus placing stricter restrictions on how the chamber is anchored to the skull. A bone chamber device that allows optical imaging of healing bone has been developed by Bao and colleagues [280]; however, the technique does not offer the depth resolving power of OCT and only a 100μm thick section of bone is imaged.

2.13 Summary

The goal of this Chapter was to provide a literature review to place this dissertaation research in the context of current approaches to the regeneration of bone tissue. It also highlights the novelty of the research. This represents the first time that BMP-2 will be delivered from crosslinked HA hydrogels, which some might argue is not too different from delivery of BMP-2 from viscous solutions of HA. However, the ability to control the degradation rate of the crosslinked scaffold and thus the persistence of both BMP-2 and HA in the defect site allows interesting questions to be asked about

the temporal progression of bone regeneration and the suitability of this materials system. Additional information can be obtained on the microstructural organization of the regenerating tissue. This review has attempted to highlight the importance of bone architecture on its mechanical and functional properties.

The other three proteins to be examined, VEGF, OPG, and LRAP, have had varying reports of their ability to induce bone formation, and this work will test their efficacy using sustained release formulations in a challenged model of bone healing. The discussion of the known effects of these proteins as well as the interplay between angiogenesis and bone growth during natural and induced processes of bone formation and remodeling indicates that these molecules may be able to enhance bone formation. It may only be a matter of delivering these proteins in the "right" manner — at the proper time, location, and dose with an appropriate carrier scaffold.

Finally, this research will develop a novel animal model for the *in vivo* imaging of angiogenesis and bone growth using OCT. As described, the processes of angiogenesis and bone growth involve the coordination of different cells, ECM molecules, and other proteins, which result in clear morphological changes. This research will be the first to utilize OCT to attempt to visualize these changes.

Chapter 3

PREPARATION AND *IN VITRO* CHARACTERIZATION OF HYALURONIC ACID HYDROGELS

3.1 Introduction

As described in the preceeding Chapter, the goal of this dissertation research was to develop regenerative scaffolds that can provide signals to stimulate bone formation as well as that can degrade over an appropriate time scale to allow tissue growth. An extensive list of the design criteria and the rationale for the selection of hyaluronic acid (HA) as the matrix material were also provided. The research described in this Chapter developed HA hydrogels as regenerative scaffolds that can provide an initial level of controlled release of proteins over a period of weeks and that can potentially promote an early angiogenic response to be followed by bone ingrowth and mineralization by serving as a matrix to support cellular ingrowth. Protein release from the HA hydrogel scaffolds can be influenced by diffusion of the protein through pores in the hydrogel network and also by electrostatic interactions between the protein and the HA. Formulation parameters can affect the crosslink density of the hydrogel, the pore size, and thus the diffusion of proteins out of the hydrogels. Additionally, electrostatic interactions between positively-charged proteins and the negatively-charged HA can further slow protein release from the hydrogels. The retention of proteins may encourage cellular migration into the scaffold as well as allow release of proteins over an extended time period while the scaffold degrades.

The chemistry utilized to form the HA hydrogels was based on established techniques of photo-initiated free radical polymerization of methacrylate-modified HA [202, 203, 204, 205, 206, 207]. Characterization of the degradation of these hydrogels

has previously focused on the ability of the enzyme hyaluronidase to still degrade the chemically modified and crosslinked forms of HA. However, it is likely that these hydrogels would see much lower levels of hyaluronidase activity *in vivo* as serum levels are low [?, 190] and an acidic pH (presumably within a cell or lysosome) is needed for optimum enzyme activity [183, 187]. Therefore, this study has also examined the ability of HA hydrogels to degrade via hydrolysis. The ester bonds formed by the addition of the methacrylate group to the HA backbone may degrade through a hydrolytic mechanism as has been shown previously for ether linkages (formed by crosslinking HA with a diepoxy compound) that are slowly degradable under physiologic conditions [208] and for ester bonds of crosslinked glycidyl methacrylate derivatized dextran that undergo hydrolysis in a pH dependent fashion [209]. Finally, the effect of crosslink density and stability on the physical properties of the hydrogels as well as on the ability of the hydrogels to control protein release through diffusive and electrostatic mechanisms was examined.

3.2 Materials and Methods

3.2.1 Materials

All materials were obtained from Sigma-Aldrich (St. Louis, MO) unless otherwise noted. All solvents were of reagent grade.

3.2.2 Glycidyl Methacrylate Modified HA (HA-GMA) Preparation Method I, after [281]

HA (either 2,000kDa from Genzyme, Boston, MA or 220kDa from Lifecore, Chaska, MN) was dissolved at 14.3 mg/mL in DI water overnight. The pH was adjusted to 9 by using 1N NaOH. A 29-fold molar excess of glycidyl methacrylate (GMA) was added, and the reaction was allowed to proceed at room temperature for 7-22 days with stirring. The reaction was stopped by adjusting the pH to 7 with 1N HCl, and

the product was purified.

3.2.3 HA-GMA Preparation Method II, after [282]

HA (220kDa) was dissolved at 50 mg/mL in 0.05M carbonate buffer (pH 11) overnight. A 1.5-fold molar excess of GMA was added, and the reaction was allowed to proceed at room temperature for 7 days with stirring. The reaction was stopped by adjusting the pH to 7 with 1N HCl, and the product was purified.

3.2.4 HA-GMA Preparation Method III, after [207]

HA (220kDa) was dissolved at 10 mg/mL in DI water overnight. Triethylamine (TEA; 5- to 20- fold molar excess), GMA (20-fold molar excess), and tetrabutyl ammonium bromide (TBA Br; equivalent amount to TEA) were added. The reaction was allowed to proceed at room temperature for 24 hours with stirring, and then the mixture was placed at 60°C for 1 hour. The reaction was stopped by adjusting the pH to 7 with 1N HCl, and the product was purified.

3.2.5 HA-GMA Preparation Method IV, after [206]

HA (220kDa) was dissolved at 20 mg/mL in DI water overnight. Dimethylaminopyridine (DMAP; 0.7 to 3.6- fold molar excess) and GMA (0.6- to 60- fold molar excess) were added. The reaction was allowed to proceed at room temperature for 48 hours with stirring. The reaction was stopped by adding 1N HCl, and the product was purified.

3.2.6 HA-GMA Preparation Method V, after [283]

HA (110kDa, Lifecore) was first converted to the tetrabutyl ammonium salt form (TBA HA). The TBA HA was dissolved in dimethyl sulfoxide (DMSO) at 20 mg/mL. A 5-fold molar excess of DMAP was added. A 2-fold molar excess of GMA was

added, and the reaction was allowed to proceed at 30°C for 16 hours. The reaction was stopped by adding 10% v/v 2.5M NaCl, and the product was purified.

3.2.7 Methacrylic Anhydride Modified HA (HA-MA) Preparation Method I, after [203]

HA (2,000kDa or 220kDa) was dissolved at 20 mg/mL in DI water overnight. A 20-fold molar excess of methacrylic anhydride (MA) was added. The pH of the reaction mixture was adjusted to 8 with 5N NaOH, and the reaction was allowed to proceed at 5°C for 24 hours with stirring. The reaction was stopped by adding 1N HCl, and the product was purified.

3.2.8 HA-MA Preparation Method II, after [205]

HA (220kDa) was dissolved at 20 mg/mL in DI water overnight. A 2-fold molar excess of TEA was added, and a 20-fold molar excess of MA was added. The reaction was allowed to proceed at 60°C for 10 hours. The reaction was stopped by adjusting the pH to 7, and the product was purified.

3.2.9 HA-GMA and HA-MA Purification

HA-GMA and HA-MA were purified from unreacted GMA, MA, or catalysts by one of the following methods: (1) 2X – 3X precipitation in ethanol, (2) dialysis using a 12,000 to 14,000 molecular weight cutoff (MWCO), (3) 1X – 2X acetone precipitation, (4) 2X tetrahydrofuran (THF) precipitation, or (5) PD-10 column. The purified product was dissolved in DI water and lyophilized.

3.2.10 Gel Permeation Chromatography (GPC)

HA-GMA or HA-MA were dissolved at 3-6 mg/mL in phosphate buffer (PB), pH 8.0, and filtered through a 0.2μm filter. Samples were run on a GPCMax (Viscotek,

Houston, TX) using poly(ethylene oxide) (PEO) standards.

3.2.11 ^{1}H-NMR Characterization

HA-GMA or HA-MA was dissolved at a minimum concentration of 10 mg/mL in deuterium oxide (D_2O, Cambridge Isotope Laboratories, Andover, MA). ^{1}H-NMR spectra were obtained on a Bruker (Billerica, MA) Avance DRX series instrument at a frequency of 499.85 MHz. The degree of substitution (DS; number of methacrylate groups per 100 disaccharide units) was calculated from the ^{1}H-NMR spectra by taking ratios of the acrylate peaks at ~5.6 and ~6.1 ppm, which arise from the methacrylate group only, and the methyl peak at 1.9 ppm, which includes protons from the methacrylate group and backbone methyl group. Extent of crosslinking, which should decrease the acrylate peaks, was determined by degrading crosslinked HA-GMA hydrogels at pH 2 and 100°C for 4 hours prior to analysis by ^{1}H-NMR.

3.2.12 HA Hydrogel Formation

HA-GMA or HA-MA was dissolved in DI water or phosphate buffered saline (PBS) and mixed with a photo-initiator in a volume ratio of 10:1 (polymer solution:initiator solution). The photo-initiator, 2-hydroxy-1-[4-(hydroxyethoxy)phenyl]-2-methyl-1-propanone (Irgacure® 2959, Ciba, Tarrytown, NY), was dissolved at a concentration of 20 mg/mL in methanol. Crosslinking was initiated by exposure to ultraviolet (UV) radiation (365nm) for 20-30 minutes to form a solid gel. Hydrogels were molded into cylinders by crosslinking in wells of multi-well plates. In most cases, after formation, the hydrogels were rinsed, frozen, and lyophilized, and then rehydrated in DI water or PBS (with or without protein).

3.2.13 Swelling Ratio Measurement

Hydrogels were prepared from 250μL solutions of modified HA as described above and were lyophilized without rinsing. The dry weight (W_d) of the lyophilized hydrogel was measured. The hydrogels were then suspended in 5mL DI water and allowed to equilibrate. The samples were blotted of excess water and weighed at different time points to give a wet weight (W_s). The swelling ratio was taken as W_s/W_d.

3.2.14 Characterization of Enzymatic Degradation

Hydrogels were suspended in 1mL of 30mM citrate buffer, pH 5.3, containing various concentrations of hyaluronidase and placed at 37°C. At selected time points, the buffer was completely removed and replaced with fresh hyaluronidase solution. The amount of HA released into the buffer was measured by a carbazole assay.

3.2.15 Characterization of Hydrolytic Degradation

Hydrogels were prepared from 100μL solutions of modified HA as described above. Hydrogels were prepared at 40 mg/mL and 20 mg/mL modified HA, and some had the addition of 4 mg/mL 1-vinyl-2-pyrrolidinone (NVP). The hydrogels were suspended at 37°C in 1mL of buffer at different pH and ionic strengths. The buffer was completely removed and replaced at selected time points, and the amount of HA released into the buffer was quantified by a carbazole assay. Buffers used included phosphate buffered saline (PBS, pH 7.4), 4-(2-hydroxyethyl)-1-piperazine ethane sulfonic acid buffered saline solution (HEPES-BSS; pH 7.2), 138mM NaCl in unbuffered DI water (pH ~5.5), and 0.1M carbonate buffer, pH 10.0.

3.2.16 Carbazole Assay for Measurement of Released HA

A carbazole assay was run in a 96-well plate format, after [284]. Samples were diluted to fall within the range of the standard curve (0.03-2 mg/mL HA). 50μL of sample or

standard was added to each well of a 96-well plate. 200μL of 25mM sodium tetraborate in sulfuric acid was added per well and mixed. The plate was heated at 100°C for 10 minutes and then cooled at room temperature for 15 minutes. 50μL of 0.125% carbazole in absolute ethanol was added per well and mixed. The plate was heated at 100°C for 10 minutes and then cooled at room temperature for 15 minutes. The absorbance was read at 550nm on a Safire 2 plate reader (Tecan, Mannedorf/Zurich, Switzerland).

3.2.17 In Vitro Protein Release

Hydrogels were prepared from a 100μL solution of HA-GMA, as described above. The hydrogels were loaded with protein by soaking the lyophilized gels in 100μL of a 10 mg/mL bovine serum albumin (BSA) solution or a 0.01 mg/mL vascular endothelial growth factor (VEGF) solution. After equilibration for 1 hour, the gels were suspended in 1mL of DI water (for BSA and BSA control samples) or 1% BSA in DI water (for VEGF and VEGF control samples) as a release buffer and placed at 37°C. The release buffer was completely removed and replaced at selected time points. The concentration of BSA in the release buffer was measured by a Coomassie Plus^{TM} (Bradford) assay (Pierce, Rockford, IL). The concentration of VEGF in the release buffer was measured by enzyme-linked immunosorbent assay (ELISA) (R&D Systems, Minneapolis, MN). Calculations of the amount of protein released were based on the actual amount of buffer retrieved from each well at each time point.

3.3 Results

3.3.1 Hyaluronic Acid Modification and Characterization

HA was first modified with GMA to conjugate reactive vinyl groups following published reports [281, 282, 207, 206, 283, 203, 205]. After purification, the degree of substitution (the number of methacrylate groups per 100 disaccharide units) and any

contaminants from the fabrication process remaining after purification were determined by ^{1}H-NMR, and the molecular weight of the polymer was determined by GPC. Hydrogels were prepared using a photo-initiated free radical polymerization with Irgacure 2959 as an initiator. The different starting modified HAs were assessed qualitatively for their ability to form a gel, and release of BSA from the hydrogels was measured. Modified HAs were prepared by seven different methods (conditions shown in Table 3.1), and their properties are summarized in Table 3.2.

As the degree of substitution should indicate the number of reactive vinyl groups available to form crosslinks, a comparison between the swelling ratio and degree of substitution was made for hydrogels fabricated using starting solutions of 20 mg/mL modified HA (Figure 3.1). The swelling ratio should indicate the extent of functional crosslinks formed. The swelling ratio was taken as W_s/W_d where W_s is the wet weight of the hydrogel after equilibration in excess DI water and W_d is the dry weight of the hydrogel. The swelling ratio of the hydrogels in water decreases with increasing degree of substitution, indicating a higher crosslink density (Figure 3.1).

The modified HA from batch HA(LMW)-GMA 1d, which had a degree of substitution of approximately 17, was initially selected for further analysis. The above crosslinking conditions (20 mg/mL HA-GMA; 30 minutes UV irradiation) resulted in the conversion of approximately 90% of the reactive vinyl groups, as measured by ^{1}H-NMR, indicating that the gels were well-crosslinked. These hydrogels were characterized *in vitro* for their degradative behavior (this Chapter) and protein release (this Chapter and Chapters 4–5) and *in vivo* in a rat calvarial critical size defect model (Chapters 4, 5, and 8).

3.3.2 HA-GMA Hydrogel Degradation

To confirm that the chemical modifications to the HA would not prevent degradation by hyaluronidase, HA-GMA hydrogels were degraded in various concentrations of hyaluronidase (Figure 3.2). The concentration of uronic acid released from the

Table 3.1: Methods used to modify HA with GMA or MA.

Batch Name	Method	MW of HA	Catalyst	GMA or MA (ME)	Reaction Conditions	Purification
HA(HMW)GMA 1c	[281]	~2,000 kDa	pH 9 by NaOH	GMA (29)	9 days; RT	(2)
HA(HMW)MA 1c	[203]	~2,000 kDa	pH 8 by NaOH	MA (27)	9 days; RT	(2)
HA(HMW)MA 1d	[203]	~2,000 kDa	pH 8 by NaOH	MA (27)	9 days; RT	(1)
HA(LMW)GMA 1a	[281]	220 kDa	pH 9 by NaOH	GMA (29)	7 days; RT	(2)
HA(LMW)-GMA 1b	[281]	220 kDa	pH 9 by NaOH	GMA (29)	7 days; RT	(3)
HA(LMW)-GMA 1c	[281]	220 kDa	pH 9 by NaOH	GMA (29)	7 days; RT	(4)
HA(LMW)-GMA 1d	[281]	220 kDa	pH 9 by NaOH	GMA (29)	7 days; RT	(4)
HA(LMW)GMA 2a	[282]	220 kDa	Carbonate Buffer	GMA (1.5)	7 days; RT	(2)
HA(LMW)-GMA 2b	[282]	220 kDa	Carbonate Buffer	GMA (1.5)	7 days; RT	(3)
HA(LMW)GMA 3a	[207]	220 kDa	TEA (20 ME); TBA Br	GMA (20)	24 hours; RT + 1 hour; 60°C	(2)
HA(LMW)GMA 3b	[207]	220 kDa	Same as 3a twice	Same as 3a twice	Same as 3a twice	(2)
HA(LMW)GMA 3d	[207]	220 kDa	TEA (20 ME); TBA Br	GMA (20)	24 hours; RT + 1 hour; 60°C	(3)
HA(LMW)GMA 4a	[206]	220 kDa	DMAP (3.6 ME)	GMA (60)	48 hours; RT	(2)
HA(LMW)GMA 4b	[206]	220 kDa	DMAP (0.7 ME)	GMA (0.6)	48 hours; RT	(2)
HA(LMW)-GMA 4c	[206]	220 kDa	DMAP (3.6 ME)	GMA (60)	48 hours; RT	(3)
HA(110)-GMA 5a	[283]	110 kDa	DMAP (5 ME)	GMA (2)	16 hours; 30°C	(2,3)
HA(LMW)MA 1a	[203]	220 kDa	pH 8 by NaOH	MA (20)	24 hours; 5°C	(2)
HA(LMW)-MA 1b	[203]	220 kDa	pH 8 by NaOH	MA (20)	24 hours; 5°C	(3)
HA(LMW)MA 2a	[205]	220 kDa	TEA (2 ME)	MA (20)	10 hours; 60°C	(2)
HA(LMW)-MA 2b	[205]	220 kDa	TEA (2 ME)	MA (20)	10 hours; 60°C	(3)

Table 3.2: Properties of HA-GMA and HA-MA.

Batch Name	Yield	MW (PI)	DS	Contamination	Gel Ability	Swelling Ratio	BSA Release (Burst; Rate)
HA(HMW)-GMA 1c	N/A	N/A	26-30%	None	Good gel	N/A	N/A
HA(HMW)-MA 1c	N/A	N/A	12-13%	None	Good gel	144.6 ± 53.1	32%; 0.58%/day
HA(HMW)-MA 1d	N/A	N/A	0.23	None	Good gel	N/A	N/A
HA(LMW)-GMA 1a	N/A	258 kDa (2.44)	21-26%	None	Good gel	67.9 ± 9.6	10%; 0.17%/day
HA(LMW)-GMA 1b	0.36	282 kDa (1.54)	45-54%	None	Good gel	38.4 ± 5.7	66%; 0.05%/day
HA(LMW)-GMA 1c	0.88	N/A	22-24%	None	Good gel	110.4 ± 7.5	N/A
HA(LMW)-GMA 1d	0.89	N/A	12-17%	None	Good gel	87.9 ± 9.4	N/A
HA(LMW)-GMA 2a	N/A	221 kDa (1.67)	0.04	None	Little gelling	N/A	N/A
HA(LMW)-GMA 2b	0.88	289 kDa (1.44)	0.04	Yes, with ?	No gel	N/A	N/A
HA(LMW)-GMA 3a	N/A	275 kDa (1.60)	8-15%	TEA and TBA Br	Gel	N/A	N/A
HA(LMW)-GMA 3b	N/A	283 kDa (1.56)	5-7%	TEA and TBA Br	Gel	80.1 ± 36.1	25%; 0.60%/day
HA(LMW)-GMA 3d	0.87	258 kDa (1.57)	3-4%	TEA and TBA Br	Gel	212.8 ± 34.3	12%; 0.21%/day
HA(LMW)-GMA 4a	N/A	274 kDa (1.85)	55-72%	DMAP	Good gel	27.1 ± 16.7	17%; 0.12%/day
HA(LMW)-GMA 4b	N/A	342 kDa (1.42)	0	DMAP	No gel	N/A	N/A
HA(LMW)-GMA 4c	0.4	297 kDa (1.60)	6-8%	DMAP	Good gel	195.6 ± 18.5	18%; 0.49%/day
HA(110)-GMA 5a	0.75	N/A	0.166	None	Good gel	N/A	N/A
HA(LMW)-MA 1a	N/A	336 kDa (1.68)	61-86%	None	Insoluble	50.4 ± 10.5	N/A
HA(LMW)-MA 1b	0.03	N/A	15-17%	None	N/A	N/A	N/A
HA(LMW)-MA 2a	N/A	275 kDa (1.76)	0.09	TEA	Gel	110.9 ± 12.9	19%; 0.44%/day
HA(LMW)-MA 2b	0.9	299 kDa (1.58)	16-22%	TEA	Good gel	102.2 ± 3.4	6%; 0.07%/day

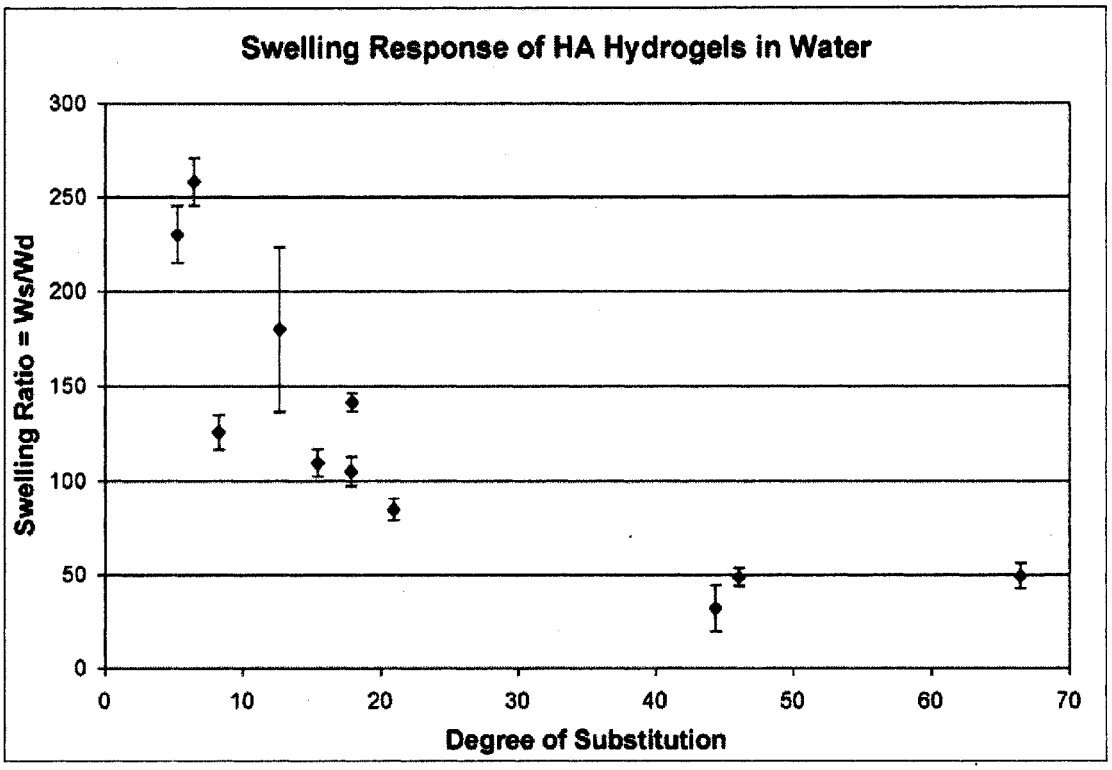

Figure 3.1: Swelling behavior of HA hydrogels as a function of degree of substitution. Swelling ratios shown as mean and standard error from triplicate samples. Degree of substitution calculated from ^{1}H-NMR spectra of the uncrosslinked polymer.

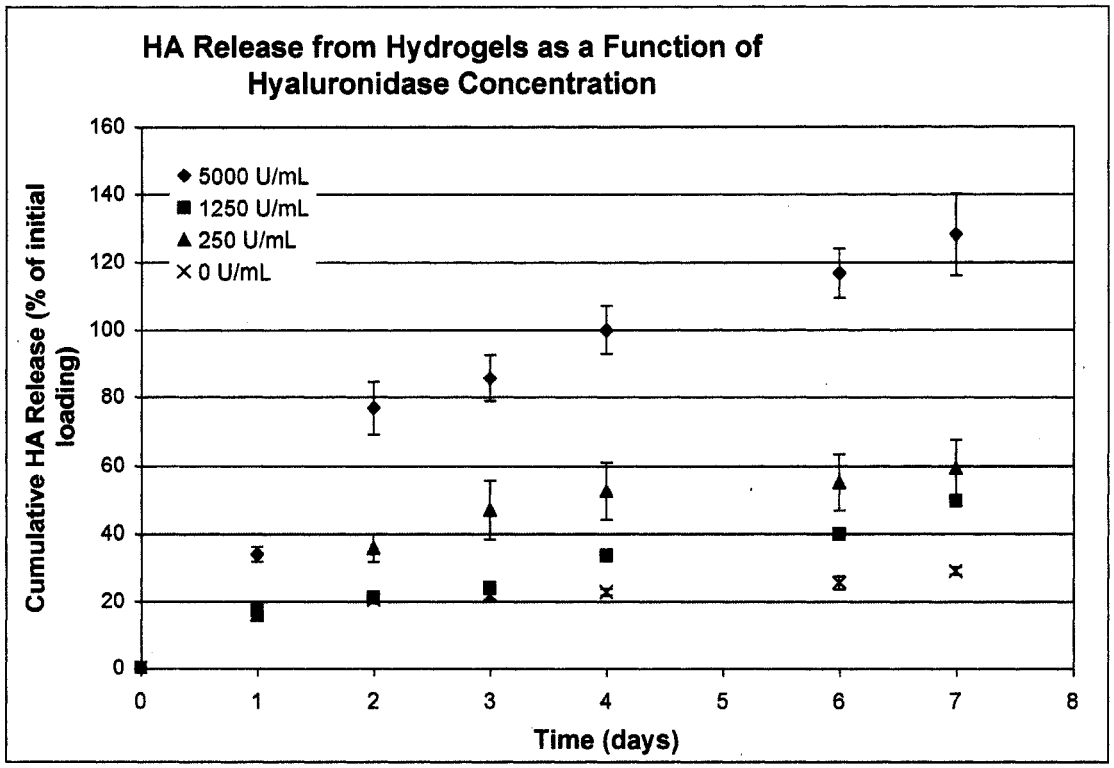

Figure 3.2: Release of HA from hydrogels as a function of hyaluronidase concentration. Release buffer was 1mL 30mM citrate buffer with various concentrations of hyaluronidase at 37°C. Results shown as mean and standard error of triplicate samples.

hydrogel was determined by a modified carbazole assay, as described in [284], compared to a standard curve made using unmodified HA. The highest concentration of hyaluronidase tested (5000 U/mL) resulted in complete degradation in 7 days; however, these concentrations were substantially higher than those required to achieve degradation in previously published studies [164, 201, 214]. This could be due to suboptimal pH conditions or partial inactivation of the enzyme during storage. However, while these hyaluronidase levels do not directly relate to physiologic levels, these results show that the chemical modifications do not prevent the enzymatic degradation of the hydrogel.

Whereas the HA-GMA hydrogels were stable in citrate buffer (pH 5.3) and in DI water (pH measured at approximately 5.5), degradation of the hydrogels via hydrolysis was rapid at physiologically relevant conditions (PBS, pH 7.4) and occurred in approximately 5 days (Figure 3.3). Hydrolytic degradation was base catalyzed, with faster degradation occurring at pH 10.0 (pH 10.0 > pH 7.4 > pH 5.5), and appeared to be independent of buffering agents (data not shown). Further confirmation that hydrolysis was affecting the ester bonds in the crosslinks and not degrading the HA backbone was confirmed by GPC analysis of unmodified HA incubated in similar buffers. No decrease in molecular weight was seen (data not shown). The hydrolytic degradation of the crosslinks was not surprising given the report that hydrolysis of ester linkages will degrade hydrogels made from methacrylate derivatized dextrans with kinetics dependent on pH [209]. Increasing the HA-GMA concentration or using a co-monomer, such as 1-vinyl-2-pyrrolidinone (NVP), to increase interchain crosslinks resulted in slowed degradation of the hydrogels (Figure 3.4). Interestingly, hydrogels prepared from modified HAs made using other methods (but with similar degrees of substitution) had different hydrolytic degradation behaviors. HA-MA hydrogels (prepared from batches HA(LMW)-MA 2a and HA(LMW)-MA 2b) were stable for >2 months in PBS at 37°C (data not shown). HA-GMA hydrogels prepared from the TBA HA salt form in DMSO (batch HA(110)-GMA 5a) were also stable for several months in PBS at 37°C (data not shown).

3.3.3 Release of Proteins from HA Hydrogels

For proteins that are uncharged or negatively charged, it was expected that release from the HA hydrogels would occur primarily through diffusion and thus be dependent on the degree of crosslinking. For proteins that are positively charged, it was expected that the proteins would interact with the negatively-charged HA and therefore be retained in the hydrogel longer with release being enhanced by degradation of the hydrogels.

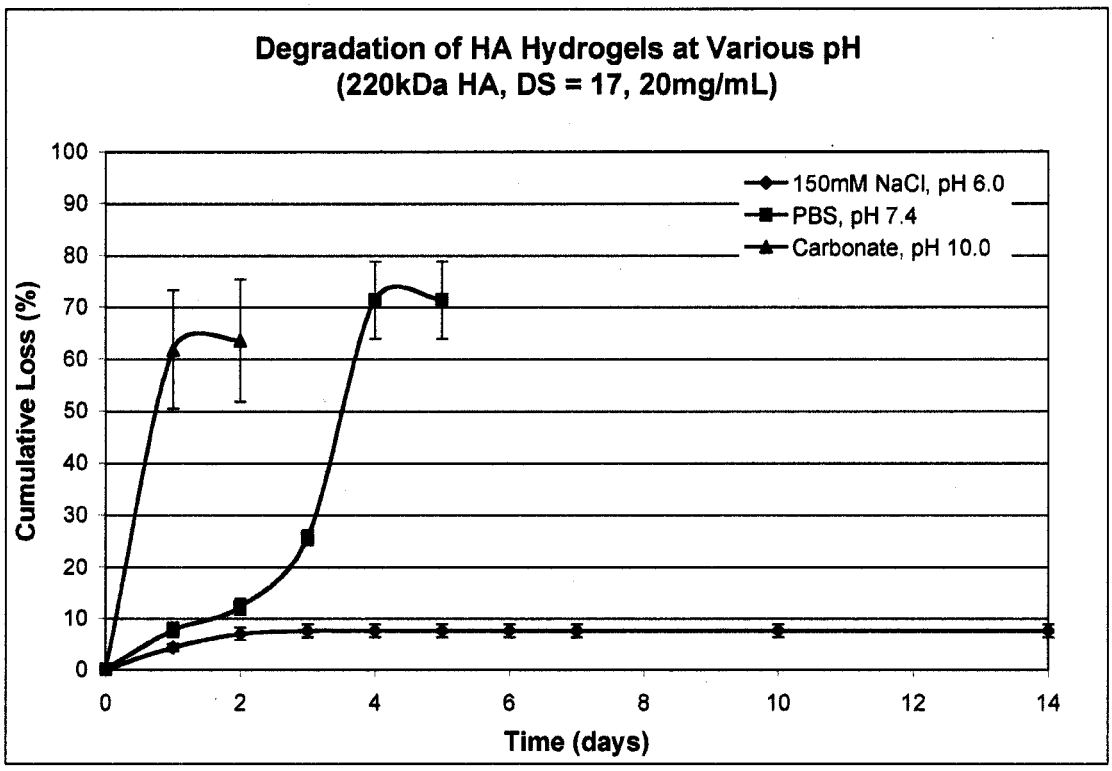

Figure 3.3: Degradation of HA hydrogels at various pH. Results shown as mean and standard error from triplicate samples. Released HA concentration determined by carbazole assay.

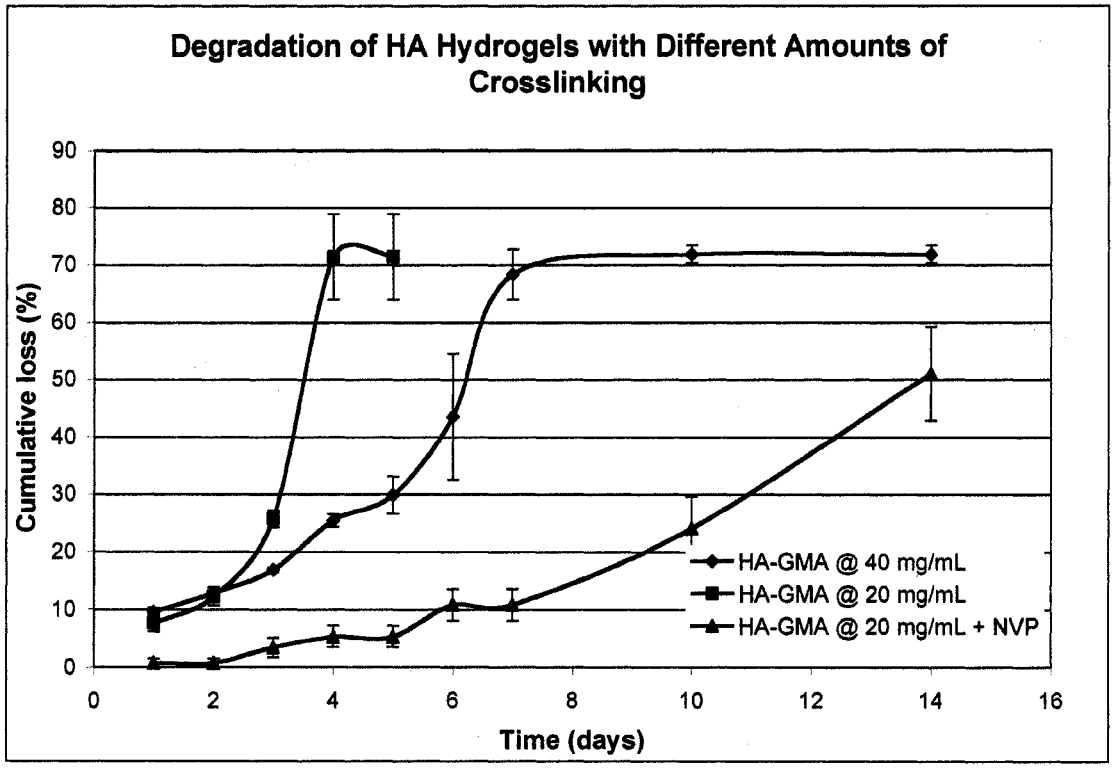

Figure 3.4: Hydrolytic degradation of HA hydrogels with increased crosslinking. Results shown as mean and standard error from triplicate samples. Released HA concentration determined by carbazole assay.

Bovine serum albumin (BSA) was used as a model protein to show diffusion-limited release. Hydrogels were formed using HA-GMA with varying modification percentages and were loaded with BSA by soaking lyophilized gels in 100μL of a 1mg/mL BSA solution. Increasing the crosslink density of the hydrogels reduced the release rate of BSA from the scaffolds (Figure 3.5). Scaffolds with a higher degree of substitution have a lower swelling ratio (Figure 3.1) and thus a smaller effective pore size. The reduced release rate of protein at higher degrees of substitution indicates that diffusion through the pores can limit the release of protein from the scaffolds. The anomalous result for the BSA-loaded gels with a degree of substitution of 5.3 is likely due to a decreased protein loading. These hydrogels had completely degraded by the 100 day time point so theoretically all of the protein should have been released. Release from these hydrogels reached a plateau in one week, which was the fastest of all the hydrogels evaluated.

Release of VEGF was found to be significantly slower than release of BSA (data not shown). After an initial burst of approximately 25% (of total released), VEGF release slowed to <10% over a period of 48 days (Figure 3.6). VEGF is a positively-charged protein, as indicated by its high pI value (Table 2.1). Electrostatic interactions between VEGF and negatively-charged HA act to slow and almost completely inhibit VEGF release from the scaffold. However, after 48 days, release of VEGF increased in conjunction with release of HA itself from the scaffold (Figure 3.6). The release rates of both VEGF and HA were accelerated using PBS, pH 7.4, as the release buffer to increase the rate of hydrolysis of the hydrogel (Figure 3.6).

3.4 Discussion and Conclusion

The strategies used to prepare the modified HAs varied the amount and type of methacrylation reagent (glycidyl methacrylate or methacrylic anhydride), the type of base catalyst used, and the reaction temperature or time. These modified HAs often had differing degrees of substitution, which affected their physical properties. The

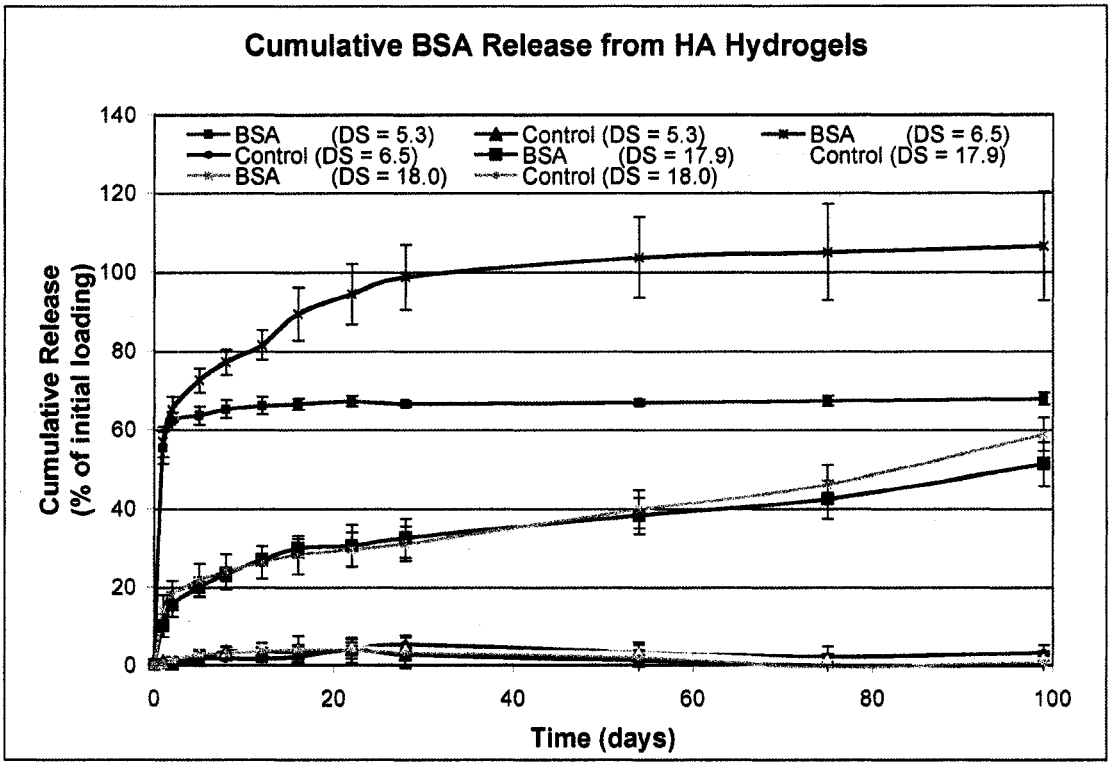

Figure 3.5: Release of BSA as a function of degree of substitution. BSA concentration measured by Bradford assay. Release buffer was 1mL DI water at 37°C. Results shown as mean and standard error from triplicate samples.

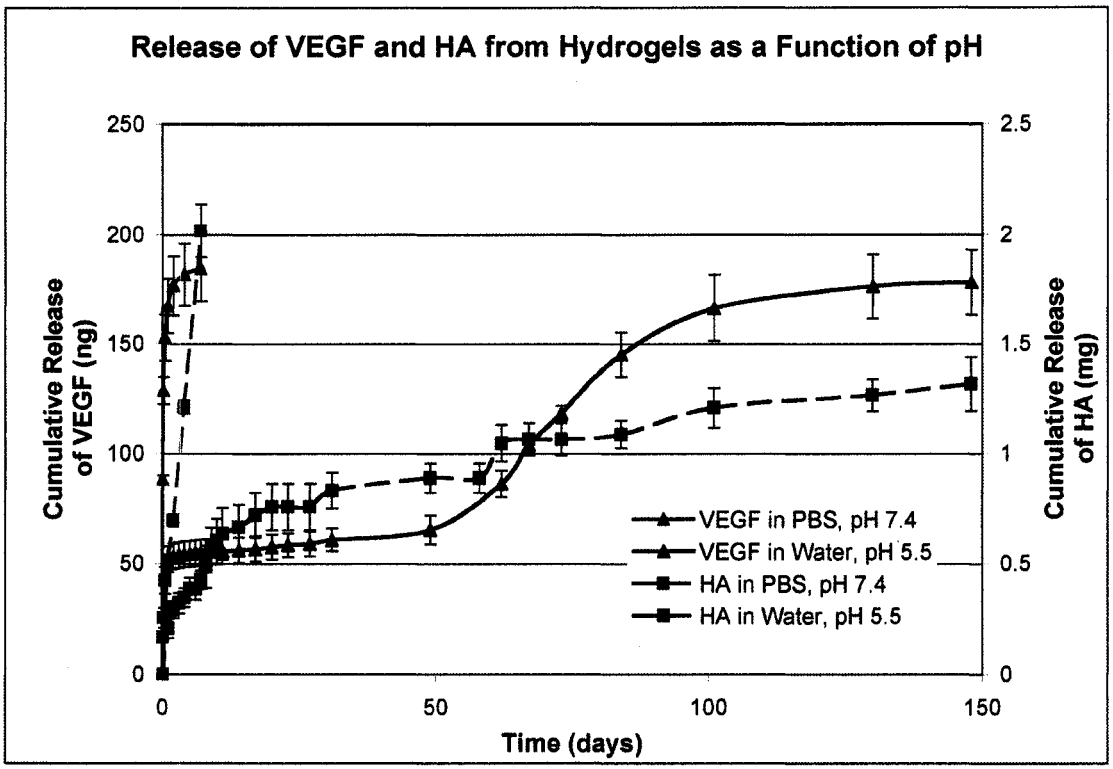

Figure 3.6: Release of VEGF and HA from HA hydrogels at different pH. VEGF concentration measured by ELISA, and HA concentration measured by carbazole assay. Release buffers were PBS, pH 7.4, and DI water, pH 5.5, at 37°C. VEGF (1μg) was loaded in a 2mg HA hydrogel. Results shown as mean and standard error from triplicate samples.

swelling ratio of the hydrogels in water decreased with increasing degree of substitution, indicating a higher crosslink density (Figure 3.2). The swelling ratio also gives a measure of the water content of the hydrogels, which may affect their degradation rate by hydrolysis. All hydrogels had a water content greater than 95% (swelling ratio ~32) and some were even greater than 99%. Tomihata and Ikada suggest that a water content below 90% is needed to slow degradation of HA hydrogels [208].

Interestingly, however, hydrogels prepared from starting modified HAs with similar degrees of substitution and similar swelling ratios exhibited different hydrolytic degradation behavior. This suggests that water content alone might not increase the likelihood of degradation, but that there might be some chemical difference between the modified HAs. As shown in Figure 3.7, different esters can be formed from the addition of glycidyl methacrylate, if there is transesterification (resulting in a product similar to the only one that can be formed from methacrylic anhydride addition) or if there is an epoxide ring opening (resulting in the presence of an additional glyceryl spacer). Additionally, the pH of the reaction mixture may affect the selectivity between reaction with the hydroxyl (primary most favored) and carboxyl groups on the HA backbone. Detailed studies of diepoxy cross-linking chemistry have shown that at low pH, diepoxy compounds form ester linkages between carboxyl groups, while at high pH, they form ether linkages between hydroxyl groups [285]. It seems to be a reasonable hypothesis, then, that a chemical difference could be responsible for the difference in hydrolytic degradation behavior that was seen. These differences are further explored in the next chapter.

The ability of the scaffold materials to degrade with time was a motivating factor in the selection of HA because it affects both protein release and tissue infiltration. The HA hydrogels as designed should degrade *in vivo* through two mechanisms: hydrolysis as discussed and enzymatic degradation of the HA backbone by hyaluronidase. However, there is wide variety in the reported levels of hyaluronidase *in vivo* and an acidic pH (presumably within a cell or lysosome) is needed for optimum enzyme activity

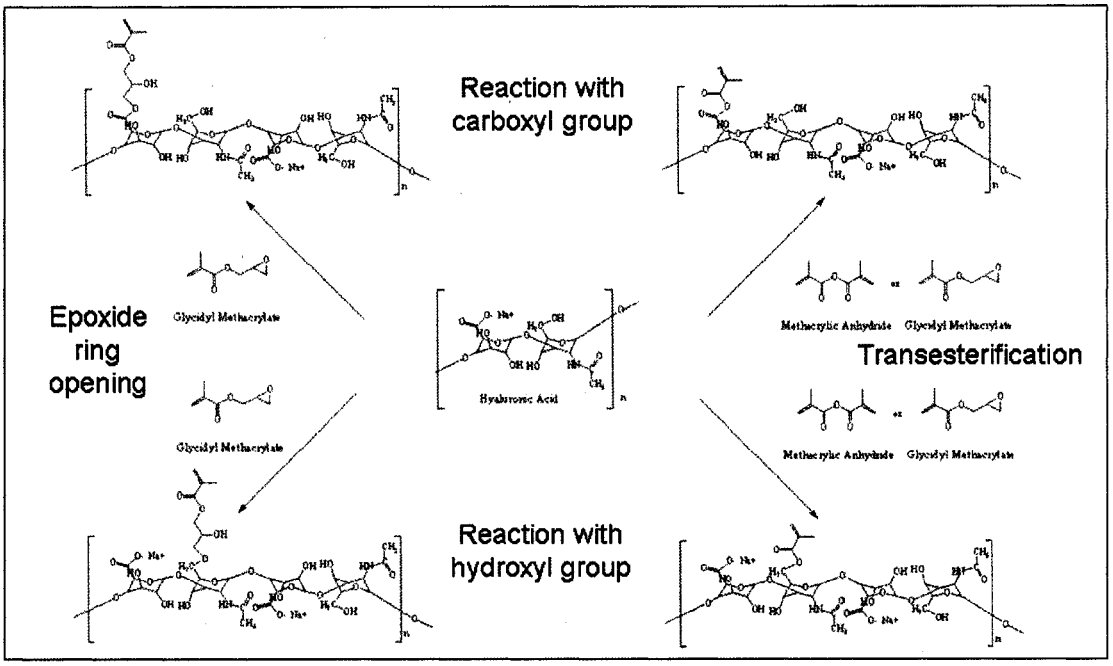

Figure 3.7: Possible methacrylation reaction schemes. The methacrylate group can attach to the carboxyl or hydroxyl group on the HA backbone. Further, reaction with GMA can proceed through an epoxide ring opening or transesterification while reaction with MA can only proceed through transesterification.

[183, 187]. Normal serum concentrations of hyaluronidase in the adult human are reported to be around 1-50 U/mL [181, 190]. However, a sheep subcutaneous model showed that hyaluronidase levels in wound fluids are much lower (300-1335 x 10^{-6} U/mL in adult sheep) [169]. Hyaluronidase is also produced in human monocytes, in a cell-associated form, at levels of 2 nU/10^6 cells [286]. The wide variation in hyaluronidase levels in various tissues and its dependence on the specific cells present make it impossible to select a relevant hyaluronidase concentration for *in vitro* testing. This could further result in differences in HA persistence at different implant sites. Therefore, the ability to control HA hydrogel degradation through hydrolytic mechanisms may be more likely to result in a hydrogel that will degrade in a controlled fashion *in vivo*. The *in vivo* behavior of these hydrogels was further explored and is detailed in the following chapters.

These results also demonstrate that while electrostatic interactions may prevent free diffusion of cationic proteins such as VEGF from the intact scaffolds, degradation of the scaffolds *in vivo* through hydrolysis or hyaluronidase activity will release VEGF from the scaffolds. Controlling the degradation rate of the hydrogels will also play a large role in determining release behavior of other cationic proteins that will associate with HA, including osteoprotegerin (OPG) and bone morphogenetic protein (BMP)-2. Chapters 4 and 5 explore, in more detail, the *in vitro* release of BMP-2, VEGF, and OPG from HA hydrogels with different hydrolytic degradation rates.

Chapter 4

DEGRADABLE HYALURONIC ACID HYDROGELS FOR CONTROLLED RELEASE OF BONE MORPHOGENETIC PROTEIN-2: EFFECT OF DEGRADATION RATE ON BONE REGENERATION

4.1 Introduction

The goal of the research described in this Chapter was to demonstrate that the scaffolds designed in Chapter 3 can support bone growth *in vivo*, particularly in conjunction with the osteoinductive molecule bone morphogenetic protein (BMP)-2. Further, the chemistry used to prepare the HA-GMA hydrogels was manipulated to obtain hydrogels that degrade *via* hydrolysis at three distinct rates. This study addressed both main hypotheses of this dissertation — that controlled release of osteoinductive signals can improve the formation and maturation of new bone tissue and that the degradation rate of the scaffold can be manipulated to optimize the healing response.

As described in Chapter 2, BMP-2 is a cationic protein that can induce ectopic bone formation as well as enhance bone regeneration in a variety of bone defects. Using a known bone-inducing factor would allow the effects of the degradation rate of the scaffold (and the corresponding differences in release rate of protein) to be elucidated. While BMP-2 has previously been used with HA formulations [195, 249], this work represents the first time that BMP-2 has been delivered from a chemically crosslinked HA hydrogel. First, further *in vitro* characterization of the HA hydrogels was performed, specifically looking at the effect of the degradation rate of the hydrogel on its ability to control the release of BMP-2. Then, hydrogels loaded with 5μg BMP-2 were tested in a rat calvarial critical size defect model. In addition to

standard measures of bone formation, i.e., measuring extent of mineralization by microcomputed tomography (microCT), the effect of the different treatments on the organization of collagen in the regenerating bone was examined.

4.2 Materials and Methods

4.2.1 Materials

All materials were obtained from Sigma-Aldrich (St. Louis, MO) unless otherwise noted. All solvents were of reagent grade.

4.2.2 Glycidyl Methacrylate Modified HA (HA-GMA) Preparation for Fast Degrading Hydrogels, after [281]

HA (220kDa from Lifecore, Chaska, MN) was dissolved at 14.3 mg/mL in DI water overnight. The pH was adjusted to 9 by using 1N NaOH. A 29-fold molar excess of glycidyl methacrylate (GMA) was added, and the reaction was allowed to proceed at room temperature for 7 days with stirring. The reaction was stopped by adjusting the pH to 7 with 1N HCl, and the product was purified by 2X precipitation in tetrahydrofuran (THF). The purified product was dissolved in DI water and lyophilized.

4.2.3 HA-GMA Preparation for Slow Degrading Hydrogels, after [283]

HA (110kDa, Lifecore) was first converted to the tetrabutyl ammonium salt form (TBA HA). The TBA HA was dissolved in dimethyl sulfoxide (DMSO) at 20 mg/mL. A 5-fold molar excess of DMAP was added. A 2-fold molar excess of GMA was added, and the reaction was allowed to proceed at 30°C for 16 hours. The reaction was stopped by adding 10% v/v 2.5M NaCl, and the product was purified by 2X precipitation in acetone followed by dialysis. The purified product was dissolved in DI water and lyophilized.

4.2.4 ^{13}C-NMR Characterization

Unmodified HA, HA-GMA, or HA-MA were dissolved at a minimum concentration of 40 mg/mL in deuterium oxide (D2O, Cambridge Isotope Laboratories, Andover, MA). ^{13}C-NMR spectra were obtained on a Bruker (Billerica, MA) Avance AV series instrument at a frequency of 500.046 MHz.

4.2.5 HA Hydrogel Formation

HA-GMA was dissolved in DI water at 20 mg/mL for the 220kDa modified HA and at 30 mg/mL for the 110kDa modified HA. The 220kDa solution was used to prepare fast degrading hydrogels; the 110kDa solution was used to prepare slow degrading hydrogels. Hydrogels with intermediate degradation rates were prepared by mixing ratios of the two starting solutions (220kDa and 110kDa) prior to crosslinking. The HA-GMA solution was mixed with a photo-initiator in a volume ratio of 10:1 (HA-GMA solution:initiator solution). The photo-initiator, 2-hydroxy-1-[4-(hydroxyethoxy)phenyl]-2-methyl-1-propanone (Irgacure® 2959, Ciba, Tarrytown, NY), was dissolved at a concentration of 20 mg/mL in methanol. Crosslinking was initiated by exposure to ultraviolet (UV) radiation (365nm) for 20-30 minutes to form a solid gel. Hydrogels were molded into cylinders by crosslinking in wells of multi-well plates. After formation, the hydrogels were rinsed, frozen, and lyophilized, and then rehydrated in DI water or PBS (with or without protein).

4.2.6 Characterization of Hydrolytic Degradation

Hydrogels were prepared from 100μL solutions of modified HA as described above. The hydrogels were suspended at 37°C in 1mL of buffer at different pH and ionic strengths. The buffer was completely removed and replaced at selected time points, and the amount of HA released into the buffer was quantified by a carbazole assay. Buffers used included phosphate buffered saline (PBS, pH 7.4), 138mM NaCl in

unbuffered DI water (pH ~5.5), and 0.1M carbonate buffer, pH 10.0.

4.2.7 Carbazole Assay for Measurement of Released HA

A carbazole assay was run in a 96-well plate format, after [284]. Samples were diluted to fall within the range of the standard curve (0.03-2 mg/mL HA). 50μL of sample or standard was added to each well of a 96-well plate. 200μL of 25mM sodium tetraborate in sulfuric acid was added per well and mixed. The plate was heated at 100°C for 10 minutes and then cooled at room temperature for 15 minutes. 50μL of 0.125% carbazole in absolute ethanol was added per well and mixed. The plate was heated at 100°C for 10 minutes and then cooled at room temperature for 15 minutes. The absorbance was read at 550nm on a Safire 2 plate reader (Tecan, Mannedorf/Zurich, Switzerland).

4.2.8 Rheological Characterization of HA Hydrogels

The elastic and storage moduli were determined for crosslinked HA-GMA films using an AR2000 rheometer (TA Instruments, New Castle, DE) with a 40mm parallel plate geometry. The HA-GMA was directly crosslinked on the bottom plate, targeting a 1mm thickness, and the top plate was lowered until the normal force measured ~1N. Measurements were taken at 37°C using a stress sweep from 1-1000 Pa at an angular frequency of 6.283 rad/s.

4.2.9 In Vitro Protein Release

Hydrogels were prepared from a 100μL solution of HA-GMA, as described above. The hydrogels were loaded with protein by soaking the lyophilized gels in 100μL of 0.01 mg/mL BMP-2 (R&D Systems, Minneapolis, MN) in 0.1% BSA in PBS or in 0.1% BSA in PBS as a control. After equilibration for 1 hour, the gels were suspended in 1mL of 0.1% BSA in PBS as a release buffer and placed at 37°C. The release buffer

was completely removed and replaced at selected time points. The concentration of BMP-2 in the release buffer was measured by ELISA (R&D Systems). Calculations of the amount of protein released were based on the actual amount of buffer retrieved from each well at each time point. At the final time point, if the hydrogels had not completely degraded, they were incubated with 1mL of 500 U/mL hyaluronidase at 37°C overnight to degrade the hydrogel, and the residual protein was measured.

4.2.10 HA Hydrogel Implants

HA hydrogels were aseptically prepared as implants in a laminar flow hood. The starting solutions described above were filtered through a 0.2μm syringe filter, and the molds used were autoclaved. Hydrogels were molded into implants by using Teflon spacers with holes (5mm diameter x 1.5mm) height that were sandwiched between a glass slide and a glass coverslip. 35μL of the HA-GMA/I2959 mixture was pipetted into the molds prior to crosslinking. After formation, the hydrogels were rinsed for several hours with sterile PBS, frozen, and lyophilized. The hydrogels were rehydrated with 35μL of sterile PBS (control) or sterile PBS with 5μg BMP-2.

4.2.11 Rat Calvarial Critical Size Defect Model

Scaffolds were evaluated for their ability to induce bone regeneration in a rat calvarial critical size defect model. The surgical protocol was conducted under approval from the University of Washington (UW) Institutional Animal Care and Use Committee (IACUC). Animals were housed in a specific pathogen free environment at the UW Department of Comparative Medicine. All animals had *ad libitum* access to food and water and were maintained in an environment with 12-hour light/dark cycles. Surgeries were performed following aseptic technique. Adult male Sprague Dawley rats (Harlan, Indianapolis, IN) were anesthetized using isoflurane (5% induce; 2.5% maintain) and were administered buprenorphine immediately pre-operatively for pain mitigation. The surgical site was shaved and disinfected. A linear incision was made

along the midline of the scalp, and the soft tissues and periosteum were reflected. A 5mm diameter circular, full thickness defect was made in the parietal bones, centered over the sagittal suture line, using a Command2 drill system with 1.0mm cross-cut fissure carbide bur (Stryker, Kalamazoo, MI) while irrigating with saline. Care was taken not to damage the underlying *dura mater* or sagittal sinus vein. The defect site was rinsed extensively with saline, and the implant was placed into the defect (or the defect was left empty as a control). The soft tissues were closed over the defect site using wound clips, and the animals were allowed to heal for 3–6 weeks.

4.2.12 Tissue Harvest and Analysis of Mineralization

After allowing the defect to heal for 3 or 6 weeks, the animals were sacrificed by carbon dioxide (CO_2 asphyxiation. The parietal bones were harvested and fixed in 10% neutral buffered formalin (Fisher, Hampton, NH) for 24 hours at room temperature. The bone pieces were rinsed and stored in 70% ethanol at 4°C until scanned. MicroCT analysis was performed by Angela Lin and Robert Guldberg of the Georgia Institute of Technology (Atlanta, GA) on a *viva*CT 40 (Scanco Medical, Bassersdorf, Switzerland) with a voltage of 55kVp, current of 109μA, and voxel size of 21μm. A 5mm diameter x 1mm tall region centered within the defect was analyzed for each sample using segmentation parameters of sigma = 1.2, support = 2, and threshold = 143.

4.2.13 Decalcification and Histology

The bone pieces were decalcified in 10% ethylenediamine tetraacetic acid (EDTA), pH 7, for 10–14 days at room temperature. Decalcified samples were dehydrated and cleared prior to embedding in paraffin for histological sectioning. Sections (5μm thick) were stained with either hematoxylin and eosin (H&E) or Masson's trichrome and viewed using standard brightfield microscopy (E800 microscope, Nikon, Melville, NY).

4.2.14 Picrosirius Red Staining

To view the collagen orientation, tissue sections were stained with picrosirius red. Tissues sections were de-waxed in xylene and rehydrated in decreasing strengths of ethanol. The sections were incubated in 0.1% sirius red (Direct Red 80) in a saturated aqueous solution of picric acid for one hour, followed by rinsing in acidified water (0.5% acetic acid). The sections were dehydrated and cleared prior to mounting using Permount mounting media (Fisher). Stained sections were viewed under polarized light microscopy (E800 microscope, Nikon, Melville, NY).

4.3 Results

4.3.1 Hydrogel Preparation and Characterization

Two HA-GMA hydrogels with differing hydrolytic degradation rates were selected from the formulations developed in the previous Chapter. Batch HA(LMW)-GMA 1d, made with 220kDa HA at 20 mg/mL, resulted in hydrogels that degraded in one week in PBS, pH 7.4, at 37°C and will be referred to as "fast degrading" hydrogels. Batch HA(110)-GMA 5a, made with 110kDa HA at 30 mg/mL, resulted in hydrogels that did not degrade even after several months in PBS, pH 7.4, at 37°C and will be referred to as "slow degrading" hydrogels. Further examination of the chemical structure of the modified HAs was performed using ^{13}C-NMR. As indicated by the presence of four additional peaks in the ^{13}C-NMR spectra of the more stable HA(110)-GMA 5a (Figure 4.1C), it appeared to have addition of just the methacrylate group to the HA backbone. In contrast, the ^{13}C-NMR spectra of HA(LMW)-GMA 1d (Figure 4.1B) had even more peaks consistent with the presence of a glyceryl spacer in addition to the methacrylate group. The ^{13}C-NMR spectra for the unmodified HA is shown in Figure 4.1A.

Mixtures of the starting solutions (20 mg/mL 220kDa and 30 mg/mL 110kDa) were made at various ratios (25:75, 50:50, 75:25), and the hydrogels formed had

Table 4.1: Rheological properties of HA-GMA hydrogels.

Hydrogel	G'	G"
Fast degrading	1–2 Pa	3 Pa
Intermediate degrading	1 Pa	3 Pa
Slow degrading	1.5 Pa	5Pa

degradation rates that fell between the fast and slow degrading hydrogels (Figure 4.2). Increasing the relative amount of 110kDa HA in the hydrogel resulted in hydrogels that degraded more slowly than the "fast degrading" hydrogels. The 50:50 mixture resulted in a hydrogel that degraded in 6–8 weeks *in vitro* and was selected as an "intermediate degrading" hydrogel formulation. The rheological properties of these formulations were also examined (Table 4.1), and all three had similar moduli.

4.3.2 In Vitro Protein Release

The HA hydrogels were expected to provide controlled release of cationic proteins through electrostatic interactions with the negatively charged HA, as was seen for VEGF in the previous Chapter. BMP-2 is another cationic protein (pI ~ 9.2; Table 2.1), and its release was slowed compared to BSA controls for all hydrogel types examined (data not shown). Altering the degradation rate of the hydrogels affected the release rate of BMP-2 (Figure 4.3). The fast degrading hydrogels released all of their BMP-2 by the time the scaffold was completely degraded (approximately one week). The slow degrading hydrogels had a high burst release of BMP-2, which was followed by release at nanogram levels per week for the duration of the 8 week study. When the still intact slow degrading hydrogels were degraded by hyaluronidase at 8 weeks, a reservoir of approximately 20% BMP-2 was found to be retained in the HA hydrogel. Similar to their degradation rates, the intermediate degrading hydrogels

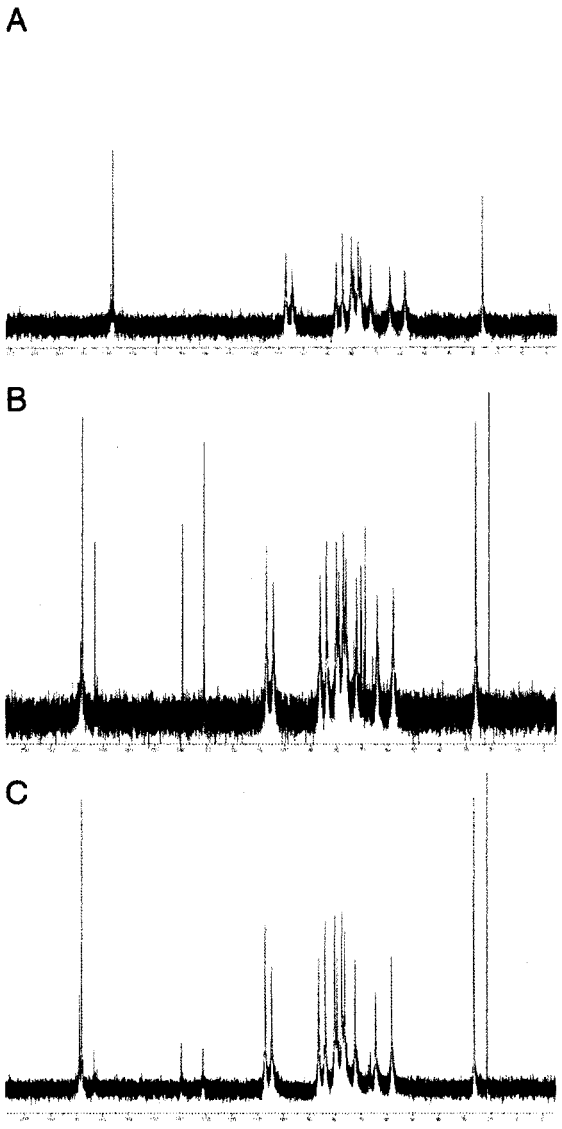

Figure 4.1: ^{13}C-NMR spectra of modified HAs. (A) Unmodified HA (220kDa). (C) HA(LMW)-GMA 1d, which resulted in hydrogels that were susceptible to hydrolysis. (C) HA(110)-GMA 5a, which resulted in hydrogels that were stable to hydrolysis.

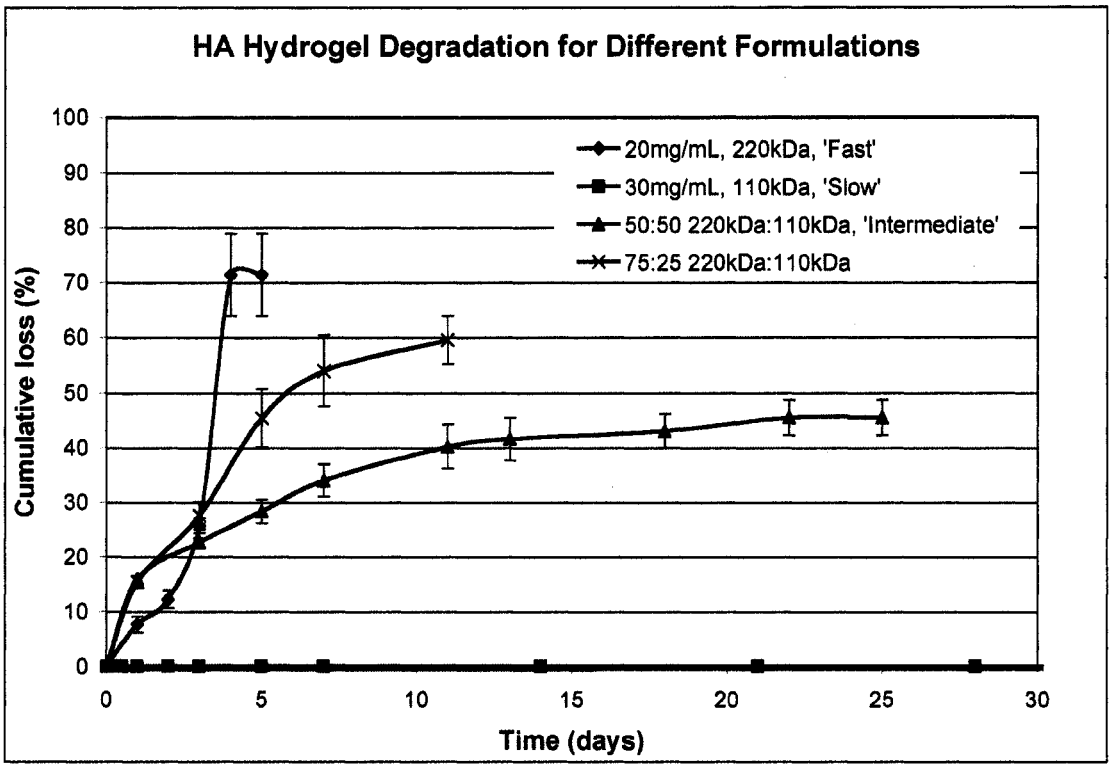

Figure 4.2: HA hydrogel hydrolytic degradation for different formulations. Fast, intermediate, and slow degradation rates were targeted. Released HA concentration determined by carbazole assay. Results shown as mean and standard error from triplicate samples.

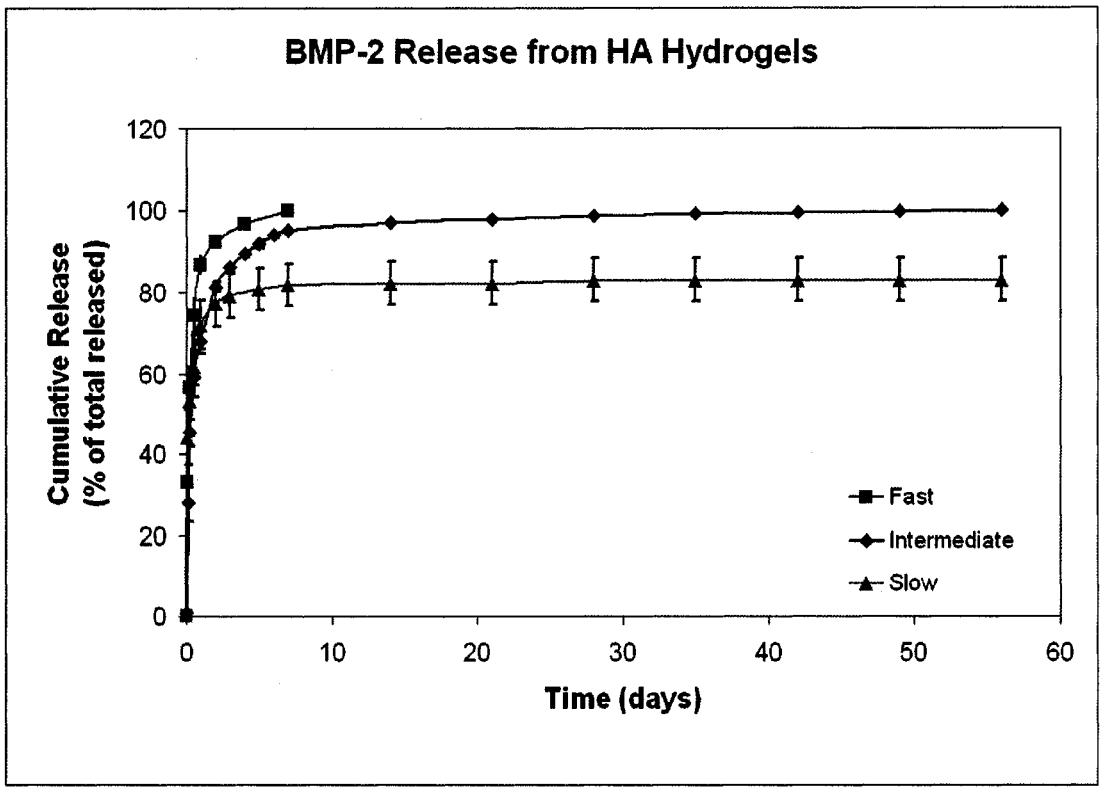

Figure 4.3: Release of BMP-2 from HA hydrogels. Hydrogels had differing degradation rates — fast (<1 week), intermediate (6–8 weeks), and slow (>8 weeks). BMP-2 concentration in release buffer was determined by ELISA. Results shown as mean and standard error of triplicate samples.

had intermediate release profiles. Release of BMP-2 was fairly rapid for the first week. It slowed over the next 7 weeks, although still remaining faster than release from the slow degrading hydrogels, and almost 100% was released by the final 8 week time point.

4.3.3 In Vivo Bone Regeneration

The fast, intermediate, and slow degrading hydrogels were evaluated for their ability to support BMP-2 induced bone growth in a rat calvarial critical size defect model.

Hydrogel scaffolds containing 5μg BMP-2 or no protein as control were implanted in a 5mm defect. Tissues were harvested and analyzed for extent of mineralization at 3 and 6 weeks. As seen in Figure 4.4, significant bone formation was induced for all three scaffold types in BMP-2 treated animals compared to controls at the 6 week time point ($p<0.01$). The mineral volume in the BMP-2 treated animals was similar for all three hydrogel types at 6 weeks. At the earlier time point, significant bone formation was induced for all three scaffold types in BMP-2 treated animals compared to controls ($p<0.01$), and a trend in the effect of hydrogel degradation rate on mineral formation was observed. The fast degrading scaffolds with BMP-2 had formed the most mineral while the slow degrading scaffolds with BMP-2 had formed the least mineral.

Examination of histological sections stained with Masson's trichrome at the early time point showed minimal new bone formation for all three control hydrogel groups (Figure 4.5). The fast and intermediate degrading hydrogels with BMP-2 had new bone completely bridging the defect. The slow degrading hydrogel with BMP-2 had impeded new bone formation as the hydrogel (which appears as a clear region in the histological sections) filled much of the defect space keeping new bone formation limited to the periphery of the implant. By six weeks (Figure 4.6), the control groups continued to have minimal new bone growth into the defect site although some remodeling was seen at the native bone edges. The fast and intermediate degrading hydrogels with BMP-2 appeared qualitatively the same as the three week samples. For the slow degrading hydrogels with BMP-2, additional new bone was formed compared to the three week time point. A clear region resulting from the residual hydrogel was still present in the histological sections; however, it was smaller and the defect was filled with new bone between the native bone edges and the residual scaffold. It is interesting to note that the slow degrading hydrogels with BMP-2 resulted in similar levels of mineralization as the fast and intermediate degrading hydrogels with BMP-2 at the six week time point since the defect is not completely healed by this point and

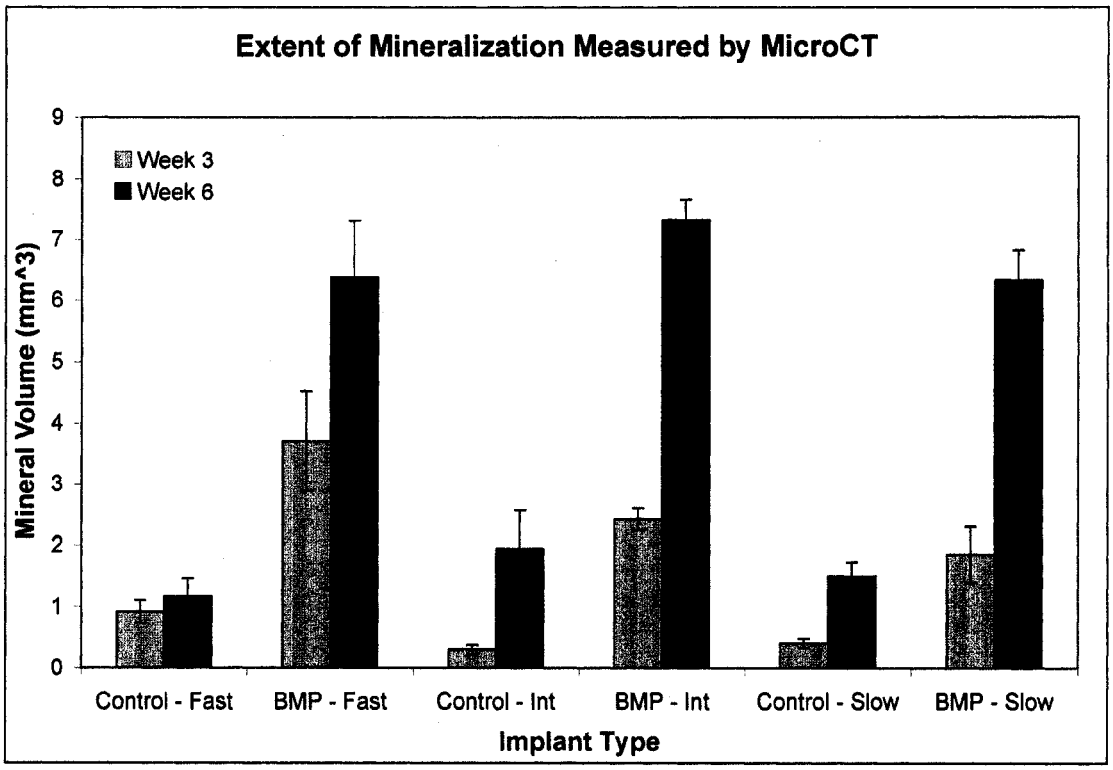

Figure 4.4: Extent of mineral formation induced by BMP-2 and control hydrogel scaffolds. Control hydrogels had no protein while BMP-2 samples were loaded with 5μg BMP-2. Fast, intermediate, and slow degrading HA hydrogels were evaluated at 3 and 6 weeks. Mineral volume was measured by microCT for a 5mm diameter x 1mm tall region centered in the defect site. Results are shown as mean and standard error of a minimum n = 6.

there would be additional space for bone to grow as the hydrogel scaffold continues to degrade.

4.3.4 Collagen Orientation

While BMP-2 delivery from the HA hydrogel scaffolds can clearly induce mineralized bone tissue formation, a more interesting question is whether the degradation rate of the scaffold (coupled with a different release rate of protein) can affect the organization of the collagen matrix in the regenerating bone. Polarized light microscopy allows one

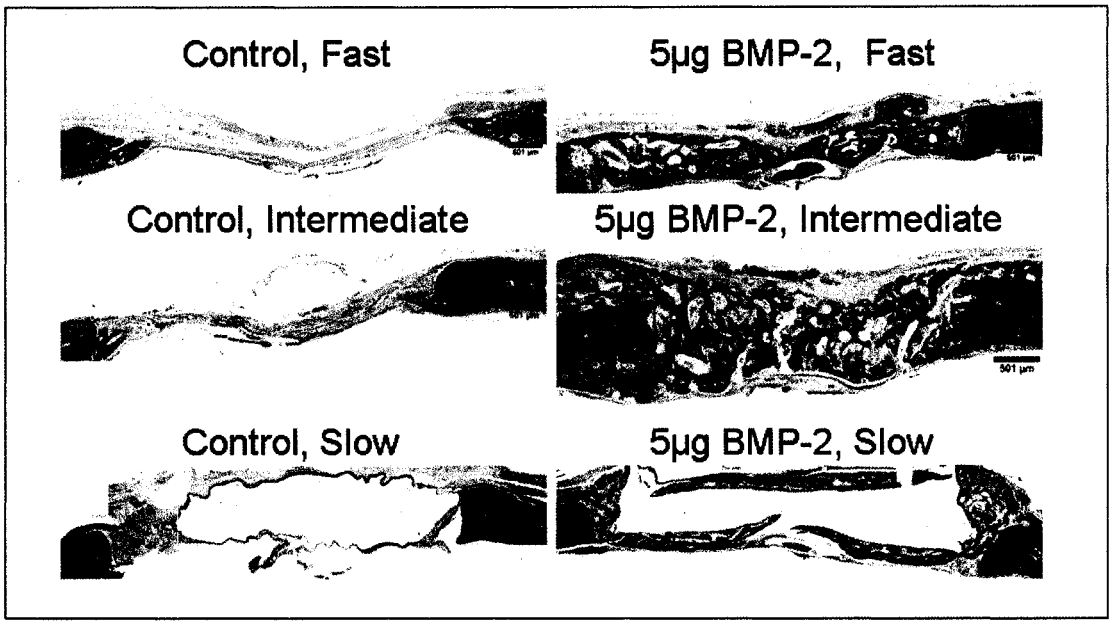

Figure 4.5: Masson's trichrome stained histological sections at three weeks. Representative histological sections showing cross-section of entire defect for animals treated with control or BMP-2 loaded hydrogels that were fast, intermediate, or slow degrading. Bone is stained dark blue. Native bone can be seen at the edges of each image. The scale bar in each image is 500μm.

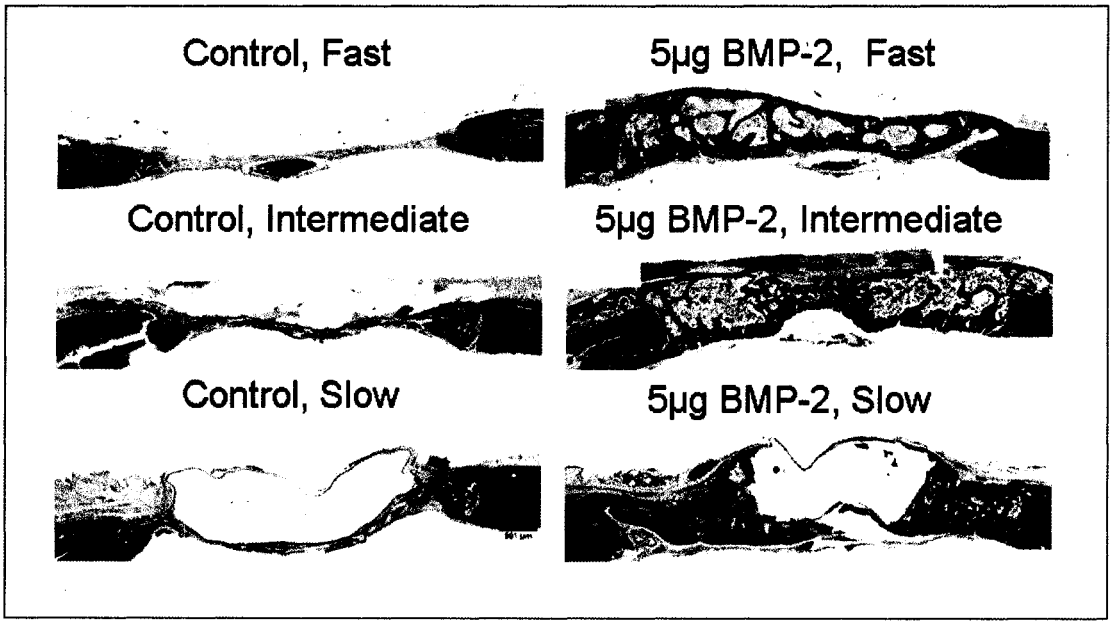

Figure 4.6: Masson's trichrome stained histological sections at six weeks. Same as conditions as Figure 4.5 but for six week samples.

to utilize the natural birefringence of collagen to examine its orientation. Further, the use of picrosirius red stain can enhance collagen's birefringence, and in conjunction with polarized light microscopy, it is accepted as a specific stain for collagen [287]. Histological sections were stained with picrosirius red and examined under polarized light so that the lamellar collagen in the native bone at the edges of the defect was oriented approximately 45° from the incident light. This should result in maximal birefringence for newly formed bone that is oriented in the same direction as the native bone. Representative images showing the picrosirius red stain are in Figure 4.7A. In these images, well-ordered collagen in the native bone and in regions of the newly formed bone appeared green while disordered collagen appeared red. Interestingly, while the slow degrading hydrogels with BMP-2 had the least amount of new bone tissue formation because a large region of the defect was taken up by the undegraded scaffold, the new bone that was formed seemed more organized. Organized bone

was also seen in the fast degrading hydrogels with BMP-2 while less organized bone was seen in the intermediate degrading samples. The amount of organized bone was quantified by thresholding the images using the green color of the native lamellar bone. Measurements of % threshold of the defect area are seen in Figure 4.7B. Both fast and slow degrading samples had more organized bone than the intermediate degrading samples. The % threshold for the fast and slow degrading samples was approximately the same when the area of the residual scaffold was subtracted from measurements of the slow degrading samples.

4.4 Discussion and Conclusion

In this study, the HA hydrogels developed in Chapter 3 were shown to be able to support bone growth *in vivo* when used in combination with appropriate osteoinductive molecules. By utilizing mixtures of two different forms of modified HAs, hydrogels with a range of degradation rates were able to be prepared. Differences in the ^{13}C-NMR spectra suggest that the slow degrading hydrogels may have the methacrylated product formed via transesterification while the fast degrading hydrogels may have the additional presence of a glyceryl spacer. These hydrogels should present a similar chemical and mechanical (Table 4.1) environment while allowing the persistence of the HA and BMP-2 within the defect site to be varied. The temporal progression of bone regeneration could be modulated by altering the degradation rate of the scaffold. Interestingly, all three degradation rates tested resulted in similar amounts of bone formation (measured by mineral volume) at the latest (six week) time point examined. However, the fastest and slowest degrading scaffolds seemed to result in more organized bone than the intermediate degrading scaffold, which was designed to degrade in 6–8 weeks to match the healing time.

These results ran counter to the original postulate that matching the degradation rate of the scaffold to the regeneration rate of the tissue would lead to optimal bone formation. It is possible that a scaffold that degrades in 6–8 weeks is not matched to

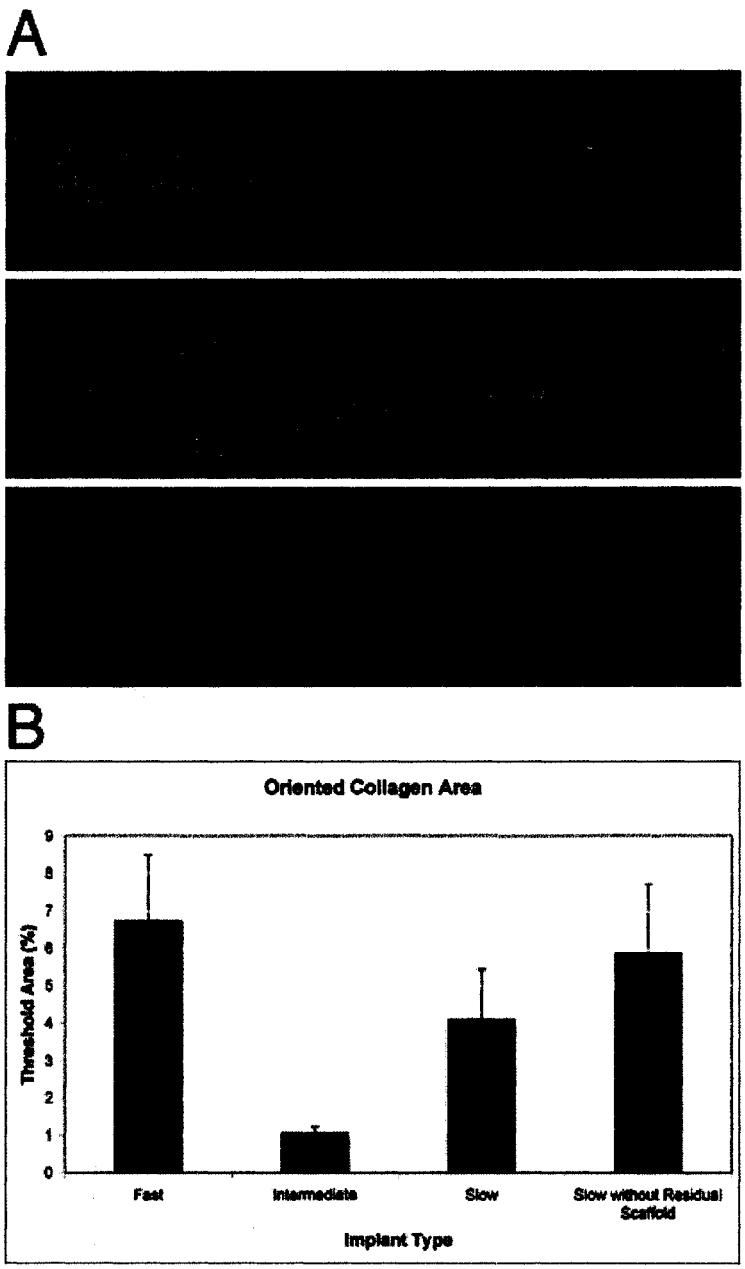

Figure 4.7: Picrosirius red stain showing collagen orientation in regenerating bone. Histological sections from rat calvarial critical size defect model showing cross-section of defect with native bone at edges. Animals were treated with HA hydrogel scaffolds delivering BMP-2 from scaffolds with different degradation rates (fast, intermediate, and slow).

an optimal healing time, as it was selected to approximate the end point of the study. However, the improved collagen orientation seen with the fast and slow degrading hydrogels suggest some interesting alternatives. The fast degrading hydrogels with BMP-2 may be able to induce enough bone formation quickly that the new bone then had time to remodel during the six weeks of healing. In contrast, the slow degrading hydrogels with BMP-2 may retard bone formation enough so that the new bone is deposited in a more organized fashion from the beginning.

The results of this study further suggest that analysis of bone regeneration in this particular model and with these materials should be taken out to later time points. It is possible that mineralization has reached a maximum plateau by 6 weeks. However, it is more likely that increased mineralization would be seen at later time points, particularly for the slow degrading hydrogels as there is a large area still to be filled with bone even at week 6. Further examination of the organization of the collagen using picrosirius red and polarized light microscopy is also warranted. Quantitatively, the fast and slow degrading hydrogels with BMP-2 appear to produce more organized collagen. Qualitatively, the fast and slow degrading hydrogels with BMP-2 have regions that appear similar in morphology to the native bone. However, these regions appear green, which is typically associated with smaller collagen fibers while thicker, more organized collagen fibers appear red [288, 289].

Chapter 5

DEGRADABLE HYALURONIC ACID HYDROGELS FOR CONTROLLED RELEASE OF VASCULAR ENDOTHELIAL GROWTH FACTOR AND OSTEOPROTEGERIN: EFFECTS ON BONE REGENERATION AND ANGIOGENESIS

5.1 Introduction

The goal of the research described in this Chapter was to test the hypothesis that angiogenic growth factors delivered from hyaluronic acid (HA) hydrogels could be used to encourage bone formation in the critical size defect model. As described in Chapter 2, angiogenesis is linked to bone growth in the processes of enchondral ossification, skeletal development, fracture repair, and distraction osteogenesis, so it seems likely that angiogenic factors may be able to stimulate or enhance bone formation. However, few groups have examined the direct effects of vascular endothelial growth factor (VEGF) delivery on bone regeneration. Street *et al.* showed significant increases in callus calcification with sustained release of VEGF in both a murine femoral "challenged" fracture healing model and a rabbit radius segmental gap model [255]. Others, including Mooney's group [256, 257, 258, 259], have shown synergy between VEGF and various pro-mineralization treatments. A second growth factor with potential angiogenic effects [100] is osteoprotegerin (OPG). OPG is even more interesting as an angiogenic molecule to promote bone formation when considering its bone protective effects [97].

The previous Chapter demonstrated that the HA hydrogels could support bone growth *in vivo* when used with appropriate signals so they were utilized again as scaffold materials. Further, they were shown to provide controlled release of cationic

proteins due to electrostatic interactions. Similar to BMP-2, both VEGF and OPG are positively charged so should associate with HA. While hydrogels with three different degradation rates (fast, intermediate, slow) were tested with various doses of VEGF and OPG, particular attention was paid to the fast degrading hydrogels. As before with BMP-2, HA hydrogels were examined for *in vitro* protein release and *in vivo* bone regeneration.

5.2 Materials and Methods

With the exceptions described below, the materials and methods for this Chapter are identical to those in Chapter 4.

5.2.1 Materials

VEGF or OPG was used in place of BMP-2. VEGF was obtained from Genentech (South San Francisco, CA) and OPG was obtained from R&D Systems (Minneapolis, MN).

5.2.2 Tissue Harvest and Analysis of Mineralization

At the desired time points, the rats were sacrificed by CO_2 asphyxiation, and the parietal bones were harvested and fixed in 10% neutral buffered formalin (Fisher). Extent of mineralization was measured by X-ray or microcomputed tomography (microCT). X-rays were performed with X-Omat AR film (Kodak, Rochester, NY) in an enclosed X-ray unit (Picker X-ray Corporation, Cleveland, OH) using a distance of 64cm, voltage of 35 kVp, current of 5 mA, and exposure time of 5-30 seconds. Developed X-ray films were scanned into digital format, and X-ray intensity was quantified using the MetaMorph® imaging system (Molecular Devices Corporation, Sunnyvale, CA). MicroCT analysis was performed by Angela Lin and Robert Guldberg of the Georgia Institute of Technology (Atlanta, GA) on a *viva*CT 40 (Scanco Medical, Bassersdorf,

Switzerland) with a voltage of 55kVp, current of 109μA, and voxel size of 21μm. A 5mm diameter x 1mm tall region centered within the defect was analyzed for each sample using segmentation parameters of sigma = 1.2, support = 2, and threshold = 143.

5.3 Results

5.3.1 In Vitro Protein Release

VEGF and OPG are cationic proteins (pI ~ 7.3 and 8.3, respectively; Table 2.1), and their release was slowed compared to BSA controls for all hydrogel types examined (data not shown). Similar to the effects seen with BMP-2, altering the degradation rate of the hydrogels affected the release rate of VEGF and OPG (data not shown). The fast degrading hydrogels released all of their protein by the time the scaffold was completely degraded (approximately one week). The slow degrading hydrogels had a high burst release of protein, which was followed by release at nanogram levels per week for the duration of the 8 week study. When the still intact slow degrading hydrogels were degraded at 8 weeks, reservoirs of approximately 10% VEGF and 40% OPG were found to be retained in the HA hydrogel. Similar to their degradation rates, the intermediate degrading hydrogels had intermediate release profiles.

5.3.2 In Vivo Bone Regeneration with VEGF

The effect of VEGF delivered from the fast degrading HA hydrogels was evaluated at two different doses — 5μg and 25μg — in the rat calvarial critical size defect model. Measuring the extent of mineralization using X-rays, the 25μg dose resulted in radioopacity (intensity/area) that was higher than both negative controls (empty defect and defect with HA hydrogel without protein; $p<0.1$) as well as the 5μg VEGF dose at a three week time point (Figure 5.1). The level of mineralization was similar to that observed in the animals treated with 5μg BMP-2. Examination of histological

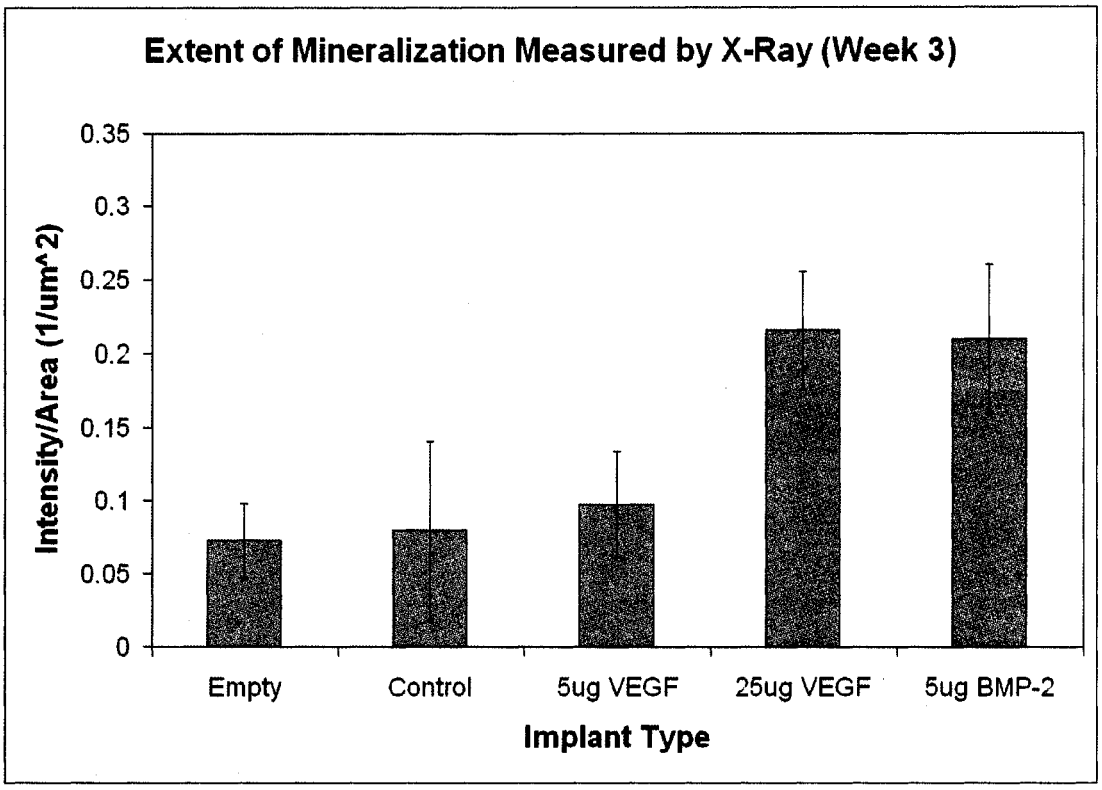

Figure 5.1: Dose response with VEGF delivered from fast degrading HA hydrogels. VEGF was tested at doses of 5μg and 25μg and compared with unloaded hydrogels and empty defects as negative controls as well as hydrogels loaded with 5μg BMP-2 as a positive control. Extent of mineralization was measured as the radiographic intensity for a 5mm diameter circular area centered over the defect. Results shown as mean and standard error of triplicate samples.

sections from these animals showed that the higher VEGF dose resulted in a greater volume of tissue filling the defect, as seen with the considerably thicker region of tissue in the center of the defect for the 25μg dose (Figure 5.2), although this tissue did not have the morphology of bone with only small regions of densely packed collagen. Looking at a later (6 week) time point with the higher dose of VEGF showed that the radioopacity decreased to levels comparable with the controls (Figure 5.3).

Changing the degradation rate of the scaffold appeared to change the rate of bone

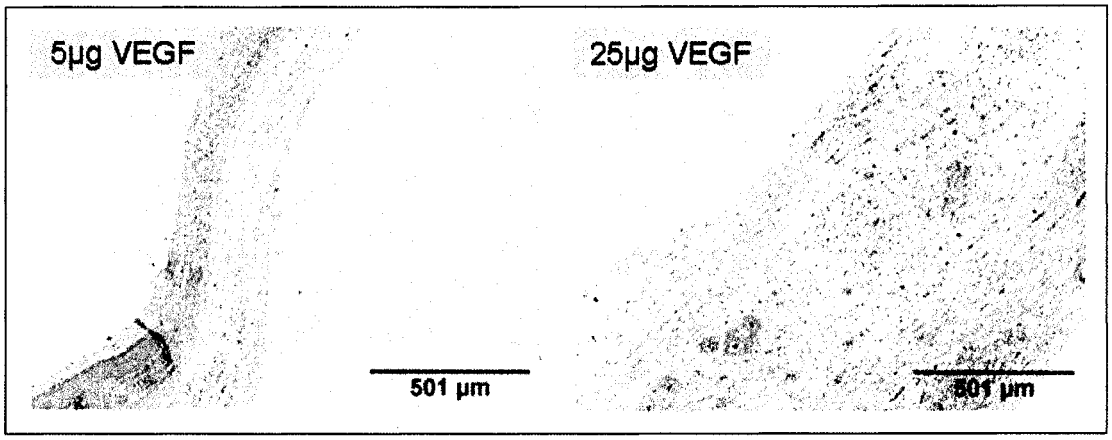

Figure 5.2: H&E stained histological sections of defects treated with VEGF. Micrographs show region in the center of the defect. The image on the left was from an animal treated with 5μg VEGF while the image on the right was from an animal treated with 25μg VEGF. Scale bars are approximately 500μm.

formation. Increased radioopacity was only seen for 25μg VEGF delivered from intermediate degrading HA hydrogels at the six week time point (Figure 5.3). However, this result was not confirmed with the more sensitive technique of microCT (Figure 5.4). MicroCT analysis showed that mineral volume in the animals treated with intermediate degrading hydrogels with 25μg VEGF was actually lower than the negative controls. When looking at histological sections stained with Masson's trichrome for fast (Figure 5.5) and intermediate (Figure 5.6) degrading hydrogels, the animals treated with 25μg VEGF had more tissue filling the defect site; however, this tissue did not stain the dark blue typical of collagen in bone. Taken together, these results suggest that radiographs are an insufficient technique for measuring mineralization. It is likely that other components in the tissue instead of the formation of mineralized bone are contributing to the radioopacity.

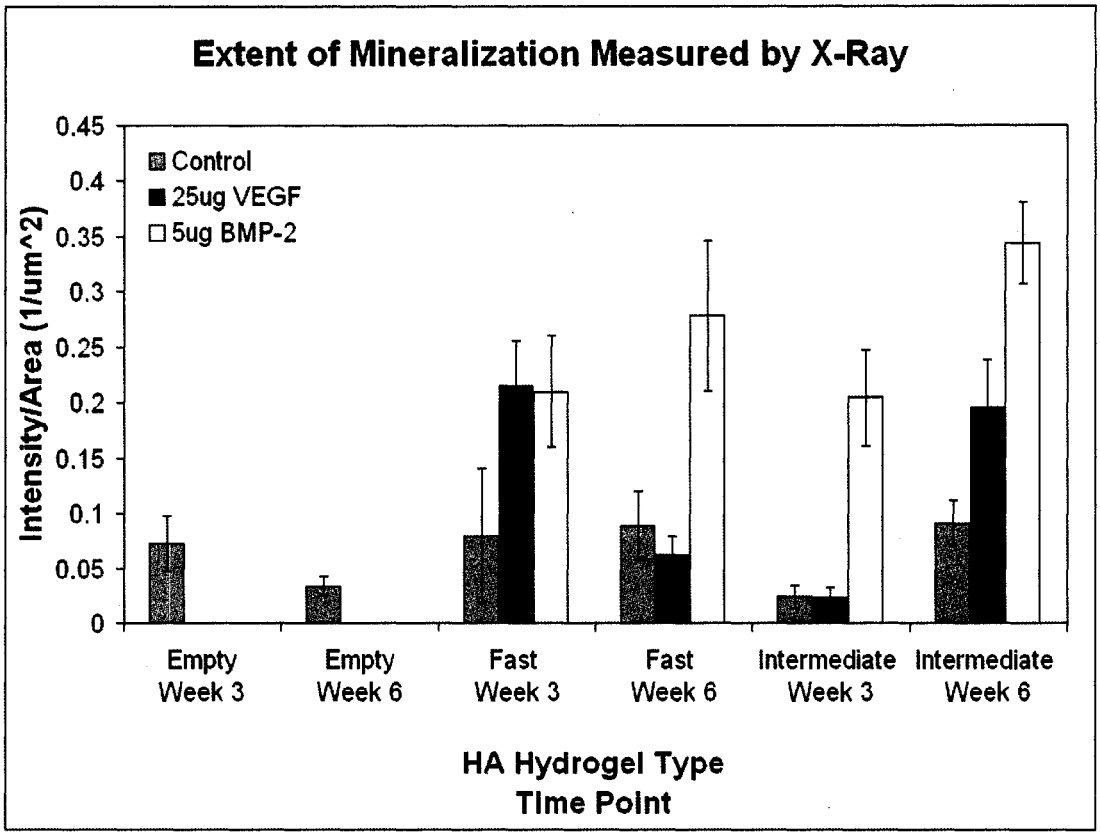

Figure 5.3: Temporal response with VEGF delivered from fast and intermediate degrading HA hydrogels. VEGF was tested at a dose of 25μg and compared with empty defects and unloaded hydrogels as negative controls as well as hydrogels loaded with 5μg BMP-2 as a positive control. Defects were evaluated after 3 and 6 weeks of healing. Extent of mineralization was measured as the radiographic intensity for a 5mm diameter circular area centered over the defect. Results shown as mean and standard error of triplicate samples.

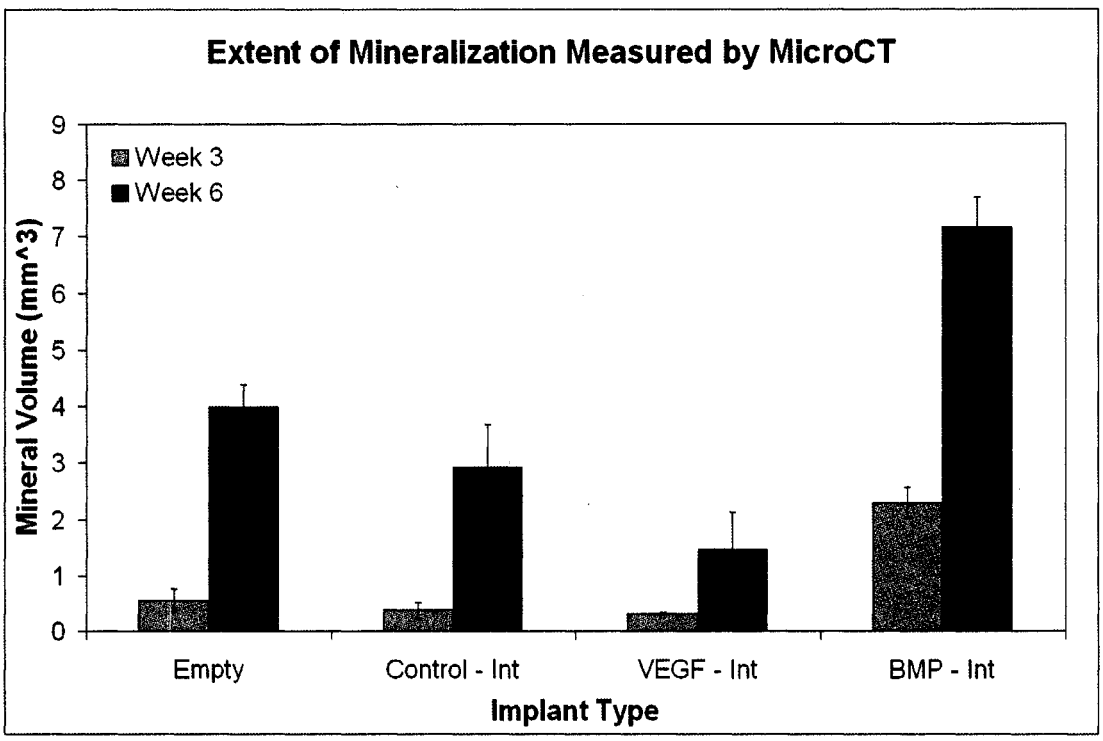

Figure 5.4: Mineralization measured by microCT for VEGF delivered from intermediate degrading hydrogels. VEGF was tested at a dose of 25μg and compared with empty defects and unloaded hydrogels as negative controls as well as hydrogels loaded with 5μg BMP-2 as a positive control. Defects were evaluated after 3 and 6 weeks of healing. A 5mm diameter x 1mm tall region centered within the defect was analyzed. Results shown as mean and standard error of triplicate samples.

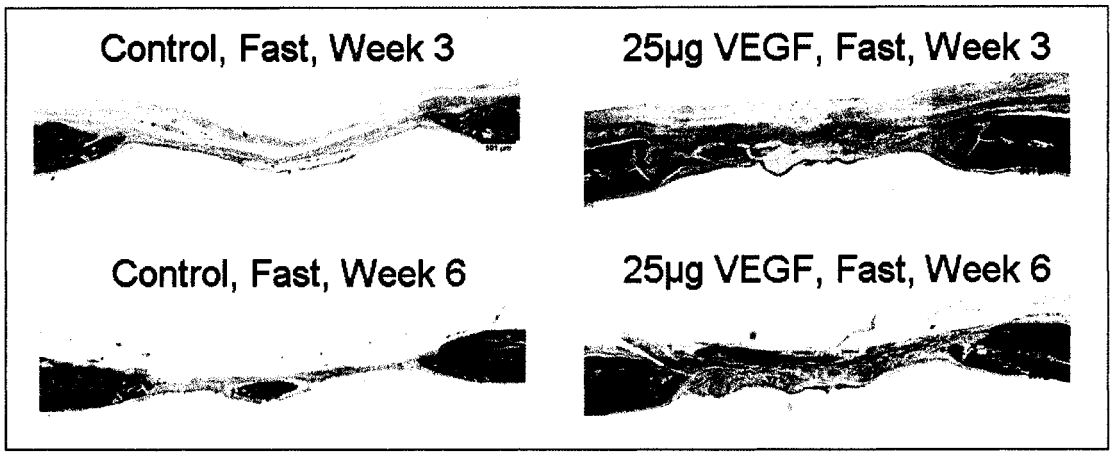

Figure 5.5: Masson's trichrome stained histological sections for fast degrading HA hydrogels. Representative histological sections showing cross-section of entire defect for animals treated with control or VEGF loaded hydrogels after three or six weeks of healing. Bone is stained dark blue. Native bone can be seen at the edges of each image. The scale bar in each image is 500μm.

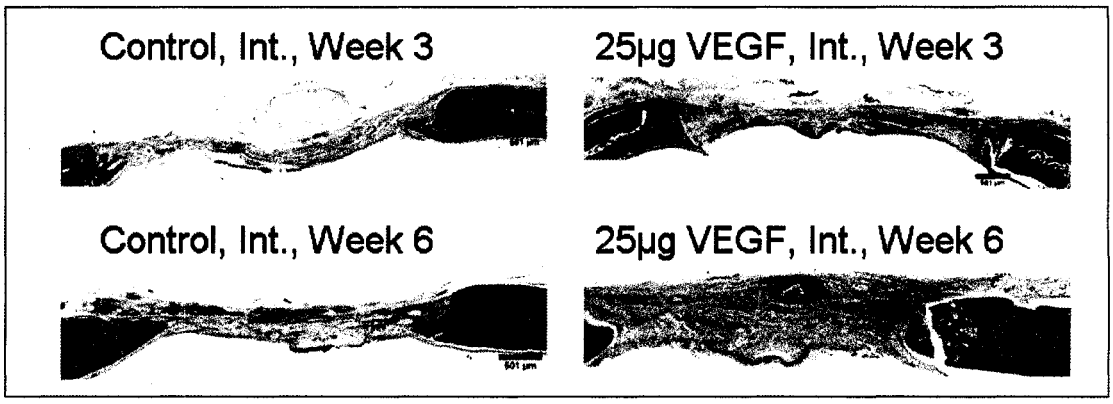

Figure 5.6: Masson's trichrome stained histological sections for intermediate degrading HA hydrogels. Same conditions as Figure 5.5 but for the intermediate degrading hydrogels.

5.3.3 Co-Delivery of BMP-2 and VEGF

Co-delivery of VEGF and BMP-2 from the fast degrading hydrogels was evaluated at a 6-week time point and compared to delivery of VEGF or BMP alone. While VEGF did not increase mineralization on its own, delivery of 25μg VEGF in combination with 5μg BMP-2 increased the mineral formation compared to BMP-2 delivery alone (Figure 5.7). With a p-value just less than 0.075, this effect was not statistically significant but indicated that co-delivery of angiogenic factors may enhance bone formation.

5.3.4 In Vivo Bone Regeneration with OPG

The effect of OPG delivered from the fast degrading HA hydrogels was evaluated at a dose of 25μg in the rat calvarial critical size defect model. The 25μg dose resulted in mineralization volumes, as measured by microCT, that were comparable to control hydrogels (Figure 5.8); however, the variability between samples was high. Examination of histological sections from these animals showed that some animals appeared to have near complete bridging of the defect with new bone while others exhibited minimal bone formation (Figure 5.9). Further exploration of the effects of OPG with an increased number of replicates would be needed to determine if it has a true osteoinductive effect.

5.4 Discussion and Conclusion

The angiogenic molecules tested, VEGF and OPG, did not have an osteoinductive effect *in vivo*. OPG, which has known bone-protective [97] and pro-angiogenic [100] effects, was the more promising candidate because of the high variability observed in the histological sections (Figure 5.9) and mineral volume measured by microCT (Figure 5.8). This variability suggested that OPG might be active in some cases, and the testing of additional replicates may be warranted.

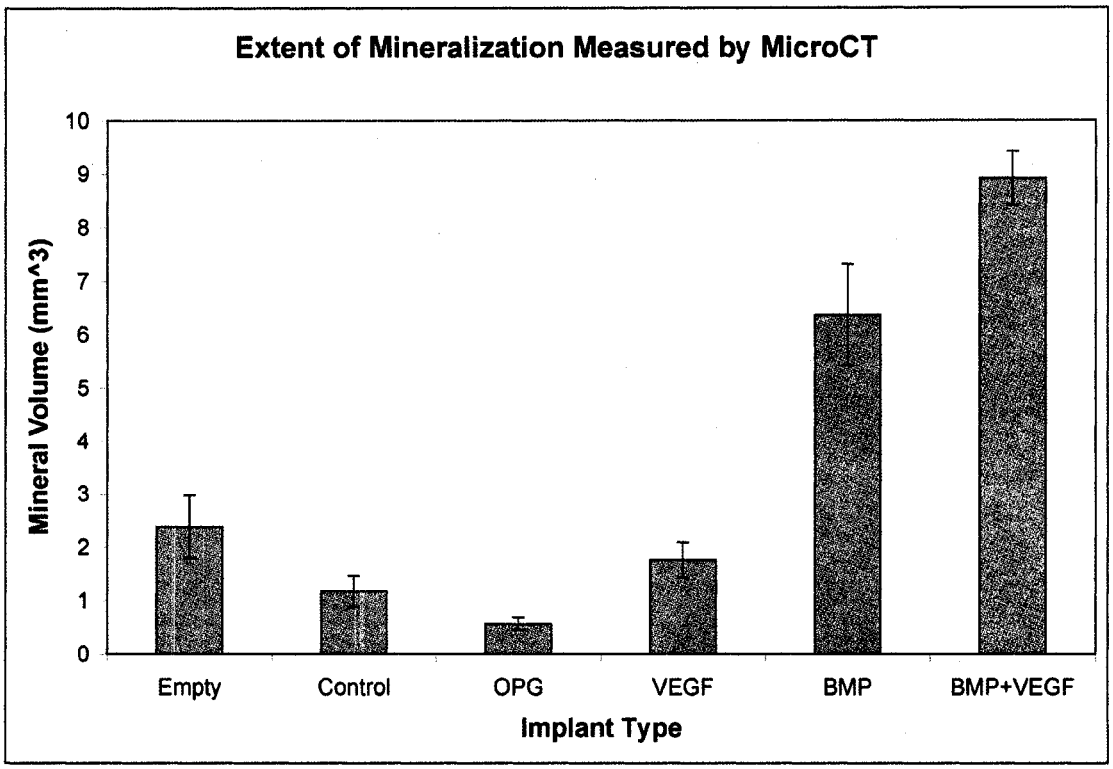

Figure 5.7: Mineralization measured by microCT for co-delivery of VEGF and BMP-2. VEGF was tested at a dose of 25μg and BMP-2 was tested at a dose of 5μg. Delivery of VEGF and BMP-2 together was compared with delivery of each growth factor individually as well as with empty defects and unloaded hydrogels as negative controls. Defects were evaluated after 6 weeks of healing. A 5mm diameter x 1mm tall region centered within the defect was analyzed. Results shown as mean and standard error of a minimum n = 4.

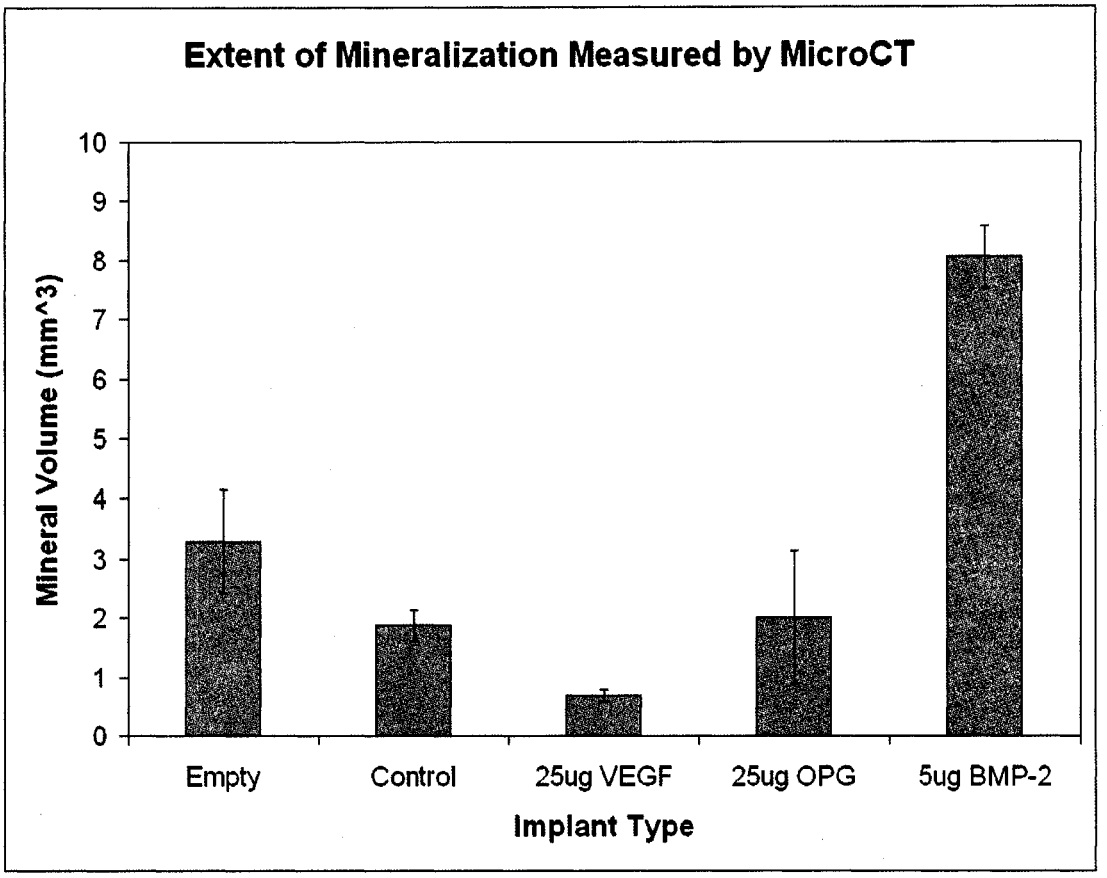

Figure 5.8: Mineralization measured by microCT for OPG delivered from fast degrading hydrogels. OPG was tested at a dose of 25μg and compared with empty defects and unloaded hydrogels as negative controls as well as hydrogels loaded with 5μg BMP-2 as a positive control. Defects were evaluated after 6 weeks of healing. A 5mm diameter x 1mm tall region centered within the defect was analyzed. Results shown as mean and standard error of triplicate samples.

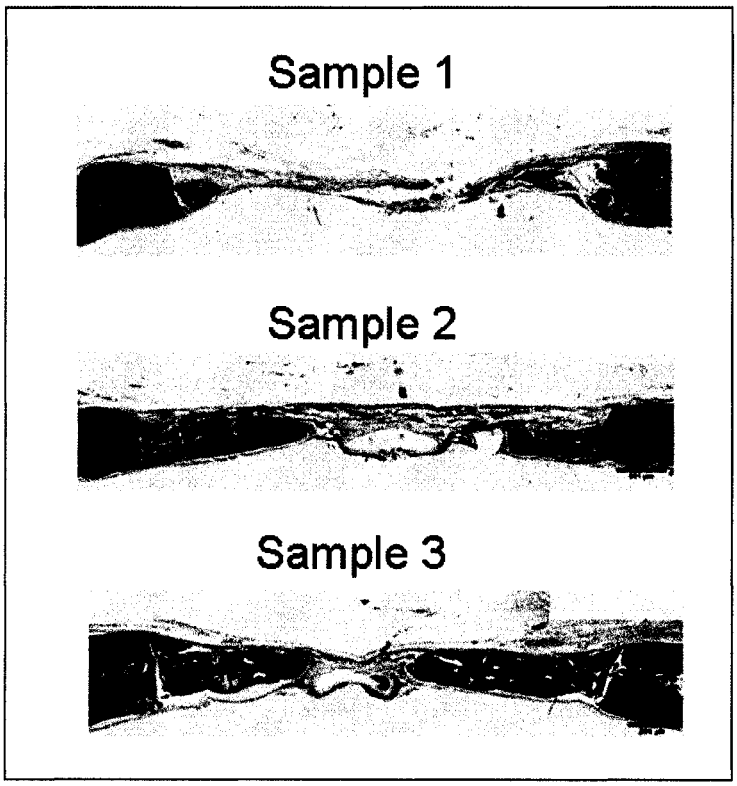

Figure 5.9: Masson's trichrome stained histological sections for fast degrading HA hydrogels with OPG. Histological sections showing cross-section of entire defect for three different animals treated with OPG loaded hydrogels after six weeks of healing. Bone is stained dark blue. Native bone can be seen at the edges of each image. The scale bar in each image is 500μm.

Use of radiographs to measure mineralization indicated that VEGF may have a potential dose effect and temporal response on bone growth; however, this was not confirmed by the more sensitive technique of microCT. Qualitative examination of the harvested tissues using histology generally indicated a greater tissue volume filling the defect area for samples treated with VEGF compared to controls, which could account for the increased radioopacity. Further examination of the effects of VEGF and OPG on angiogenesis as well as on the amount of cellular infiltration and/or extracellular matrix (ECM) production is warranted. A more comprehensive quantitative analysis of the number of blood vessels induced by VEGF in the present studies would indicate if VEGF was having its expected angiogenic effect. Then one could possibly deliver VEGF in conjunction with an osteoinductive molecule such as BMP-2 to form new bone tissue that is well-vascularized. As bone has been shown to regenerate in this site through a mechanism similar to intramembranous ossification [33] and VEGF may not have strong osteogenic activity there [261], successful (and unsuccessful) treatments may have different effects in other anatomical locations. Finally, co-delivery of VEGF and BMP-2 showed a slight increase in mineral formation compared to delivery of BMP-2 alone. The angiogenic factor may be acting to increase mineral formation by increasing blood vessel formation and thus nutrient delivery to the tissue. Additional quantification of blood vessel formation would confirm if this effect.

Chapter 6

CONTROLLED RELEASE OF LRAP FROM PLGA MICROSPHERES FOR BONE REGENERATION

6.1 Introduction

Leucine-rich amelogenin peptide (LRAP) is an alternatively spliced product of amelogenin and is described in detail in Chapter 2.5.5 and 2.10.4. LRAP plays a key role during the process of amelogenesis, where it forms part of the extracellular matrix (ECM) prior to enamel mineralization. Dr. Martha Somerman's group at the University of Washington Dental School has also explored the ability of this peptide to act as a signaling molecule during cementogenesis. They have shown that LRAP can down-regulate osteocalcin (OCN) and up-regulate osteopontin (OPN) and osteoprotegerin (OPG) as well as can inhibit mineralization for immortalized murine cementoblasts (OCCM-30) in culture [68]. The highest dose of LRAP (1.0 μg/mL/day) invoked a significant response *versus* controls while two lower doses (0.01 and 0.1 μg/mL/day) indicated a dose-response effect [68].

Relevant to the goals of this dissertation, LRAP has been shown to have chondrogenic and osteogenic activity *in vitro* as well as *in vivo* [65, 67]. However, the ability of LRAP to induce bone formation has not been conclusively demonstrated in a bone model [66]. In an ectopic oral mucosal mouse model, LRAP-coated agarose beads induced expression of osteo-chondrogenic markers, including RP59, Sox9, OPN, and bone sialoprotein (BSP); however, ectopic mineralization was not observed [67]. In contrast, ectopic mineralization, vascularization, and BSP and bone acidic glycoprotein-75 (BAG-75) expression were observed after LRAP delivery from a poly(lactide-co-glycolide) (PLGA) scaffold in an ectopic rat muscle model [65]. In the most relevant

model, LRAP loaded in a collagen sponge was implanted as a parietal bone onlay and induced bone formation in the sponge and adjacent to the existing bone [66]. However, the full details of this study have yet to be published.

These prior studies indicate that LRAP may be a potentially interesting therapeutic molecule for regenerating several mineralized tissues in the craniofacial region. In the study described in this chapter, the ability of LRAP to mediate bone formation was directly evaluated. LRAP was formulated into biodegradable PLGA microspheres for controlled release in a rat calvarial critical size defect model. It was hypothesized that this model of challenged bone healing would provide a means to evaluate the osteoinductive capacity of LRAP. Further goals of the study were to demonstrate that LRAP could be released in a controlled fashion over a period of weeks from the PLGA microspheres and that LRAP activity could be maintained during the formulation process.

6.2 Materials and Methods

6.2.1 Materials

All reagents were obtained from Sigma-Aldrich (St. Louis, MO) unless otherwise noted. Cell culture reagents were obtained from Invitrogen (Carlsbad, CA). LRAP was obtained as a glutathione S-transferase (GST) fusion of the 56 amino acid porcine LRAP as a gift from Dr. Carolyn Gibson (University of Pennsylvania, Philadelphia, PA) via Martha Somerman. LRAP was linked at the N-terminus to the GST peptide and was prepared in glutathione elution buffer (75mM 4-(2-hydroxyethyl)-1-piperazineethanesulfonic acid (HEPES), pH 7.4, 150mM sodium chloride (NaCl), 10mM reduced glutathione, 5mM 1,4-dithio-DL-threitol (DTT), and 2% N-octyl glucoside). The LRAP-GST fusion was used in all experiments and will be referred to simply as LRAP for the remainder of the chapter. A rabbit IgG antibody to the LPDLPLEAWPATDKTKREEVD sequence of LRAP [290] was also provided by Dr.

Gibson.

6.2.2 LRAP ELISA

Since LRAP was expressed as a GST fusion protein, Reacti-Bind™ anti-GST coated plates (Pierce, Rockford, IL) were used to develop an enzyme-linked immunosorbent assay (ELISA) assay to determine the concentration of LRAP in subsequent experiments. Each well was incubated with 100μL of an LRAP solution (experimental sample, blank, or standard) for one hour, washed three times, incubated with 100μL of a 1:1000 dilution of the primary antibody for one hour, washed three times, incubated with 100μL of a 1:10,000 dilution of peroxidase conjugated ImmunoPure goat anti-rabbit IgG (H+L) (Pierce) for one hour, and washed three times. ImmunoPure 2,2'-azinobis [3-ethylbenzothiazoline-6-sulfonic acid]-diammonium salt (ABTS, Pierce) was prepared, and 150μL of substrate solution was added to each well and incubated for 30 minutes prior to stopping the color development with 100μL per well of a solution of 1% sodium dodecyl sulfate (SDS). The absorbance was measured at 405nm.

6.2.3 In Vitro Activity Assay

LRAP activity was assayed *in vitro* using OCCM-30 by Erica Swanson of the Somerman lab, as previously described [68, 291]. OCCM-30 were plated at 20,000 cells/cm^2 in 24-well plates in growth medium (Dulbecco's Modified Eagle's Medium (DMEM) plus 10% fetal bovine serum (FBS), 100U/mL penicillin, and 100μg/mL streptomycin) and allowed to reach confluence in a humidified atmosphere of 5% CO_2 at 37°C. The medium was replaced with DMEM containing 5% FBS and 50μg/mL ascorbic acid, which further contained the experimental LRAP or buffer solutions. After 48 hours, RNA was harvested, and quantitative reverse transcription polymerase chain reaction (RT-PCR) was performed to determine expression levels of BSP, OCN, and OPN using the housekeeping gene glyceraldehyde-3-phosphate dehydrogenase (GAPDH) and

a calibrator for normalization.

6.2.4 Spray Freeze Drying of Proteins

The buffer for LRAP was changed from the glutathione elution buffer to 5mM sodium succinate (pH 5.0) using a PD-10 column (GE Healthcare, Piscataway, NJ). Rat serum albumin (RSA) at 3.8 mg/mL and trehalose at 0.76 mg/mL were added to the LRAP solution. A negative control solution was prepared with 3.8 mg/mL RSA and 0.76 mg/mL trehalose in 5mM sodium succinate (pH 5.0). A positive control solution was prepared with 2.9 μg/mL BMP-2 (R&D Systems, Minneapolis, MN), 3.8 mg/mL RSA, and 0.76 mg/mL trehalose in 5mM sodium succinate (pH 5.0). Each solution was sprayed through an ultrasonic nozzle with a power setting of 1.6W at a flow rate of 5mL/min and collected in a liquid nitrogen bath. The liquid nitrogen was allowed to evaporate while keeping the droplets frozen at -80°C. The spray freeze dried protein was then lyophilized.

6.2.5 Preparation of Protein Loaded PLGA Microspheres

Microspheres were fabricated using the ProLease^{TM} technique [222, 223], which is shown schematically in Figure 6.1. Briefly, the micronized protein preparations from above were suspended by ultrasonication at a target concentration of 5mg/mL in methylene chloride (Fisher Scientific, Hampton, NH) solutions containing 50mg/mL PLGA (inherent viscosity (I.V.) = 0.39 dL/g, Absorbable Polymers International, Pelham, AL). Each batch was then sprayed through an ultrasonic nozzle to produce atomized droplets. These droplets were immediately collected in a liquid nitrogen bath to freeze the particles, and then the particles were allowed to enter a cold (-80°C) ethanol (AAPER, Shelbyville, KY) bath where the methylene chloride was extracted over several days to harden the microspheres. The microspheres were collected by filtration and dried. Protein content was determined by dissolving the microspheres in methylene chloride, centrifuging the insoluble protein, and dissolving the protein

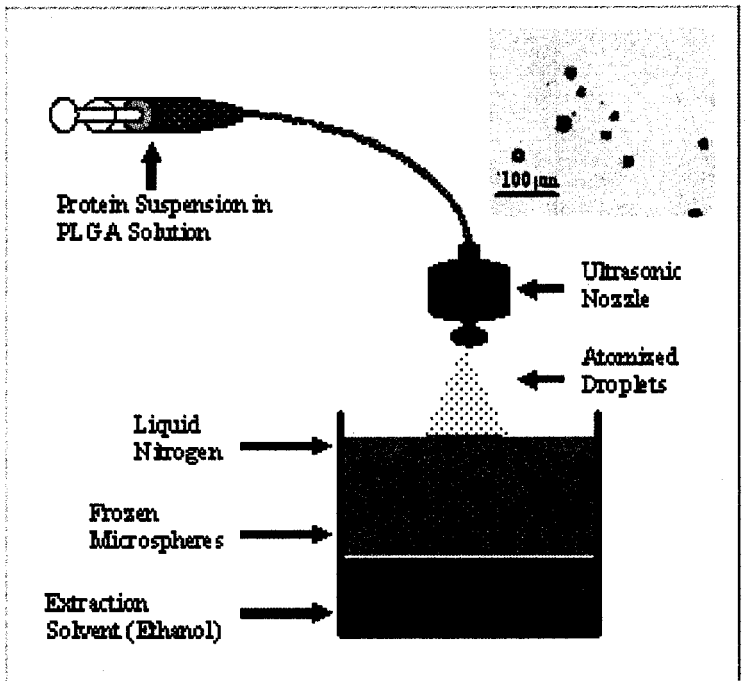

Figure 6.1: Microsphere fabrication using ProLease^{TM} method. Protein is suspended in a PLGA solution, which is sprayed through an ultrasonic nozzle to form atomized droplets. The droplets are collected in a liquid nitrogen bath and allowed to freeze before entering a cold ethanol bath to extract the solvent. Inset shows brightfield micrograph of PLGA microspheres made using this method.

pellet in DI water. The amount of protein was quantified using a bicinchoninic acid (BCA) assay (Pierce, Rockford, IL).

6.2.6 Rat Calvarial Critical Size Defect Model

Microspheres were implanted in a rat calvarial critical size defect model to evaluate their ability to induce bone regeneration. The surgical protocol was approved by the University of Washington (UW)Institutional Animal Care and Use Committee (IACUC). Surgeries were conducted under aseptic conditions using sterile materials. Adult male Sprague Dawley rats (Harlan, Indianapolis, IN) were anesthetized using isoflurane (5% induce, 2.5% maintain), and their heads were shaved and disinfected. A

linear incision was made along the midline of the scalp, and the soft tissues, including the periosteum, were reflected. A full-thickness 5mm circular defect was created in the center of the parietal bones (over the sagittal suture) using a Command2 drill system with a 1.0mm fissure carbide bur (Stryker, Kalamazoo, MI) while irrigating with saline. For animals receiving microspheres, 30-50mg of microspheres were placed into the defect. For additional negative control animals, the defect was left empty. The skin was closed over the defect site using wound clips, and the animals were allowed to heal for 4 to 12 weeks. Buprenorphine was administered immediately post-operatively for pain mitigation.

6.2.7 Tissue Harvest and Analysis of Mineralization

At the desired time points, the rats were sacrificed by CO_2 asphyxiation, and the parietal bones were harvested and fixed in 10% neutral buffered formalin (Fisher). Extent of mineralization was measured by X-ray or microcomputed tomography (microCT). X-rays were performed with X-Omat AR film (Kodak, Rochester, NY) in an enclosed X-ray unit (Picker X-ray Corporation, Cleveland, OH) using a distance of 64cm, voltage of 35 kVp, current of 5 mA, and exposure time of 5-30 seconds. Developed X-ray films were scanned into digital format, and X-ray intensity was quantified using the MetaMorph® imaging system (Molecular Devices Corporation, Sunnyvale, CA). For microCT analysis, scans were performed with a *viva*CT 40 (Scanco Medical, Bassersdorf, Switzerland) by Philippe Huber and Ted Gross at Harborview Medical Center, Seattle, WA. Scans were conducted using a voltage of 55 kVp, current of 145 μA, and voxel size of 30 μm. Images were reconstructed and analyzed using segmentation parameters of sigma = 1.2, support = 2, and threshold = 250.

6.2.8 Histology

After quantifying mineralization, the samples were decalcified using CalEx Decalcifier (Fisher) for 48 hours or in a 10% EDTA solution at pH 7 for 2 weeks. The decalcified

tissue was embedded in paraffin and sectioned into 5μm thick sections for histology. Tissue sections were stained with hematoxylin and eosin (H&E) or Masson's trichrome for qualitative analysis.

6.3 Results

6.3.1 LRAP ELISA

An ELISA was successfully developed using Reacti-Bind^{TM} anti-GST coated plates and anti-LRAP as the primary antibody that could detect LRAP in the range of 0.02 μg/mL to 0.355 μg/mL. However, incubating LRAP at 37°C for >20 hours in various buffers reduced its ability to be detected by the ELISA. This reduction in detection was also observed using a polyclonal antibody to the GST domain (Invitrogen, Carlsbad, CA) as the primary antibody, although the effect was less severe. This precluded the use of the ELISA to detect LRAP in release experiments conducted at 37°C.

6.3.2 Microsphere Preparation

The total protein content of the microspheres was measured as 29±7 μg protein/mg microspheres for the RSA microspheres, 30±2 μg protein/mg microspheres for the LRAP microspheres, and 30±1 μg protein/mg microspheres for the BMP-2 microspheres (mean and standard deviation of triplicate samples). The microspheres were formulated assuming a 100% recovery during the protein spray freeze drying process and were targeted to have a protein loading of 100 μg protein/mg microspheres. These results indicate that the spray freeze drying had an actual recovery of approximately 30%.

Using the ELISA, the concentration of LRAP was measured at 1.8 μg/mL for the staring solution and at 0.5 μg/mL after the PD-10 column, prior to spray freeze drying. The concentration of BMP-2 was provided by the manufacturer. Assuming that the ratio of LRAP or BMP-2 to RSA was not changed during the spray freeze

drying process, the microspheres would deliver a dose of 3μg LRAP/mg microspheres or 0.02μg BMP-2/mg microspheres. The expected LRAP concentration in the starting solution was 0.535 μg/μL and was expected to be diluted to 0.382 μg/μL after running through the PD-10 column, assuming no protein loss on the column. This indicates a significant fraction of the protein was lost on the PD-10 column; however, the higher than expected initial concentration resulted in a higher dose of LRAP being incorporated into the microspheres.

Overall, assuming no losses, the microspheres were formulated so that a 50mg dose of microspheres would deliver approximately 300μg LRAP or 3μg BMP-2. Due to losses during the fabrication process and variations in the starting solution concentrations, the 50mg dose would deliver approximately 150μg LRAP or 1μg BMP-2. However, dissolution of the microspheres with methylene chloride to recover the protein also interfered with the ability of the ELISA to detect LRAP so the actual final concentration of LRAP in the microspheres could not be confirmed.

6.3.3 In Vitro Activity

Because the ELISA gave inconsistent results when attempting to measure the concentration of LRAP in the microspheres, LRAP preparations from various stages of the microsphere formulation process were tested for activity using OCCM-30 cementoblasts. It was expected that LRAP would down-regulate OCN and BSP and up-regulate OPN and OPG in this system [68]. While a dose of 1.0 μg/mL was needed for a significant response, some effect was seen for doses as low as 0.01 μg/mL [68].

The three major steps during microsphere fabrication were simulated using preparations that would yield 2μg LRAP with bovine serum albumin (BSA) as the carrier protein or equivalent preparations with BSA only as a control, including (a) a 1:1000 dilution of LRAP-GST fusion into 5mM sodium succinate (pH 5.0) with 10mg/mL BSA and 2mg/mL trehalose that was lyophilized; (b) the solution of (a) sprayed through an ultrasonic nozzle into a liquid nitrogen bath, frozen, and lyophilized; and

(c) the spray-freeze dried powder of (b) exposed to 1mL methylene chloride for 30 minutes then centrifuged and dried. As seen in Figure 6.2, LRAP samples processed to simulate various steps of the microsphere fabrication process reduced expression of OCN mRNA by OCCM-30 cementoblasts *in vitro*, similar to unprocessed LRAP and as previously observed [68]. However, the control BSA-treated samples also showed a similar activity. With the spray freeze dried samples and methylene chloride treated samples, OCN mRNA expression was further reduced in LRAP samples compared to the samples containing only BSA. However, for the starting protein solutions in the 5mM sodium succinate buffer, the OCN mRNA expression levels with LRAP were higher than with BSA alone. This suggests that the effect of BSA on the samples is non-specific in addition to interfering with the ability to measure LRAP activity. The spray freeze dried and methylene chloride treated samples did not inhibit OCN mRNA expression as much as the unprocessed LRAP, which could indicate a loss of activity during processing. However, this could not be definitively concluded due to the activity shown by the BSA controls for those groups.

To determine if the effects were coming from the proteins or from other components in the buffer, the *in vitro* activity of the buffers using during microsphere fabrication was tested with OCCM-30 cementoblasts. Previously, LRAP was found to decrease OCN mRNA expression and increase OPN mRNA expression [68], and this was again observed with the unprocessed LRAP positive control. As seen in Figure 6.3, both the 5mM sodium succinate buffer and 2mg/mL trehalose in succinate buffer actually had an opposite effect compared to LRAP-treated positive control samples. The OCN mRNA expression levels were increased (Figure 6.3A), and the OPN mRNA expression levels were decreased (Figure 6.3B) for the buffer test samples. Using less buffer solution relative to OCCM-30 medium brought the OCN and OPN mRNA expression levels closer to the untreated control.

The results seen in Figures 6.2 and 6.3 indicate that BSA may be the primary formulation component masking LRAP activity. Therefore, instead of testing the

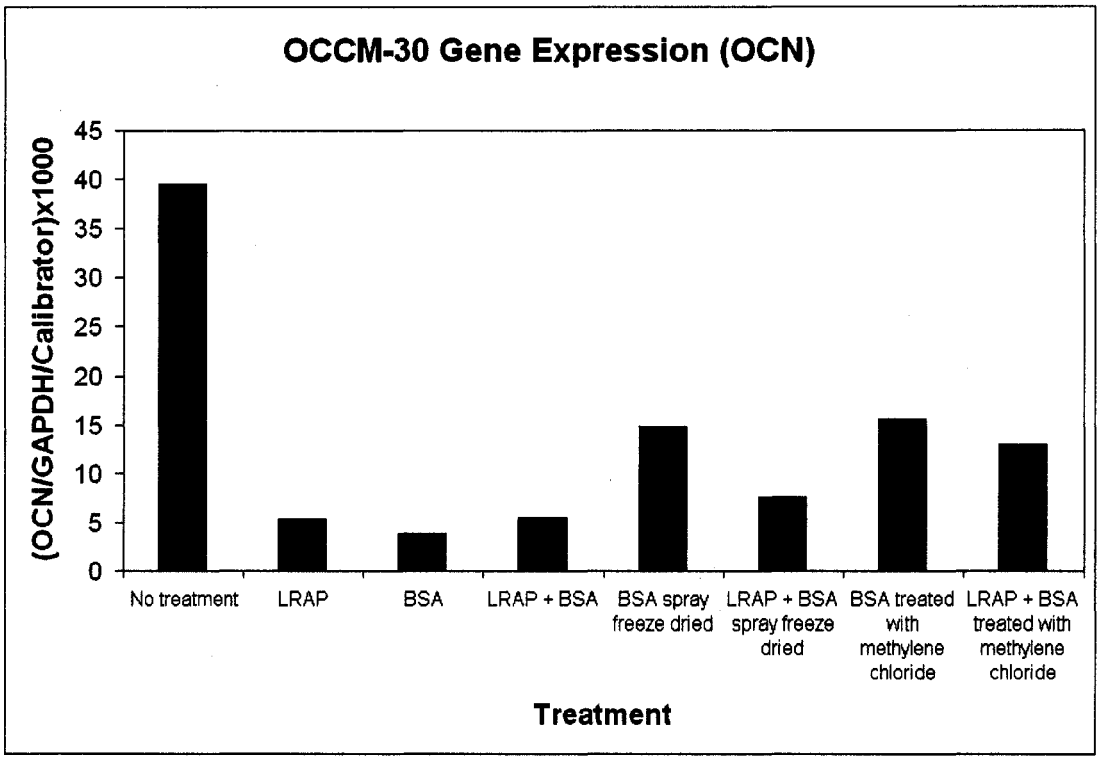

Figure 6.2: *In vitro* activity of LRAP prepared to simulate various stages of microsphere formulation. The y-axis is the mRNA level of OCN determined by RT-PCR normalized to a calibrator and the housekeeping gene GAPDH. No treatment received medium only, and LRAP used the protein as received. BSA is 10mg/mL BSA and 2mg/mL trehalose in 5mM sodium succinate (pH 5.0) that was lyophilized. LRAP + BSA is a 1:1000 dilution of LRAP-GST (final concentration is 6μg/mL LRAP-GST) into 5mM sodium succinate (pH 5.0) with 10mg/mL BSA and 2mg/mL trehalose that was lyophilized. BSA spray freeze dried is the solution of BSA sprayed through an ultrasonic nozzle into a liquid nitrogen bath, frozen, and lyophilized. BSA + LRAP spray freeze dried is the solution of LRAP + BSA sprayed through an ultrasonic nozzle into a liquid nitrogen bath, frozen, and lyophilized. BSA treated with methylene chloride is BSA spray freeze dried exposed to 1mL methylene chloride for 30 minutes then centrifuged and dried. LRAP + BSA treated with methylene chloride is LRAP + BSA spray freeze dried exposed to 1mL methylene chloride for 30 minutes then centrifuged and dried. All samples were directly resuspended in OCCM-30 growth medium to a concentration of 2μg/mL LRAP-GST prior to addition to the cells. Assay performed by Erica Swanson.

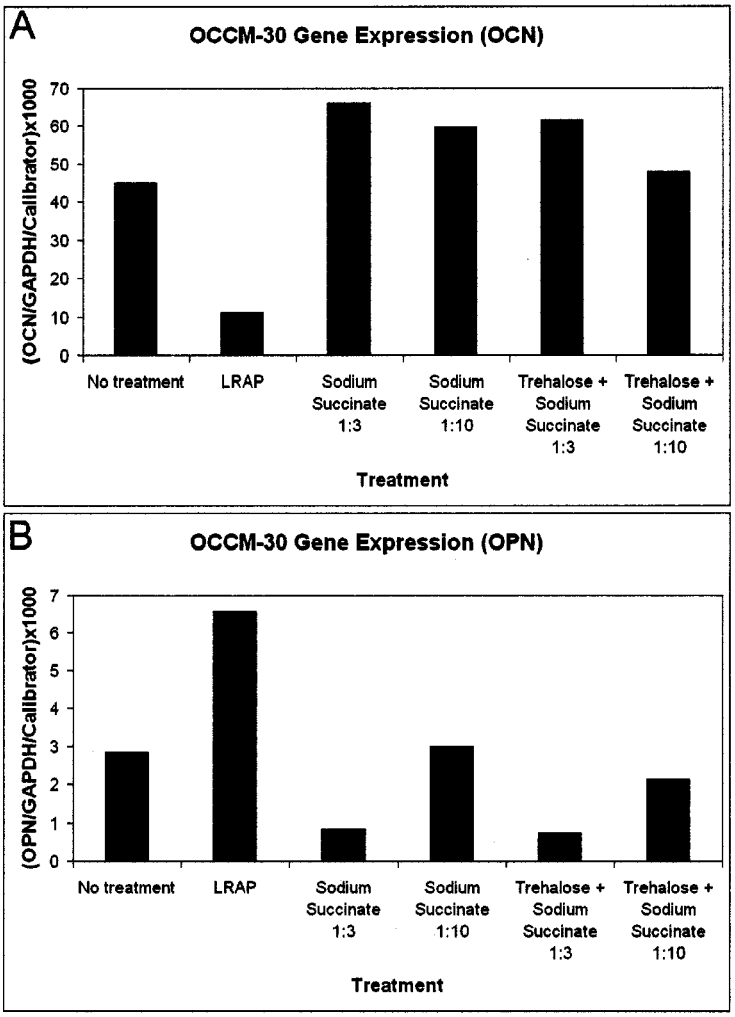

Figure 6.3: *In vitro* activity of buffers used during microsphere formulation. (A) OCN mRNA expression levels. The y-axis is the mRNA level of OCN determined by RT-PCR normalized to a calibrator and the housekeeping gene GAPDH. No treatment received medium only, and LRAP used the protein as received. Sodium Succinate 1:3 is a 1:3 dilution of 5mM sodium succinate (pH 5.0) into OCCM-30 medium. Sodium Succinate 1:10 is a 1:10 dilution of 5mM sodium succinate (pH 5.0) into OCCM-30 medium. Trehalose + Sodium Succinate 1:3 is a 1:3 dilution of 2mg/mL trehalose in 5mM sodium succinate (pH 5.0) into OCCM-30 medium. Trehalose + Sodium Succinate 1:10 is a 1:10 dilution of 2mg/mL trehalose in 5mM sodium succinate (pH 5.0) into OCCM-30 medium. (B) OPN mRNA expression levels. The y-axis is the mRNA level of OPN determined by RT-PCR normalized to a calibrator and the housekeeping gene GAPDH. The treatment conditions were the same as in (A). Assay performed by Erica Swanson.

effects of processing on LRAP, LRAP was tested at the concentrations expected to be seen in a release study. The buffer was switched from 5mM sodium succinate (pH 5.0) to PBS. The concentration of BSA was reduced from 10mg/mL to 20μg/mL. Trehalose was not included. This would determine if the activity of LRAP would be able to be determined for the protein when it was released from the microspheres. As seen in Figure 6.4, LRAP in this formulation demonstrated the expected activity, decreasing BSP (panel A) and OCN (panel B) mRNA expression compared to untreated controls. However, the negative control sample containing BSA only demonstrated a similar activity in reducing BSP and OCN mRNA levels. This non-specific effect of BSA on OCCM-30 expression of OCN and BSP mRNA made it impossible to determine LRAP activity in a release study.

6.3.4 Early In Vivo Response

In a pilot study, approximately 50mg PLGA microspheres were implanted in the rat calvarial critical size defect model (one animal each per type of microspheres and one empty defect control). This 50mg dose would deliver approximately 150μg LRAP or 1μg BMP-2. The microspheres were initially retained by tightly packing the microspheres within the defect site. The microspheres also stuck together once wetted by residual blood and saline in the defect. The animals were allowed to heal for 4 weeks (6 weeks for the BMP-2 animal) before sacrifice. Extent of mineralization was measured by X-ray. As quantified in Figure 6.5A, minimal mineralization occurred for all samples at these early time points. This can further be seen in representative images of X-rays of the defect sites in Figure 6.5B–E.

As seen in the histological sections in Figure 6.6, the microspheres were not degraded by the four week time point. The microspheres showed up as void space on the histological sections and made up a large fraction of the cross-sectional area. By six weeks, the microspheres were more degraded as indicated by a smaller void space with less well-defined margins. Both the empty and RSA microsphere controls induced

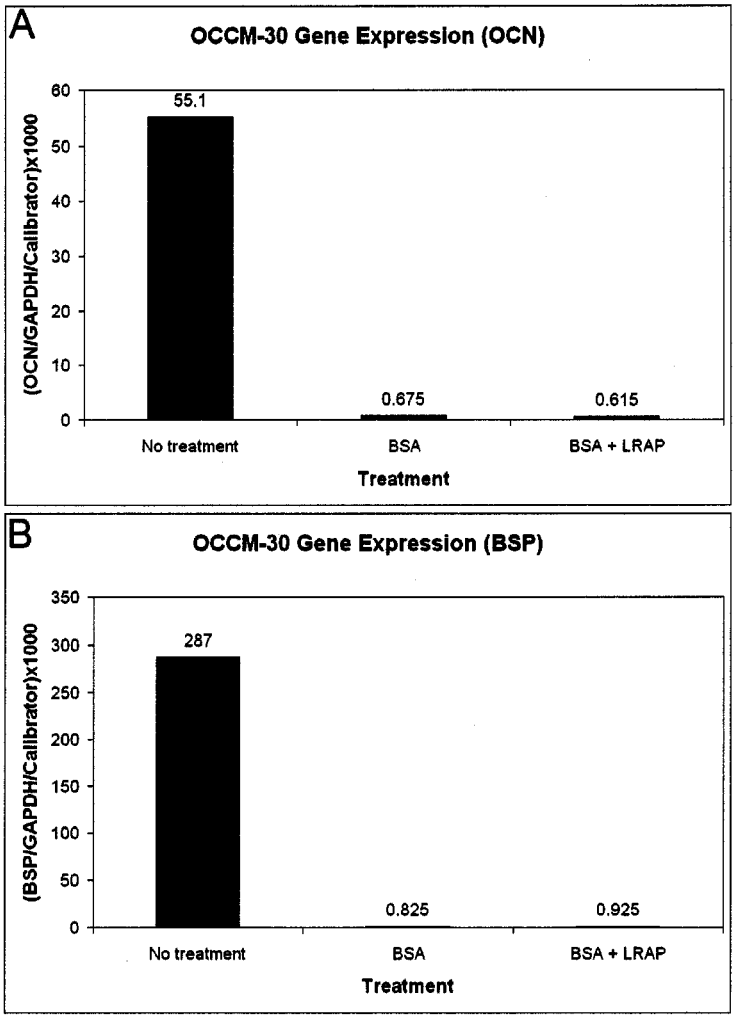

Figure 6.4: *In vitro* activity of LRAP versus BSA simulating release conditions. (A) OCN mRNA expression levels in cementoblasts treated with LRAP. The y-axis is the mRNA level of OCN determined by RT-PCR normalized to a calibrator and the housekeeping gene GAPDH. No treatment received medium only. BSA is 20μg/mL BSA in PBS. BSA + LRAP is 2μg/mL LRAP-GST and 20μg/mL BSA in PBS. Protein samples in buffer were lyophilized then resuspended in OCCM-30 growth medium. Two wells were tested with each treatment. (B) BSP mRNA expression levels in cementoblasts treated with LRAP. The y-axis is the mRNA level of BSP determined by RT-PCR normalized to a calibrator and the housekeeping gene GAPDH. The treatment conditions were the same as in (A). Assay performed by Erica Swanson.

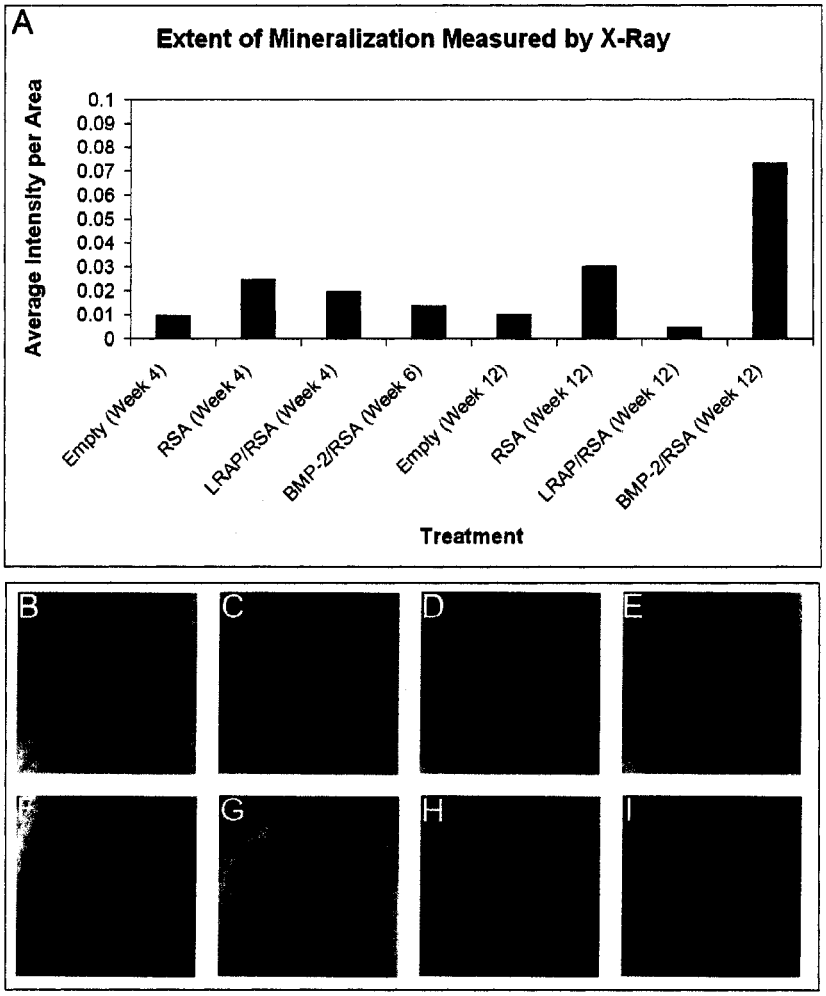

Figure 6.5: Mineralization measured by X-ray for microspheres in rat calvarial critical size defect model. (A) Extent of mineralization within defect region was measured by taking average X-ray intensity for a circular region centered over the defect. Background correction was performed by subtracting the average intensity of a region outside the tissue region. Treatment groups had either an empty defect or a defect filled with either RSA microspheres, LRAP/RSA microspheres, or BMP-2/RSA microspheres. Animals at 4 or 6 weeks were treated with 50mg microspheres while animals at 12 weeks were treated with 30mg microspheres. Representative X-rays for (B) Empty, Week 4; (C) RSA microspheres, Week 4; (D) LRAP/RSA microspheres, Week 4; (E) BMP-2/RSA microspheres, Week 6; (F) Empty, Week 12; (G) RSA microspheres, Week 12; (H) LRAP/RSA microspheres, Week 12; and (I) BMP-2/RSA microspheres, Week 12.

minimal tissue growth into the defect. As expected, the BMP-2/RSA microspheres induced tissue infiltration with collagen deposition (light blue stain); however, by the six week time point minimal new bone was formed. Interestingly, the LRAP/RSA microspheres also induced tissue infiltration with collagen deposition and minimal new bone. It is possible that the effect of the LRAP/RSA microspheres was an inflammatory response as some neutrophils (noted by their horseshoe-shaped nuclei in the histological sections) were present in the cellular infiltrate. However, it is also possible that this new tissue represented an early phase of bone matrix deposition. A later time point (12 weeks) was therefore examined.

6.3.5 Late In Vivo Response

In a second study, approximately 30mg PLGA microspheres were implanted in the rat calvarial critical size defect model (two animals each per type of microspheres and one empty defect control). This 30mg dose would deliver approximately 100μg LRAP or 0.6μg BMP-2. The smaller dose was selected as the 50mg dose well exceeded the volume of the defect site, as clearly seen in Figure 6.6B. The animals were allowed to heal for 12 weeks before sacrifice. Extent of mineralization was measured by both X-ray and microCT, and both methods gave similar results. In the quantitative radiographic results (Figure 6.5A), the BMP-2/RSA microspheres induced bone formation and mineralization in the defect site whereas the other treatment groups did not. This can be seen visually in representative X-ray images from the 12 week time point animals (Figure 6.5F–I). New bone can clearly be seen within the defect site of the BMP-2/RSA microsphere treated animals (Figure 6.5I). MicroCT analysis (Figure 6.7) confirmed the results seen with the radiographic analysis. The average mineral volume measured for the BMP-2/RSA microsphere treated animals (15mm^3) indicates that approximately 75% of the defect (5mm diameter x 1mm height) was filled with new bone by this time point. Mineralization for the LRAP/RSA microsphere and RSA microsphere treated animals was at a level similar to the empty defect

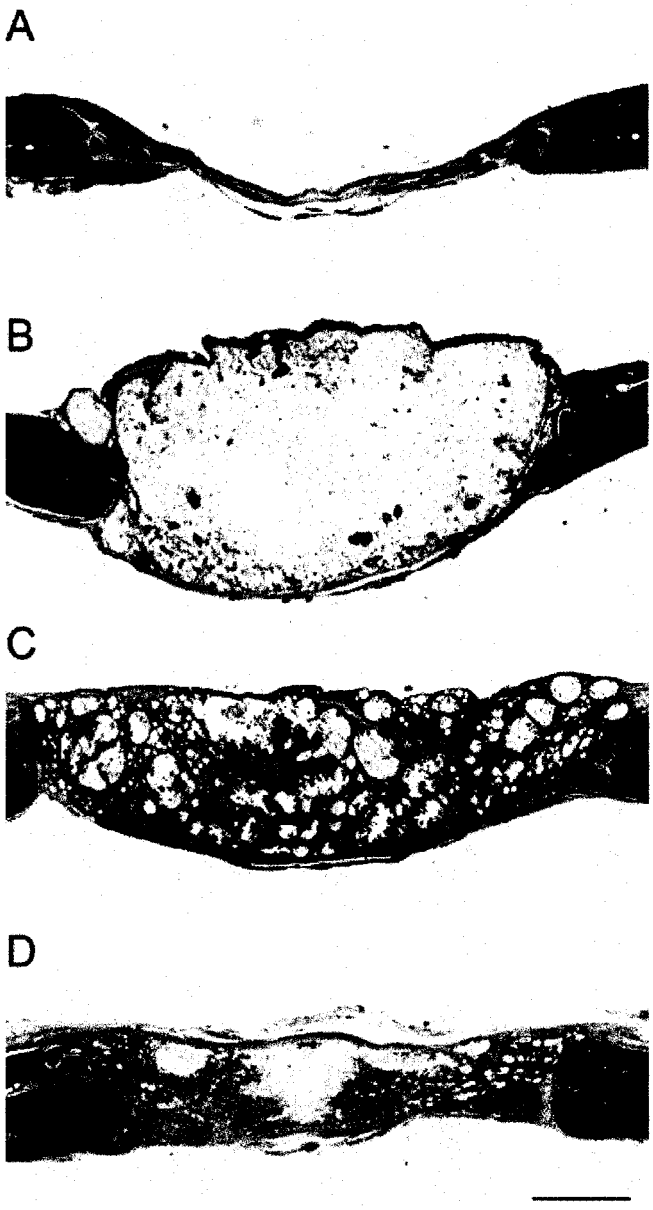

Figure 6.6: Histology showing early *in vivo* response. Histological sections stained with Masson's trichrome where bone is dark blue. Cross-sections in the frontal plane showing the native bone at the margins of the defect. (A) Empty defect, Week 4. (B) Defect with RSA microspheres, Week 4. (C) Defect with LRAP/RSA microspheres, Week 4. (D) Defect with BMP-2/RSA microspheres, Week 6. Scale bar is 1mm.

negative control. It should be noted that the RSA microspheres were implanted in the frontal bones and not parietal bones of the two animals receiving this treatment. This should represent a fairly similar site for evaluating healing; however, some slight morphological differences (particularly the relation to the suture lines) were observed and can be seen in Figure 6.7C.

In contrast to the early *in vivo* response, histological sections showing the *in vivo* response at 12 weeks indicated that the LRAP/RSA microsphere treated animals were more similar to the RSA microsphere and empty defect control animals than the BMP-2/RSA microsphere treated animals (Figure 6.8). By this time point, the microspheres were completely degraded, and no void spaces were observed in the histological sections. Treatment with BMP-2/RSA microspheres resulted in complete closure of the defect with new bone (dark blue stain) by the 12 week time point (Figure 6.8D). Some minimal bone growth and remodeling could be observed in histological sections for the empty defect, RSA microsphere, and LRAP/RSA microsphere treated animals; however, this remodeling was predominantly limited to the defect margins. The LRAP/RSA microsphere treated defects (Figure 6.8C) appeared to have a slightly thicker and more dense collagenous tissue filling the center of the defect; however, the limited sample number made definitive conclusions impossible.

6.4 Discussion and Conclusions

This study demonstrates that PLGA microspheres can be used to control the release of protein therapeutics, thus providing sustained delivery that can induce a tissue healing response. Whereas this study showed this effect indirectly by looking at the tissue response at two different time points, the following chapter will further examine the controlled release behavior of PLGA microspheres by directly looking at the *in vitro* release of similarly formulated microspheres delivering a model protein, BSA. By the 12-week time point, BMP-2 delivery from PLGA microspheres resulted in clear mineralization as measured both by X-ray and microCT (Figures 6.5 and 6.7)

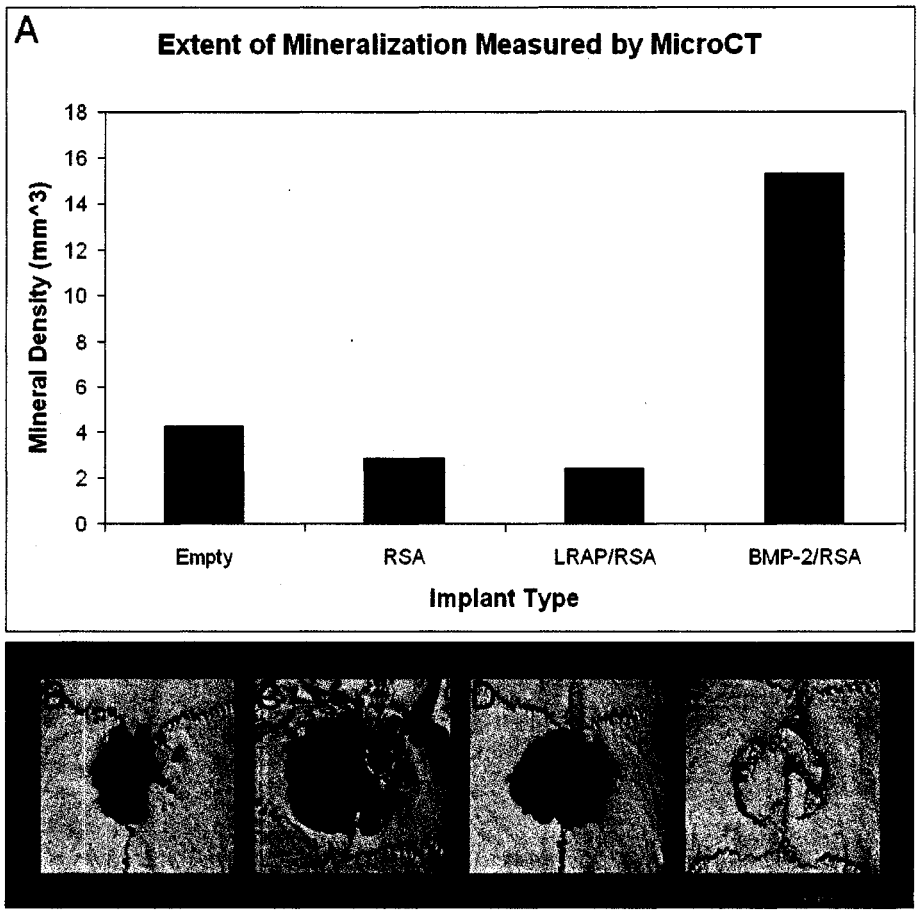

Figure 6.7: Mineralization measured by microCT for microspheres in rat calvarial critical size defect model. (A) Extent of mineralization was measured for a 5mm diameter circular region centered over the defect. Treatment groups had either an empty defect or a defect filled with either RSA microspheres, LRAP/RSA microspheres, or BMP-2/RSA microspheres. Animals were treated with 30mg microspheres and were analyzed at a 12-week time point. Representative microCT image reconstructions for (B) empty defect, (C) defect with RSA microspheres, (D) defect with LRAP/RSA microspheres, and (E) defect with BMP-2/RSA microspheres. MicroCT scanning and analysis performed by Philippe Huber and Ted Gross at Harborview Medical Center, Seattle, WA.

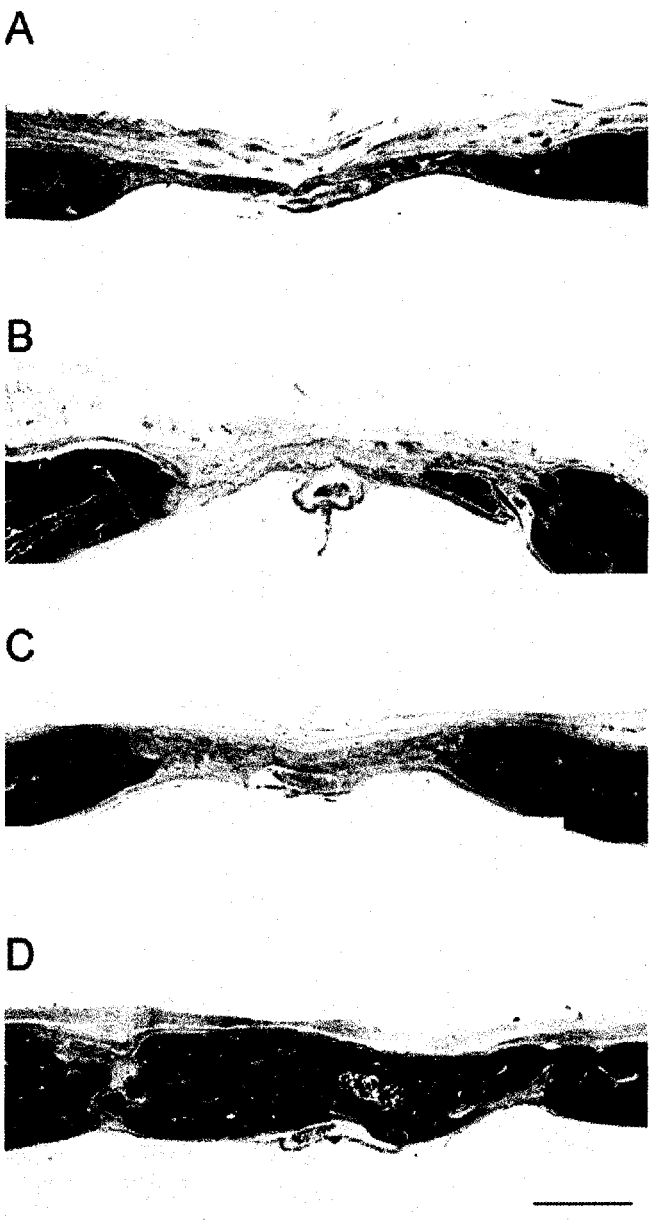

Figure 6.8: Histology showing late *in vivo* response. Histological sections stained with Masson's trichrome where bone is dark blue. Cross-sections in the frontal plane showing the native bone at the margins of the defect. (A) Empty defect, Week 12. (B) Defect with RSA microspheres, Week 12. (C) Defect with LRAP/RSA microspheres, Week 12. (D) Defect with BMP-2/RSA microspheres, Week 12. Scale bar is 1mm.

and in bridging of the defect with new bone as seen in the histological sections (Figure 6.8D). Delivery from PLGA microspheres also demonstrated the osteoinductive effect of BMP-2. Large amounts of new bone were formed within the center of the defect with limited connectivity to the native bone at the defect margins, indicating direct differentiation of osteoblasts within this region. In contrast, limited amounts of predominantly appositional bone formation were seen at the defect margins for animals receiving all other treatments. The PLGA microspheres also seem to provide slower release kinetics than the hyaluronic acid (HA) hydrogels described in Chapters 3 through 5. At a six week time point, BMP-2 delivery from the PLGA microspheres resulted in minimal mineralization whereas BMP-2 delivery from HA hydrogels resulted in significant mineralization compared to control hydrogels ($p<0.1$). However, by 12 weeks, the mineral volume in the BMP-2/RSA microsphere samples exceeded the 6 week mineralization in the BMP-2 hydrogel samples.

While the BMP-2/RSA microspheres clearly induced bone growth and mineralization *in vivo*, an osteoinductive capacity for LRAP was not observed in the present study. At both time points, LRAP delivery resulted in minimal mineralization. A robust cellular infiltrate at the earlier four week time point indicated that LRAP might be having some effect on the tissue; however, by 12 weeks, the tissue morphology of the LRAP samples was more similar to that of the negative controls. These results are in contrast to the LRAP-induced mineralization observed by Veis and colleagues in both ectopic [65] and orthotopic [66] models; however, the results are in line with Lacerda-Pinheiro *et al.* who did not observe mineralization with LRAP in an ectopic oral mucosal mouse model [67]. A more detailed examination of the osteochondrogenic activity of LRAP, by looking at expression of markers such as RP59, Sox9, OPN, BSP, or BAG-75, was not performed. It is possible that LRAP has some osteo-chondrogenic activity while being an insufficient signal to promote full tissue regeneration and mineralization in a challenged model of bone healing, such as the calvarial critical size defect model. Alternatively, use of LRAP as a GST fusion pro-

tein or inactivation of the peptide during microsphere fabrication may have affected the functional ability of LRAP in this study. The studies by Veis *et al.* and Lacerda-Pinheiro *et al.* expressed LRAP as a GST fusion protein; however, the GST domain was cleaved off using thrombin prior to functional assessment of LRAP [65, 67].

The ability to assess the function of LRAP in this study was limited by the insensitivity of the ELISA and OCCM-30 cementoblast assays. The ELISA showed reduced detection of LRAP after subjecting it to heat (37°C) or methylene chloride solvent. While the OCCM-30 cementoblast assay showed the expected effects of LRAP regardless of treatment condition, a nonspecific effect of the carrier protein BSA made it impossible to conclude that the LRAP remained active. It is likely, however, that the LRAP formulated into the PLGA microspheres should have retained its activity. BMP-2 formulated under identical conditions clearly retained its activity. The ProLease^{TM} method used to fabricate the microspheres offers advantages over other microsphere preparation techniques for maintaining the activity of proteins. The lack of an aqueous/organic interface during processing should help to prevent protein denaturation [222, 223]. Therefore, the effects (or lack thereof) seen with the LRAP/RSA microsphere samples could truly indicate that LRAP is not osteoconductive when delivered by this system in this particular bone regeneration setting.

Chapter 7

IN SITU CHARACTERIZATION OF THE DEGRADATION OF PLGA MICROSPHERES IN HYALURONIC ACID HYDROGELS BY OPTICAL COHERENCE TOMOGRAPHY

7.1 Introduction

Optical coherence tomography (OCT) is a high resolution optical imaging technique that is suitable for imaging biological specimens. The principles of this technique have been described in detail in section 2.11. OCT has primarily been applied to distinguish normal from pathologic tissues both *in vivo* and *ex vivo*, including esophagus [264], artery [270], and cartilage [265], etc.; however, it is becoming an attractive technique to monitor and evaluate therapies, particularly when using a tissue engineering or regenerative medicine approach. OCT has been used to image bone tissue engineering constructs *in vitro* [266, 267, 268]. These *in vitro* studies utilized OCT to obtain structural information on the distribution and remodeling effects of cells seeded within scaffolds. Yang *et al.* also used OCT to measure differences in scaffolds fabricated with different formulation parameters [267]. In the present study, the use of OCT is further extended to characterize temporal changes within the scaffold materials themselves. These morphological changes in the scaffolds are linked to their potential to promote healing, particularly through variations in the release rate of protein therapeutics, which is controlled by the degradation of protein-loaded poly(lactide-co-glycolide) (PLGA) microspheres.

PLGA has been used for over 40 years as a degradable implant material. PLGA is a member of the poly(α-hydroxy acid) family of polymers, which degrade via hydrol-

ysis *in vitro* and *in vivo* [292]. Hydration of the polymeric implant leads to eventual hydrolytic cleavage of the PLGA chains into low molecular weight fragments that will be dissolved and cleared. The ratio of lactide to glycolide, enantiomeric form, crystallinity, and initial molecular weight of the polymer all affect the degradation rate. *In vitro* studies by Vert and coworkers have shown heterogeneous degradation occurs in PLGA devices, with a faster degradation rate in the core than at the surface due to an autocatalytic effect from degradation products trapped within the core [293, 294, 295, 296, 297, 298]. Whereas they initially suggested that microspheres might fall below a critical dimensional limit and degrade homogeneously [298], additional studies by that group and others have shown that degradation at the surface of microspheres also proceeds more slowly [299, 224]. The degradation of PLGA microspheres has also been well characterized *in vivo* [300, 301, 302]; however, these studies used destructive end points, such as transmission electron microscopy (TEM), scanning electron microscopy (SEM), and light microscopy, to monitor morphological changes. Visscher *et al.* showed that there was no loss of microsphere integrity as the polymer initially degraded, which was characterized by molecular weight loss [302]. Erosion and disintegration into particulates only became apparent at later time points [302]. The ability of OCT to nondestructively image microsphere morphology *in situ* could provide a means of monitoring microsphere degradation in vivo and directly tie morphological changes to therapeutic protein release. This study presents the first steps towards this goal by correlating changes in microsphere morphology imaged in vitro with measured protein release rates.

7.2 Materials and Methods

7.2.1 Materials

All reagents were obtained from Sigma-Aldrich (St. Louis, MO) unless otherwise noted.

7.2.2 Preparation of Glycidyl Methacrylate Modified Hyaluronic Acid (HA-GMA)

HA (220,000 Da, Lifecore, Chaska, MN) was modified with glycidyl methacrylate (GMA) to conjugate reactive vinyl groups, similar to previously published techniques [207]. An aqueous solution of HA at pH 9 (14.3mg/mL) was reacted with a 29-fold molar excess of GMA for 7 days at room temperature. The HA-GMA was purified by 2X precipitation in tetrahydrofuran (THF; Fisher Scientific, Hampton, NH), redissolved in DI water, frozen, and lyophilized. The degree of substitution (number of methacrylate groups per 100 disaccharide units) for HA-GMA dissolved in D_2O was determined by ^{1}H-NMR (Bruker Avance DRX-499).

7.2.3 Preparation of Protein-Loaded PLGA Microspheres

PLGA microspheres were fabricated using the ProLease^{TM} technique [223]. Briefly, BSA was micronized by spray freeze-drying a solution of 10mg/mL BSA and 2mg/mL trehalose in 5mM sodium succinate (pH 5). The micronized BSA/trehalose was suspended by ultrasonication at 11mg/mL in a methylene chloride (Fisher) solution containing 100mg/mL PLGA (inherent viscosity (I.V.) = 0.17 dL/g or 0.39 dL/g, Absorbable Polymers International, Pelham, AL) and was then sprayed through an ultrasonic nozzle to produce atomized droplets. These droplets were immediately collected in a liquid nitrogen bath to freeze the particles, and then the particles were allowed to enter a cold (-80°C) ethanol (AAPER, Shelbyville, KY) bath where the methylene chloride was extracted over several days to harden the microspheres. The microspheres were collected by filtration and dried. Protein content was determined by dissolving the microspheres in methylene chloride, centrifuging the insoluble protein, and dissolving the protein pellet in DI water. The amount of protein was quantified using a bicinchoninic acid (BCA) assay (Pierce, Rockford, IL).

7.2.4 Preparation of Cross-Linked HA-GMA Hydrogels with or without PLGA Microspheres

Hydrogels containing microspheres were formed by mixing equal volumes of a microsphere suspension (200mg/mL in DI water) and an HA-GMA solution (40mg/mL in DI water). The HA-GMA/microsphere suspension was mixed with a photo-initiator at a ratio of 10:1 (polymer:initiator). The photo-initiator, 2-hydroxy-1-[4-(hydroxyethoxy)phenyl]-2-methyl-1-propanone (Irgacure®2959 – Ciba, Tarrytown, NY), was dissolved at a concentration of 20mg/mL in methanol. Cross-linking was initiated by exposure to UV radiation (365nm) for 30 minutes. Gels were molded into cylinders by cross-linking in wells of multi-well plates. To measure protein release and microsphere morphology, 100μL hydrogels were fabricated in wells of a 96-well plate with a total loading of 10mg microspheres. HA hydrogels without microspheres were formed by diluting the 40mg/mL HA-GMA solution to 20mg/mL with DI water prior to the addition of the photo-initiator.

7.2.5 Protein Release from PLGA Microspheres

Microspheres were suspended at a concentration of 10mg/mL in DI water and placed at 37°C on a rotating shaker. At selected time points, the microspheres were pelleted by centrifugation, the release buffer was removed and replaced with fresh DI water, and the microspheres were resuspended. Protein in the release buffer was quantified using a BCA assay.

7.2.6 Protein Release from HA Hydrogels

HA hydrogels were frozen and lyophilized prior to rehydration in a solution of BSA (100μg BSA in 100μL DI water) or DI water (control). Hydrogels were allowed to swell for 2 hours at room temperature and then placed at 37°C in 12-well plates with 3mL DI water as the release buffer. At selected time points, the release buffer was

completely removed and replaced with fresh DI water. Protein concentration in the release buffer was quantified using a Coomassie Plus™ assay (Pierce).

7.2.7 Protein Release from PLGA Microspheres within HA Hydrogels

Hydrogels with or without PLGA microspheres were placed in Snapwell® inserts (Corning, Acton, MA) immediately after formation, and the inserts were glued to 6-well plates to prevent motion. The well was filled with 3mL DI water as a release buffer, and an additional 400μL DI water was added to the insert to equilibrate and swell the hydrogel. The samples were placed at 37°C, except during the time of imaging when they were at room temperature. Additional DI water was added to the wells at intermediate time points to compensate for evaporation of the release buffer from the wells. Further, a humidified chamber and plate sealers were used to reduce evaporation. The release buffer was completely removed and replaced after imaging at the selected time points. Protein concentration in the release buffer was quantified using a Coomassie Plus™ assay. Calculations of the amount of protein released were based on the actual amount of buffer retrieved from each well at each time point.

7.2.8 In Vitro OCT Imaging

For each imaging session, each 6-well plate was attached to the imaging stage in a fixed position and orientation. The starting x-y coordinates for each well were recorded during the first imaging session and used as reference for subsequent imaging sessions. Registration of the laser incident position was confirmed with reference ink marks on the imaging stage as well as on each plate. OCT imaging was performed with a light source having a center wavelength of 825nm and a spectral bandwidth of 150nm, and the axial resolution was about 2.8μm. 3-D scan series consisted of multiple 2-D cross-sectional images and were performed by scanning a 1mm wide cross-section, stepping 2.5μm between each adjacent 2-D scan. For each 2-D scan, the beam focus was stepwise tracked in the z-direction ten times in 40μm increments, starting from

the top surface of the hydrogels, and images within the focal zones were digitally combined to create in-focus cross-sectional images.

7.2.9 In Vivo OCT Imaging

A hydrogel with PLGA microspheres (25μL hydrogel with 0.75mg microspheres, formed as described above) was implanted in a modified rat calvarial critical size defect model and imaged using OCT. The surgical protocol was approved by the University of Washington (UW) Institutional Animal Care and Use Committee (IACUC) and was conducted under aseptic conditions using sterile materials. See section 8.2.4 for a detailed description of the surgical procedure. OCT imaging was performed on the anesthetized animal using the above *in vitro* imaging parameters. The animal was then sacrificed, and OCT imaging was repeated *post mortem.*

7.2.10 Image Processing and Analysis

Raw OCT intensity values were used to generate grayscale TIFF images for quantification. Multiple images with different focal regions were processed in MATLAB® (The Math Works, Natick, MA) to create composite in-focus images. The z-dimension was scaled by the index of refraction of the hydrogel (i.e., ~1.33). The 3-D image stacks were also re-sectioned and reconstructed using MATLAB®. Contrast enhancement using a linear mapping to 8-bit grayscale with background subtraction was performed on the images for display. The MetaMorph® Imaging System (Molecular Devices Corporation, Sunnyvale, CA) was used to measure microsphere diameters and to quantify the number of particles per volume. To determine the diameter of the microspheres, the circumference of an individual microsphere was traced in each cross-sectional image, and the greatest width was selected as the overall microsphere diameter. Incompletely sectioned microspheres that did not reach a maximum width in the image sequence were not measured or counted.

7.3 Results

7.3.1 Scaffold Fabrication

The presence of acrylate peaks at ~5.6 and ~6.1 ppm in the HA-GMA ^{1}H-NMR spectrum compared to the unmodified HA ^{1}H-NMR spectrum confirmed the functionalization of the HA (data not shown). The degree of substitution (number of methacrylate groups per 100 disaccharide units), which indicates the amount of potential cross-links that can be formed, was determined to be 17. It was calculated by taking ratios of the acrylate peaks, which arise from the methacrylate group only, and the methyl peak at 1.9 ppm, which includes protons from the methacrylate group and backbone methyl group. Hydrogels formed at 20mg/mL HA-GMA exhibited a swelling ratio of 88, which also indicates the extent of cross-linking. The swelling ratio was calculated as W_s/W_d where W_s is the wet weight of the hydrogel after equilibration in excess DI water and W_d is the dry weight of the hydrogel. The hydrogels were molded to swell to completely fill the Snapwell® inserts after equilibrating in DI water so that OCT imaging could be performed over nearly the same region at different time points. The hydrogel matrix remained intact for over 6 weeks during the study. By 10 weeks in DI water, the hydrogels began to exhibit dimensional instability and were partially collapsed or completely disintegrated so the imaging study was terminated.

7.3.2 Protein Release

The microspheres had a total protein content of 66μg BSA per mg microspheres. Two different molecular weights of 50:50 D,L-PLGA were used to control the protein release rate. As seen in Figure 7.1A, microspheres fabricated from a lower molecular weight PLGA (I.V. = 0.17 dL/g or approximately 12kDa) degraded faster and released protein faster than microspheres fabricated from a higher molecular weight PLGA (I.V. = 0.39 dL/g or approximately 40kDa). The 12kDa PLGA microspheres had a higher initial burst (74% of protein content) compared to the 40kDa PLGA

microspheres (9% of protein content). After the initial burst, the release rates of BSA were about the same for the first 3 weeks for both 12kDa and 40kDa PLGA microspheres (0.6μg BSA/mg microspheres/day). After 3 weeks, release from the 12kDa PLGA microspheres slowed to 0.2μg BSA/mg microspheres/day. By 6 weeks the total protein released reached a plateau, which was approximately 100% of the initial protein content. Release from the 40kDa PLGA microspheres continued at 0.6μg BSA/mg microspheres/day for 6 weeks before beginning to slow to 0.2μg BSA/mg microspheres/day. Release continued at this rate for at least 70 days.

A Bradford-based, Coomassie Plus^{TM} assay was used to quantify protein release from HA hydrogels because components that leached from the HA hydrogels interfered with the BCA assay. The release profile of BSA directly loaded in the HA hydrogel is shown in Figure 7.1B. Release of protein from the HA hydrogels is influenced by electrostatic interactions between the protein and HA, which are in turn affected by the pI of the protein and the pH of the release buffer. While the pI of BSA is low (5.75; Table 2.1, suggesting rapid release, the pH of the DI water used as the release buffer was approximately 5.5 and acted to slow release. When the microspheres were suspended within HA hydrogels and placed in the Snapwell® insert, the measured release of protein was slowed due to diffusion of protein through the hydrogel, electrostatic interactions between BSA and HA, and limitation of release to only the bottom surface of the cylindrical hydrogel through the Snapwell® membrane. However, the faster release of protein from the 12kDa PLGA microspheres relative to the 40kDa PLGA microspheres was again observed. As seen in Figure 7.1C, both formulations had an initial lag before beginning to release protein — 14 days for the 12kDa PLGA microspheres within the HA hydrogels and 21 days for the 40kDa PLGA microspheres within the HA hydrogels. After this lag, the 12kDA PLGA microspheres within the HA hydrogels released protein at a rate of 0.3μg/mg microspheres/day for 6 weeks and then slowed to 0.05μg/mg microspheres/day. The 40kDa PLGA microspheres within the HA hydrogels released protein steadily at a rate of 0.1μg/mg microspheres/day

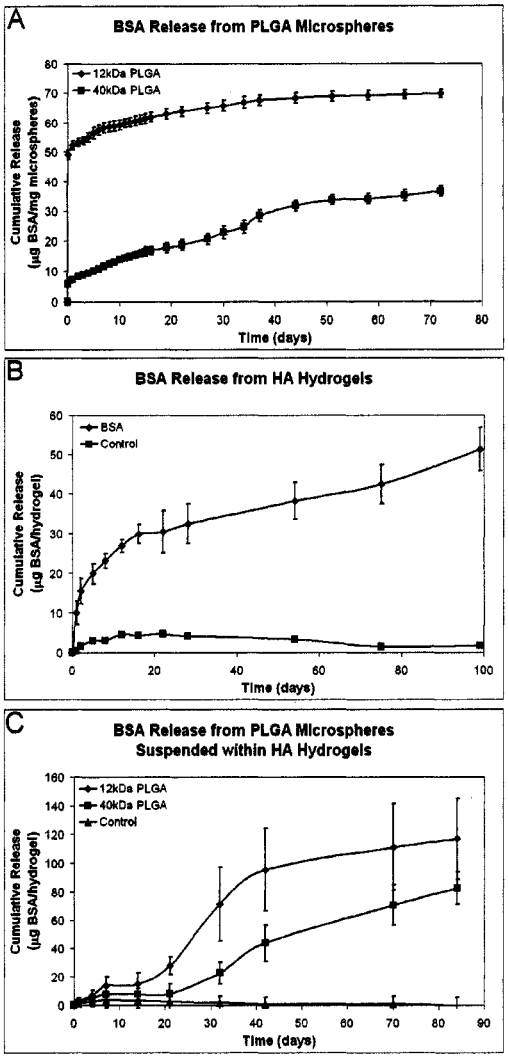

Figure 7.1: Release of BSA from various constructs. (A) Cumulative BSA release (measured by BCA assay) from microspheres made with two different molecular weights of PLGA (12kDa and 40kDa). The microspheres contained 66μg BSA per mg of microspheres. Microspheres were suspended at a concentration of 10mg/mL in DI water at 37°C with shaking. (B) Release of BSA (measured by Coomassie Plus^{TM} assay) from HA hydrogels loaded with 100μg BSA. Control hydrogels contained no protein. The hydrogels were placed at 37°C in 3mL DI water as release buffer. (C) Release of BSA (measured by Coomassie Plus^{TM} assay) from microspheres, as in (A), suspended within HA hydrogels. Control hydrogels contained no microspheres. The scaffolds were suspended in Snapwell® inserts with 3mL DI water as release buffer and were placed at 37°C. Results are shown as mean and standard error from triplicate samples.

after the initial lag for the duration of the entire measurement period.

7.3.3 OCT Imaging and Initial Microsphere Morphology

OCT images of control and microsphere-loaded HA hydrogels were successfully obtained. Composite in-focus cross-sectional images were digitally prepared in a way similar to ultrasound C-mode imaging. As seen in Figure 7.2, OCT images of control HA hydrogels without microspheres confirmed that the hydrogels were optically transparent. Besides a dark line due to the reflection from the surface of the hydrogel (i.e., the air-hydrogel interface), no structures were visible in these images, even with contrast enhancement. OCT images of HA hydrogels with 12kDa or 40kDa PLGA microspheres both showed the presence of particulates embedded within the hydrogel (Figure 7.2, Day 1). At early time points, these particles were solid with a graded intensity. The reduced intensity at the bottom end of each particle is consistent with loss of the incident light's power deeper within the nontransparent material. Particles located further down within the hydrogels, beneath other particles, also appeared lower in intensity. The particles themselves were oval-shaped with a greater height than width. This lengthening of the particles in the z-dimension is resultant from the mismatch in index of refraction between the PLGA microspheres and the hydrated HA hydrogel. When converting the raw OCT data to TIFF image format, the images were digitally rescaled in the z-dimension using the index of refraction of the HA hydrogel, which was experimentally measured at 1.33 and is similar to that of water. Assuming the particles to be truly spherical, the index of refraction of the PLGA microspheres could be calculated by taking the ratio of the height to width of the particles within the OCT images. The average ratio of height-to-width was measured to be 1.25 for the 12kDa PLGA microspheres and 1.14 for the 40kDa PLGA microspheres at Day 1. Correcting for the original scaling factor (n=1.33), this would result in a measured index of refraction of 1.51 to 1.67 for PLGA. This refractive index is consistent with that reported for other polymers, such as polystyrene (n=1.57

to 1.61) [303] or a different polyester (n=1.54) [304]. Additionally, re-sectioning of the 3-D scan series in the XY plane (or the horizontal plane), which should not be affected by the index of refraction, confirmed that these particles initially appeared spherical (Figure 7.3). The 3-D scan data were also used to obtain a measure of the overall diameter for each microsphere. The width of each slice through an individual microsphere was measured in each cross-sectional image, and the greatest width was selected as the overall microsphere diameter. The average microsphere diameter was thus determined to be 26±10μm for the 12kDa PLGA microspheres and 30±12μm for the 40kDa PLGA microspheres at Day 1. Since the microspheres were fabricated using similar conditions, it was expected that they would be about the same size prior to degradation.

7.3.4 Temporal Characterization of Morphological Changes

Images from a 1000μm x 200μm x 50μm region of a hydrogel with either 12kDa or 40kDa PLGA microspheres were analyzed at each time point. Only particles that were greater than 50% contained within the region (i.e., reached maximum diameter) were included in the analysis for particle counts as well as refractive index and diameter measurements. Qualitative assessment of the OCT images showed morphological changes of the microspheres with time, which was particularly apparent in the 12kDa PLGA samples (Figure 7.2). No changes occurred in the control samples, which remained completely free of any structures for the 6 weeks of imaging. By 10 weeks, all hydrogels had begun to degrade, and all images had a reduced height between the top surface of the hydrogel and the supporting membrane or had no visible hydrogel. The ratio of particle height-to-width remained fairly constant throughout the study (Figure 7.4A), which indicates that the calculated refractive index is not changing with time. Measurement of microsphere diameter, as described above, showed that both samples had a trend of decreasing particle size with time. As seen in Figure 7.4B, the average particle size of the microspheres remained approximately the same or slightly

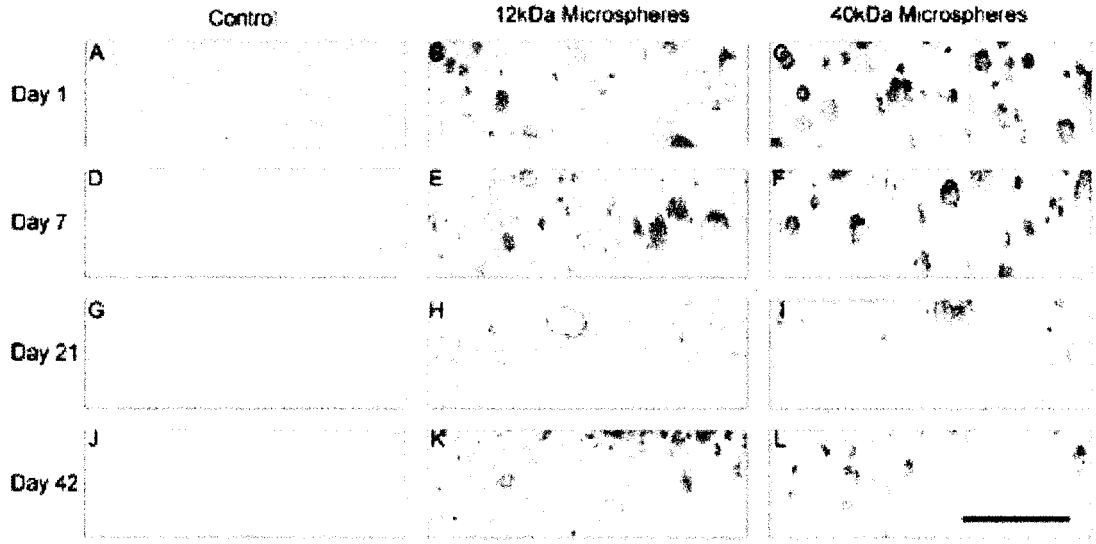

Figure 7.2: Temporal sequence of OCT images of degrading PLGA microspheres. High resolution OCT images of PLGA microspheres within HA hydrogels at different times during the release study. Approximately the same region of the hydrogel was imaged at each time point by fixing the plate in the same location on the stage and aligning the beam to reference points on the stage and plate. Images show a small region selected directly beneath the top surface of the hydrogel, which was visible as a dark line running horizontally across the image. (A, D, G, J) Control HA hydrogels. (B, E, H, K) HA hydrogels with 12kDa PLGA microspheres. (C, F, I, L) HA hydrogels with 40kDa PLGA microspheres. (A-C) Day 1. (D-F) Day 7. (G-I) Day 21. (J-L) Day 42. The scale bar represents 200μm.

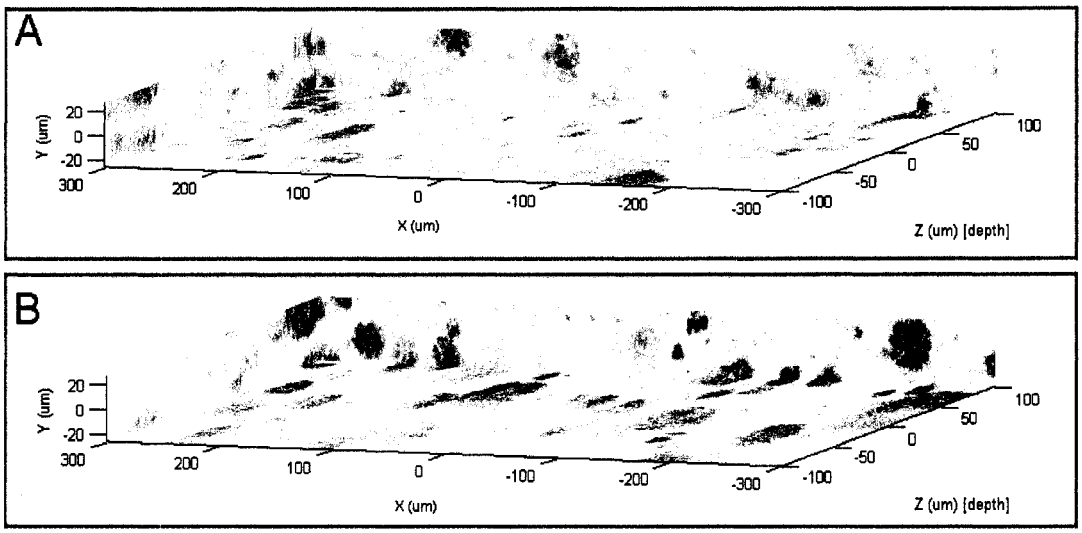

Figure 7.3: 3-D reconstruction of high resolution OCT images of PLGA microspheres within HA hydrogels. (A) 12kDa PLGA microspheres in HA hydrogel at Day 1. (B) 40kDa PLGA microspheres in HA hydrogel at Day 1.

increased for 2 weeks before beginning to decrease. In images of hydrogels with the 40kDa PLGA microspheres, the particle cross-sections also predominantly remained solid throughout the course of the experiment (Figure 7.4D). The images of hydrogels with the 12kDa PLGA microspheres initially contained particles that looked similar to those in the 40kDa PLGA samples. With contrast enhancement, the background in the 12kDa PLGA microsphere images was more uneven, with the appearance of smaller particulates (not included in the measurements) that persisted for the duration of the study. At later time points, some of the 12kDa PLGA microsphere cross-sections developed a ring-like appearance (example seen in Figure 7.2H). These hollow structures, which increased in number with time (Figure 7.4D), could indicate that the core of the 12kDa PLGA microspheres had degraded and dissolved away, leaving just the outer shell.

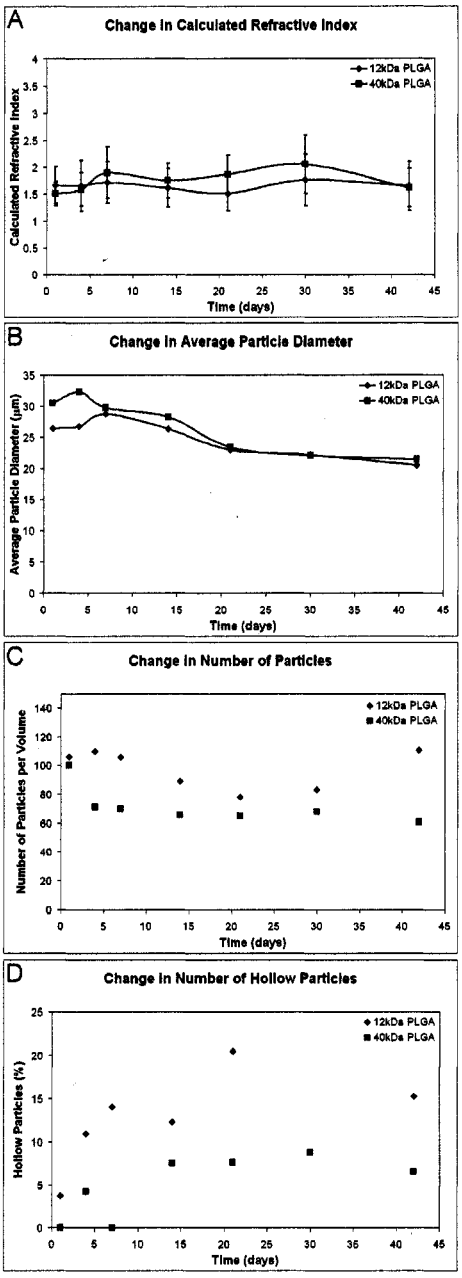

Figure 7.4: Morphological characterization of low and high molecular weight PLGA microspheres suspended within HA hydrogels as a function of time. Measurements taken for particles within a 1000μm x 200μm x 50μm region in the 3-D OCT image stack. (A) Calculated refractive index. (B) Average particle diameter. (C) Total particle count per measured volume. (D) Hollow particle count per measured volume.

7.3.5 In Vivo OCT Imaging

The surgical procedure for attachment of the "window chamber" over the critical size defect was successful. During live animal imaging, significant distortion of the image occurred due to breathing and heartbeat. Holding the rat's head with ear bars in a modified stereotactic frame was able to significantly reduce (although not completely eliminate) this motion artifact. The rat was imaged again immediately after sacrifice, and representative post mortem images of a microsphere-loaded hydrogel in the defect are shown in Figure 7.5. The microspheres are clearly visible in the hydrogel, which is approximately 0.9mm thick. The cover slip, which is made of plastic, appears as a region of high contrast at the top of the image. Within the hydrogel scaffold region, particles similar to those seen *in vitro* could be observed. In images obtained by stepping the focal zone down through the implant (Figure 7.5B and 7.5C), these particles were also shown to be solid with an oval cross-section, again resulting from the refractive index mismatch between the PLGA microsphere and HA hydrogel. The particles were evenly distributed throughout the depth of the hydrogel. A darker line, about 100μm thick, ran beneath the implant and can be clearly seen in Figure 7.5C. This structure is consistent in size and location with the *dura mater*, the thin membrane that runs between the parietal bones and the brain. This demonstrates that OCT was able to image through the full thickness of the implant within the defect.

7.4 Discussion and Conclusion

Degradable microspheres provide a means for controlled release of encapsulated proteins (or drugs) and allow therapeutic dosing to be maintained over an extended period of time from a single administration. Recently, techniques to embed microspheres within a scaffold matrix have been developed [226, 305, 221, 230]. These composite scaffolds offer altered protein release profiles compared to microspheres alone,

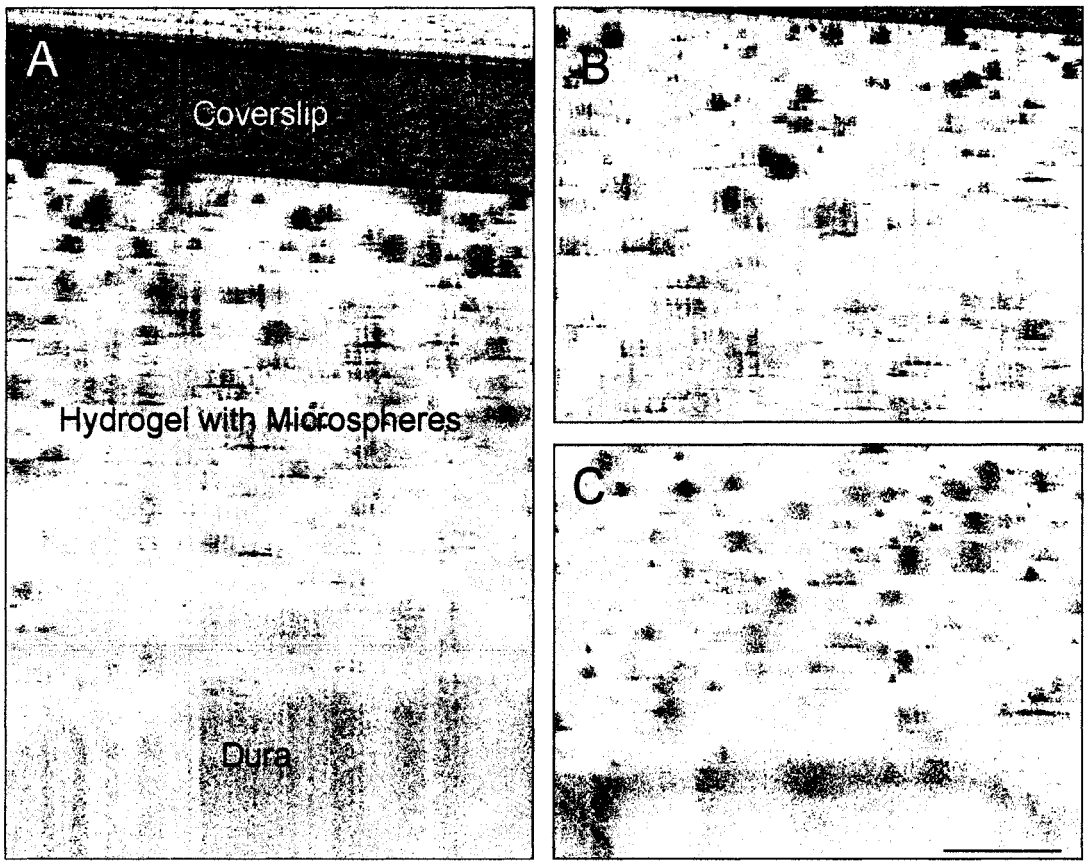

Figure 7.5: High resolution OCT images of scaffold in rat calvarial defect after sacrifice. OCT was able to penetrate through entire scaffold and image to the *dura mater*. Microspheres within the scaffold appear as dark shapes on a light background. (A) 2mm depth scan showing plastic coverslip through *dura*. (B) In-focus image of top half of implant, showing part of the plastic coverslip at top. (C) In-focus image of bottom half of implant, showing *dura* at bottom. The scale bar represents 200μm.

extended release of protein compared to protein directly loaded into the scaffold matrix, and better retention of the microspheres within an implant site. Characterization of composite scaffold performance, however, has been limited to traditional techniques used with degradable implants, namely *in vitro* protein release testing, monitoring of scaffold morphology by destructive examination such as SEM, and measuring therapeutic endpoints *in vivo*. This study reports the first use of the noninvasive imaging technique, OCT, to follow temporal changes in scaffold morphology *in situ*. These morphological changes were further compared to measurements of protein release from the scaffolds, which is indicative of their therapeutic potential. Whereas the focus of this correlation was an *in vitro* study, the potential to extend these results to *in vivo* monitoring of scaffold performance was demonstrated by the addition of a "window chamber" to the rat calvarial critical size defect model.

Protein release from the microspheres embedded within the hydrogels (Figure 7.1C) was slower than protein release from the hydrogels alone (Figure 7.1B), which is expected and further supported by other studies [221]. Compared to an aqueous suspension of microspheres (Figure 7.1A), suspending the microspheres within the hydrogel matrix slowed the overall rate of protein release and reduced the initial burst release (Figure 7.1C). While the measured rate of protein release was artificially reduced by suspending the samples within a Snapwell® insert, the observed changes in the release profile are supported by the results of others who have examined protein release from a microsphere-embedded hydrogel system [305]. The slower release of BSA from the HA hydrogels compared to that reported for similar hydrogel systems [221] is likely due to interactions between the BSA and HA that are affected by the pI of the protein and pH of the release buffer. Using a release buffer with a higher pH accelerated the release of BSA from HA hydrogels (data not shown).

Two different molecular weights of PLGA were selected that degrade at different rates, thus providing differing release kinetics with all other formulation parameters remaining the same. Since the 12kDa PLGA microspheres released 100% of the

protein loaded by 5 weeks when placed in aqueous suspension, it was expected that these microspheres would have undergone significant degradation during the course of the OCT imaging. Conversely, since the 40kDa PLGA microspheres released only approximately 50% of the protein loaded after 10 weeks in suspension, it was expected that these microspheres might still be fairly intact. These expectations were met in the temporal sequence of OCT images (Figure 7.2). The initial solid morphology of the particles in the OCT images may likely be due to the heterogeneous nature of the microspheres, which contain particulates of protein/trehalose within the PLGA matrix, potentially resulting in a refractive index mismatch throughout the particle. The initial slight increase in particle size for the microspheres could be a result of particle swelling upon hydration.

Quantitatively, the 12kDa PLGA microspheres within the HA hydrogels showed a 23% decrease in average microsphere diameter over 6 weeks as well as an increase in the number of measurable particles per volume at the last time point (Figure 7.4C). This suggests that the 12kDa PLGA microspheres are breaking down over the time course of the experiment. More importantly, the 12kDa PLGA images also showed the presence of hollow particles, which increased in number at later time points (Figure 7.4D). The hollow morphology indicates that there is no refractive index mismatch within the core once the polymer is degraded and cleared and protein is released. This hollow morphology is consistent with faster polymer degradation within the core of the microsphere followed by dissolution and clearing of the lower molecular weight fragments, which was also observed in SEM studies by Visscher *et al* [300, 301, 302]. There was also a smaller particulate seen in the background of the contrast-enhanced images that could be associated with smaller pieces of PLGA dissociating from the faster degrading 12kDa PLGA microspheres. When measuring the particle diameters, the 40kDa PLGA microspheres within the HA hydrogels also decreased in size; however, they remained fairly constant in number with time (Figure 7.4C). The particle cross-sections remained solid and did not change much in appearance,

suggesting that they had not yet reached the point of dissolution of small molecular weight fragments within the core.

The clear morphological differences observed between the two microsphere types as well as changes observed over time suggest that OCT may be a useful imaging technique for more sophisticated characterization of microsphere degradation. With careful registration, OCT could be used to track changes in the morphology of individual particles with time. This would offer advantages over techniques which monitor the degradation of the microspheres in bulk or that analyze different samples at each time point by destructive measurement methods. It would further provide the potential for analysis of the effect of particle size on degradation rate without the need to separate and group samples into particle size ranges before characterization and analysis. More importantly, OCT could be used to characterize microsphere degradation *in vivo*. By comparing morphological changes *in vivo* to those *in vitro*, it may indicate if the measured *in vitro* release profiles are actually predictive of those *in vivo*. This would give a more realistic measure of the controlled release properties and degradability of the microspheres in their true therapeutic setting. The novel "window chamber" modification to the critical size defect model also provides an opportunity for repeated imaging of the healing defect over time in the same animal. In addition to changes in scaffold morphology, tissue regeneration can be observed, as has been seen with HA hydrogel scaffolds loaded directly with growth factors (see Chapter 8). A major limitation of OCT images taken of live animals is the motion artifact due to breathing and heartbeat; however, this can be further minimized by a faster acquisition rate and by post-processing of the images with a cross-correlation routine in addition to the use of stabilizing ear bars. High speed OCT is becoming available for *in vivo* imaging with speed increases by more than a factor of 100–300. A secondary limitation observed in the *in vivo* images in this study is the distortion of some of the particles that are located beneath defects in the cover slip. This can be reduced by using a glass (rather than a plastic) cover slip, which will be opti-

cally transparent. Overall, this study demonstrates the potential of OCT for *in situ* temporal characterization of changes in scaffold morphology and develops an animal model that could be used to extend this characterization to measure *in vivo* scaffold performance.

Chapter 8

OPTICAL COHERENCE TOMOGRAPHY FOR TEMPORAL CHARACTERIZATION OF BONE REGENERATION INDUCED BY ANGIOGENIC AND OSTEOINDUCTIVE HYDROGEL SCAFFOLDS

8.1 Introduction

This Chapter addresses a major limitation in the field of regenerative medicine — the ability to monitor tissue regeneration *in situ*. Current analytical techniques, such as histology, require harvesting and destructive analysis of the tissues to evaluate a response. One technique that can noninvasively monitor repair processes in a living animal is optical coherence tomography (OCT), which is described in further detail in Chapters 2.11 and 7.

In this study, OCT will be used to characterize morphological changes during the temporal progression of bone regeneration and angiogenesis in a rat calvarial critical size defect model. Tissue healing will be induced using the degradable hyaluronic acid (HA) hydrogels described in Chapters 3 through 5 to provide controlled release of angiogenic and osteoinductive molecules. Defects greater than the critical size, which is 5mm in an adult rat [274], will not heal spontaneously, thus providing a means to evaluate an implant's ability to improve bone healing. In this study, a custom-designed "window chamber" will be used in a novel modification of the critical size defect model to allow noninvasive imaging using OCT at different time points. The "window chamber" has two purposes: the cover glass allows OCT imaging of the defect site while the stainless steel chamber prevents closure of the skin over the defect site.

As previously described, OCT has been used to image many types of tissue. This study is the first to report the use of OCT to image regenerating bone, although it has previously been used to image bone structure in the process of imaging cartilage morphological features. OCT images were used to score the degeneration of the cartilage/bone interface during osteoarthritis [306] and to examine the bone/cartilage interface after chondrocyte implantation into a cartilage defect [269]. Calvarial bone morphology was further obtained during *ex vivo* imaging experiments to measure the attenuation coefficient of periosteal tissue [307]. OCT has also been used to image bone tissue engineering constructs [266, 268]; however, these scaffolds were only evaluated after culturing *in vitro*. This study is also the first to utilize OCT for imaging of angiogenic blood vessels *in vivo*. This extends the range of OCT for vascular applications, as it has previously be shown to be able to image arterial wall microstructure [270], *in vitro* tissue engineered blood vessels [271], and subcutaneous blood vessels [272].

8.2 Materials and Methods

8.2.1 Materials

All reagents were obtained from Sigma-Aldrich (St. Louis, MO) unless otherwise noted. All solvents were of reagent grade.

8.2.2 Preparation of Glycidyl Methacrylate Modified Hyaluronic Acid (HA-GMA)

HA (~220,000 Da, Lifecore, Chaska, MN) was modified with glycidyl methacrylate (GMA) to conjugate reactive vinyl groups, similar to previously published techniques [207, 281]. An aqueous solution of HA (14.3mg/mL) at pH 9 was reacted with a 29-fold molar excess of GMA for 7 days at room temperature, and then the reaction mixture was neutralized with 1N HCl (VWR, West Chester, PA). The HA-GMA was purified by 2X precipitation in tetrahydrofuran, dissolved in DI water, frozen, and

lyophilized. The degree of substitution was determined by ^{1}H-NMR on a Bruker (Billerica, MA) Avance DRX series instrument at a frequency of 499.85 MHz. The degree of substitution (DS; number of methacrylate groups per 100 disaccharide units) was calculated from the ^{1}H-NMR spectra by taking ratios of the acrylate peaks at ~5.6 and ~6.1 ppm, which arise from the methacrylate group only, and the methyl peak at 1.9 ppm, which includes protons from the methacrylate group and backbone methyl group.

8.2.3 Preparation of Cross-Linked HA-GMA Hydrogels

Hydrogels were prepared under aseptic conditions using sterile supplies. All solutions were either sterile as supplied or were sterile filtered using a 0.2μm syringe filter. To form the hydrogels, HA-GMA (20mg/mL in DI water) was mixed with a photo-initiator in a ratio of 10:1 (polymer: initiator). The photo-initiator, 2-hydroxy-1-[4-(hydroxyethoxy)phenyl]-2-methyl-1-propanone (Irgacure®2959 – Ciba, Tarrytown, NY), was dissolved at a concentration of 20mg/mL in methanol. Cross-linking was initiated by exposure to UV irradiation (365nm) for 30 minutes. Disk-shaped implants were formed by cross-linking the HA-GMA in 5mm diameter Teflon molds sandwiched between two glass coverslips. These disks were rinsed in PBS, pH 7.4, at room temperature overnight, and then frozen and lyophilized. Dried hydrogels were rehydrated with (a) 35μL PBS only as a control, (b) 35μL PBS with 5μg bone morphogenetic protein (BMP)-2 (R&D Systems, Minneapolis, MN), (c) 35μL 5mM sodium succinate buffer, pH 5.0, with 5μg vascular endothelial growth factor (VEGF; Genentech, South San Francisco, CA), or (d) 35μL 5mM sodium succinate buffer, pH 5.0, with 25μg VEGF. The hydrogels were allowed to swell in protein solution for at least 2 hours prior to implantation.

8.2.4 "Window Chamber" Defect Surgery Protocol

HA hydrogels were implanted in a rat calvarial critical size defect model, which was modified with a "window chamber" to allow OCT imaging (Figure 8.1). The surgical protocol was approved by the University of Washington (UW) Institutional Animal Care and Use Committee (IACUC). Surgeries were performed following aseptic technique. Adult male Sprague Dawley rats (Harlan, Indianapolis, IN) were anesthetized using isoflurane (5% induce, 2.5% maintain), and their heads were shaved and disinfected. Buprenorphine was administered immediately pre-operatively for pain mitigation. A linear incision was made along the midline of the scalp, and the soft tissues, including the periosteum, were reflected. A full-thickness 5mm circular defect was created in the center of the parietal bones (over the sagittal suture) using a Command2 drill system with a 1.0mm fissure carbide bur (Stryker, Kalamazoo, MI) while irrigating with saline. A hydrogel scaffold was placed in the defect, and the defect region was then covered with a custom-designed "window chamber". The "window chamber" was an 8mm ID stainless steel cylinder with a glass coverslip at the bottom to create an imaging window. The chamber was 3mm tall to prevent closure of the skin over the defect site. The chamber was affixed to the skull using miniature screws (Small Parts, Miami Lakes, FL) and Jet dental acrylic (Lang Dental, Wheeling, IL). The animals were allowed to wake up and recover for at least one week prior to commencing OCT imaging.

8.2.5 In Vivo OCT Imaging

The animals were anesthetized using isoflurane (5% induce, 2.5% maintain) and held in place using a modified stereotactic frame. Animals were imaged at most once per week for approximately one hour per imaging session. OCT imaging was performed using a 7-fs pulsed Ti:sapphire laser with a center wavelength of 825nm, a spectral bandwidth of 150nm, and an axial resolution of 2.6μm. 1mm x 0.8mm cross-sectional

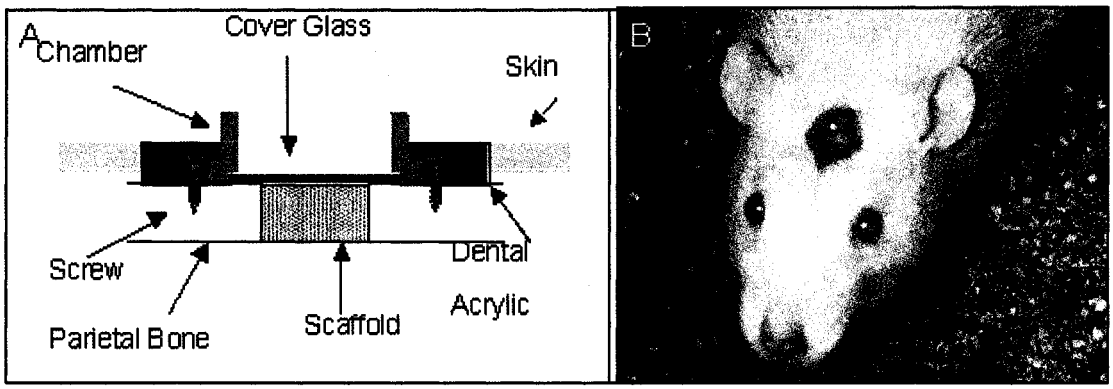

Figure 8.1: Window chamber" calvarial defect model. (A) Cross-sectional schematic of defect model. A full-thickness defect in the bone is filled with the scaffold. The chamber made of stainless steel prevents closure of the skin over the area of interest while the coverglass both protects the defect site and provides an optically transparent window for imaging. (B) Rat with "window chamber" implant for *in situ* OCT imaging after several weeks of healing.

scans were obtained at a frame rate of approximately 0.08Hz. The focus was stepped in 40-100μm increments in the z-direction. 3-D scan series were performed by stepping 2.5μm between cross-sections. Cross-sectional images across the full 8mm diameter of the viewing window were obtained by scanning in 1mm increments along the greatest diameter of the chamber.

8.2.6 Image Processing and Analysis

Multiple images with different focal regions were processed in MATLAB® (The Math Works, Natick, MA) to create composite in-focus images. The z-dimension was scaled by the index of refraction of tissue (1.3). After background subtraction, contrast enhancement using a linear mapping to 8-bit grayscale or copper colormap was performed on the images for display. These composite images were manually fused in Photoshop (Adobe, San Jose, CA) to create complete (8mm) cross-sectional images. A cross-correlation routine was applied to suppress motion artifacts in some images.

The MetaMorph® Imaging System (Molecular Devices Corporation, Sunnyvale, CA) was used to re-section the 3-D image stacks.

8.2.7 Tissue Harvest and Analysis of Mineralization

Rats were sacrificed at selected time points using carbon dioxide (CO_2 asphyxiation. The "window chamber" was removed, and the parietal bones containing the defect region were harvested and fixed for 24 hours in 10% neutral buffered formalin (Fisher Scientific, Hampton, NH). To quantify mineralization, X-rays or microcomputed tomography (microCT) scans were performed on the bone pieces. X-rays were performed using X-Omat AR film (Kodak, Rochester, NY) in an enclosed X-ray unit (Picker X-ray Corporation, Cleveland, OH) with a distance of 64cm, voltage of 35 Kvp, current of 5mA, and exposure time of 5 seconds. Developed X-ray films were scanned into digital format and X-ray intensity was quantified using MetaMorph®. For microCT analysis, scans were performed by Philippe Huber and Ted Gross at Harborview Medical Center (Seattle, WA) with a *viva*CT 40 (Scanco Medical, Bassersdorf, Switzerland). Scans were conducted using a voltage of 55 kVp, current of 145μA, and voxel size of 30μm. Images were reconstructed and analyzed using segmentation parameters of sigma = 1.2, support = 2, and threshold = 250.

8.2.8 Ex Vivo OCT Imaging

The parietal bones were imaged again after harvest (*ex vivo*). The bone pieces were marked on either side of the defect with an ink that would be visible in both OCT images and histology sections. OCT imaging and image processing were performed as described above with the following modifications. The focus was stepped in 400μm increments in the z-direction. 3-D scan series were performed by stepping 10μm between cross-sections. Cross-sectional images across the full diameter of the defect were obtained by scanning in 1mm increments between the ink marks. Imaging was performed on both the top (periosteal) and bottom (dural) sides of the bone.

8.2.9 Histology and Immunohistochemistry

After quantifying mineralization, the samples were decalcified in a 10% EDTA solution at pH 7 for 2 weeks. The decalcified tissue was embedded in paraffin and sectioned into 5μm thick sections for histology. Tissue sections were stained with hematoxylin and eosin (H&E) or Masson's trichrome for qualitative analysis. Immunohistochemistry using antibodies for bone sialoprotein (BSP; Chemicon, Temecula, CA), vonWillebrand factor (vWF; DakoCytomation, Carpinteria, CA), or Rat Endothelial Cell Antigen (RECA)-1 (Abcam, Cambridge, MA) was also performed. Antigen retrieval was performed by incubating the tissue sections in 10mM Tris/1mM EDTA, pH 9, at 95-99°C for 20 min; in 2mg/mL hyaluronidase in PBS at 37°C for 30 min; and in 20μg/mL Proteinase K (Invitrogen, South San Francisco, CA) in 50mM Tris/1mM EDTA, pH 8, at room temperature for 10 min. The primary antibodies were detected using the Histostain®-SAP Kit (Invitrogen).

8.3 Results

8.3.1 Surgical Procedure

A total of 37 surgeries were performed. Three animals had the "window chamber" fall off and were sacrificed. At minimum for each implant group, animals were sacrificed at a 6-week time point (n=3) as well as at intermediate time points of 2 weeks (n=1) and 4 weeks (n=1). The 6-week time point samples were evaluated for extent of mineralization by X-ray and/or microCT and then were decalcified and sectioned for histology. The earlier time points were utilized for comparison of histology sections with the OCT images taken at intermediate time points. A number of animals demonstrated cloudiness under part of the window "chamber", particularly near the edges of the chamber and at later time points. The cloudiness was likely due to skin closure into gaps between the chamber or acrylic and the bone. Further, an exudate consistent with a slight topical infection also contributed to the cloudiness. Care was

taken to avoid imaging these regions as the cloudiness obscured the tissue below. No signs of systemic infection were observed in any of the animals.

8.3.2 In Vivo Bone Regeneration

Quantification of mineralization using X-ray intensity and microCT analysis showed that HA hydrogel scaffolds loaded with 5μg BMP-2 resulted in significant mineralization ($p<0.05$ for X-ray; $p=0.075$ for microCT) compared to control hydrogels after 6 weeks of healing (Figure 8.2). The earliest time points evaluated for each treatment group had less mineralization than the 6-week time point; however, a statistically significant temporal progression of mineralization could not be confirmed due to the limited sample numbers at the earlier time points (data not shown). Histological sections stained with Masson's trichrome showed complete bridging of the defect in animals receiving the BMP-2 implants, which had dark blue staining indicative of the dense collagen in bone (Figure 8.3). By the 6-week time point, the new bone also matched the full thickness of the original parietal bones across the entire defect. While new bone filled the entire width and depth of the defect, this bone was less organized than the lamellar bone seen in the intact bone at the margins of the defect. This is consistent with reduced mineralization (indicated by reduced X-ray intensity) induced by BMP-2 in the defect site compared to native bone at adjacent locations. At earlier time points, the bone exhibited a pattern of bone growth in from the defect margins and up from the *dura mater*. At two weeks, a thin layer of bone completely bridged the bottom of the defect. This layer seemed to thicken with time until it completely filled the defect region. Minimal bone growth was limited to the margins of the VEGF and control samples, even after 6 weeks (Figure 8.3). This bone appeared to have well-organized collagen, indicated by dark blue staining in the Masson's trichrome samples; however, this bone region extended for less than 1mm from the original bone edge for both the control, 5μg VEGF, and 25μg VEGF samples. The remaining defect region appeared to be filled with a loose connective

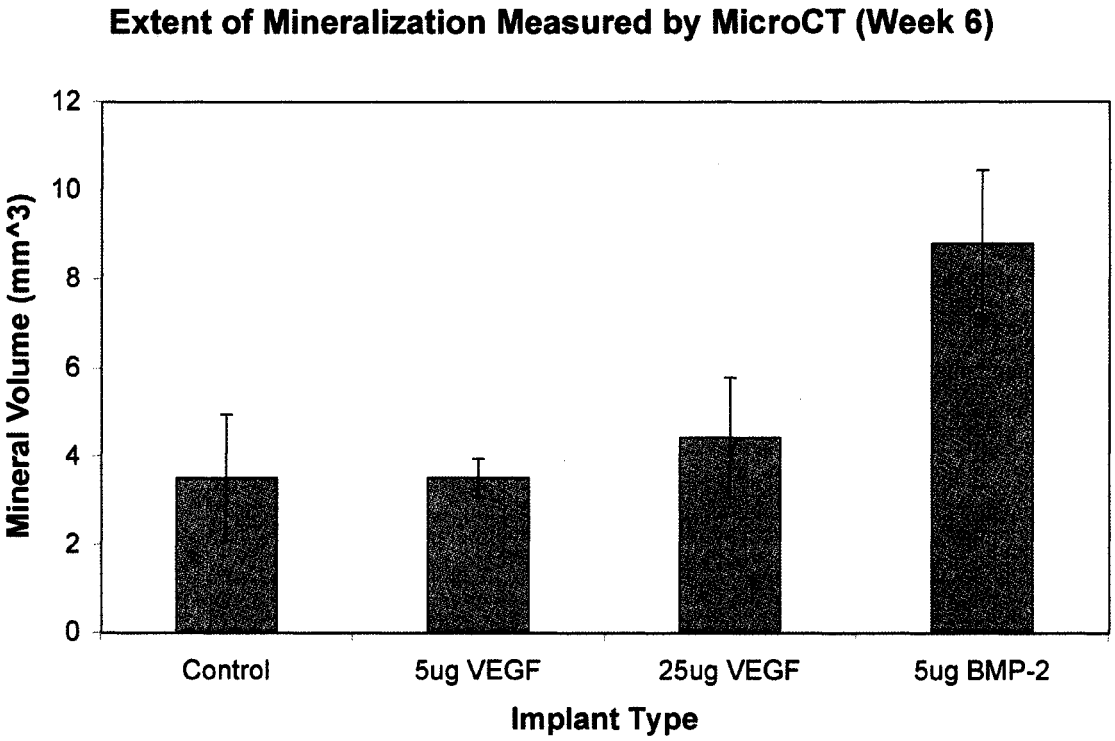

Figure 8.2: Quantification of mineralization for different treatment groups using microCT. Mineral volume was determined for a 5mm diameter x 1mm tall cylinder centered within the defect region. Results are shown as mean and standard deviation of triplicate samples.

tissue with less dense collagen (light blue stain).

8.3.3 In Situ Imaging of Defect Healing over Time

For all treatment groups at the earliest time point of imaging, a clear region consistent with the size of the defect (5mm diameter) could be observed. This region was considered to be the hydrogel, which was confirmed to be optically transparent during *in vitro* imaging (see Chapter 7). The defect edge was defined as the region of high signal intensity at the edge of this clear region. An additional region of high signal intensity was also seen running along the bottom of the defect, which is consistent

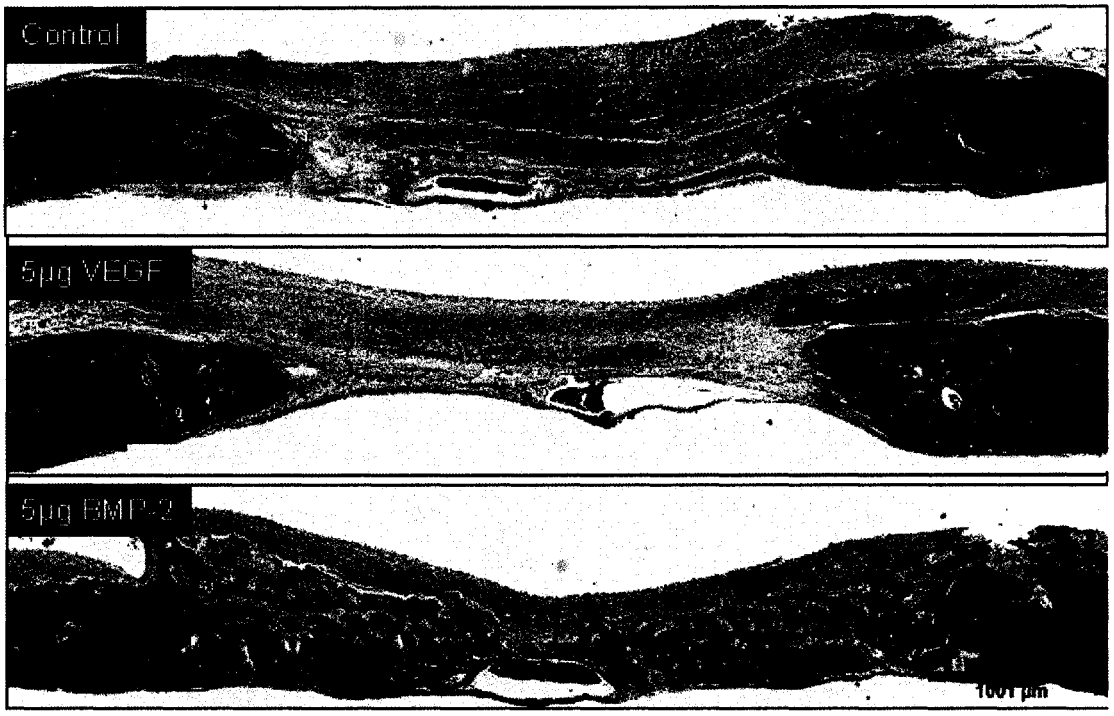

Figure 8.3: Representative histology sections. Week 6 samples were stained with Massons trichrome, where bone is dark blue. Arrows indicate original defect margins.

with the *dura mater* forming the lower boundary of the defect. Cross-sectional OCT images of the entire defect region with the 5μg BMP-2 hydrogel implant taken from the same animal over time showed a clear migration of the defect edge towards the center of the defect over time as well as an overall shrinkage in the height of the defect region (Figure 8.4). This pattern was seen in the temporal series of OCT images taken for several animals receiving the BMP-2 implants. The pattern of growth in from the bone edge and up from the dura mater is expected because osteoblast progenitor cells found in the perivascular connective tissues of the *dura* [275] can be induced to migrate up and differentiate in addition to the osteoblasts found in the bone at the margins of the defect migrating in. The OCT images also agreed with qualitative comparison to histology sections from animals sacrificed at the intermediate time points. In the histology sections, it was noted that the hydrogel scaffold appeared to be replaced by a loose network of collagen (light blue stain) and cells within the defect site. It is likely that this tissue is not scattering enough to generate an OCT signal until the density of the cells, collagen, or mineral is high enough, for example at the regenerating defect edge. To further probe the tissue architecture at the defect edge, a cross-correlation routine was applied to remove the motion artifact from individual OCT images (Figure 8.5). These OCT images showed a region of high signal intensity that extended for a hundred to a few hundred microns at the regenerating defect edge followed by a drop-off in signal intensity. In Figure 8.5, this region of high signal intensity is approximately 100μm thick. The decrease in signal intensity below this region could be due to mineralization of the growing tissue or to organization of the collagen into a denser, well-ordered matrix, indicating the formation of bone. The morphology of the tissue in this area of weaker signal intensity was similar to morphology seen in images of intact bone taken *in vivo* and *ex vivo* (data not shown).

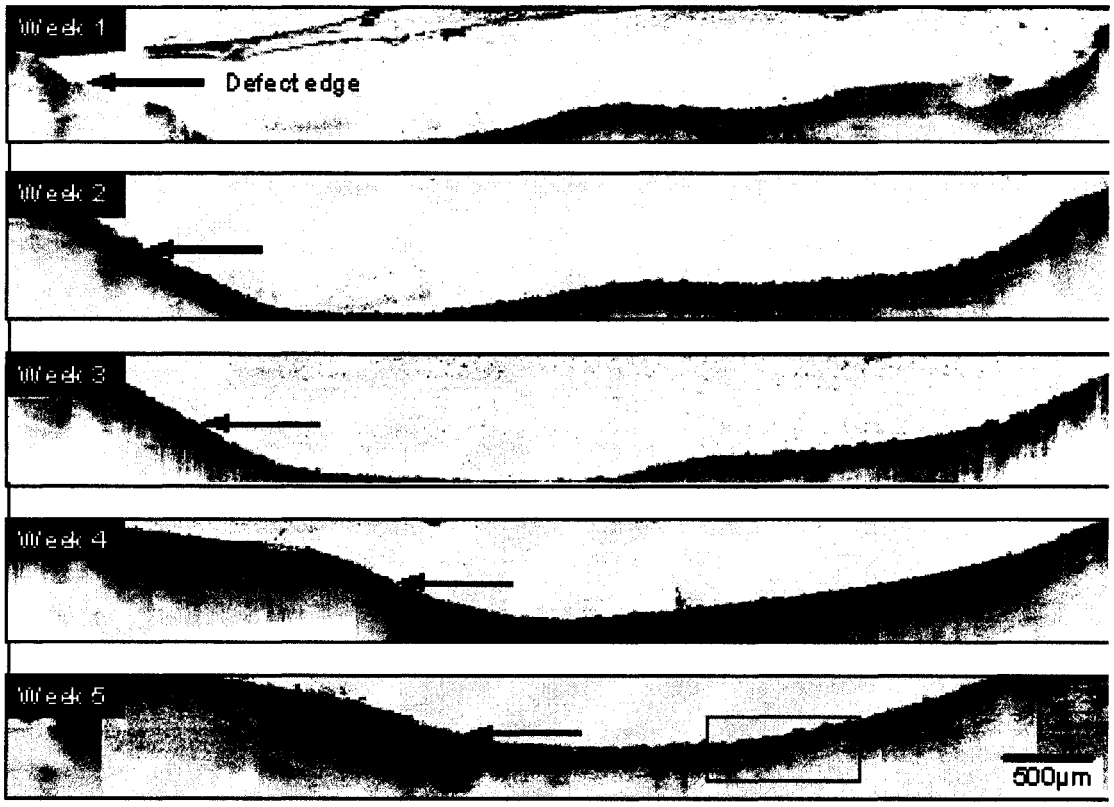

Figure 8.4: Cross-sectional OCT images of the entire defect region with 5μg BMP-2 hydrogel implant. Images are from the same animal over time. Arrows indicate the defect edge, which migrates inward and upward over time. The top of each panel is the bottom edge of the coverglass.

Figure 8.5: OCT image of regenerating defect edge for animal receiving 5μg BMP-2 hydrogel implant at Week 5. Boxed region in Figure 4. A cross-correlation routine was applied to the image to reduce motion artifacts.

8.3.4 Imaging of Angiogenesis using OCT

Cross-sectional OCT images of the entire defect for animals receiving hydrogels loaded with 5μg or 25μg VEGF were similar to images of the animals receiving BMP-2 at early time points (Figure 8.6). A clear region consistent with the size of the defect could be observed. At later time points (4-6 weeks), thin vessel-like structures were seen penetrating into this hydrogel/defect region. These structures formed a network that traversed the entire defect region in some images and were consistent in size with larger angiogenic blood vessels (10 to approximately 50 microns in diameter). Smaller angiogenic blood vessels may be beyond the resolution capabilities of the imaging system. The thinnest structures also appeared somewhat discontinuous, again indicating that the limits of resolution may have been reached or suggesting that the vessels may be running in and out of the imaging plane. Comparing OCT images near the defect edge to histological sections in a similar location, the vessel-like structures were similar in size, organization, and density to the larger blood vessels, which were confirmed by immunostaining for von Willebrand Factor (vWF), an endothelial cell marker (Figure 8.7). In addition to endothelial cells lining the vessels, many of the larger vessels also contained red blood cells (RBCs) in the lumen of the vessels. While it is possible that the OCT signal came from the endothelial cells forming the blood vessels, a more likely source of contrast for OCT is the scattering of the RBCs themselves. The images also contained a region of high signal intensity at the bottom of the defect region; however, this region appeared thicker than in the images from animals receiving BMP-2. When comparing to the Masson's trichrome stained histology images, no bone tissue, indicated by dark blue staining, was seen bridging the bottom of the defect region at any time point. Images reconstructed from 3-D OCT scans for animals receiving the higher 25μg dose of VEGF showed that these vessel-like structures were present in all three planes, which confirmed their cylindrical nature (Figure 8.8). They also showed branching and connectivity consistent with

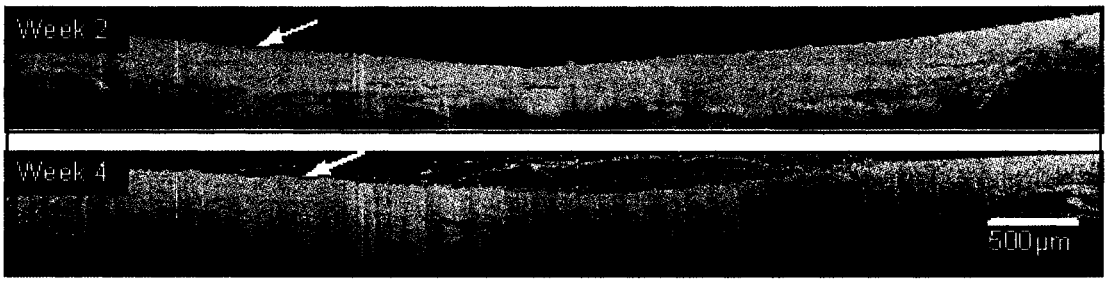

Figure 8.6: Cross-sectional OCT images of entire defect region with 5μg VEGF hydrogel implant. Images are from the same animal over time. Arrows indicate the defect edge. The top of each panel is the bottom edge of the coverglass. Images are shown in reverse contrast with a copper colormap.

blood vessels. In some images, including those in Figure 8.8, these vessel-like structures almost had an appearance of beads on a string, which could possibly indicate RBCs moving through the vessels.

8.4 Discussion and Conclusion

Overall, a novel "window chamber" model was successfully developed for non-invasive imaging of healing in a rat calvarial critical size defect. These "window chamber" implants were well tolerated by the animals, which was expected. This procedure is similar to the "head cap", a long-term implant for electrophysiological recording [276, 277], which has also been used to attach a fiberscope for high resolution imaging of the brain using two-photon microscopy [278]. A simplified cranial window has also been used extensively by Jain and colleagues to image angiogenesis near the brain [279]. However, the "window chamber" model differs significantly from the "head cap" and cranial window because the bone around the margins of the defect must be preserved to allow normal healing to occur, thus placing stricter restrictions on how the chamber is anchored to the skull. A bone chamber device that allows optical imaging of healing cortical bone has been developed by Bao and colleagues [280]; however, the technique does not offer the depth resolving power of OCT and only a

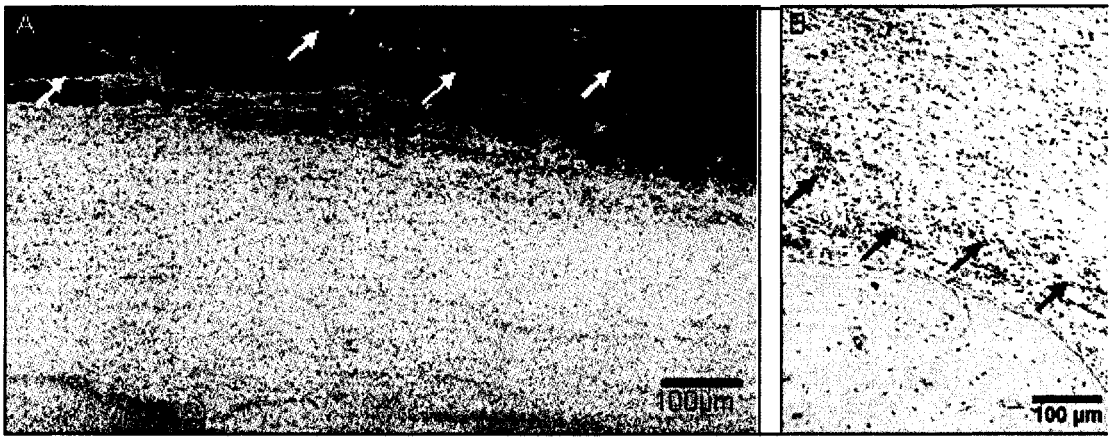

Figure 8.7: Images of defect edge for animal receiving 5μg VEGF hydrogel implant at Week 5. Images are shown in reverse contrast with a copper colormap. (A) OCT image. Arrows show vessel-like structures penetrating into hydrogel/defect region. (B) Histology section with angiogenic blood vessels stained for vWF.

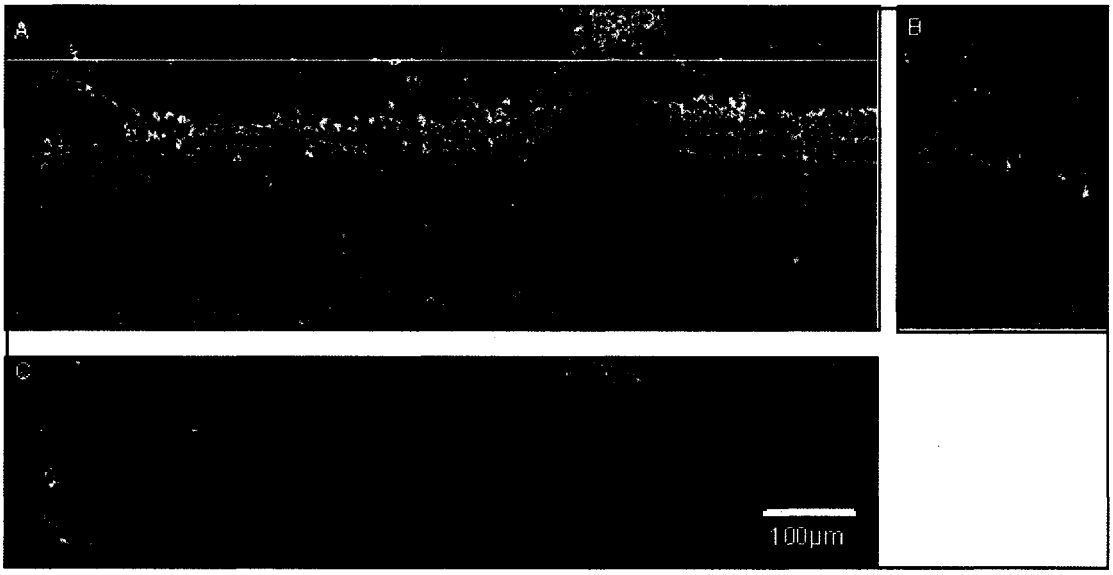

Figure 8.8: Image reconstruction from 3-D OCT scan series near defect edge for animal receiving 25μg VEGF hydrogel implant at Week 4. Images are shown in reverse contrast with a copper colormap. (A) XZ plane. Lines indicate planes shown in (B) and (C). (B) YZ plane. (C) XY plane. The top of panels (A) and (B) is the bottom edge of the coverglass.

100μm thick section of bone is imaged. The "window chamber" model consistently allowed OCT imaging of depths of 1-2mm within the defect site.

An initial obstacle to obtaining high quality images from live animals was image distortion due to breathing and heartbeat motion artifacts. The use of ear bars in a simplified stereotactic frame was able to substantially reduce the motion artifacts as well as to maintain a fixed orientation of the animal during scanning. The use of a cross-correlation routine during image processing was further able to reduce the appearance of the motion artifact. For future studies, increasing the image acquisition speed should reduce the motion artifacts. Further, coupling of the OCT objective to the "window chamber", similar to the head-mounted fiberscope developed by Helmchen *et al.* [278], may further reduce the motion artifacts.

The results show that HA hydrogel scaffolds with controlled degradation and protein release properties can induce significant bone regeneration when loaded with BMP-2. The "window chamber" did not appear to interfere with healing, as measured by standard metrics of bone formation. Similar levels of mineralization were observed for the "window chamber" model compared to the traditional critical size defect model, which also showed significant mineralization for the 5μg BMP-2 implants at the 6-week time point (Chapter 4). This finding was positive, although somewhat unexpected, because the presence of a coverglass on one side of the defect, compared to the normal closure of skin, may have led to impaired healing by limiting diffusion of nutrients and oxygen to and clearance of wastes from the top side of the defect. Also, the window chamber attachment would remove the contribution to the healing process of osteoblast progenitors found in the periosteum as the periosteum is removed during the surgical procedure. Additionally, topical infections seen in animals where the skin began to grow underneath the dental cement anchoring the chamber could have adversely affected the healing rate.

The temporal progression of healing, particularly that induced by HA hydrogels loaded with 5μg BMP-2, could be observed in living animals using OCT by imaging

the migration of the defect edge. The defect edge was found to move in from the side margins of the defect and up from the dural surface, resulting in a defect region that became progressively smaller with time. This is consistent with known mechanisms of healing and sources of progenitor cells and was in agreement with histological sections taken at selected time points. Overall, this indicates that OCT may be able to be used to measure the healing rate of the tissue *in situ*.

The results also provide the first report of OCT imaging of angiogenic blood vessels in a live animal model. Structures consistent with the neovascularization of the implant could clearly be observed at later time points for animals receiving VEGF-loaded implants. These structures correlated with the location of blood vessels seen in histological sections and showed interconnectivity and branching in three dimensions. These vessel-like structures were present in OCT images of all treatment groups from time to time, but qualitatively they appeared to a greater extent in the images of the VEGF-treated groups at later time points. Blood vessels were also observed within the defect site in histology sections for all samples.

This study also demonstrated the capability of OCT to create 3-D image series of angiogenic blood vessels. The ability of OCT to optically section a sample and generate 3-D images provides advantages over traditional 2-D analysis techniques, such as histology. It should be possible to define quantifiable metrics, such as number of branch points or vessel orientation, to evaluate the effects of different treatments on angiogenesis. For these scaffolds, increasing the dose of VEGF or waiting for a longer time point might result in a significant measure of healing. Finally, this study could be further extended by the use of Doppler OCT [308] to measure blood vessel patency.

Chapter 9

CONCLUSIONS AND FUTURE DIRECTIONS

9.1 Primary Conclusions

Overall, this dissertation research developed novel combinations of materials and growth factors as a controlled delivery system for increasing tissue regeneration in models of challenged bone healing. Testing these materials in a rat calvarial critical size defect model provided support to the hypotheses that controlled delivery of regenerative signals can modulate the formation of bone during regeneration and that altering the scaffold degradation rate can affect the temporal progression of healing. Additionally, the ability of the scaffold degradation rate (and its corresponding effect on the persistence of growth factors within the defect site) to affect the morphology of the regenerating bone, thus improving bone quality, was indicated.

Hyaluronic acid (HA) hydrogels were designed to have tunable degradation rates through hydrolysis of ester bonds in the crosslinks formed during the gelation process and to provide controlled release of cationic growth factors through electrostatic interactions with the negatively charged HA. While other groups have prepared HA hydrogels using a similar strategy of photo-initiated free radical polymerization of methacrylate-modified HA [202, 203, 204, 205, 206, 207], this work represents the first extensive characterization of the degradation of these hydrogels through a hydrolytic mechanism (Chapter 3). Further, these HA hydrogels were shown to be able to support bone growth when used in combination with appropriate signaling molecules. Bone morphogenetic protein-2 (BMP-2) delivery from the HA hydrogels had a clear osteoinductive effect *in vivo* (Chapter 4). The temporal progression of this effect could be modulated by altering the degradation rate of the scaffold. Interest-

ingly, all three degradation rates tested resulted in similar amounts of bone formation (measured by mineral volume) at the latest (six week) time point examined. However, the fastest and slowest degrading scaffolds seemed to result in more organized bone than the intermediate degrading scaffold, which was designed to degrade in 6–8 weeks to match the healing time.

The angiogenic molecules tested, vascular endothelial growth factor (VEGF) and osteoprotegerin (OPG), did not have a strong osteoinductive effect *in vivo* (Chapter 5). OPG, which has both bone-protective [97] and pro-angiogenic [100] effects, was the more promising candidate. The highest dose of OPG tested (25μg) resulted in higher mineral volumes than controls; however, the high variability in the measurements precluded definitive conclusions about its activity. Use of radiographs to measure mineralization indicated that VEGF may have a potential dose effect on bone growth and that the temporal response could be modulated by the scaffold degradation rate; however, this was not able to be confirmed by the more sensitive technique of microcomputed tomography (microCT). Qualitative examination of the harvested tissues using histology generally indicated a greater tissue volume filling the defect area for samples treated with VEGF compared to controls, which could account for the increased radioopacity. Most interestingly, co-delivery of VEGF with BMP-2 appeared to increase the amount of bone formation compared to BMP-2 delivery alone. Further examination of the effects of VEGF and OPG on angiogenesis as well as on the amount of cellular infiltration and/or extracellular matrix (ECM) production is warranted.

The final protein examined, leucine rich amelogenin peptide (LRAP), also did not induce bone formation. Because the LRAP-GST fusion protein has a fairly low pI, it was not expected to be retained in the HA hydrogels and thus was formulated into poly(lactide-co-glycolide) (PLGA) microspheres to provide controlled release. It also did not exhibit any osteoinductive effects in the calvarial defect model with no mineralization seen at 12 weeks, compared to extensive mineralization seen with PLGA

microspheres loaded with BMP-2 as a positive control (Chapter 6). The mineralization seen with BMP-2 indicated that these microspheres are suitable for controlled release of osteoinductive molecules. The lack of effect seen for LRAP could indicate that it is unable to induce bone formation and mineralization or that its activity was altered during the formulation process. Interference of buffer components with *in vitro* experiments to assess the activity of LRAP made it impossible to determine if the latter case was true.

A second major goal of this dissertation research was to utilize optical coherence tomography (OCT) to noninvasively image morphological changes during angiogenesis and bone regeneration induced by the scaffolds described above in the calvarial defect model. However, to first demonstrate the ability of OCT to detect morphological changes in materials, OCT was used to examine changes in PLGA microspheres suspended within HA hydrogels in an *in vitro* degradation study (Chapter 7). The microspheres were loaded with bovine serum albumin (BSA) as a model protein. Microsphere degradation and thus protein release were controlled by the initial molecular weight of the PLGA. Microspheres formulated from a lower molecular weight PLGA released protein faster and underwent morphological changes consistent with degradation including a decrease in particle size, an increase in "particulate" number, and the presence of a "hollow" morphology in an increasing number of particles. These results were similar to observations made in previous studies using destructive measurement techniques, such as scanning electron microscopy (SEM), to examine microsphere morphology [300, 301, 302]. The higher molecular weight PLGA microspheres released protein slower and did not have extensive morphological changes in the OCT images.

For *in vivo* use of OCT, a novel "window chamber" model was successfully developed for noninvasive imaging of healing in the rat calvarial critical size defect (Chapter 8). Bone regeneration, as measured by standard metrics such as microCT and histology, was similar to the traditional defect model used in Chapters 4 and 5. The

temporal progression of healing could be observed in living animals using OCT by imaging the migration of the bone/defect interface over time, particularly for animals receiving HA hydrogels loaded with 5μg BMP-2. Additionally, structures consistent with the neovascularization of the implant could clearly be observed at later time points for animals receiving HA hydrogels loaded with VEGF. These structures correlated with the location of blood vessels seen in histological sections and showed interconnectivity and branching in three dimensions.

9.2 Implications for Tissue Engineering

The HA hydrogel/PLGA microsphere system developed as part of this research represents a generic delivery device that could be implemented in many forms of varying complexity as well as that could be utilized for the engineering of a diverse range of tissues. Theoretically, any protein therapeutic could be incorporated into the scaffold, either directly in the HA hydrogel or encapsulated within PLGA microspheres. The formulation parameters used, such as crosslink density or PLGA molecular weight, could be varied to provide an appropriate release profile. As described in the "future directions" section later in this chapter, the delivery system could be made more complex by incorporating several different proteins, each with different release profiles, or by spatially patterning the proteins within the scaffold. Additionally, this work has addressed two areas of fundamental importance to the field of tissue engineering: (1) the balance between scaffold degradation and tissue growth and (2) the induction of angiogenesis during tissue healing. Finally, this research has explored the use of OCT as a noninvasive imaging modality to assess morphological changes of bone tissue during the healing process *in vivo* and of the scaffold materials during degradation studies *in vitro*.

The improved bone organization seen with the fastest and slowest degrading scaffolds compared to the intermediate degrading scaffold appears to contradict the tissue engineering tenet that matching the time course of scaffold degradation to tissue re-

generation can optimize new tissue formation (i.e., induce the greatest level of healing in the shortest time period). It is possible that the targeted 6–8 week degradation time of the intermediate degrading scaffold was not matched to the regeneration rate of the tissue. However, there is another, more interesting, implication of this result. Since both the fastest and slowest degrading hydrogels resulted in better quality bone, it suggests two possible mechanisms of bone formation and maturation. For the fast degrading hydrogels, bone may be induced to form quickly and then have time to remodel into a more mature lamellar phenotype. For the slow degrading hydrogels, the hydrogel may retard the growth of new bone but encourage it to be formed in an already mature lamellar morphology. Clinically, these different treatments would be applicable in two different scenarios. For people who are otherwise healthy, inducing rapid bone formation that can be remodeled naturally may be the most sensible treatment. However, for people with impaired bone regeneration capacity from osteoporosis or other diseases, encouraging slower formation of more organized bone might provide the best therapy.

While the angiogenic factor, VEGF, did not have an osteoinductive effect in this particular system, qualitative changes in tissue morphology for animals treated with VEGF indicates that it is inducing some sort of regenerative response. Having a sufficient vascular supply is essential to maintain the viability of all "engineered" tissues. As seen in *in vitro* release studies, VEGF could be delivered in a controlled fashion from the HA hydrogels. A more comprehensive quantitative analysis of the number of blood vessels induced by VEGF in the present studies would indicate if VEGF was having its expected angiogenic effect. The increased mineralization observed with co-delivery of VEGF and BMP-2 could be due to enhanced nutrient delivery from an increase in blood vessels in the regenerating tissue.

This research represents the first application of OCT to image morphological changes during bone regeneration and angiogenesis. The ability to noninvasively monitor healing would find wide application in evaluating tissue engineering treat-

ments. By developing metrics that could assess the extent of tissue regeneration, the use of noninvasive imaging technologies would significantly reduce the number of animals needed for as well as the costs of *in vivo* pre-clinical longitudinal studies. Instead of histology, which provides a single sample per time point, OCT could be used to image the same animal at several time points. Additionally, this would provide a more statistically robust design for experiments by giving the opportunity to compare different time points in a single animal. Finally, OCT can be used to obtain three-dimensional (3-D) data sets, which may provide more information on spatial orientation of morphological features within the tissues than two-dimensional (2-D) histological sections.

9.3 Limitations of System

There are several limitations to the controlled delivery system designed as part of this research, both of the materials themselves and of the methods used to evaluate them. As described in Chapter 2, a major limitation to the scaffold design for use in bone regeneration applications is that hydrogels have fairly weak mechanical properties. The compressive modulus of HA hydrogels, which was measured on the order of 10kPa for similarly prepared hydrogels [214], is very low compared to the modulus of bone. It would not be able to be used alone in a weight-bearing site. However, it would be possible to use the hydrogel scaffold in conjunction with a fixation device or as part of a composite device where the hydrogel material can fill the pores of a more rigid scaffold. Additionally, while the scaffold materials provide a basic template that can be used with a number of proteins, the controlled release profile would have to be characterized for each protein used and the formulation parameters would have to be adjusted to optimize the release for a given protein (i.e., one could not simply switch to a different protein and expect to get the same results). This can be seen in the different release profiles obtained for three of the proteins studied here: BMP-2, VEGF, and OPG.

There are also several limitations to the methods used to characterize the scaffolds, both *in vitro* and *in vivo*. The use of *in vitro* release and degradation studies can confirm that specific combinations of materials will behave differently from others; however, the results can only be used qualitatively to predict *in vivo* effects. For example, the hydrogels were able to easily be degraded by hyaluronidase *in vitro* (Chapter 3), and the activity of hyaluronidase is the major mechanism of HA degradation and clearance of native HA *in vivo*. However, the hydrogels' *in vivo* degradation rates more closely resembled their *in vitro* hydrolytic degradation rates at physiologic pH. Techniques which can be used both *in vitro* and *in vivo*, such as the morphological changes observed in the scaffold materials using OCT (Chapter 7), may help to provide a correlation between responses and allow one to be more predictive of *in vivo* performance.

The rat calvarial critical size defect model also has its limitations. There are conflicting reports on the size of the defect needed for it to be critical size, ranging from 5mm [274] to 8mm [33]. Additionally, this model may not be as demanding on the healing response as a "challenged" fracture model. Positive results in the calvarial defect model may not translate to clinically meaningful therapies. The calvarial bones of the rat have well-organized lamellar bone, making it an appealing site to evaluate the effects of a treatment on regenerated bone orientation. However, as bone has been shown to regenerate in this site through a mechanism similar to intramembranous ossification [33] and VEGF may not have strong osteogenic activity there [261], successful (and unsuccessful) treatments may have different effects in other anatomical locations.

9.4 Future Directions

9.4.1 Extensions of Present Studies

There are several areas where the present studies could be expanded to obtain more data on the HA hydrogels as a scaffold material and on the particular growth factors tested, some of which were touched upon in the discussion sections of each chapter. Most importantly, a more challenging model of bone healing, such as a larger calvarial defect model or a fracture fixation model, is needed to test the efficacy of the HA hydrogels. The use of an alternative anatomical site may also be warranted to test the osteogenic effects of VEGF, as varied effects have been seen by other groups using mouse and rat calvarial defect models [255, 261]. Additionally, the effects of VEGF on angiogenesis can be more carefully quantified, and the cell types infiltrating the defect area and the composition of the new ECM formed in the defect can be determined. This may provide insights into the regenerative effects that VEGF is having since it is clearly not inducing mineralized bone tissue formation. The variable results seen with OPG suggests that this molecule has potential for regenerating bone, and further evaluation of the dosage and/or delivery method may result in a successful treatment. Further *in vitro* testing of the activity of LRAP during microsphere processing may indicate if the fabrication methods are too harsh on the protein. Additionally, testing of LRAP as just the peptide instead of the full GST fusion protein would be more appropriate for determining its effects *in vivo*. Improvements in the image acquisition times and image processing methods would enhance the quality of the OCT images obtained, particularly helping to reduce motion artifacts. Further, functional assessment of blood vessels could be obtained by using Doppler OCT.

9.4.2 Spatial Patterning

The scaffold delivery system designed in this dissertation research can be easily manipulated to prepare more sophisticated devices with spatial patterning of proteins

and/or PLGA microspheres as well as with multiple proteins potentially each with a different release profile. As many growth factors act in concert during the processes of angiogenesis and bone growth, systems that can deliver multiple proteins in a controlled fashion may result in even better bone growth. While testing these composite structures was beyond the scope of this dissertation, methods for the spatial localization of protein within the HA hydrogel scaffolds were developed. For proteins whose release can be controlled by electrostatic interactions with the HA hydrogel, a laminating approach can be used to create a gradient of protein within the scaffold. For uncharged or negatively-charged proteins, a spatial gradient can be generated by placing a depot of degradable microspheres in one region of the hydrogel and allowing diffusion of proteins released from the microspheres to drive the formation of a gradient.

9.4.3 A Laminating Approach to Create Spatial Gradients of Protein

A laminating approach can theoretically be used to create spatial gradients of positively-charged proteins within the negatively-charged HA matrix. Electrostatic interactions will limit diffusion of the proteins within the hydrogel, and the gradient should persist for an extended period of time until the scaffold degrades or until cells infiltrate and start to remodel the scaffold. Radial gradients of protein within the scaffolds can be formed by molding disks with increasing diameter and decreasing protein concentration (Figure 9.1). As proof of concept, laminated gels containing a fluorescently labeled protein were created by layering of HA-GMA solutions containing different fluorescein isothiocyanate (FITC)-BSA concentrations. A reduced UV irradiation time of 5 minutes per layer was used to allow the subsequent layers to adhere while providing sufficient crosslinking to prevent mixing between layers. Gels were sectioned immediately after formation to minimize diffusion of the FITC-BSA and imaged using fluorescence microscopy (Figure 9.2). The micrograph shows distinct regions of higher fluorescence in the layers that received the FITC-BSA. Artifacts resulted from

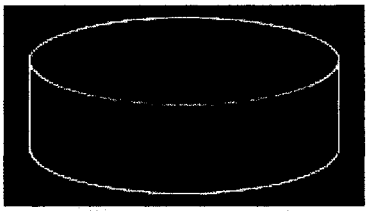

Figure 9.1: Schematic of hydrogel with radial gradient of loaded protein. Gradient indicated by the green color. The highest concentration is in the center of the device.

sectioning of the gel and from out-of-focus planes. While these results do not show that the gradients will persist over time, they indicate that a laminating approach can successfully be used to pattern protein within the hydrogel.

9.4.4 A Molding Approach to Localize Microspheres in Center of the Hydrogel

For proteins that will diffuse quickly through the hydrogels, a different approach is needed to establish a spatial gradient within the scaffold. One approach is to load a depot of protein that will be released in a controlled fashion within one region of the hydrogel to drive the gradient formation. As an example, if the depot is placed in the center of the hydrogel, the protein will diffuse out from the highly concentrated center near the depot to the edges of the gel (Figure 9.3). If the depot releases protein in a controlled manner, such as from degradable microspheres, a stable gradient could be established. As proof of concept, a molding approach was used to localize microspheres within the center of a HA hydrogel. Microspheres were fabricated from 40 kDa PLGA and loaded with FITC-BSA and Nile Red (a fluorescent dye which stably labels the microspheres [309]). Microspheres were mixed with HA-GMA solution and crosslinked in a small well. The hydrogel containing the microspheres was then placed in the center of HA-GMA solution in a larger well and crosslinked. Samples were placed in DI water to allow protein to be released from the microspheres and diffuse out of the center of the hydrogel. The hydrogels were then imaged using

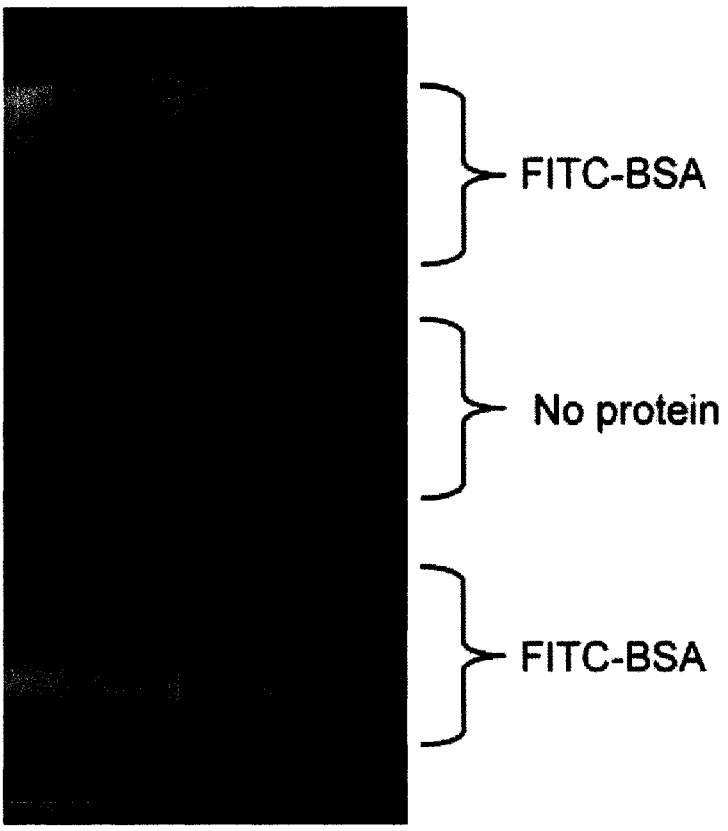

Figure 9.2: Composite HA hydrogel formed by laminating process. Fluorescence micrograph (FITC filter) of cross-section of laminated HA hydrogel with 2 layers of FITC-BSA surrounding a layer with no protein.

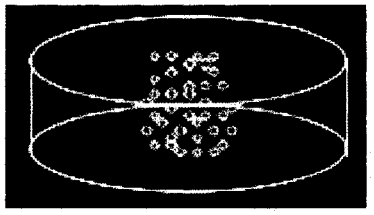

Figure 9.3: Schematic of hydrogel with depot of microspheres. Gradient indicated by the green color. The highest concentration of protein is in the center of the device where the microspheres are localized.

fluorescence microscopy (Figure 9.4). The micrograph shows that the microspheres remain in the center of the hydrogel while the protein diffuses outward. Artifacts result from out-of-focus planes.

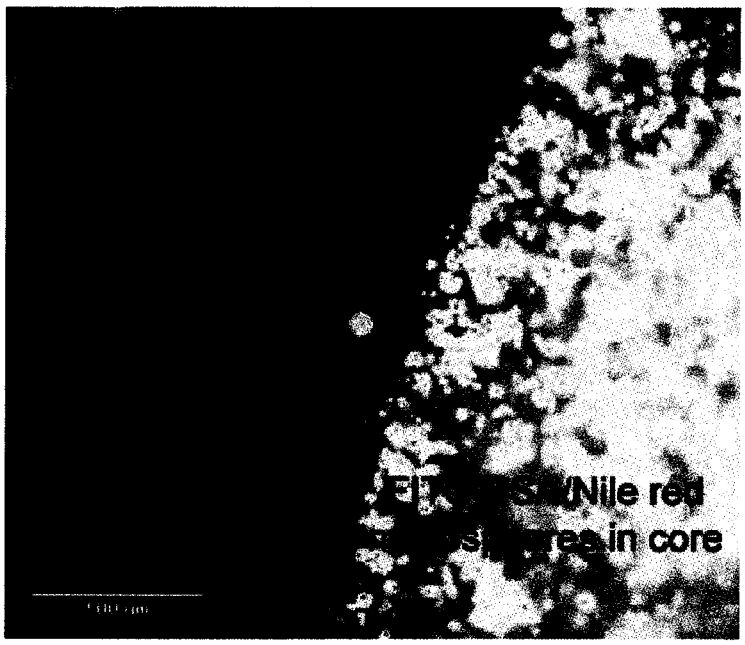

Figure 9.4: Composite HA hydrogel formed by molding process. Overlay of fluorescence micrographs FITC filter (green) shows FITC-BSA; RHOD filter (red) shows Nile red labeled microspheres; overlapping regions are yellow. FITC-BSA loaded/Nile red labeled microspheres are localized in the center of the HA hydrogel while FITC-BSA diffuses out into the surrounding hydrogel.

BIBLIOGRAPHY

[1] J. Glowacki, L. Griffith, C. Kelley, D. Mooney, D. Rekow, P. Robey, M. Snead, and S. Stupp. NIDCR scientific expert panel: Repair and restoration of oral, dental, and craniofacial tissues. *http://www.nidcr.nih.gov/Research/LongRangeResearchOpportunities/PanelOnRepairAndRegeneration.htm*, Accessed:February 28, 2007, 2002.

[2] E. Alsberg, E. E. Hill, and D. J. Mooney. Craniofacial tissue engineering. *Crit Rev Oral Biol Med*, 12(1):64–75, 2001.

[3] C.W. Cummings, P.W. Flint, B.H. Haughey, K.T. Robbins, J.R. Thomas, L.A. Harker, M.A. Richardson, and D.E. Schuller. *Otolaryngology: Head and Neck Surgery.* Mosby, 4th edition, 2005.

[4] V. Kumar, A.K. Abbas, and N. Fausto. *Robbins and Cotran: Pathologic Basis of Disease.* Elsevier, 7th edition, 2005.

[5] S. Teng, I. W. Choi, S. W. Herring, and J. M. Rensberger. Stereological analysis of bone architecture in the pig zygomatic arch. *Anat Rec*, 248(2):205–213, Jun 1997.

[6] R. Langer and J. P. Vacanti. Tissue engineering. *Science*, 260(5110):920–926, May 1993.

[7] J. A. Buckwalter, M. J. Glimcher, R. R. Cooper, and R. Recker. Bone biology. I: Structure, blood supply, cells, matrix, and mineralization. *Instr Course Lect*, 45:371–386, 1996.

[8] H. Gray. *Anatomy of the Human Body.* Bartleby.com, 20th edition, 2000.

[9] X. Wang, X. Li, R. A. Bank, and C. M. Agrawal. Effects of collagen unwinding and cleavage on the mechanical integrity of the collagen network in bone. *Calcif Tissue Int*, 71(2):186–192, Aug 2002.

[10] X. Wang, R. A. Bank, J. M. TeKoppele, G. B. Hubbard, K. A. Athanasiou, and C. M. Agrawal. Effect of collagen denaturation on the toughness of bone. *Clin Orthop Relat Res*, 71(371):228–239, Feb 2000.

[11] W. J. Landis, K. J. Hodgens, J. Arena, M. J. Song, and B. F. McEwen. Structural relations between collagen and mineral in bone as determined by high voltage electron microscopic tomography. *Microsc Res Tech*, 33(2):192–202, Feb 1996.

[12] W. Traub, T. Arad, and S. Weiner. Three-dimensional ordered distribution of crystals in turkey tendon collagen fibers. *Proc Natl Acad Sci U S A*, 86(24):9822–9826, Dec 1989.

[13] J. A. Buckwalter, M. J. Glimcher, R. R. Cooper, and R. Recker. Bone biology. II: Formation, form, modeling, remodeling, and regulation of cell function. *Instr Course Lect*, 45:387–399, 1996.

[14] Mixing anatomy and automobiles. *Hightech Report*, 1:60–62, 2003.

[15] E. B. Giesen, M. Ding, M. Dalstra, and T. M. van Eijden. Mechanical properties of cancellous bone in the human mandibular condyle are anisotropic. *J Biomech*, 34(6):799–803, Jun 2001.

[16] L. J. van Ruijven, E. B W Giesen, and T. M G J van Eijden. Mechanical significance of the trabecular microstructure of the human mandibular condyle. *J Dent Res*, 81(10):706–710, Oct 2002.

[17] M. M. Cohen. The new bone biology: pathologic, molecular, and clinical correlates. *Am J Med Genet A*, 140(23):2646–2706, Dec 2006.

[18] H. P. Gerber and N. Ferrara. Angiogenesis and bone growth. *Trends Cardiovasc Med*, 10(5):223–228, Jul 2000.

[19] A. M. Parfitt. Osteonal and hemi-osteonal remodeling: the spatial and temporal framework for signal traffic in adult human bone. *J Cell Biochem*, 55(3):273–286, Jul 1994.

[20] S. C. Manolagas. Birth and death of bone cells: basic regulatory mechanisms and implications for the pathogenesis and treatment of osteoporosis. *Endocr Rev*, 21(2):115–137, Apr 2000.

[21] J. E. Aubin. Regulation of osteoblast formation and function. *Rev Endocr Metab Disord*, 2(1):81–94, Jan 2001.

[22] T. Katagiri and N. Takahashi. Regulatory mechanisms of osteoblast and osteoclast differentiation. *Oral Dis*, 8(3):147–159, May 2002.

[23] J. R. Lieberman, A. Daluiski, and T. A. Einhorn. The role of growth factors in the repair of bone. Biology and clinical applications. *J Bone Joint Surg Am*, 84-A(6):1032–1044, Jun 2002.

[24] P. Ducy, R. Zhang, V. Geoffroy, A. L. Ridall, and G. Karsenty. Osf2/Cbfa1: a transcriptional activator of osteoblast differentiation. *Cell*, 89(5):747–754, May 1997.

[25] T. Komori, H. Yagi, S. Nomura, A. Yamaguchi, K. Sasaki, K. Deguchi, Y. Shimizu, R. T. Bronson, Y. H. Gao, M. Inada, M. Sato, R. Okamoto, Y. Kitamura, S. Yoshiki, and T. Kishimoto. Targeted disruption of Cbfa1 results in a complete lack of bone formation owing to maturational arrest of osteoblasts. *Cell*, 89(5):755–764, May 1997.

[26] W. Liu, S. Toyosawa, T. Furuichi, N. Kanatani, C. Yoshida, Y. Liu, M. Himeno, S. Narai, A. Yamaguchi, and T. Komori. Overexpression of Cbfa1 in osteoblasts inhibits osteoblast maturation and causes osteopenia with multiple fractures. *J Cell Biol*, 155(1):157–166, Oct 2001.

[27] K. Nakashima, X. Zhou, G. Kunkel, Z. Zhang, J. M. Deng, R. R. Behringer, and B. de Crombrugghe. The novel zinc finger-containing transcription factor osterix is required for osteoblast differentiation and bone formation. *Cell*, 108(1):17–29, Jan 2002.

[28] M. Weinreb, D. Shinar, and G. A. Rodan. Different pattern of alkaline phosphatase, osteopontin, and osteocalcin expression in developing rat bone visualized by in situ hybridization. *J Bone Miner Res*, 5(8):831–842, Aug 1990.

[29] P. V. Hauschka, J. B. Lian, D. E. Cole, and C. M. Gundberg. Osteocalcin and matrix Gla protein: vitamin K-dependent proteins in bone. *Physiol Rev*, 69(3):990–1047, Jul 1989.

[30] P. Ducy, C. Desbois, B. Boyce, G. Pinero, B. Story, C. Dunstan, E. Smith, J. Bonadio, S. Goldstein, C. Gundberg, A. Bradley, and G. Karsenty. Increased bone formation in osteocalcin-deficient mice. *Nature*, 382(6590):448–452, Aug 1996.

[31] J. Chen, H. S. Shapiro, and J. Sodek. Development expression of bone sialoprotein mRNA in rat mineralized connective tissues. *J Bone Miner Res*, 7(8):987–997, Aug 1992.

[32] R. Fujisawa and Y. Kuboki. Affinity of bone sialoprotein and several other bone and dentin acidic proteins to collagen fibrils. *Calcif Tissue Int*, 51(6):438–442, Dec 1992.

[33] J. Wang, M. J. Glimcher, J. Mah, H. Y. Zhou, and E. Salih. Expression of bone microsomal casein kinase II, bone sialoprotein, and osteopontin during the repair of calvarial defects. *Bone*, 22(6):621–628, Jun 1998.

[34] M. R. Urist. Bone: formation by autoinduction. *Science*, 150(698):893–899, Nov 1965.

[35] J. M. Wozney. Bone morphogenetic proteins. *Prog Growth Factor Res*, 1(4):267–280, 1989.

[36] J. M. Wozney, V. Rosen, A. J. Celeste, L. M. Mitsock, M. J. Whitters, R. W. Kriz, R. M. Hewick, and E. A. Wang. Novel regulators of bone formation: molecular clones and activities. *Science*, 242(4885):1528–1534, Dec 1988.

[37] B. L. Hogan. Bone morphogenetic proteins: multifunctional regulators of vertebrate development. *Genes Dev*, 10(13):1580–1594, Jul 1996.

[38] Q. Kang, M. H. Sun, H. Cheng, Y. Peng, A. G. Montag, A. T. Deyrup, W. Jiang, H. H. Luu, J. Luo, J. P. Szatkowski, P. Vanichakarn, J. Y. Park, Y. Li, R. C. Haydon, and T-C. He. Characterization of the distinct orthotopic bone-forming activity of 14 BMPs using recombinant adenovirus-mediated gene delivery. *Gene Ther*, 11(17):1312–1320, Sep 2004.

[39] J. M. Wozney. *Cellular and Molecular Biology of Bone.* Academic Press, 1993.

[40] E. H. Riley, J. M. Lane, M. R. Urist, K. M. Lyons, and J. R. Lieberman. Bone morphogenetic protein-2: biology and applications. *Clin Orthop Relat Res*, 324(324):39–46, Mar 1996.

[41] A. H. Reddi. Bone and cartilage differentiation. *Curr Opin Genet Dev*, 4(5):737–744, Oct 1994.

[42] H. Nakamine, A. Kamegai, J.-I. Yasuda, N. Kanematsu, and M. Mori. Glycosaminoglycan distribution in chondro-osteogenesis induced by bone morphogenetic protein in mouse muscle tissue with the use of monoclonal antibodies. *Acta Histochem Cytochem*, 27(3):227–238, 1994.

[43] S. D. Boden, K. McCuaig, G. Hair, M. Racine, L. Titus, J. M. Wozney, and M. S. Nanes. Differential effects and glucocorticoid potentiation of bone morphogenetic protein action during rat osteoblast differentiation in vitro. *Endocrinology*, 137(8):3401–3407, Aug 1996.

[44] F. J. Hughes, J. Collyer, M. Stanfield, and S. A. Goodman. The effects of bone morphogenetic protein-2, -4, and -6 on differentiation of rat osteoblast cells in vitro. *Endocrinology*, 136(6):2671–2677, Jun 1995.

[45] A. H. Reddi. Role of morphogenetic proteins in skeletal tissue engineering and regeneration. *Nat Biotechnol*, 16(3):247–252, Mar 1998.

[46] D. M. Kingsley, A. E. Bland, J. M. Grubber, P. C. Marker, L. B. Russell, N. G. Copeland, and N. A. Jenkins. The mouse short ear skeletal morphogenesis locus is associated with defects in a bone morphogenetic member of the TGF beta superfamily. *Cell*, 71(3):399–410, Oct 1992.

[47] G. Luo, C. Hofmann, A. L. Bronckers, M. Sohocki, A. Bradley, and G. Karsenty. BMP-7 is an inducer of nephrogenesis, and is also required for eye development and skeletal patterning. *Genes Dev*, 9(22):2808–2820, Nov 1995.

[48] A. C. McPherron, A. M. Lawler, and S. J. Lee. Regulation of anterior/posterior patterning of the axial skeleton by growth/differentiation factor 11. *Nat Genet*, 22(3):260–264, Jul 1999.

[49] A. T. Dudley, K. M. Lyons, and E. J. Robertson. A requirement for bone morphogenetic protein-7 during development of the mammalian kidney and eye. *Genes Dev*, 9(22):2795–2807, Nov 1995.

[50] M. J. Solloway, A. T. Dudley, E. K. Bikoff, K. M. Lyons, B. L. Hogan, and E. J. Robertson. Mice lacking Bmp6 function. *Dev Genet*, 22(4):321–339, 1998.

[51] M. M. Cohen. Merging the old skeletal biology with the new. II. Molecular aspects of bone formation and bone growth. *J Craniofac Genet Dev Biol*, 20(2):94–106, 2000.

[52] K. Anselme. Osteoblast adhesion on biomaterials. *Biomaterials*, 21(7):667–681, Apr 2000.

[53] W. J. Grzesik and P. G. Robey. Bone matrix RGD glycoproteins: immunolocalization and interaction with human primary osteoblastic bone cells in vitro. *J Bone Miner Res*, 9(4):487–496, Apr 1994.

[54] E. Alsberg, K. W. Anderson, A. Albeiruti, J. A. Rowley, and D. J. Mooney. Engineering growing tissues. *Proc Natl Acad Sci U S A*, 99(19):12025–12030, Sep 2002.

[55] B. Ganss, R. H. Kim, and J. Sodek. Bone sialoprotein. *Crit Rev Oral Biol Med*, 10(1):79–98, 1999.

[56] G. K. Hunter and H. A. Goldberg. Nucleation of hydroxyapatite by bone sialoprotein. *Proc Natl Acad Sci U S A*, 90(18):8562–8565, Sep 1993.

[57] M. L. Paine, S. N. White, W. Luo, H. Fong, M. Sarikaya, and M. L. Snead. Regulated gene expression dictates enamel structure and tooth function. *Matrix Biol*, 20(5-6):273–292, Sep 2001.

[58] A. G. Fincham, J. Moradian-Oldak, T. G. Diekwisch, D. M. Lyaruu, J. T. Wright, P. Bringas, and H. C. Slavkin. Evidence for amelogenin "nanospheres" as functional components of secretory-stage enamel matrix. *J Struct Biol*, 115(1):50–59, 1995.

[59] J. Kirkham, J. Zhang, S. J. Brookes, R. C. Shore, S. R. Wood, D. A. Smith, M. L. Wallwork, O. H. Ryu, and C. Robinson. Evidence for charge domains on developing enamel crystal surfaces. *J Dent Res*, 79(12):1943–1947, Dec 2000.

[60] Y. Doi, E. D. Eanes, H. Shimokawa, and J. D. Termine. Inhibition of seeded growth of enamel apatite crystals by amelogenin and enamelin proteins in vitro. *J Dent Res*, 63(2):98–105, Feb 1984.

[61] H. L. Viswanathan, J. E. Berry, B. L. Foster, C. W. Gibson, Y. Li, A. B. Kulkarni, M. L. Snead, and M. J. Somerman. Amelogenin: a potential regulator of cementum-associated genes. *J Periodontol*, 74(10):1423–1431, Oct 2003.

[62] B. Bäckman and U. Adolfsson. Craniofacial structure related to inheritance pattern in amelogenesis imperfecta. *Am J Orthod Dentofacial Orthop*, 105(6):575–582, Jun 1994.

[63] C. Gibson, E. Golub, R. Herold, M. Risser, W. Ding, H. Shimokawa, M. Young, J. Termine, and J. Rosenbloom. Structure and expression of the bovine amelogenin gene. *Biochemistry*, 30(4):1075–1079, Jan 1991.

[64] D. R. Nebgen, H. Inoue, B. Sabsay, K. Wei, C. S. Ho, and A. Veis. Identification of the chondrogenic-inducing activity from bovine dentin (bCIA) as a low-molecular-mass amelogenin polypeptide. *J Dent Res*, 78(9):1484–1494, Sep 1999.

[65] A. Veis, K. Tompkins, K. Alvares, K. Wei, L. Wang, X. S. Wang, A. G. Brownell, S. M. Jengh, and K. E. Healy. Specific amelogenin gene splice products have signaling effects on cells in culture and in implants in vivo. *J Biol Chem*, 275(52):41263–41272, Dec 2000.

[66] A. Veis. Amelogenin gene splice products: potential signaling molecules. *Cell Mol Life Sci*, 60(1):38–55, Jan 2003.

[67] S. Lacerda-Pinheiro, D. Septier, K. Tompkins, A. Veis, M. Goldberg, and H. Chardin. Amelogenin gene splice products A+4 and A-4 implanted in soft tissue determine the reorientation of CD45-positive cells to an osteo-chondrogenic lineage. *J Biomed Mater Res A*, 79(4):1015–1022, Dec 2006.

[68] F. Boabaid, C. W. Gibson, M. A. Kuehl, J. E. Berry, M. L. Snead, F. H. Nociti, E. Katchburian, and M. J. Somerman. Leucine-rich amelogenin peptide: a candidate signaling molecule during cementogenesis. *J Periodontol*, 75(8):1126–1136, Aug 2004.

[69] E. Jimi, I. Nakamura, H. Amano, Y. Taguchi, T. Tsurukai, M. Tamura, N. Takahashi, and T. Suda. Osteoclast function is activated by osteoblastic cells through a mechanism involving cell-to-cell contact. *Endocrinology*, 137(8):2187–2190, Aug 1996.

[70] H. Yasuda, N. Shima, N. Nakagawa, K. Yamaguchi, M. Kinosaki, S. Mochizuki, A. Tomoyasu, K. Yano, M. Goto, A. Murakami, E. Tsuda, T. Morinaga, K. Higashio, N. Udagawa, N. Takahashi, and T. Suda. Osteoclast differentiation factor is a ligand for osteoprotegerin/osteoclastogenesis-inhibitory factor and is identical to TRANCE/RANKL. *Proc Natl Acad Sci U S A*, 95(7):3597–3602, Mar 1998.

[71] E. Jimi, S. Akiyama, T. Tsurukai, N. Okahashi, K. Kobayashi, N. Udagawa, T. Nishihara, N. Takahashi, and T. Suda. Osteoclast differentiation factor acts as a multifunctional regulator in murine osteoclast differentiation and function. *J Immunol*, 163(1):434–442, Jul 1999.

[72] B. R. Wong, J. Rho, J. Arron, E. Robinson, J. Orlinick, M. Chao, S. Kalachikov, E. Cayani, F. S. Bartlett, W. N. Frankel, S. Y. Lee, and Y. Choi. TRANCE is a novel ligand of the tumor necrosis factor receptor family that activates c-Jun N-terminal kinase in T cells. *J Biol Chem*, 272(40):25190–25194, Oct 1997.

[73] D. M. Anderson, E. Maraskovsky, W. L. Billingsley, W. C. Dougall, M. E. Tometsko, E. R. Roux, M. C. Teepe, R. F. DuBose, D. Cosman, and L. Galibert.

A homologue of the TNF receptor and its ligand enhance T-cell growth and dendritic-cell function. *Nature*, 390(6656):175–179, Nov 1997.

[74] V. Kartsogiannis, H. Zhou, N. J. Horwood, R. J. Thomas, D. K. Hards, J. M. Quinn, P. Niforas, K. W. Ng, T. J. Martin, and M. T. Gillespie. Localization of RANKL (receptor activator of NF kappa B ligand) mRNA and protein in skeletal and extraskeletal tissues. *Bone*, 25(5):525–534, Nov 1999.

[75] L. C. Hofbauer, F. Gori, B. L. Riggs, D. L. Lacey, C. R. Dunstan, T. C. Spelsberg, and S. Khosla. Stimulation of osteoprotegerin ligand and inhibition of osteoprotegerin production by glucocorticoids in human osteoblastic lineage cells: potential paracrine mechanisms of glucocorticoid-induced osteoporosis. *Endocrinology*, 140(10):4382–4389, Oct 1999.

[76] L. C. Hofbauer, D. L. Lacey, C. R. Dunstan, T. C. Spelsberg, B. L. Riggs, and S. Khosla. Interleukin-1beta and tumor necrosis factor-alpha, but not interleukin-6, stimulate osteoprotegerin ligand gene expression in human osteoblastic cells. *Bone*, 25(3):255–259, Sep 1999.

[77] T. Nakashima, Y. Kobayashi, S. Yamasaki, A. Kawakami, K. Eguchi, H. Sasaki, and H. Sakai. Protein expression and functional difference of membrane-bound and soluble receptor activator of NF-kappaB ligand: modulation of the expression by osteotropic factors and cytokines. *Biochem Biophys Res Commun*, 275(3):768–775, Sep 2000.

[78] H. Chung, Y. S. Kang, C. S. Hwang, I. K. Moon, C. H. Yim, K. H. Choi, K. O. Han, H. C. Jang, H. K. Yoon, and I. K. Han. Deflazacort increases osteoclast formation in mouse bone marrow culture and the ratio of RANKL/OPG mRNA expression in marrow stromal cells. *J Korean Med Sci*, 16(6):769–773, Dec 2001.

[79] D. L. Lacey, E. Timms, H. L. Tan, M. J. Kelley, C. R. Dunstan, T. Burgess, R. Elliott, A. Colombero, G. Elliott, S. Scully, H. Hsu, J. Sullivan, N. Hawkins, E. Davy, C. Capparelli, A. Eli, Y. X. Qian, S. Kaufman, I. Sarosi, V. Shalhoub, G. Senaldi, J. Guo, J. Delaney, and W. J. Boyle. Osteoprotegerin ligand is a cytokine that regulates osteoclast differentiation and activation. *Cell*, 93(2):165–176, Apr 1998.

[80] T. L. Burgess, Y. Qian, S. Kaufman, B. D. Ring, G. Van, C. Capparelli, M. Kelley, H. Hsu, W. J. Boyle, C. R. Dunstan, S. Hu, and D. L. Lacey. The ligand for osteoprotegerin (OPGL) directly activates mature osteoclasts. *J Cell Biol*, 145(3):527–538, May 1999.

[81] Y. Y. Kong, H. Yoshida, I. Sarosi, H. L. Tan, E. Timms, C. Capparelli, S. Morony, A. J. Oliveira dos Santos, G. Van, A. Itie, W. Khoo, A. Wakeham, C. R. Dunstan, D. L. Lacey, T. W. Mak, W. J. Boyle, and J. M. Penninger. OPGL is a key regulator of osteoclastogenesis, lymphocyte development and lymph-node organogenesis. *Nature*, 397(6717):315–323, Jan 1999.

[82] W. C. Dougall, M. Glaccum, K. Charrier, K. Rohrbach, K. Brasel, T. De Smedt, E. Daro, J. Smith, M. E. Tometsko, C. R. Maliszewski, A. Armstrong, V. Shen, S. Bain, D. Cosman, D. Anderson, P. J. Morrissey, J. J. Peschon, and J. Schuh. RANK is essential for osteoclast and lymph node development. *Genes Dev*, 13(18):2412–2424, Sep 1999.

[83] A. E. Grigoriadis, Z. Q. Wang, M. G. Cecchini, W. Hofstetter, R. Felix, H. A. Fleisch, and E. F. Wagner. c-Fos: a key regulator of osteoclast-macrophage lineage determination and bone remodeling. *Science*, 266(5184):443–448, Oct 1994.

[84] H. Huang, E.-J. Chang, J. Ryu, Z. H. Lee, Y. Lee, and H.-H. Kim. Induction of c-Fos and NFATc1 during RANKL-stimulated osteoclast differentiation is mediated by the p38 signaling pathway. *Biochem Biophys Res Commun*, 351(1):99–105, Dec 2006.

[85] M. A. Lomaga, W. C. Yeh, I. Sarosi, G. S. Duncan, C. Furlonger, A. Ho, S. Morony, C. Capparelli, G. Van, S. Kaufman, A. van der Heiden, A. Itie, A. Wakeham, W. Khoo, T. Sasaki, Z. Cao, J. M. Penninger, C. J. Paige, D. L. Lacey, C. R. Dunstan, W. J. Boyle, D. V. Goeddel, and T. W. Mak. TRAF6 deficiency results in osteopetrosis and defective interleukin-1, CD0, and LPS signaling. *Genes Dev*, 13(8):1015–1024, Apr 1999.

[86] Z. Q. Wang, C. Ovitt, A. E. Grigoriadis, U. Möhle-Steinlein, U. Rüther, and E. F. Wagner. Bone and haematopoietic defects in mice lacking c-fos. *Nature*, 360(6406):741–745, 1992.

[87] R. J. Sells Galvin, C. L. Gatlin, J. W. Horn, and T. R. Fuson. TGF-beta enhances osteoclast differentiation in hematopoietic cell cultures stimulated with RANKL and M-CSF. *Biochem Biophys Res Commun*, 265(1):233–239, Nov 1999.

[88] J. M. Quinn, K. Itoh, N. Udagawa, K. Hausler, H. Yasuda, N. Shima, A. Mizuno, K. Higashio, N. Takahashi, T. Suda, T. J. Martin, and M. T. Gillespie. Transforming growth factor beta affects osteoclast differentiation via direct and indirect actions. *J Bone Miner Res*, 16(10):1787–1794, Oct 2001.

[89] K. Itoh, N. Udagawa, T. Katagiri, S. Iemura, N. Ueno, H. Yasuda, K. Higashio, J. M. Quinn, M. T. Gillespie, T. J. Martin, T. Suda, and N. Takahashi. Bone morphogenetic protein 2 stimulates osteoclast differentiation and survival supported by receptor activator of nuclear factor-kappab ligand. *Endocrinology*, 142(8):3656–3662, Aug 2001.

[90] O. Kudo, Y. Fujikawa, I. Itonaga, A. Sabokbar, T. Torisu, and N. A. Athanasou. Proinflammatory cytokine (TNFalpha/IL-1alpha) induction of human osteoclast formation. *J Pathol*, 198(2):220–227, Oct 2002.

[91] O. Kudo, A. Sabokbar, A. Pocock, I. Itonaga, Y. Fujikawa, and N. A. Athanasou. Interleukin-6 and interleukin-11 support human osteoclast formation by a RANKL-independent mechanism. *Bone*, 32(1):1–7, Jan 2003.

[92] A. Sabokbar, O. Kudo, and N. A. Athanasou. Two distinct cellular mechanisms of osteoclast formation and bone resorption in periprosthetic osteolysis. *J Orthop Res*, 21(1):73–80, Jan 2003.

[93] Y. Azuma, K. Kaji, R. Katogi, S. Takeshita, and A. Kudo. Tumor necrosis factor-alpha induces differentiation of and bone resorption by osteoclasts. *J Biol Chem*, 275(7):4858–4864, Feb 2000.

[94] K. Kobayashi, N. Takahashi, E. Jimi, N. Udagawa, M. Takami, S. Kotake, N. Nakagawa, M. Kinosaki, K. Yamaguchi, N. Shima, H. Yasuda, T. Morinaga, K. Higashio, T. J. Martin, and T. Suda. Tumor necrosis factor alpha stimulates osteoclast differentiation by a mechanism independent of the ODF/RANKL-RANK interaction. *J Exp Med*, 191(2):275–286, Jan 2000.

[95] T. Suda, K. Kobayashi, E. Jimi, N. Udagawa, and N. Takahashi. The molecular basis of osteoclast differentiation and activation. *Novartis Found Symp*, 232:235–47; discussion 247–50, 2001.

[96] E. Jimi, I. Nakamura, L. T. Duong, T. Ikebe, N. Takahashi, G. A. Rodan, and T. Suda. Interleukin 1 induces multinucleation and bone-resorbing activity of osteoclasts in the absence of osteoblasts/stromal cells. *Exp Cell Res*, 247(1):84–93, Feb 1999.

[97] W. S. Simonet, D. L. Lacey, C. R. Dunstan, M. Kelley, M. S. Chang, R. Lthy, H. Q. Nguyen, S. Wooden, L. Bennett, T. Boone, G. Shimamoto, M. DeRose, R. Elliott, A. Colombero, H. L. Tan, G. Trail, J. Sullivan, E. Davy, N. Bucay, L. Renshaw-Gegg, T. M. Hughes, D. Hill, W. Pattison, P. Campbell, S. Sander, G. Van, J. Tarpley, P. Derby, R. Lee, and W. J. Boyle. Osteoprotegerin: a novel

secreted protein involved in the regulation of bone density. *Cell*, 89(2):309–319, Apr 1997.

[98] E. Tsuda, M. Goto, S. Mochizuki, K. Yano, F. Kobayashi, T. Morinaga, and K. Higashio. Isolation of a novel cytokine from human fibroblasts that specifically inhibits osteoclastogenesis. *Biochem Biophys Res Commun*, 234(1):137–142, May 1997.

[99] J. G. Emery, P. McDonnell, M. B. Burke, K. C. Deen, S. Lyn, C. Silverman, E. Dul, E. R. Appelbaum, C. Eichman, R. DiPrinzio, R. A. Dodds, I. E. James, M. Rosenberg, J. C. Lee, and P. R. Young. Osteoprotegerin is a receptor for the cytotoxic ligand TRAIL. *J Biol Chem*, 273(23):14363–14367, Jun 1998.

[100] U. M. Malyankar, M. Scatena, K. L. Suchland, T. J. Yun, E. A. Clark, and C. M. Giachelli. Osteoprotegerin is an alpha vbeta 3-induced, NF-kappa B-dependent survival factor for endothelial cells. *J Biol Chem*, 275(28):20959–20962, Jul 2000.

[101] L. B. Pritzker, M. Scatena, and C. M. Giachelli. The role of osteoprotegerin and tumor necrosis factor-related apoptosis-inducing ligand in human microvascular endothelial cell survival. *Mol Biol Cell*, 15(6):2834–2841, Jun 2004.

[102] I. Buschmann and W. Schaper. Arteriogenesis versus angiogenesis: Two mechanisms of vessel growth. *News Physiol Sci*, 14:121–125, Jun 1999.

[103] G. D. Yancopoulos, S. Davis, N. W. Gale, J. S. Rudge, S. J. Wiegand, and J. Holash. Vascular-specific growth factors and blood vessel formation. *Nature*, 407(6801):242–248, Sep 2000.

[104] A. G. Mikos, S. W. Herring, P. Ochareon, J. Elisseeff, H. H. Lu, R. Kandel, F. J. Schoen, M. Toner, D. Mooney, A. Atala, M. E. Van Dyke, D. Kaplan, and G. Vunjak-Novakovic. Engineering complex tissues. *Tissue Eng*, 12(12):3307–3339, Dec 2006.

[105] N. Ferrara, H.-P. Gerber, and J. LeCouter. The biology of VEGF and its receptors. *Nat Med*, 9(6):669–676, Jun 2003.

[106] D. W. Leung, G. Cachianes, W. J. Kuang, D. V. Goeddel, and N. Ferrara. Vascular endothelial growth factor is a secreted angiogenic mitogen. *Science*, 246(4935):1306–1309, Dec 1989.

[107] N. Ferrara, D. W. Leung, G. Cachianes, J. Winer, and W. J. Henzel. Purification and cloning of vascular endothelial growth factor secreted by pituitary folliculostellate cells. *Methods Enzymol*, 198:391–405, 1991.

[108] H. P. Gerber, A. McMurtrey, J. Kowalski, M. Yan, B. A. Keyt, V. Dixit, and N. Ferrara. Vascular endothelial growth factor regulates endothelial cell survival through the phosphatidylinositol 3'-kinase/Akt signal transduction pathway. Requirement for Flk-1/KDR activation. *J Biol Chem*, 273(46):30336–30343, Nov 1998.

[109] V. Midy and J. Plouët. Vasculotropin/vascular endothelial growth factor induces differentiation in cultured osteoblasts. *Biochem Biophys Res Commun*, 199(1):380–386, Feb 1994.

[110] H. F. Dvorak, L. F. Brown, M. Detmar, and A. M. Dvorak. Vascular permeability factor/vascular endothelial growth factor, microvascular hyperpermeability, and angiogenesis. *Am J Pathol*, 146(5):1029–1039, May 1995.

[111] P. J. Keck, S. D. Hauser, G. Krivi, K. Sanzo, T. Warren, J. Feder, and D. T. Connolly. Vascular permeability factor, an endothelial cell mitogen related to PDGF. *Science*, 246(4935):1309–1312, Dec 1989.

[112] A. P. Levy, N. S. Levy, S. Wegner, and M. A. Goldberg. Transcriptional regulation of the rat vascular endothelial growth factor gene by hypoxia. *J Biol Chem*, 270(22):13333–13340, Jun 1995.

[113] H. P. Gerber, F. Condorelli, J. Park, and N. Ferrara. Differential transcriptional regulation of the two vascular endothelial growth factor receptor genes. Flt-1, but not Flk-1/KDR, is up-regulated by hypoxia. *J Biol Chem*, 272(38):23659–23667, Sep 1997.

[114] T. Cohen, H. Gitay-Goren, R. Sharon, M. Shibuya, R. Halaban, B. Z. Levi, and G. Neufeld. VEGF121, a vascular endothelial growth factor (VEGF) isoform lacking heparin binding ability, requires cell-surface heparan sulfates for efficient binding to the VEGF receptors of human melanoma cells. *J Biol Chem*, 270(19):11322–11326, May 1995.

[115] H. Gitay-Goren, S. Soker, I. Vlodavsky, and G. Neufeld. The binding of vascular endothelial growth factor to its receptors is dependent on cell surface-associated heparin-like molecules. *J Biol Chem*, 267(9):6093–6098, Mar 1992.

[116] H. Gitay-Goren, R. Halaban, and G. Neufeld. Human melanoma cells but not normal melanocytes express vascular endothelial growth factor receptors. *Biochem Biophys Res Commun*, 190(3):702–708, Feb 1993.

[117] D. R. Senger, S. J. Galli, A. M. Dvorak, C. A. Perruzzi, V. S. Harvey, and H. F. Dvorak. Tumor cells secrete a vascular permeability factor that promotes accumulation of ascites fluid. *Science*, 219(4587):983–985, Feb 1983.

[118] N. Ferrara and W. J. Henzel. Pituitary follicular cells secrete a novel heparin-binding growth factor specific for vascular endothelial cells. *Biochem Biophys Res Commun*, 161(2):851–858, Jun 1989.

[119] K. A. Houck, D. W. Leung, A. M. Rowland, J. Winer, and N. Ferrara. Dual regulation of vascular endothelial growth factor bioavailability by genetic and proteolytic mechanisms. *J Biol Chem*, 267(36):26031–26037, Dec 1992.

[120] B. A. Keyt, L. T. Berleau, H. V. Nguyen, H. Chen, H. Heinsohn, R. Vandlen, and N. Ferrara. The carboxyl-terminal domain (111-165) of vascular endothelial growth factor is critical for its mitogenic potency. *J Biol Chem*, 271(13):7788–7795, Mar 1996.

[121] M. F. Carlevaro, S. Cermelli, R. Cancedda, and F. Descalzi Cancedda. Vascular endothelial growth factor (VEGF) in cartilage neovascularization and chondrocyte differentiation: auto-paracrine role during endochondral bone formation. *J Cell Sci*, 113 (Pt 1):59–69, Jan 2000.

[122] A. Horner, N. J. Bishop, S. Bord, C. Beeton, A. W. Kelsall, N. Coleman, and J. E. Compston. Immunolocalisation of vascular endothelial growth factor (VEGF) in human neonatal growth plate cartilage. *J Anat*, 194 (Pt 4):519–524, May 1999.

[123] H. P. Gerber, T. H. Vu, A. M. Ryan, J. Kowalski, Z. Werb, and N. Ferrara. VEGF couples hypertrophic cartilage remodeling, ossification and angiogenesis during endochondral bone formation. *Nat Med*, 5(6):623–628, Jun 1999.

[124] C. E. Farnum and N. J. Wilsman. Cellular turnover at the chondro-osseous junction of growth plate cartilage: analysis by serial sections at the light microscopical level. *J Orthop Res*, 7(5):654–666, 1989.

[125] J. K. Burkus, T. M. Ganey, and J. A. Ogden. Development of the cartilage canals and the secondary center of ossification in the distal chondroepiphysis of the prenatal human femur. *Yale J Biol Med*, 66(3):193–202, 1993.

[126] T. M. Ganey, S. M. Love, and J. A. Ogden. Development of vascularization in the chondroepiphysis of the rabbit. *J Orthop Res*, 10(4):496–510, Jul 1992.

[127] P. Carmeliet, V. Ferreira, G. Breier, S. Pollefeyt, L. Kieckens, M. Gertsenstein, M. Fahrig, A. Vandenhoeck, K. Harpal, C. Eberhardt, C. Declercq, J. Pawling, L. Moons, D. Collen, W. Risau, and A. Nagy. Abnormal blood vessel development and lethality in embryos lacking a single VEGF allele. *Nature*, 380(6573):435–439, Apr 1996.

[128] N. Ferrara, K. Carver-Moore, H. Chen, M. Dowd, L. Lu, K. S. O'Shea, L. Powell-Braxton, K. J. Hillan, and M. W. Moore. Heterozygous embryonic lethality induced by targeted inactivation of the VEGF gene. *Nature*, 380(6573):439–442, Apr 1996.

[129] E. Zelzer, W. McLean, Y.-S. Ng, N. Fukai, A. M. Reginato, S. Lovejoy, P. A. D'Amore, and B. R. Olsen. Skeletal defects in VEGF(120/120) mice reveal multiple roles for VEGF in skeletogenesis. *Development*, 129(8):1893–1904, Apr 2002.

[130] J. J. Haigh, H. P. Gerber, N. Ferrara, and E. F. Wagner. Conditional inactivation of VEGF-A in areas of collagen2a1 expression results in embryonic lethality in the heterozygous state. *Development*, 127(7):1445–1453, Apr 2000.

[131] E. Zelzer, R. Mamluk, N. Ferrara, R. S. Johnson, E. Schipani, and B. R. Olsen. VEGFA is necessary for chondrocyte survival during bone development. *Development*, 131(9):2161–2171, May 2004.

[132] J. Glowacki. Angiogenesis in fracture repair. *Clin Orthop Relat Res*, 355(Suppl):S82–S89, Oct 1998.

[133] J. Hollinger. Factors for osseous repair and delivery. Part I. *J Craniofac Surg*, 4(2):102–108, Apr 1993.

[134] T. Pufe, B. Wildemann, W. Petersen, R. Mentlein, M. Raschke, and G. Schmidmaier. Quantitative measurement of the splice variants 120 and 164 of the angiogenic peptide vascular endothelial growth factor in the time flow of fracture healing: a study in the rat. *Cell Tissue Res*, 309(3):387–392, Sep 2002.

[135] S. Weiss, G. Zimmermann, R. Baumgart, P. Kasten, M. Bidlingmaier, and P. Henle. Systemic regulation of angiogenesis and matrix degradation in bone regeneration–distraction osteogenesis compared to rigid fracture healing. *Bone*, 37(6):781–790, Dec 2005.

[136] G. Li, A. H. Simpson, J. Kenwright, and J. T. Triffitt. Effect of lengthening rate on angiogenesis during distraction osteogenesis. *J Orthop Res*, 17(3):362–367, May 1999.

[137] I. H. Choi, C. Y. Chung, T.-J. Cho, and W. J. Yoo. Angiogenesis and mineralization during distraction osteogenesis. *J Korean Med Sci*, 17(4):435–447, Aug 2002.

[138] N. M. Rowe, B. J. Mehrara, J. S. Luchs, M. E. Dudziak, D. S. Steinbrech, P. B. Illei, G. J. Fernandez, G. K. Gittes, and M. T. Longaker. Angiogenesis during mandibular distraction osteogenesis. *Ann Plast Surg*, 42(5):470–475, May 1999.

[139] A. Rachmiel, N. Rozen, M. Peled, and D. Lewinson. Characterization of midface maxillary membranous bone formation during distraction osteogenesis. *Plast Reconstr Surg*, 109(5):1611–1620, Apr 2002.

[140] I. H. Choi, J. H. Ahn, C. Y. Chung, and T. J. Cho. Vascular proliferation and blood supply during distraction osteogenesis: a scanning electron microscopic observation. *J Orthop Res*, 18(5):698–705, Sep 2000.

[141] J. Aronson. Temporal and spatial increases in blood flow during distraction osteogenesis. *Clin Orthop Relat Res*, 301(301):124–131, Apr 1994.

[142] J. Hu, S. Zou, J. Li, Y. Chen, D. Wang, and Z. Gao. Temporospatial expression of vascular endothelial growth factor and basic fibroblast growth factor during mandibular distraction osteogenesis. *J Craniomaxillofac Surg*, 31(4):238–243, Aug 2003.

[143] A. B. M. Rabie, L. Shum, and A. Chayanupatkul. VEGF and bone formation in the glenoid fossa during forward mandibular positioning. *Am J Orthod Dentofacial Orthop*, 122(2):202–209, Aug 2002.

[144] L. Shum, A. B. M. Rabie, and U. Hägg. Vascular endothelial growth factor expression and bone formation in posterior glenoid fossa during stepwise mandibular advancement. *Am J Orthod Dentofacial Orthop*, 125(2):185–190, Feb 2004.

[145] M. M. Deckers, M. Karperien, C. van der Bent, T. Yamashita, S. E. Papapoulos, and C. W. Löwik. Expression of vascular endothelial growth factors and their receptors during osteoblast differentiation. *Endocrinology*, 141(5):1667–1674, May 2000.

[146] D. S. Wang, K. Yamazaki, K. Nohtomi, K. Shizume, K. Ohsumi, M. Shibuya, H. Demura, and K. Sato. Increase of vascular endothelial growth factor mRNA expression by 1,25-dihydroxyvitamin D3 in human osteoblast-like cells. *J Bone Miner Res*, 11(4):472–479, Apr 1996.

[147] D. S. Wang, M. Miura, H. Demura, and K. Sato. Anabolic effects of 1,25-dihydroxyvitamin D3 on osteoblasts are enhanced by vascular endothelial growth factor produced by osteoblasts and by growth factors produced by endothelial cells. *Endocrinology*, 138(7):2953–2962, Jul 1997.

[148] M. M. L. Deckers, R. L. van Bezooijen, G. van der Horst, J. Hoogendam, C. van Der Bent, S. E. Papapoulos, and C. W. G. M. Löwik. Bone morphogenetic proteins stimulate angiogenesis through osteoblast-derived vascular endothelial growth factor A. *Endocrinology*, 143(4):1545–1553, Apr 2002.

[149] P. J. Bouletreau, S. M. Warren, J. A. Spector, Z. M. Peled, R. P. Gerrets, J. A. Greenwald, and M. T. Longaker. Hypoxia and VEGF up-regulate BMP-2 mRNA and protein expression in microvascular endothelial cells: implications for fracture healing. *Plast Reconstr Surg*, 109(7):2384–2397, Jun 2002.

[150] J. Mandelin, T. F. Li, M. Liljeström, M. E. Kroon, R. Hanemaaijer, S. Santavirta, and Y. T. Konttinen. Imbalance of rANKL/RANK/OPG system in interface tissue in loosening of total hip replacement. *J Bone Joint Surg Br*, 85(8):1196–1201, Nov 2003.

[151] H. D. Kim and R. F. Valentini. Retention and activity of BMP-2 in hyaluronic acid-based scaffolds in vitro. *J Biomed Mater Res*, 59(3):573–584, Mar 2002.

[152] J.-K. Min, Y.-M. Kim, Y.-M. Kim, E.-C. Kim, Y. S. Gho, I.-J. Kang, S.-Y. Lee, Y.-Y. Kong, and Y.-G. Kwon. Vascular endothelial growth factor up-regulates expression of receptor activator of NF-kappa B (RANK) in endothelial cells. Concomitant increase of angiogenic responses to RANK ligand. *J Biol Chem*, 278(41):39548–39557, Oct 2003.

[153] H. Ito, M. Koefoed, P. Tiyapatanaputi, K. Gromov, J. J. Goater, J. Carmouche, X. Zhang, P. T. Rubery, J. Rabinowitz, R. J. Samulski, T. Nakamura, K. Soballe, R. J. O'Keefe, B. F. Boyce, and E. M. Schwarz. Remodeling of cortical bone allografts mediated by adherent rAAV-RANKL and VEGF gene therapy. *Nat Med*, 11(3):291–297, Mar 2005.

[154] M. Nakagawa, T. Kaneda, T. Arakawa, S. Morita, T. Sato, T. Yomada, K. Hanada, M. Kumegawa, and Y. Hakeda. Vascular endothelial growth factor

(VEGF) directly enhances osteoclastic bone resorption and survival of mature osteoclasts. *FEBS Lett*, 473(2):161–164, May 2000.

[155] S. Niida, M. Kaku, H. Amano, H. Yoshida, H. Kataoka, S. Nishikawa, K. Tanne, N. Maeda, S. Nishikawa, and H. Kodama. Vascular endothelial growth factor can substitute for macrophage colony-stimulating factor in the support of osteoclastic bone resorption. *J Exp Med*, 190(2):293–298, Jul 1999.

[156] I. Kodama, S. Niida, M. Sanada, Y. Yoshiko, M. Tsuda, N. Maeda, and K. Ohama. Estrogen regulates the production of VEGF for osteoclast formation and activity in op/op mice. *J Bone Miner Res*, 19(2):200–206, Feb 2004.

[157] B. Barleon, S. Sozzani, D. Zhou, H. A. Weich, A. Mantovani, and D. Marmé. Migration of human monocytes in response to vascular endothelial growth factor (VEGF) is mediated via the VEGF receptor flt-1. *Blood*, 87(8):3336–3343, Apr 1996.

[158] S. Yao, D. Liu, F. Pan, and G. E. Wise. Effect of vascular endothelial growth factor on RANK gene expression in osteoclast precursors and on osteoclastogenesis. *Arch Oral Biol*, 51(7):596–602, Jul 2006.

[159] S. E. Aldridge, T. W J Lennard, J. R. Williams, and M. A. Birch. Vascular endothelial growth factor acts as an osteolytic factor in breast cancer metastases to bone. *Br J Cancer*, 92(8):1531–1537, Apr 2005.

[160] K. Henriksen, M. Karsdal, J.-M. Delaisse, and M. T. Engsig. RANKL and vascular endothelial growth factor (VEGF) induce osteoclast chemotaxis through an ERK1/2-dependent mechanism. *J Biol Chem*, 278(49):48745–48753, Dec 2003.

[161] W. P. Ren, D. C. Markel, R. Zhang, X. Peng, B. Wu, H. Monica, and P. H. Wooley. Association between UHMWPE particle-induced inflammatory osteoclastogenesis and expression of RANKL, VEGF, and Flt-1 in vivo. *Biomaterials*, 27(30):5161–5169, Oct 2006.

[162] K. A. Athanasiou, C. Zhu, D. R. Lanctot, C. M. Agrawal, and X. Wang. Fundamentals of biomechanics in tissue engineering of bone. *Tissue Eng*, 6(4):361–381, Aug 2000.

[163] J. M. Lane and H. S. Sandhu. Current approaches to experimental bone grafting. *Orthop Clin North Am*, 18(2):213–225, Apr 1987.

[164] J. B. Leach, K. A. Bivens, C. N. Collins, and C. E. Schmidt. Development of photocrosslinkable hyaluronic acid-polyethylene glycol-peptide composite hydrogels for soft tissue engineering. *J Biomed Mater Res A*, 70(1):74–82, Jul 2004.

[165] J. R. Fraser, T. C. Laurent, and U. B. Laurent. Hyaluronan: its nature, distribution, functions and turnover. *J Intern Med*, 242(1):27–33, Jul 1997.

[166] M. A. Pozo, E. A. Balazs, and C. Belmonte. Reduction of sensory responses to passive movements of inflamed knee joints by hylan, a hyaluronan derivative. *Exp Brain Res*, 116(1):3–9, Aug 1997.

[167] J. G. Peyron. Intraarticular hyaluronan injections in the treatment of osteoarthritis: state-of-the-art review. *J Rheumatol Suppl*, 39:10–15, Aug 1993.

[168] B. P. Toole. Hyaluronan in morphogenesis. *J Intern Med*, 242(1):35–40, Jul 1997.

[169] D. C. West, D. M. Shaw, P. Lorenz, N. S. Adzick, and M. T. Longaker. Fibrotic healing of adult and late gestation fetal wounds correlates with increased hyaluronidase activity and removal of hyaluronan. *Int J Biochem Cell Biol*, 29(1):201–210, Jan 1997.

[170] B. Gerdin and R. Hällgren. Dynamic role of hyaluronan (HYA) in connective tissue activation and inflammation. *J Intern Med*, 242(1):49–55, Jul 1997.

[171] W. Y. Chen and G. Abatangelo. Functions of hyaluronan in wound repair. *Wound Repair Regen*, 7(2):79–89, 1999.

[172] P. Pavasant, T. M. Shizari, and C. B. Underhill. Distribution of hyaluronan in the epiphysial growth plate: turnover by CD44-expressing osteoprogenitor cells. *J Cell Sci*, 107 (Pt 10):2669–2677, Oct 1994.

[173] P. Pavasant, T. Shizari, and C. B. Underhill. Hyaluronan contributes to the enlargement of hypertrophic lacunae in the growth plate. *J Cell Sci*, 109 (Pt 2):327–334, Feb 1996.

[174] O. Oksala, T. Salo, R. Tammi, L. Häkkinen, M. Jalkanen, P. Inki, and H. Larjava. Expression of proteoglycans and hyaluronan during wound healing. *J Histochem Cytochem*, 43(2):125–135, Feb 1995.

[175] P. H. Weigel, S. J. Frost, R. D. LeBoeuf, and C. T. McGary. The specific interaction between fibrin(ogen) and hyaluronan: possible consequences in haemostasis, inflammation and wound healing. *Ciba Found Symp*, 143:248–61; discussion 261–4, 281–5, 1989.

[176] A. Aruffo, I. Stamenkovic, M. Melnick, C. B. Underhill, and B. Seed. CD44 is the principal cell surface receptor for hyaluronate. *Cell*, 61(7):1303–1313, Jun 1990.

[177] C. Hardwick, K. Hoare, R. Owens, H. P. Hohn, M. Hook, D. Moore, V. Cripps, L. Austen, D. M. Nance, and E. A. Turley. Molecular cloning of a novel hyaluronan receptor that mediates tumor cell motility. *J Cell Biol*, 117(6):1343–1350, Jun 1992.

[178] E. A. Turley, P. W. Noble, and L. Y. W. Bourguignon. Signaling properties of hyaluronan receptors. *J Biol Chem*, 277(7):4589–4592, Feb 2002.

[179] M. I. Tammi, A. J. Day, and E. A. Turley. Hyaluronan and homeostasis: a balancing act. *J Biol Chem*, 277(7):4581–4584, Feb 2002.

[180] V. Nehls and W. Hayen. Are hyaluronan receptors involved in three-dimensional cell migration? *Histol Histopathol*, 15(2):629–636, Apr 2000.

[181] B. A. Neudecker, R. Stern, and M. K. Connolly. Aberrant serum hyaluronan and hyaluronidase levels in scleroderma. *Br J Dermatol*, 150(3):469–476, Mar 2004.

[182] J. George and R. Stern. Serum hyaluronan and hyaluronidase: very early markers of toxic liver injury. *Clin Chim Acta*, 348(1-2):189–197, Oct 2004.

[183] P. G. McGuire, J. J. Castellot, and R. W. Orkin. Size-dependent hyaluronate degradation by cultured cells. *J Cell Physiol*, 133(2):267–276, Nov 1987.

[184] D. C. West and S. Kumar. The effect of hyaluronate and its oligosaccharides on endothelial cell proliferation and monolayer integrity. *Exp Cell Res*, 183(1):179–196, Jul 1989.

[185] M. Culty, H. A. Nguyen, and C. B. Underhill. The hyaluronan receptor (CD44) participates in the uptake and degradation of hyaluronan. *J Cell Biol*, 116(4):1055–1062, Feb 1992.

[186] C. N. Bertolami, S. Berg, and D. V. Messadi. Binding and internalization of hyaluronate by human cutaneous fibroblasts. *Matrix*, 12(1):11–21, Feb 1992.

[187] D. H. Bernanke and R. W. Orkin. Hyaluronidase activity in embryonic chick heart muscle and cushion tissue and cells. *Dev Biol*, 106(2):351–359, Dec 1984.

[188] C. K. Ng, C. J. Handley, B. N. Preston, and H. C. Robinson. The extracellular processing and catabolism of hyaluronan in cultured adult articular cartilage explants. *Arch Biochem Biophys*, 298(1):70–79, Oct 1992.

[189] C. B. Underhill, H. A. Nguyen, M. Shizari, and M. Culty. CD44 positive macrophages take up hyaluronan during lung development. *Dev Biol*, 155(2):324–336, Feb 1993.

[190] G. I. Frost and R. Stern. A microtiter-based assay for hyaluronidase activity not requiring specialized reagents. *Anal Biochem*, 251(2):263–269, Sep 1997.

[191] J. P. Fisher, Z. Lalani, C. M. Bossano, E. M. Brey, N. Demian, C. M. Johnston, D. Dean, J. A. Jansen, M. E. K. Wong, and A. G. Mikos. Effect of biomaterial properties on bone healing in a rabbit tooth extraction socket model. *J Biomed Mater Res A*, 68(3):428–438, Mar 2004.

[192] E. J. P. Jansen, R. E. J. Sladek, H. Bahar, A. Yaffe, M. J. Gijbels, R. Kuijer, S. K. Bulstra, N. A. Guldemond, I. Binderman, and L. H. Koole. Hydrophobicity as a design criterion for polymer scaffolds in bone tissue engineering. *Biomaterials*, 26(21):4423–4431, Jul 2005.

[193] L. S. Liu, A. Y. Thompson, M. A. Heidaran, J. W. Poser, and R. C. Spiro. An osteoconductive collagen/hyaluronate matrix for bone regeneration. *Biomaterials*, 20(12):1097–1108, Jun 1999.

[194] L. Huang, Y. Y. Cheng, P. L. Koo, K. M. Lee, L. Qin, J. C Y Cheng, and S. M. Kumta. The effect of hyaluronan on osteoblast proliferation and differentiation in rat calvarial-derived cell cultures. *J Biomed Mater Res A*, 66(4):880–884, Sep 2003.

[195] H. Eckardt, K. S. Christensen, M. Lind, E. S. Hansen, D. W. R. Hall, and I. Hvid. Recombinant human bone morphogenetic protein 2 enhances bone healing in an experimental model of fractures at risk of non-union. *Injury*, 36(4):489–494, Apr 2005.

[196] M. L. Radomsky, T. B. Aufdemorte, L. D. Swain, W. C. Fox, R. C. Spiro, and J. W. Poser. Novel formulation of fibroblast growth factor-2 in a hyaluronan gel accelerates fracture healing in nonhuman primates. *J Orthop Res*, 17(4):607–614, Jul 1999.

[197] D. C. West, I. N. Hampson, F. Arnold, and S. Kumar. Angiogenesis induced by degradation products of hyaluronic acid. *Science*, 228(4705):1324–1326, Jun 1985.

[198] P. Rooney, M. Wang, P. Kumar, and S. Kumar. Angiogenic oligosaccharides of hyaluronan enhance the production of collagens by endothelial cells. *J Cell Sci*, 105 (Pt 1):213–218, May 1993.

[199] R. Deed, P. Rooney, P. Kumar, J. D. Norton, J. Smith, A. J. Freemont, and S. Kumar. Early-response gene signalling is induced by angiogenic oligosaccharides of hyaluronan in endothelial cells. Inhibition by non-angiogenic, high-molecular-weight hyaluronan. *Int J Cancer*, 71(2):251–256, Apr 1997.

[200] H. F. Dvorak, V. S. Harvey, P. Estrella, L. F. Brown, J. McDonagh, and A. M. Dvorak. Fibrin containing gels induce angiogenesis. Implications for tumor stroma generation and wound healing. *Lab Invest*, 57(6):673–686, Dec 1987.

[201] X. Z. Shu, Y. Liu, Y. Luo, M. C. Roberts, and G. D. Prestwich. Disulfide cross-linked hyaluronan hydrogels. *Biomacromolecules*, 3(6):1304–1311, 2002.

[202] W.N.E. van Dijk-Wolthuis, O. Franssen, H. Talsma, M.J. van Steenbergen, J.J. Kettenes van den Bosch, and W.E. Hennink. Synthesis, characterization, and polymerization of glycidyl methacrylate derivatized dextran. *Macromolecules*, 28(18):6317–6322, 1995.

[203] K. A. Smeds, A. Pfister-Serres, D. L. Hatchell, and M. W. Grinstaff. Synthesis of a novel polysaccharide hydrogel. *J M S - Pure Appl Chem*, A36:981–989, 1999.

[204] M. Inukai, Y. Jin, C. Yomota, and M. Yonese. Preparation and characterization of hyaluronate-hydroxyethyl acrylate blend hydrogel for controlled release device. *Chem Pharm Bull (Tokyo)*, 48(6):850–854, Jun 2000.

[205] S. H. Kim and C. C. Chu. Synthesis and characterization of dextran-methacrylate hydrogels and structural study by SEM. *J Biomed Mater Res*, 49(4):517–527, Mar 2000.

[206] J. Trudel and S. P. Massia. Assessment of the cytotoxicity of photocrosslinked dextran and hyaluronan-based hydrogels to vascular smooth muscle cells. *Biomaterials*, 23(16):3299–3307, Aug 2002.

[207] J.B. Leach, K.A. Bivens, C.W. Patrick, and C.E. Schmidt. Photocrosslinked hyaluronic acid hydrogels: Natural, biodegradable tissue engineering scaffolds. *Biotechnol Bioeng*, 82(5):578–589, 2003.

[208] K. Tomihata and Y. Ikada. Preparation of cross-linked hyaluronic acid films of low water content. *Biomaterials*, 18(3):189–195, Feb 1997.

[209] W. N. van Dijk-Wolthuis, M. J. van Steenbergen, W. J. Underberg, and W. E. Hennink. Degradation kinetics of methacrylated dextrans in aqueous solution. *J Pharm Sci*, 86(4):413–417, Apr 1997.

[210] J. B. Leach and C. E. Schmidt. *Encyclopedia of Biomaterials and Biomedical Engineering*, chapter Hyaluronan, pages 779–789. Marcel Dekker, 2004.

[211] J. R. Glass, K. T. Dickerson, K. Stecker, and J. W. Polarek. Characterization of a hyaluronic acid-Arg-Gly-Asp peptide cell attachment matrix. *Biomaterials*, 17(11):1101–1108, Jun 1996.

[212] X. Z. Shu, K. Ghosh, Y. Liu, F. S. Palumbo, Y. Luo, R. A. Clark, and G. D. Prestwich. Attachment and spreading of fibroblasts on an RGD peptide-modified injectable hyaluronan hydrogel. *J Biomed Mater Res A*, 68(2):365–375, Feb 2004.

[213] L. Benedetti, R. Cortivo, T. Berti, A. Berti, F. Pea, M. Mazzo, M. Moras, and G. Abatangelo. Biocompatibility and biodegradation of different hyaluronan derivatives (Hyaff) implanted in rats. *Biomaterials*, 14(15):1154–1160, Dec 1993.

[214] J. A. Burdick, C. Chung, X. Jia, M. A. Randolph, and R. Langer. Controlled degradation and mechanical behavior of photopolymerized hyaluronic acid networks. *Biomacromolecules*, 6(1):386–391, 2005.

[215] L. A. Solchaga, J. E. Dennis, V. M. Goldberg, and A. I. Caplan. Hyaluronic acid-based polymers as cell carriers for tissue-engineered repair of bone and cartilage. *J Orthop Res*, 17(2):205–213, Mar 1999.

[216] J. Gao, J. E. Dennis, L. A. Solchaga, A. S. Awadallah, V. M. Goldberg, and A. I. Caplan. Tissue-engineered fabrication of an osteochondral composite graft

using rat bone marrow-derived mesenchymal stem cells. *Tissue Eng*, 7(4):363–371, Aug 2001.

[217] J. Gao, J. E. Dennis, L. A. Solchaga, V. M. Goldberg, and A. I. Caplan. Repair of osteochondral defect with tissue-engineered two-phase composite material of injectable calcium phosphate and hyaluronan sponge. *Tissue Eng*, 8(5):827–837, Oct 2002.

[218] G. Lisignoli, N. Zini, G. Remiddi, A. Piacentini, A. Puggioli, C. Trimarchi, M. Fini, N. M. Maraldi, and A. Facchini. Basic fibroblast growth factor enhances in vitro mineralization of rat bone marrow stromal cells grown on non-woven hyaluronic acid based polymer scaffold. *Biomaterials*, 22(15):2095–2105, Aug 2001.

[219] N. J. Turner, C. M. Kielty, M. G. Walker, and A. E. Canfield. A novel hyaluronan-based biomaterial (Hyaff-11) as a scaffold for endothelial cells in tissue engineered vascular grafts. *Biomaterials*, 25(28):5955–5964, Dec 2004.

[220] W. E. Hennink, H. Talsma, J. C. H. Borchert, S. C. DeSmedt, and J. Demeester. Controlled release of proteins from dextran hydrogels. *J Control Release*, 39:47–55, 1996.

[221] J. B. Leach and C. E. Schmidt. Characterization of protein release from photocrosslinkable hyaluronic acid-polyethylene glycol hydrogel tissue engineering scaffolds. *Biomaterials*, 26(2):125–135, Jan 2005.

[222] W. R. Gombotz, M. S. Healy, and L. R. Brown. Very low temperature casting of controlled release microspheres. U. S. Patent:5,019,400, 1991.

[223] O. L. Johnson, W. Jaworowicz, J. L. Cleland, L. Bailey, M. Charnis, E. Duenas, C. Wu, D. Shepard, S. Magil, T. Last, A. J. Jones, and S. D. Putney. The stabilization and encapsulation of human growth hormone into biodegradable microspheres. *Pharm Res*, 14(6):730–735, Jun 1997.

[224] J. L. Cleland, E. T. Duenas, A. Park, A. Daugherty, J. Kahn, J. Kowalski, and A. Cuthbertson. Development of poly-(D,L-lactide–coglycolide) microsphere formulations containing recombinant human vascular endothelial growth factor to promote local angiogenesis. *J Control Release*, 72(1-3):13–24, May 2001.

[225] D. H. R. Kempen, L. Lu, C. Kim, X. Zhu, W. J. A. Dhert, B. L. Currier, and M. J. Yaszemski. Controlled drug release from a novel injectable biodegradable microsphere/scaffold composite based on poly(propylene fumarate). *J Biomed Mater Res A*, 77(1):103–111, Apr 2006.

[226] Y. Hu, J. O. Hollinger, and K. G. Marra. Controlled release from coated polymer microparticles embedded in tissue-engineered scaffolds. *J Drug Target*, 9(6):431–438, 2001.

[227] J. L. Smith, L/ Jin, T. Parsons, T. Turek, E. Ron, C. M. Philbrook, R. A. Kenley, L. Marden, J. Hollinger, M. P. G. Bostrom, E. Tomin, and J. M. Lane. Osseous regeneration in preclinical models using bioabsorbable delivery technology for recombinant human bone morphogenetic protein-2 (rhBMP-2). *J Control Release*, 36(1-2):183–195, 1995.

[228] S. S. Duggirala, J. B. Rodgers, and P. P. DeLuca. The evaluation of lyophilized polymer matrices for administering recombinant human bone morphogenetic protein-2. *Pharm Dev Technol*, 1(2):165–174, Jul 1996.

[229] B. H. Woo, B. F. Fink, R. Page, J. A. Schrier, Y. W. Jo, G. Jiang, M. DeLuca, H. C. Vasconez, and P. P. DeLuca. Enhancement of bone growth by sustained delivery of recombinant human bone morphogenetic protein-2 in a polymeric matrix. *Pharm Res*, 18(12):1747–1753, Dec 2001.

[230] T. P. Richardson, M. C. Peters, A. B. Ennett, and D. J. Mooney. Polymeric system for dual growth factor delivery. *Nat Biotechnol*, 19(11):1029–1034, Nov 2001.

[231] Y. H. Yun, D. J. Goetz, P. Yellen, and W. Chen. Hyaluronan microspheres for sustained gene delivery and site-specific targeting. *Biomaterials*, 25(1):147–157, Jan 2004.

[232] S. T. Lim, G. P. Martin, D. J. Berry, and M. B. Brown. Preparation and evaluation of the in vitro drug release properties and mucoadhesion of novel microspheres of hyaluronic acid and chitosan. *J Control Release*, 66(2-3):281–292, May 2000.

[233] S. T. Lim, B. Forbes, D. J. Berry, G. P. Martin, and M. B. Brown. In vivo evaluation of novel hyaluronan/chitosan microparticulate delivery systems for the nasal delivery of gentamicin in rabbits. *Int J Pharm*, 231(1):73–82, Jan 2002.

[234] S. Lu, W. F. Ramirez, and K. S. Anseth. Photopolymerized, multilaminated matrix devices with optimized nonuniform initial concentration profiles to control drug release. *J Pharm Sci*, 89(1):45–51, Jan 2000.

[235] X. Yu, G. P. Dillon, and R. B. Bellamkonda. A laminin and nerve growth factor-laden three-dimensional scaffold for enhanced neurite extension. *Tissue Eng*, 5(4):291–304, Aug 1999.

[236] Y. An and J. A. Hubbell. Intraarterial protein delivery via intimally-adherent bilayer hydrogels. *J Control Release*, 64(1-3):205–215, Feb 2000.

[237] J.A. Rowley, Z. Sun, D. Goldman, and D.J. Mooney. Biomaterials to spatially regulate cell fate. *Advanced Materials*, 14(12):886–889, 2002.

[238] Y. Luo and M. S. Shoichet. A photolabile hydrogel for guided three-dimensional cell growth and migration. *Nat Mater*, 3(4):249–253, Apr 2004.

[239] http://www.embl-heidelberg.de/cgi/pi wrapper.pl. EMBL WWW gateway to isoelectric point service.

[240] A. L. Lehninger. *Biochemistry: the molecular basis of cell structure and function.* Worth Publishers, 1979.

[241] C. Hilger, F. Grigioni, C. De Beaufort, G. Michel, J. Freilinger, and F. Hentges. Differential binding of IgG and IgA antibodies to antigenic determinants of bovine serum albumin. *Clin Exp Immunol*, 123(3):387–394, Mar 2001.

[242] D. B. Smith and K. S. Johnson. Single-step purification of polypeptides expressed in Escherichia coli as fusions with glutathione S-transferase. *Gene*, 67(1):31–40, Jul 1988.

[243] A. G. Fincham and J. Moradian-Oldak. Amelogenin post-translational modifications: carboxy-terminal processing and the phosphorylation of bovine and porcine "trap" and "lrap" amelogenins. *Biochem Biophys Res Commun*, 197(1):248–255, Nov 1993.

[244] K. Weindel, D. Marmé, and H. A. Weich. AIDS-associated Kaposi's sarcoma cells in culture express vascular endothelial growth factor. *Biochem Biophys Res Commun*, 183(3):1167–1174, Mar 1992.

[245] V. M. Paralkar, A. K. Nandedkar, R. H. Pointer, H. K. Kleinman, and A. H. Reddi. Interaction of osteogenin, a heparin binding bone morphogenetic protein, with type IV collagen. *J Biol Chem*, 265(28):17281–17284, Oct 1990.

[246] A. Hemmati-Brivanlou, O. G. Kelly, and D. A. Melton. Follistatin, an antagonist of activin, is expressed in the Spemann organizer and displays direct neuralizing activity. *Cell*, 77(2):283–295, Apr 1994.

[247] H. G. Schmoekel, F. E. Weber, J. C. Schense, K. W. Grätz, P. Schawalder, and J. A. Hubbell. Bone repair with a form of BMP-2 engineered for incorporation into fibrin cell ingrowth matrices. *Biotechnol Bioeng*, 89(3):253–262, Feb 2005.

[248] M. Yamamoto, K. Kato, and Y. Ikada. Effect of the structure of bone morphogenetic protein carriers on ectopic bone regeneration. *Tissue Eng*, 2(4):315–326, 1996.

[249] O. A. Arosarena and W. L. Collins. Bone regeneration in the rat mandible with bone morphogenetic protein-2: a comparison of two carriers. *Otolaryngol Head Neck Surg*, 132(4):592–597, Apr 2005.

[250] T. J. Gao, T. S. Lindholm, A. Marttinen, and T. Puolakka. Bone inductive potential and dose-dependent response of bovine bone morphogenetic protein combined with type IV collagen carrier. *Ann Chir Gynaecol Suppl*, 207:77–84, 1993.

[251] U. Ripamonti, B. Van Den Heever, T. K. Sampath, M. M. Tucker, D. C. Rueger, and A. H. Reddi. Complete regeneration of bone in the baboon by recombinant human osteogenic protein-1 (hOP-1, bone morphogenetic protein-7). *Growth Factors*, 13(3-4):273–89,color plates III–VIII,pre.bk, 1996.

[252] F. Suwa, Y. R. Fang, I. Toda, C. S. Tang, L. J. Yang, Y. H. Gao, and Y. Ueda. SEM study on microvascular changes following implantation of bone morphogenetic protein combined with hydroxyapatite into experimental bone defects. *J Osaka Dent Univ*, 32(1):27–34, Apr 1998.

[253] A. H. Zisch, M. P. Lutolf, M. Ehrbar, G. P. Raeber, S. C. Rizzi, N. Davies, H. Schmkel, D. Bezuidenhout, V. Djonov, P. Zilla, and J. A. Hubbell. Cell-demanded release of VEGF from synthetic, biointeractive cell ingrowth matrices for vascularized tissue growth. *FASEB J*, 17(15):2260–2262, Dec 2003.

[254] Y. M. Elçin, V. Dixit, and G. Gitnick. Extensive in vivo angiogenesis following controlled release of human vascular endothelial cell growth factor: implications for tissue engineering and wound healing. *Artif Organs*, 25(7):558–565, Jul 2001.

[255] J. Street, M. Bao, L. deGuzman, S. Bunting, F. V. Peale, N. Ferrara, H. Steinmetz, J. Hoeffel, J. L. Cleland, A. Daugherty, N. van Bruggen, H. P. Redmond, R. A. D. Carano, and E. H. Filvaroff. Vascular endothelial growth factor stimulates bone repair by promoting angiogenesis and bone turnover. *Proc Natl Acad Sci U S A*, 99(15):9656–9661, Jul 2002.

[256] W. L. Murphy, M. C. Peters, D. H. Kohn, and D. J. Mooney. Sustained release of vascular endothelial growth factor from mineralized poly(lactide-co-glycolide) scaffolds for tissue engineering. *Biomaterials*, 21(24):2521–2527, Dec 2000.

[257] W. L. Murphy, C. A. Simmons, D. Kaigler, and D. J. Mooney. Bone regeneration via a mineral substrate and induced angiogenesis. *J Dent Res*, 83(3):204–210, Mar 2004.

[258] D. Kaigler, Z. Wang, K. Horger, D. J. Mooney, and P. H. Krebsbach. VEGF scaffolds enhance angiogenesis and bone regeneration in irradiated osseous defects. *J Bone Miner Res*, 21(5):735–744, May 2006.

[259] Y.-C. Huang, D. Kaigler, K. G. Rice, P. H. Krebsbach, and D. J. Mooney. Combined angiogenic and osteogenic factor delivery enhances bone marrow stromal cell-driven bone regeneration. *J Bone Miner Res*, 20(5):848–857, May 2005.

[260] H. Peng, V. Wright, A. Usas, B. Gearhart, H.-C. Shen, J. Cummins, and J. Huard. Synergistic enhancement of bone formation and healing by stem cell-expressed VEGF and bone morphogenetic protein-4. *J Clin Invest*, 110(6):751–759, Sep 2002.

[261] H. Peng, A. Usas, A. Olshanski, A. M. Ho, B. Gearhart, G. M. Cooper, and J. Huard. VEGF improves, whereas sFlt1 inhibits, BMP2-induced bone formation and bone healing through modulation of angiogenesis. *J Bone Miner Res*, 20(11):2017–2027, Nov 2005.

[262] D. Huang, E. A. Swanson, C. P. Lin, J. S. Schuman, W. G. Stinson, W. Chang, M. R. Hee, T. Flotte, K. Gregory, and C. A. Puliafito. Optical coherence tomography. *Science*, 254(5035):1178–1181, Nov 1991.

[263] P. J. Tadrous. Methods for imaging the structure and function of living tissues and cells: 1. Optical coherence tomography. *J Pathol*, 191(2):115–119, Jun 2000.

[264] G. J. Tearney, M. E. Brezinski, B. E. Bouma, S. A. Boppart, C. Pitris, J. F. Southern, and J. G. Fujimoto. In vivo endoscopic optical biopsy with optical coherence tomography. *Science*, 276(5321):2037–2039, Jun 1997.

[265] X. Li, S. Martin, C. Pitris, R. Ghanta, D. L. Stamper, M. Harman, J. G. Fujimoto, and M. E. Brezinski. High-resolution optical coherence tomographic imaging of osteoarthritic cartilage during open knee surgery. *Arthritis Res Ther*, 7(2):R318–R323, 2005.

[266] W. Tan, A. Sendemir-Urkmez, L. J. Fahrner, R. Jamison, D. Leckband, and S. A. Boppart. Structural and functional optical imaging of three-dimensional engineered tissue development. *Tissue Eng*, 10(11-12):1747–1756, 2004.

[267] Y. Yang, P. O. Bagnaninchi, M. A. Wood, A. J. El Haj, E. Guyot, A. Dubois, and R. K. Wang. Monitoring cell profile in tissue engineered constructs by oct. *Proceedings of SPIE*, 5695:51–57, 2005.

[268] Y. Yang, A. Dubois, X.-P. Qin, J. Li, A. El Haj, and R. K. Wang. Investigation of optical coherence tomography as an imaging modality in tissue engineering. *Phys Med Biol*, 51(7):1649–1659, Apr 2006.

[269] C. W. Han, C. R. Chu, N. Adachi, A. Usas, F. H. Fu, J. Huard, and Y. Pan. Analysis of rabbit articular cartilage repair after chondrocyte implantation using optical coherence tomography. *Osteoarthritis Cartilage*, 11(2):111–121, Feb 2003.

[270] M. E. Brezinski, G. J. Tearney, B. E. Bouma, J. A. Izatt, M. R. Hee, E. A. Swanson, J. F. Southern, and J. G. Fujimoto. Optical coherence tomography for optical biopsy. Properties and demonstration of vascular pathology. *Circulation*, 93(6):1206–1213, Mar 1996.

[271] J. C. Gladish, G. Yao, N. L'Heureux, and M. A. Haidekker. Optical transillumination tomography for imaging of tissue-engineered blood vessels. *Ann Biomed Eng*, 33(3):323–327, Mar 2005.

[272] G. Vargas, A. Readinger, S. S. Dozier, and A. J. Welch. Morphological changes in blood vessels produced by hyperosmotic agents and measured by optical coherence tomography. *Photochem Photobiol*, 77(5):541–549, May 2003.

[273] R. D. Ray and J. A. Holloway. Bone implants; preliminary report of an experimental study. *J Bone Joint Surg Am*, 39-A(5):1119–1128, Oct 1957.

[274] C. Bosch, B. Melsen, and K. Vargervik. Importance of the critical-size bone defect in testing bone-regenerating materials. *J Craniofac Surg*, 9(4):310–316, Jul 1998.

[275] K. Takagi and M. R. Urist. The reaction of the dura to bone morphogenetic protein (BMP) in repair of skull defects. *Ann Surg*, 196(1):100–109, Jul 1982.

[276] T. W. Gardiner and L. A. Toth. Stereotactic surgery and long-term maintenance of cranial implants in research animals. *Contemp Top Lab Anim Sci*, 38(1):56–63, Jan 1999.

[277] M. Fà, G. Mereu, V. Ghiglieri, A. Meloni, P. Salis, and G. L. Gessa. Electrophysiological and pharmacological characteristics of nigral dopaminergic neurons in the conscious, head-restrained rat. *Synapse*, 48(1):1–9, Apr 2003.

[278] F. Helmchen, M. S. Fee, D. W. Tank, and W. Denk. A miniature head-mounted two-photon microscope. high-resolution brain imaging in freely moving animals. *Neuron*, 31(6):903–912, Sep 2001.

[279] D. Fukumura, T. Gohongi, A. Kadambi, Y. Izumi, J. Ang, C. O. Yun, D. G. Buerk, P. L. Huang, and R. K. Jain. Predominant role of endothelial nitric oxide synthase in vascular endothelial growth factor-induced angiogenesis and vascular permeability. *Proc Natl Acad Sci U S A*, 98(5):2604–2609, Feb 2001.

[280] H. Winet and J. Y. Bao. Fibroblast growth factor-2 alters the effect of eroding polylactide-polyglycolide on osteogenesis in the bone chamber. *J Biomed Mater Res*, 40(4):567–576, Jun 1998.

[281] C. D. Brown. *Cross-linked hydrogels for the delivery of growth factors in tissue engineering.* PhD thesis, University of Washington, 2003.

[282] Y. Jin, J. Yamanaka, S. Sato, I. Miyata, C. Yomota, and M. Yonese. Recyclable characteristics of hyaluronate-polyhydroxyethyl acrylate blend hydrogel for controlled releases. *J Control Release*, 73(2-3):173–181, Jun 2001.

[283] J. J. Hwang. PhD thesis, University of Washington, 2007.

[284] M. Cesaretti, E. Luppi, F. Maccari, and N. Volpi. A 96-well assay for uronic acid carbazole reaction. *Carbohydrate Polymers*, 54(1):59–61, 2003.

[285] X. B. Zhao, J. E. Fraser, C. Alexander, C. Lockett, and B. J. White. Synthesis and characterization of a novel double crosslinked hyaluronan hydrogel. *J Mater Sci Mater Med*, 13(1):11–16, Jan 2002.

[286] N. Girard, C. Maingonnat, P. Bertrand, H. Tilly, J.-P. Vannier, and B. Delpech. Human monocytes synthesize hyaluronidase. *Br J Haematol*, 119(1):199–203, Oct 2002.

[287] L. C. Junqueira, G. Bignolas, and R. R. Brentani. Picrosirius staining plus polarization microscopy, a specific method for collagen detection in tissue sections. *Histochem J*, 11(4):447–455, Jul 1979.

[288] L. C. Junqueira, G. S. Montes, and E. M. Sanchez. The influence of tissue section thickness on the study of collagen by the Picrosirius-polarization method. *Histochemistry*, 74(1):153–156, 1982.

[289] D. Dayan, Y. Hiss, A. Hirshberg, J. J. Bubis, and M. Wolman. Are the polarization colors of picrosirius red-stained collagen determined only by the diameter of the fibers? *Histochemistry*, 93(1):27–29, 1989.

[290] C. W. Gibson, U. Kucich, P. Collier, G. Shen, S. Decker, M. Bashir, and J. Rosenbloom. Analysis of amelogenin proteins using monospecific antibodies to defined sequences. *Connect Tissue Res*, 32(1-4):109–114, 1995.

[291] E. C. Swanson, H. K. Fong, B. L. Foster, M. L. Paine, C. W. Gibson, M. L. Snead, and M. J. Somerman. Amelogenins regulate expression of genes associated with cementoblasts in vitro. *Eur J Oral Sci*, 114 Suppl 1:239–43, May 2006.

[292] R. L. Kronenthal. Biodegradable polymers in medicine and surgery. *Polym Sci Technol*, 8:119–127, 1974.

[293] S. M. Li, H. Garreau, and M. Vert. Structure-property relationships in the case of the degradation of massive aliphatic poly-(alpha-hydroxy acids) in aqueous media, part 1: Poly(DL-lactic acid). *J Mater Sci Mater Med*, 1:123–130, 1990.

[294] S. M. Li, H. Garreau, and M. Vert. Structure-property relationships in the case of the degradation of massive aliphatic poly-(alpha-hydroxy acids) in aqueous media, part 2: Degradation of lactide-glycolide copolymers: PLA37.5GA25 and PLA75GA25. *J Mater Sci Mater Med*, 1:131–139, 1990.

[295] S. M. Li, H. Garreau, and M. Vert. Structure-property relationships in the case of the degradation of massive aliphatic poly-(alpha-hydroxy acids) in aqueous media, part 3: Influence of morphology of poly(L-lactic acid). *J Mater Sci Mater Med*, 1:198–206, 1990.

[296] M. Therin, P. Christel, S. Li, H. Garreau, and M. Vert. In vivo degradation of massive poly(alpha-hydroxy acids): validation of in vitro findings. *Biomaterials*, 13(9):594–600, 1992.

[297] M. Vert, J. Mauduit, and S. Li. Biodegradation of PLA/GA polymers: increasing complexity. *Biomaterials*, 15(15):1209–1213, Dec 1994.

[298] I. Grizzi, H. Garreau, S. Li, and M. Vert. Hydrolytic degradation of devices based on poly(DL-lactic acid) size-dependence. *Biomaterials*, 16(4):305–311, Mar 1995.

[299] G. Spenlehauer, M. Vert, J. P. Benoit, and A. Boddaert. In vitro and in vivo degradation of poly(D,L lactide/glycolide) type microspheres made by solvent evaporation method. *Biomaterials*, 10(8):557–563, Oct 1989.

[300] G. E. Visscher, J. E. Pearson, J. W. Fong, G. J. Argentieri, R. L. Robison, and H. V. Maulding. Effect of particle size on the in vitro and in vivo degradation rates of poly(DL-lactide-co-glycolide) microcapsules. *J Biomed Mater Res*, 22(8):733–746, Aug 1988.

[301] G. E. Visscher, M. A. Robison, and G. J. Argentieri. Tissue response to biodegradable injectable microcapsules. *J Biomater Appl*, 2(1):118–131, Jul 1987.

[302] G. E. Visscher, R. L. Robison, H. V. Maulding, J. W. Fong, J. E. Pearson, and G. J. Argentieri. Biodegradation of and tissue reaction to 50:50 poly(DL-lactide-co-glycolide) microcapsules. *J Biomed Mater Res*, 19(3):349–365, Mar 1985.

[303] X. Ma, J. Q. Lu, R. S. Brock, K. M. Jacobs, P. Yang, and X.-H. Hu. Determination of complex refractive index of polystyrene microspheres from 370 to 1610 nm. *Phys Med Biol*, 48(24):4165–4172, Dec 2003.

[304] M. Firbank and D. T. Delpy. A design for a stable and reproducible phantom for use in near infra-red imaging and spectroscopy. *Phys Med Biol*, 38:847–853, 1993.

[305] A. J. DeFail, C. R. Chu, N. Izzo, and K. G. Marra. Controlled release of bioactive TGF-beta 1 from microspheres embedded within biodegradable hydrogels. *Biomaterials*, 27(8):1579–1585, Mar 2006.

[306] S. B. Adams, P. R. Herz, D. L. Stamper, M. J. Roberts, S. Bourquin, N. A. Patel, K. Schneider, S. D. Martin, S. Shortkroff, J. G. Fujimoto, and M. E. Brezinski. High-resolution imaging of progressive articular cartilage degeneration. *J Orthop Res*, 24(4):708–715, Apr 2006.

[307] X. Xu, R. K. Wang, and A. El Haj. Investigation of changes in optical attenuation of bone and neuronal cells in organ culture or three-dimensional constructs in vitro with optical coherence tomography: relevance to cytochrome oxidase monitoring. *Eur Biophys J*, 32(4):355–362, Jul 2003.

[308] A. M. Rollins, S. Yazdanfar, J. K. Barton, and J. A. Izatt. Real-time in vivo color Doppler optical coherence tomography. *J Biomed Opt*, 7(1):123–129, Jan 2002.

[309] P. Pietzonka, B. Rothen-Rutishauser, P. Langguth, H. Wunderli-Allenspach, E. Walter, and H. P. Merkle. Transfer of lipophilic markers from PLGA and polystyrene nanoparticles to caco-2 monolayers mimics particle uptake. *Pharm Res*, 19(5):595–601, May 2002.

VITA

EDUCATION

- Ph.D. Candidate, Department of Bioengineering, University of Washington (UW), 2001 to present
- BSE, Department of Chemical Engineering, Princeton University, 1994-1998

AWARDS AND HONORS

- National Science Foundation Fellowship – 2003-2006
- Henry L. Gray Memorial Fellowship (UW) – 2001-2002
- Sigma Xi Grant-in-Aid-of-Research – 2006
- Society of Women Engineers' Outstanding Graduate Female Award for Department of Bioengineering (UW) – 2006
- Finalist in National Student Poster Competition (Society of Women Engineers National Conference) – 2006
- Student Travel Award (BMES Annual Meeting) – 2003

RESEARCH AND WORK EXPERIENCE

- Graduate Research Associate, Department of Bioengineering, University of Washington, Seattle, WA 2001 to present

- Technical Project Coordinator, Therics, Inc., Princeton, NJ 2000-2001 Research Associate, Therics, Inc., Princeton, NJ 1998-2000

- Undergraduate Research Project, Princeton University, Princeton, NJ 1997-1998

- Research Assistant, MIT, Cambridge, MA Summers 1996, 1997

PUBLICATIONS

- West MW, Wang W, Patterson J, Mancias JD, Beasley JR & Hecht MH. (1999) De novo amyloid proteins from designed combinatorial libraries. Proc Natl Acad Sci U S A 1999 Sep 28; 96(20):11211-6.

- Hecht MH, West MW, Patterson J, Mancias JD, Beasley JR, Broome BM & Wang W. (2001) Designed Combinatorial Libraries of Novel Amyloid-like Proteins. Pages 127-138 in Self-assembling Peptide Systems in Biology, Medicine and Engineering, (edited by A. Aggeli, N. Boden, S. Zhang) Kluwer Academic Publishers, The Netherlands.

PATENTS

- Beam HA, Bradbury TJ, Chesmel KD, Gaylo CM, Litwak AA, Liu Q, Materna PA, Monkhouse D, Patterson J, Pryor TJ, Saini S, Surprenant HL, Wang CC, West TG, & Yoo J. Method and apparatus for engineered regenerative biostructures such as hydroxyapatite substrates for bone healing applications. US Patent #7,122,057 (October, 2006).

UNDERGRADUATE JOURNALS

- Thomas D, Patterson J & Stayton PS. (2005) In Vitro Evaluation of the Cytotoxicity of Hyaluronic Acid Hydrogels. JURIBE Summer 2005: 49-52.

CONFERENCE ABSTRACTS

- Patterson J, Siew R, Pak MG, Herring SW, Li X, & Stayton PS. Angiogenic and Osteoinductive Hydrogel Scaffolds for Bone Regeneration. Society of Women Engineers National Conference; October 2006, Kansas City, MO. (Poster competition finalist)

- Patterson J, Siew R, Herring SW & Stayton PS. Angiogenic and Osteoinductive Hydrogel Scaffolds for Bone Regeneration. Society for Biomaterials Annual Meeting; April 2006, Pittsburgh, PA. (Oral presentation)

- Patterson J, Siew R, Herring SW, Li X & Stayton PS. Temporal Characterization of Bone Regeneration Induced by Angiogenic and Osteoinductive Hydrogel Scaffolds. Regenerate World Congress on Tissue Engineering and Regenerative Medicine; April 2006, Pittsburgh, PA. (Poster presentation)

- Patterson J, Herring SW, Stayton PS & Li X. In Vivo Imaging of Bone Regeneration Induced by Angiogenic and Osteoinductive Hydrogel Scaffolds. Biomedical Optics Meeting (Optical Society of America); March 2006, Fort Lauderdale, FL. (Poster presentation)

- Siew R, Patterson J, McGonigle J, Scatena M, Herring S & Stayton PS. Characterization of Hyaluronic Acid Hydrogels with OPG for Bone Regeneration. Sigma Xi Annual Meeting and Student Research Conference; November 2005, Seattle, WA. (Gold ribbon awarded to Ruth in undergraduate poster competition)

- McGonigle JS, Huynh D, Patterson J, Stayton PS, Hoffman AS, Giachelli CM & Scatena M. Controlled Release of Osteoprotegerin for the Promotion of Angiogenesis. The American Society for Cell Biology 2005 Summer Meeting on Engineering Cell BiologyThe Cell in Context; July 2005, Seattle, WA.

- Patterson J, Herring SW, Stayton PS & Li X. Optical Coherence Tomography of Bone Tissue Engineering Scaffolds. BIOS 2005 (The International Society for Optical Engineering); January 2005, San Jose, CA. (Oral presentation)

- Patterson J, Li X, Herring SW & Stayton PS. Regenerative Matrices for the Controlled Release of Osteogenic Factors. Regenerate; June 2004, Seattle, WA. (Oral presentation)

- Patterson J & Stayton PS. Regenerative Matrices for Oriented Craniofacial Bone Growth. Biomedical Engineering Society; October 2003, Nashville, TN. (Oral presentation)

- Simon JL, Parsons JR, Rekow ED, Chesmel K, Patterson J, Thompson VP, Kemnitzer J & Ricci JL. Effect of Pore Architecture on Bone In-growth in 3-D Printed Scaffolds. Society for Biomaterials; April 2002, Tampa, FL.

- Dutta Roy T, Patterson J, Chesmel K, Simon J, Rekow D, Thompson V, Ricci J & Parsons R. In Vivo Histological Response of Ceramic Structures Created Via Three-Dimensional Fabrication Techniques. Society for Biomaterials; April 2002, Tampa, FL.

- Dutta Roy T, Patterson J, Chesmel K, Payumo F, Doshi A, Choi J & Parsons JR. An In Vivo Analysis of Bone Repair Products Made by Three-Dimensional Fabrication Techniques. Orthopedic Research Society; February 2001, San Francisco, CA.

- Dutta Roy T, Patterson J, Chesmel K, Payumo F, Sabatino C, Nadkami P, Hoonjan A & Parsons JR. In Vivo Analysis of Materials for Bone Repair Products Made by Three-Dimensional Fabrication Techniques. Society for Biomaterials; April 2001, Saint Paul, MN.